Internal Report
DESY F35D-95-05
August 1995

A Measurement of the Proton Structure Function F_2 with the ZEUS Detector at HERA

by

L. Hagge

A Measurement of the Proton Structure Function F_2 with the ZEUS Detector at HERA

Dissertation

zur Erlangung des Doktorgrades
des Fachbereichs Physik
der Universität Hamburg

vorgelegt von

Lars Hagge
aus Hamburg

Hamburg
1995

Gutachter der Dissertation:	Prof. Dr. E. Lohrmann Prof. Dr. V. Blobel
Gutachter der Disputation:	Prof. Dr. E. Lohrmann Prof. Dr. G. Heinzelmann
Datum der Disputation:	30. Juni 1995
Sprecher des Fachbereichs Physik und Vorsitzender des Promotionsausschusses:	Prof. Dr. B. Kramer

The intellect of men is forced to choose
the perfection of life
or the perfection of work.

W. B. Yeats. *The Choice*

Abstract

The proton structure function F_2 has been extracted from data which was taken by the ZEUS experiment at HERA during 1993. The analysis extends to values of Q^2 up to $2000\,\mathrm{GeV}^2$ and x down to $2 \cdot 10^{-4}$. The event kinematics have been obtained from different reconstruction methods, the data has been binned in (x, Q^2) and (y, Q^2), and the structure function has been unfolded iteratively and by matrix inversion. Results for the different analysis methods are found to agree. Reconstructing y from the hadronic final state and Q^2 from the scattered electron allows to connect the measured phase space with results from fixed target experiments.

Zusammenfassung

Die Proton-Strukturfunktion F_2 wurde aus Daten extrahiert, die 1993 mit dem ZEUS Experiment am HERA Speicherring genommen wurden. Die Analyse erstreckt sich in Q^2 zu Werten von bis zu $2000\,\mathrm{GeV}^2$, in x zu Werten bis herab zu $2 \cdot 10^{-4}$. Die Ereignis-Kinematik wurde aus verschiedenen Rekonstruktions-Verfahren bestimmt, die Daten wurden in (x, Q^2) und (y, Q^2) gebinnt, und die Strukturfunktion wurde iterativ und durch Inversion der Transfer-Matrix entfaltet. Die aus den verschiedenen Analysemethoden gewonnenen Resultate stimmen miteinander überein. Wird y aus dem hadronischen Endzustand rekonstruiert und Q^2 über das gestreute Elektron, so kann der gemessene Phasenraum an Resultate aus Fixed-Target Experimenten angeschlossen werden.

Contents

List of Tables

List of Figures

Chapter 1

Introduction

If anyone doesn't understand a passage,
all he needs do is read it aloud.

James Joyce

The idea that particles are built from smaller constituents has been developed in a long interplay of theoretical predictions and experimental observations, which can be traced back as far as the famous experiments and the atomic model of Ernest Rutherford. It cumulated in the electron-proton scattering experiments at SLAC and DESY and the emergence of the quark-parton model in the sixties, followed by the (ongoing) development and experimental exploration of Quantum Chromodynamics.

The compositeness of nucleons is described by structure functions. Their asymptotic behaviour in $x \to 0$ and $Q^2 \to \infty$ reflects the nature of both the partons and their interactions — the self-coupling of gluons and quark pair production at low values of x, and asymptotic freedom, or possible new layers of compositeness at high values of Q^2.

The precise knowledge of the nucleon structure function is an essential ingredient for the analysis of particle reactions involving high transverse momenta. The dominant (hard) process may be calculable at parton-level, but it still has to be folded with the probability for the occurence of a certain parton within the hadron. Absolute values of structure functions can presently be determined only from experiment, however several theoretical concepts are at hand to make a QCD evolution of the structure function in x and Q^2 and interpret their shape.

With the advent of the HERA experiments, the kinematic region of structure function measurements has been extended by two orders of magnitude towards lower values of x and higher values of Q^2. The initial measurements were based on 20nb^{-1} of data taken during fall 1992 [H1 93a, ZEU93d]. They reported for the first time a rise of the structure function towards lower values of x, as it has been predicted for a Lipatov-like gluon distribution. The rise of F_2 has been confirmed by the subsequent measurements based on the twenty-fold statistics collected during 1993 [H1 95, ZEU95c].

In the 1993 data taking period, about 1.1 million events were recorded for structure function studies, providing comfortable statistics for an F_2 analysis, and focussing the efforts on sys-

tematic studies of the analysis method. This thesis extracts the proton structure function, $F_2(x, Q^2)$, from the data which was taken with the ZEUS experiment during 1993. Special emphasis is put on the methodology: the event kinematics are reconstructed from different sets of measured quantities, the data are binned in different kinematic variables, and two different approaches are used for unfolding detector effects from the observed event distribution. The structure function is extracted for all these methods, and the results are compared.

The thesis first summarizes some experiments and concepts which led to the present understanding of deep inelastic scattering and gives a brief introduction to QCD (chapter 2), followed by a short description of the experimental setup, HERA and ZEUS (chapter 3). Chapter 4 discusses in detail the different procedures involved in extracting $F_2(x, Q^2)$ from the data, and chapter 5 presents and compares the resulting structure functions. The thesis is concluded by a brief summary (chapter 6).

Chapter 2

Nucleon Structure from ep Scattering

Work without Hope draws nectar in a sieve,
but Hope without an object cannot live.
Samuel Taylor Coleridge, *Work without Hope*

2.1 Early Results

Based on Rutherford's [Rut11] famous work, which led to the discovery of atomic nuclei, α-Particles were scattered off gold atoms [GM13]. Because the nucleus is so small, the cross section in these experiments is to a good approximation given by elastic scattering of charged particles from the potential of a point-like source ($Z = 1$). In the non-relativistic case, for $Z = 1$ of both the projectile and the source,

$$\frac{d\sigma}{d\Omega} = \frac{\alpha^2}{4(p\beta)^2}\frac{1}{\sin^4\frac{\theta}{2}}, \tag{2.1}$$

where p is the momentum of the projectile, θ its scattering angle, both measured in the laboratory frame where the target is at rest.

Mott [Mot29] calculated the cross section for relativistic electrons scattering off a point-like target,

$$\left(\frac{d\sigma}{d\Omega}\right)_{\text{Mott}} = \frac{\alpha^2}{4E^2}\frac{\cos^2\frac{\theta}{2}}{\sin^4\frac{\theta}{2}}\frac{1}{1+\frac{2E}{M}\sin^2\frac{\theta}{2}}. \tag{2.2}$$

where the different terms arise from Rutherford scattering, the target recoil, and the spin of the electron. E is the energy of the electron, M is the target mass.

In the case of non-point-like targets, eqn. (2.2) has to be modified by a form factor $F(q)$ which accounts for the extended charge distribution,

$$\frac{d\sigma}{d\Omega} = \left(\frac{d\sigma}{d\Omega}\right)_{\text{Mott}} |F(q)|^2. \tag{2.3}$$

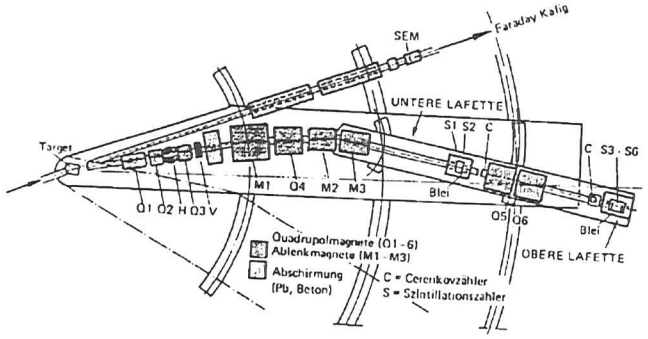

Figure 2.1: Schematic view of a one-arm spectrometer. The electron hits the target (left) and is detected with the spectrometer arm. Q and M label quadrupole focusing and dipole bending magnets. C are Cerenkov counters, and S1-S6 indicate scintillator counter-hodoscopes [B+67, Hab89].

where q is the four-momentum transferred from the electron to the target. For static spin-less targets, the form factor is the Fourier transform of the spatial charge distribution $\rho(x)$.

$$F(q) = \int d^3x \, e^{iqx} \rho(x). \tag{2.4}$$

For ep scattering, however, eqn. (2.3) is still not suitable, because it ignores the proton spin. A second form factor is required to account for the proton's anomalous magnetic moment. The calculation has been first performed by Rosenbluth [Ros50].

$$\frac{d\sigma}{d\Omega} = \left(\frac{d\sigma}{d\Omega}\right)_{\text{Mott}} \left\{ \frac{G_E^2 + \tau G_M^2}{1+\tau} + 2\tau G_M^2 \tan^2\frac{\theta}{2} \right\}. \tag{2.5}$$

where $\tau = -q^2/4M^2$. Thus, the electric and magnetic form factors G_E and G_M can be measured by plotting $\frac{d\sigma}{d\Omega}$ versus $\tan^2\frac{\theta}{2}$.

Fig. 2.1 shows a one-arm spectrometer, which is a typical setup of a first-generation fixed-target ep scattering experiment. An incident electron beam hits a (liquid hydrogen) target and is monitored downstream with a Faraday cage. Scattered electrons are detected with a movable spectrometer arm. The electrons are tagged in scintillator counter-hodoscopes and discriminated against muons and hadrons with Čerenkov counters. A sequence of bending dipole and focusing quadrupole magnets is used to analyze the electron's momentum.

The first relativistic ep scattering experiment has been carried out at SLAC in 1953 [FHM53]. The measurement of the elastic cross section for different incident electron energies at different scattering angles gave the first experimental evidence for a finite size of the proton [HM55, CH56]. With more accurate data, phenomenological fits were applied to the measured form

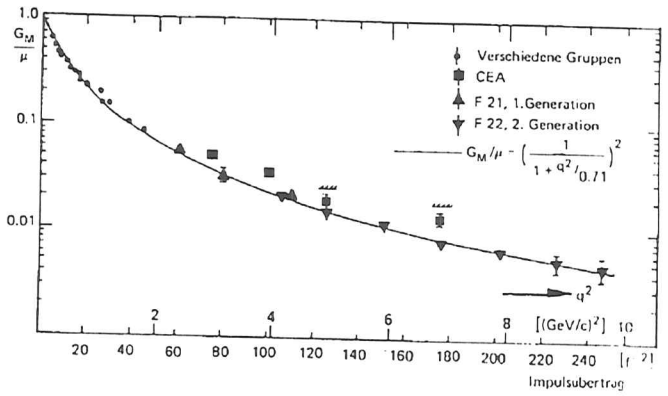

Figure 2.2: q^2 dependence of the magnetic form factor G_M obtained from experiment [Hab89].

factors, and the q^2 dependence of the elastic form factors was parameterized by [B+70, B+79].

$$G_E^p(q^2) \cong \frac{G_M^p(q^2)}{2.79} \cong \frac{G_M^N(q^2)}{-1.91} \cong \frac{1}{\left(1 + \frac{|q|^2}{0.71\,\text{GeV}^2}\right)^2}. \tag{2.6}$$

thus explicitly introducing a length scale (cf. fig. 2.2).

For inelastic ep scattering, and expressions for the cross section which is similar to eqn. (2.5) has been obtained by extending the concept of single virtual photon exchange to those processes [DW64].

$$\left(\frac{d^2\sigma}{dE'd\Omega}\right)_{ep\to eX} = \frac{\alpha^2}{4E^2}\frac{\cos^2\frac{\theta}{2}}{\sin^4\frac{\theta}{2}} \left\{ W_2(\nu, Q^2) + 2W_1(\nu, Q^2)\tan^2\frac{\theta}{2} \right\}. \tag{2.7}$$

where E and E' are the energies of the incident and scattered electron. The inelastic form factors, W_1 and W_2, are related to their counterparts in elastic scattering, G_E and G_M. They are functions of two invariant variables[1], $\nu = pq/M$ and $Q^2 = -(k-k')^2$, which refer to the energy and momentum transfer, respectively. In the target rest frame,

$$\nu = E - E'. \tag{2.8}$$

$$-q^2 = Q^2 = 4EE'\sin^2\frac{\theta}{2} \tag{2.9}$$

Bjorken has introduced a dimension-less variable x to investigate the structure functions W_1 and W_2 in the limit $\nu, Q^2 \longrightarrow \infty$, ν/Q^2 fixed.[2]

$$x = \frac{Q^2}{2M\nu}. \tag{2.10}$$

[1] The kinematic variables used in lepton nucleon scattering are summarized in section 2.2.1. Here, p, k and k' are the four-momenta of the target, the incident and the final electron, and M is the target mass.

[2] $0 < x < 1$, with $x = 1$ for elastic scattering.

In this Bjorken limit he predicted the structure functions to tend to functions of the ratio x only [Bjo69], ie

$$\lim_{\text{Bj}} MW_1(\nu, Q^2) = F_1(x) + \mathcal{O}(\frac{1}{Q^2}). \tag{2.11}$$

$$\lim_{\text{Bj}} \nu W_2(\nu, Q^2) = F_2(x) + \mathcal{O}(\frac{1}{Q^2}). \tag{2.12}$$

This scaling behaviour has first been observed by experiments for x around the value $\frac{1}{3}$ and $Q^2 \gtrsim 4\,\text{GeV}^2$ [Tay75, A+76, B+79].

Scaling is characteristic for scattering off point-like objects. Hence at high values of Q^2, ep-scattering can be interpreted as an electron scattering off point-like objects within the proton. These so-called partons were soon related through Feynman's quark-parton model (QPM) [Fey72] to the quarks which were predicted by Gell-Mann [GM64] as constituents of the nucleon. The QPM succeeded in attributing the inelastic form factors to the distributions of the quarks within the proton.

Combination of data from different scattering angles θ at the same values of ν and Q^2 allowed to separate W_1 and W_2 [A+69]. The data was compatible with the Callan-Gross relationship [CG69],

$$2xF_1(x) = F_2(x). \tag{2.13}$$

which holds only for spin-$\frac{1}{2}$ partons.

With more precise inelastic data covering a larger range in x and Q^2 evidence for scale breaking was found. At low values of x ($x \lesssim 0.3$) F_2 is observed to rise logarithmically with increasing Q^2, while at high values of x F_2 decreases logarithmically with Q^2. By mere coincidence the first F_2 measurements at SLAC were carried out in the region of x where the variations of F_2 with Q^2 are small. Scaling violations are expected from QCD processes, ie gluon bremsstrahlung and quark pair production.

2.2 Calculation of Cross Sections

2.2.1 Kinematic Variables in Lepton Nucleon Scattering

The diagram for deep inelastic lepton-nucleon scattering in lowest order of α is shown in fig. 2.3. An incident electron, $k = (E, \mathbf{k_e})$, is deflected by a nucleon target $p = (M, \mathbf{p})$ of mass M and is observed at an angle θ with $k' = (E', \mathbf{k'_e})$. The nucleon transforms into a hadronic final state X with invariant mass squared $W^2 = M'^2 = p'^2$.

Table 2.1 summarizes the kinematic variables used in lepton-nucleon deep inelastic scattering (DIS). Q^2 and ν are Lorentz scalars which refer to the momentum transfer and energy loss of the incident lepton, x is the Bjorken scaling variable, and y is the fractional energy transfer to the nucleon in the target rest frame.

k	=	$(E, \mathbf{k_e})$	4-vector of incident electron
k'	=	$(E', \mathbf{k'_e})$	4-vector of scattered electron
p	=	$(E_p, \mathbf{p})$	4-vector of initial proton
p'	=	$(E'_h, \mathbf{p'})$	4-vector of hadronic final state
q	=	$k - k'$	4-vector of virtual photon
	=	$p' - p$	
E	=		energy of incident electron (HERA frame)
E_p	=		energy of incident proton (HERA frame)
E'	=		energy of scattered lepton (HERA frame)
θ	=		angle of scattered electron (lab* frame)
M			mass of target nucleon
W^2	=	$(p+q)^2$	inv. mass of hadronic final state
	=	p'^2	
Q^2	=	$-q^2 > 0$	
	=	$4EE'\sin^2\frac{\theta}{2}$	
ν	=	$(p \cdot q)/M$	
s	=	$(k+p)^2$	CMS energy squared
	=	$4EE_p$	(HERA frame)
x	=	$Q^2/2M\nu$	Bjorken scaling variable
	=	1	for elastic scattering
y	=	$(p \cdot q)/(p \cdot k)$	
Q^2	=	sxy	(high E limit)

Table 2.1: Kinematic variables in DIS (* in the HERA frame, θ is measured against the direction of the incident proton).

2.2.2 Cross Section in Lowest Order QED

Using first order perturbation theory, the amplitude T_{fi} for electron-proton scattering in the one-photon exchange picture is

$$T_{fi} = -i \int j_\mu \frac{-g^{\mu\nu}}{q^2} J^\nu d^4x. \tag{2.14}$$

j_μ and J^ν refer to the electron and proton current, and q is the four-momentum of the exchanged photon (cf. fig. 2.3, tab. 2.1).

$$j_\mu = -e\overline{u}(k')\gamma_\mu u(k) e^{i(k'-k)x} \tag{2.15}$$

$$J^\nu = -e\overline{u}(p')\Gamma^\nu u(p) e^{i(p'-p)x}. \tag{2.16}$$

The proton coupling differs from the electron because it is no point particle. Thus, similar to the Rosenbluth equation (2.5), the proton structure has to be parameterized in Γ^ν (cf. [HM84]).

$$\Gamma^\nu = F_1(q^2)\gamma^\nu + \frac{\kappa}{2M} F_2(q^2) i\sigma^{\nu\rho} q_\rho \tag{2.17}$$

where κ is the anomalous magnetic moment. However, eqns. (2.16) and (2.17) hold only for elastic scattering. In case of inelastic scattering the proton breaks up, and the final state

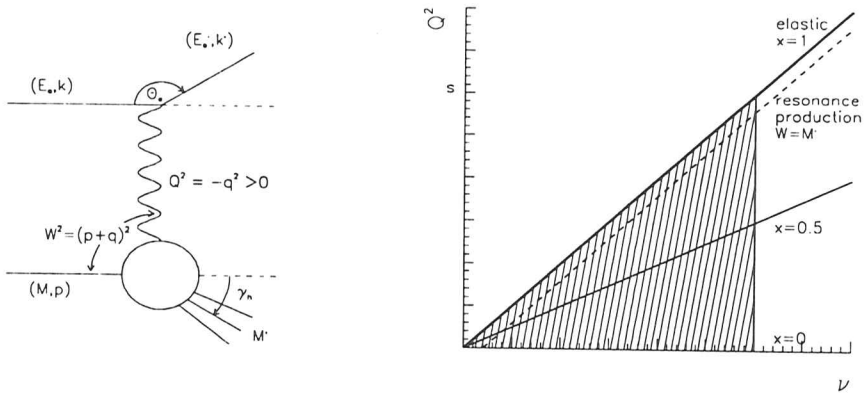

Figure 2.3: Left: Diagram in lowest order α and kinematic variables used in deep inelastic scattering (Note that in the HERA frame θ_e is measured against the direction of the incident proton.). Right: Phase space available to lepton nucleon collisions (Resonances in inelastic scattering correspond to lines parallel to the elastic line.).

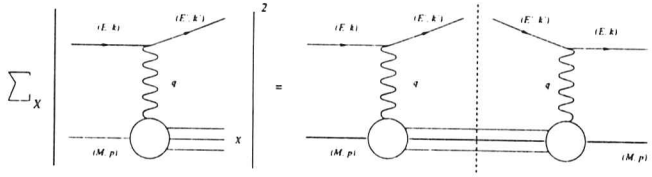

Figure 2.4: Hadronic tensor $W_{\mu\nu}$ and Thomson amplitude $T_{\mu\nu}$ are related through the optical theorem.

consists of several hadrons which can no longer be described by a single Dirac fermion spinor $u(p)$. Thus, for QED-like calculations of the cross section, usually the hadronic tensor $W_{\mu\nu}$ is parameterized instead of the proton current J^ν. The hadronic tensor is related to the Thomson amplitude (2.14) through the optical theorem (cf. fig. 2.4).

$$W_{\mu\nu} = \frac{1}{4\pi}\mathrm{Im}\, T_{\mu\nu}. \tag{2.18}$$

In terms of lepton and hadron tensor, the cross section for deep inelastic electron proton scattering reads

$$\left(\frac{d^2\sigma}{dE'd\Omega}\right)_{ep\to eX} = \frac{\alpha^2}{q^4}\frac{E'}{E}(L')^{\mu\nu}W_{\mu\nu}. \tag{2.19}$$

$(L')^{\mu\nu}$ is the electron tensor which is known from QED. After having summed and averaged

over the spins.

$$(L')^{\mu\nu} = 2(k'^\mu k^\nu + k'^\nu k^\mu - (k'\cdot k - m^2)\,g^{\mu\nu}). \tag{2.20}$$

$W_{\mu\nu}$ is a second rank tensor because the current operators are four-vectors. It can depend on q_μ, p_μ and $g_{\mu\nu}$. γ_μ is not included in $W_{\mu\nu}$ as the cross section has already been summed and averaged over spins. Parity violating terms $\varepsilon_{\mu\nu\rho\sigma}p^\mu q^\sigma$ cannot occur because the currents are polar vectors. Anti-symmetric terms need not be included to $W_{\mu\nu}$ because they don't contribute to the cross section due to the symmetry of $(L')^{\mu\nu}$. Thus, exploiting the continuity equation

$$\partial_\mu J^\mu = 0 \implies q_\mu W_{\mu\nu} = W_{\mu\nu}q_\nu = 0. \tag{2.21}$$

the most general form of the hadronic tensor can be written as

$$W_{\mu\nu} = W_1\left(-g_{\mu\nu} + \frac{q_\mu q_\nu}{q^2}\right) + W_2\frac{1}{M^2}\left(p_\mu - \frac{p\cdot q}{q^2}q_\mu\right)\left(p_\nu - \frac{p\cdot q}{q^2}q_\nu\right). \tag{2.22}$$

where W_1 and W_2 are scalar functions which can depend on the Lorentz scalars which can be constructed from the kinematic variables at the hadronic vertex.

Contracting $(L')^{\mu\nu}$ and $W_{\mu\nu}$ yields

$$(L')^{\mu\nu}W_{\mu\nu} = 4W_1(k'\cdot k - 2m^2) + 2W_2\frac{1}{M^2}\left[(p\cdot k')(p\cdot k) - M^2(k\cdot k' - m^2)\right]. \tag{2.23}$$

Including the flux factor and neglecting the electron mass gives the expression for the cross section which was already given in the previous section.

$$\left(\frac{d^2\sigma}{dE'd\Omega}\right)_{ep\to eX} = \frac{\alpha^2}{4E^2}\frac{\cos^2\frac{\theta}{2}}{\sin^4\frac{\theta}{2}}\left\{W_2(\nu, Q^2) + 2W_1(\nu, Q^2)\tan^2\frac{\theta}{2}\right\}. \tag{2.24}$$

Comparison with the Rosenbluth equation (2.5) suggests that the structure functions can be intuitively related to G_E and G_M in case of inelastic ep scattering.

With the help of the formulae of section 2.2.1 the cross-section can be written in terms of the Lorentz-invariant variables x, y, or Q^2.

$$\left(\frac{d^2\sigma}{dxdQ^2}\right)_{ep\to eX} = \frac{4\pi\alpha^2}{xQ^4}\left\{(1-y)F_2(x) + xy^2F_1(x)\right\}. \tag{2.25}$$

$$\text{or}\quad \left(\frac{d^2\sigma}{dxdy}\right)_{ep\to eX} = \frac{4\pi\alpha^2}{sx^2y^2}\left\{(1-y)F_2(x) + xy^2F_1(x)\right\}. \tag{2.26}$$

In an alternative approach [DW64, Han63], the cross section (2.5) is related to the absorption cross sections for transverse and longitudinally polarized virtual photons, σ_T and σ_L.

$$\left(\frac{d^2\sigma}{dE'd\Omega}\right)_{ep\to eX} = \frac{\alpha^2}{2E^2}\frac{K}{M^2}\frac{1}{1-\varepsilon}\frac{\sigma_T + \varepsilon\sigma_L}{\sigma_0} \tag{2.27}$$

with

$$\sigma_0 = \frac{4\pi^2\alpha}{M^2} = 127\mu b. \quad (2.28)$$

$$K = \frac{W^2 - M^2}{2M} = \nu - \frac{Q^2}{2M}. \quad (2.29)$$

$$\varepsilon = \left(1 - \left(1 + \frac{\nu^2}{Q^2}\right)\tan^2\frac{\theta}{2}\right)^{-1}. \quad (2.30)$$

where ε is a polarization parameter. σ_T and σ_L are related to the structure functions via

$$\sigma_T = \frac{4\pi^2\alpha}{K} W_1. \quad (2.31)$$

$$\sigma_L = \frac{4\pi^2\alpha}{K}\left[\left(1 + \frac{\nu^2}{Q^2}\right) W_2 - W_1\right]. \quad (2.32)$$

or in terms of the dimension-less structure functions, F_1 and F_2, and using that $\nu/Q^2 \gg 1$ in the phase space accessible to HERA,

$$\sigma_T = \frac{4\pi^2\alpha}{Q^2} F_1. \quad (2.33)$$

$$\sigma_L = \frac{4\pi^2\alpha}{Q^2}\left[\frac{F_2}{2x} - F_1\right]. \quad (2.34)$$

The latter expression is used to introduce the longitudinal structure function, F_L, which vanishes for spin-$\frac{1}{2}$ partons.

$$F_L = F_2 - 2xF_1. \quad (2.35)$$

In the literature, also the ratio $R = \sigma_L/\sigma_T$ is used.

2.2.3 Exchange of Weak Bosons

Neutral Current Deep Inelastic Scattering.

At high values of Q^2, Z exchange has to be included in the cross section for ep scattering. The neutral current then becomes

$$j_\mu^{NC} = \overline{u}(k')\gamma_\mu \frac{1}{2}(c_V^e - c_A^e\gamma_5)u(k). \quad (2.36)$$

c_V^e and c_A^e are the electro-weak coupling constants of the electron as defined in the Standard Model. The lepton tensor becomes

$$L^{\mu\nu} = 4c_V^e\left[k^\mu k'^\nu + k'^\mu k^\nu - g^{\mu\nu}\left(k'\cdot k - m^2\right)\right] + 4ic_A^e\varepsilon_{\mu\nu\rho\sigma}k^\rho k'^\sigma. \quad (2.37)$$

Thus in case of weak currents, anti-symmetric components contribute to the cross-section, and $q^\mu W_{\mu\nu}$ no longer vanishes since the weak current is not conserved. $W_{\mu\nu}$ needs now to be

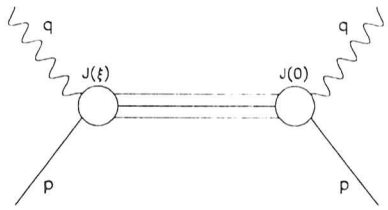

Figure 2.5: Amplitude for forward $\gamma^* p$ scattering. ξ is the space-time separation of the two current operators.

parameterized in terms of six structure functions [Nac91], three of which can be dropped when exploiting CP invariance and neglecting the lepton mass [Rob90].

The resulting cross section can be written similar to eqn. (2.26).

$$\left(\frac{d^2\sigma}{dxdy}\right)_{e^\pm p\to eX} = \frac{4\pi\alpha^2}{sx^2y^2}\left\{(1-y)F_2(x) + xy^2F_1(x) \pm (y - \frac{y^2}{2})xF_3(x)\right\}. \quad (2.38)$$

However, compared to eqn. (2.26) the structure functions F_i now parameterize the exchange of photons, the exchange of Z-bosons, and the electro-weak interference. Factors containing the coupling constants and Z propagator are absorbed in the F_i's. The additional structure function F_3 parameterizes the anti-symmetric, parity violating contribution of the Z to the cross section.

The structure functions have to be evaluated within the quark parton model (sect. 2.3) or perturbative QCD (sect. 2.4.2). The expressions are discussed below (eqns. 2.52, 2.53), where it is demonstrated that $F_3(x, Q^2)$ can be neglected for this analysis.

2.3 Quark Parton Model

The observation of scaling suggested the existence of point-like constituents (partons) in the proton. The quark parton model (QPM) [Fey72, Jaf85] treats high-energetic hadrons as "jets" of fast parallel-moving partons which share the nucleon's three-momentum. An incident probe is supposed to see a "frozen" snapshot of the hadron and interact with one of the partons, which in this model are treated as quasi-free particles. Cross sections for hadronic processes are obtained by taking the elastic cross section at parton level and then summing incoherently over all the partons which are involved in the interaction.

2.3.1 Light Cone Dominance

The basic assumption of the parton model is that boson-parton interaction takes place at shorter time-scales and distances than interactions between the partons. It is therefore approximated

by elastic scattering on a quasi-free parton. The hadronic tensor $W_{\mu\nu}$ can be written in a form which is similar to current-current interactions in QED.

$$W_{\mu\nu} = \frac{1}{4\pi}\sum_N\left(\frac{1}{2}\sum_s\right)\int\prod_{n=1}^{N}\left(\frac{d^3p_n}{2E'_n(2\pi)^3}\right)\times \sum_{s_n} < p,s|J^+_\mu(0)|X >< X|J_\nu(0)|p,s > (2\pi)^4\delta^4(p+q-\sum_n p_n). \quad (2.39)$$

The expression [HM84] includes a sum over all N-particle states X into which the proton may break up. Using the optical theorem and closure,

$$W_{\mu\nu} = \frac{i}{4\pi}\sum_s\int d^4\xi e^{iq\cdot\xi} < p,s|J^+_\mu(\xi)J_\nu(0)|p,s > \quad (2.40)$$

where the delta function of (2.39) has been written as an exponential, and ξ can be interpreted as the space-time separation of the absorption and re-emission of the virtual photon (cf. fig. 2.5).

The integral can be analyzed in the target rest frame with the negative z-axis collinear with the virtual photon. Then,

$$q = \left(\nu,0,0,-\sqrt{\nu^2+Q^2}\right) \xrightarrow{\lim_{Bj}} (\nu,0,0,-\nu-Mx). \quad (2.41)$$

Using light cone variables, $q^\pm = (q^0 \pm q^3)/\sqrt{2}$, the scalar product in the exponential becomes $q\cdot\xi = q^+\xi^- + q^-\xi^+$. Since q and ξ are conjugate variables, it follows from general theorems on Fourier transforms (cf eg [Jaf85]) that in the Bjorken limit, ie. $Q^2\to\infty$, x fixed,

$$q^-\to\infty \implies \xi^+\to 0 \quad (2.42)$$

$$\text{and } q^+ = \frac{Mx}{\sqrt{2}} \implies |\xi^-| < \frac{\sqrt{2}}{Mx}. \quad (2.43)$$

The integrand of eqn. 2.40 is singular at $\xi^+ = 0$ since it must vanish for $\xi^2 < 0$. Again, it is taken from theorems on Fourier transforms that in the Bjorken limit $W_{\mu\nu}$ is dominated from the behaviour of the integrand around singularities, ie at $\xi^+ \cong 0$.

Causality requires ξ^2 to be positive, forcing $\xi^2\to 0$ in the Bjorken limit. The limits on ξ^+ and ξ^- imply both

$$|\xi^0| < \frac{1}{Mx} \quad \text{and} \quad |\xi^3| < \frac{1}{Mx}. \quad (2.44)$$

Hence in the Bjorken limit, DIS takes place "on the light cone", and all components of ξ (except ξ^-) vanish, justifying the assumptions of the QPM that time scales and distances of parton processes are shorter than those of strong interactions. In the small-x limit, however, both time scales and distances can become very large [Jaf85].

2.3.2 Naive Quark Parton Model

In an infinite momentum frame, neglecting parton transverse momenta, the momentum of the ith parton is $\mathbf{p}_i = \xi_i\mathbf{p}$, where $\mathbf{p}$ is the nucleon's three-momentum and the ξ_i sum to one. For

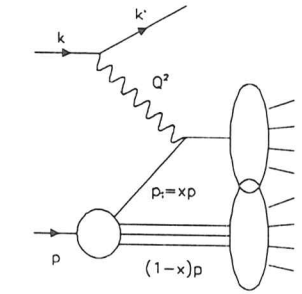

Figure 2.6: Deep inelastic scattering at parton level. The electron scatters elastically off a quasi-free parton, exchanging a virtual photon.

elastic scattering, $W^2 = (p+q)^2 = M^2$, hence by comparing the expressions for a proton and an on-shell parton with zero rest mass,

$$\text{proton}: \quad 0 = q^2 + 2M\nu. \quad (2.45)$$

$$\text{parton}: \quad 0 = q^2 + 2(p_i\cdot q) = q^2 + 2\xi p\cdot q. \quad (2.46)$$

$$\implies \xi = \frac{Q^2}{2M\nu} = x. \quad (2.47)$$

the Bjorken-scaling variable, x, can be interpreted as the fraction of the proton's momentum, ξ, which was carried by the struck quark (cf. fig. 2.6).

The cross section for elastic scattering of electrons on spin-$\frac{1}{2}$ is

$$\frac{d\sigma}{dQ^2} = \frac{4\pi\alpha^2}{Q^4}\left(1-\frac{Q^2}{s'}+\frac{1}{2}\left(\frac{Q^2}{s'}\right)^2\right). \quad (2.48)$$

with $s' = xs$. Using the parton distribution $q_i(x)dx$, which specifies the probability for finding a parton of type i, charge $e_i e$ and momentum fraction x, the cross section for deep inelastic electron-proton scattering at parton level becomes

$$\frac{d^2\sigma}{dxdQ^2} = \frac{4\pi\alpha^2}{Q^4}\left(1-y+\frac{y^2}{2}\right)\sum_i e_i^2 q_i(x). \quad (2.49)$$

Comparison with eqn. (2.25) gives expressions for the structure functions at parton level and yields the Callan-Gross relation (2.13) [CG69].

$$F_1(x) = \frac{1}{2}\sum_i e_i^2 q_i(x). \quad (2.50)$$

$$F_2(x) = \sum_i e_i^2 x\, q_i(x) = 2xF_1(x). \quad (2.51)$$

Verification of the Callan-Gross relation by experiment [B+79] has shown that the partons have spin $\frac{1}{2}$

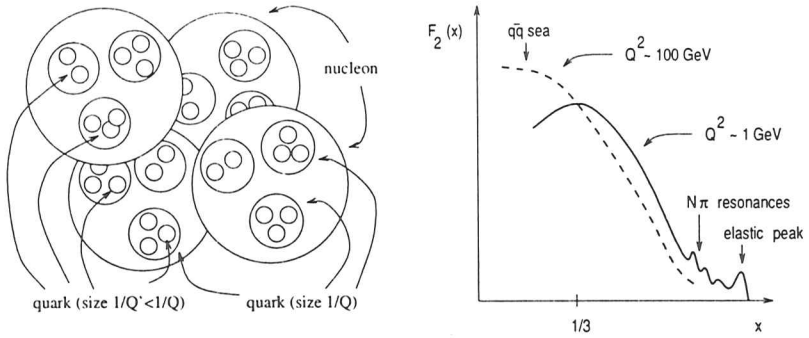

Figure 2.7: Left: nucleon constructed hierarchically from quarks [KS74]. Right: Evolution of the structure function as predicted by QCD [Tay91].

2.3.3 NC DIS Cross Section

In a less naive version, the density of anti-quarks, $\overline{q}_f(x)$, is introduced, and Z exchange is included. Eqn. (2.38) becomes [IR89, Rob90]

$$F_2(x) = 2xF_1(x) = \sum_{f=u,d,s,c} A_f(Q^2)\left[xq_f(x) + x\overline{q}_f(x)\right]. \quad (2.52)$$

$$xF_3(x) = \sum_{f=u,d,s,c} B_f(Q^2)\left[xq_f(x) - x\overline{q}_f(x)\right]. \quad (2.53)$$

The parton distributions $q_f(x)$ and $\overline{q}_f(x)$ refer directly to quarks and anti-quarks of flavour f. The flavour dependent coefficients $A_f(Q^2)$ and $B_f(Q^2)$ contain the vector and axial coupling constants for electrons and partons[3], $c_V^{e,f}$ and $c_A^{e,f}$, and the propagator terms P_Z.

$$A_f(Q^2) = e_f^2 - 2e_f c_V^e \cdot c_V^f P_Z + (c_V^{e\,2} + c_A^{e\,2})(c_V^{f\,2} + c_A^{f\,2})P_Z{}^2. \quad (2.54)$$

$$B_f(Q^2) = -2e_f c_A^e c_A^f P_Z + 4c_V^e \cdot c_V^f \cdot c_A^e c_A^f P_Z{}^2. \quad (2.55)$$

$$\text{with} \quad P_Z = \frac{Q^2}{Q^2 + M_Z^2}. \quad (2.56)$$

At small values of Q^2, the propagator P_Z can be neglected. The tables in the appendix show that for this analysis, contributions to the cross section due to Z exchange are negligible except for the highest values of Q^2, where they are somewhat less than 5%.

2.3.4 Limits and Success of the QPM, Scaling Violations

Data from the early fixed-target experiments provided an overwhelming evidence in support of the quark parton model. Bjorken scaling had been established, the Callan-Gross relationship

[3] $c_V^i = I_z^i - 2e_i \sin^2\theta_W$, $c_V^{e,f} = I_z^{3i}$, where I_z^{3i} is the third component of the weak isospin and e_i the charge of fermion i

was found to hold [B+79], and a comparison of structure functions from electron and neutrino scattering was compatible with fractional quark charges [EMC81, CDH83].

The parton model has been formulated covariantly by "putting it on the light cone" [LP72], but it still cannot be derived from fundamental principles [Nac91] which is an obvious flaw of the model [Loh92]. When interpreting experimental data, however, the parton model often provides a unique link between theory and experiment. The QPM has been applied successfully to other processes like electron-positron annihilation into hadrons (eg [WW79]), or lepton pair production in nucleon-nucleon collisions (Drell-Yan process, [DY70, DY71]).

The QPM is based on two fundamental assumptions, which at the same time define the limits of the model. The assumption of time-scales and distances being shorter than in strong interactions is valid only in the Bjorken limit, that is in an infinite momentum frame where the parton transverse momenta are negligible. The approximation of elastic scattering on quasi-free partons requires the intermediate physical states to be on-shell, which is of course wrong as quarks are confined to the nucleon via gluon exchange.

According to the present understanding, the confinement of quarks in the nucleon via gluon exchange is described by Quantum Chromodynamics (QCD). In QCD, a quark can radiate a gluon, which in turn can split into a $q\overline{q}$-pair. Thus an initial quark is able to share its momentum fraction x over several subsequent steps via a cascade of gluon emission and quark pair production, and a nucleon can be pictured as being constructed from quarks, which are constructed from "smaller (x)" quarks, and so on [KS74](cf fig. 2.7, left).

The level of partons which is probed in an interaction depends on the resolution provided by the incident photon. The resolution of a virtual photon is proportional to $1/Q$, hence the parton densities become functions of both x and Q^2, and they lose their status of being unambiguously measurable quantities with an intuitive physical interpretation. Partons with small values of x are likely to have originated from a quark-gluon cascade, leading to an increased number of partons towards smaller values of x. At low x the parton density should also increase with increasing Q^2, because "small" quarks are better visible with high-resolution (ie high-Q^2) photons (cf fig. 2.7, right [Tay91]).

2.4 QCD Corrections

Quantum Chromodynamics (QCD) describes the strong interactions of quarks and gluons. At sufficiently high Q^2 the running coupling constant, $\alpha_s(Q^2)$, gets small enough to allow perturbative calculations. The quarks behave like free particles ("asymptotic freedom"). The following sections briefly introduce some basic concepts of QCD (cf eg [Pen83]).

2.4.1 Gauge Invariance, Running Coupling Constant and Renormalization Group Equation

The success of QED for electromagnetic interactions suggested to construct a similar theory for strong interactions. Pauli's exclusion principle could be maintained in the baryon decuplet by introducing three strong "colour" charges, hence colour SU(3) was a tempting gauge group for strong interactions. However, requiring local SU(3) gauge symmetry yields a non-Abelian field theory, which leads to fundamental differences between QCD and the Abelian QED.

QCD Lagrangian and Gauge Invariance.

The QCD Lagrangian is

$$\mathcal{L} = \sum_{f=1}^{N_f} \overline{q}_f (i\gamma_\mu D^\mu - m_f) q_f - \frac{1}{2} G^a_{\mu\nu} G^{\mu\nu}_a, \tag{2.57}$$

q_f quark spinor, flavour $f = 1 \ldots N_f$

where D^μ is the covariant derivative, and $G^{\mu\nu}_a$ the gluon tensor.

$$D^\mu = \partial^\mu - igT_a A^\mu_a, \tag{2.58}$$

$$G^{\mu\nu}_a = \partial^\mu A^\nu_a - \partial^\nu A^\mu_a + g f_{abc} A^\mu_b A^\nu_c, \tag{2.59}$$

A^μ_a gluon vector field, colour $a = 1 \ldots 8$

The theory has two fields, q_k and A^μ_a, and one coupling, g. It is assumed that $m_f = 0$. The operators T_a represent the gluons and form an SU(3) algebra. They are related to the Gell-Mann matrices, $T_a = \frac{1}{2}\lambda_a$, and define the structure constants of the group.

$$[T_a, T_b] = i f_{abc} T_c. \tag{2.60}$$

The commutator is the source for interactions among the gauge bosons. In an Abelian theory (like QED) the commutator vanishes, and photon-photon couplings are impossible; in QCD it describes the gluon-gluon interaction.

The Lagrangian is invariant under a local SU(3) transformation.

$$U = e^{igT^a \varepsilon_a(x)}$$

$$\cong 1 + ig\varepsilon_a(x) T^a, \ \varepsilon_a(x) \text{ infinitesimal.} \tag{2.61}$$

if the fields are transformed accordingly, ie

$$q_f \longrightarrow q'_f = q_f - iT^a q_f \varepsilon_a \tag{2.62}$$

$$\overline{q}_f \longrightarrow \overline{q}'_f = \overline{q}_f - i\overline{q}_f T^a \varepsilon_a \tag{2.63}$$

$$A^\mu_a \longrightarrow A^{\mu\prime}_a = A^\mu_a + f_{abc}\varepsilon_b A^\mu_c - \frac{1}{g}\partial^\mu \varepsilon_a. \tag{2.64}$$

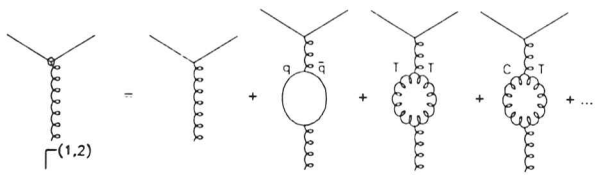

Figure 2.8: Expansion of the quark-gluon vertex, $\Gamma^{(1,2)}$, up to one-loop diagrams. Renormalization of the coupling, $\alpha_s(Q^2)$, requires evaluation (measurement) of the rhs at a specific scale $Q^2 = \mu^2$. C and T denote Coulomb and Transverse gluons.

Running Coupling Constant $\alpha_s(Q^2)$.

The coupling, g, which was introduced in(2.57), is the bare coupling, while the quantity experimentally accessible is the effective coupling $\overline{g}$. Fig. 2.8 defines the effective coupling $\overline{g}$ (or $\Gamma^{(1,2)}$, see below) up to one-loop contributions.

Fig. 2.8 can be used to evaluate $\overline{g}$ [Pen83, Rob90],

$$\overline{g}(Q^2) = g - \beta_0 \frac{g^3}{32\pi^2} \ln \frac{Q^2}{\kappa^2} + \mathcal{O}\left(g^5 \ln^2 \frac{Q^2}{\kappa^2}\right). \tag{2.65}$$

$\beta_0 = \frac{1}{3}(33 - 2N_f)$, where N_f specifies the number of contributing flavours, and κ is an unphysical ultra-violet cut-off parameter which was introduced to avoid divergences from integration over loops. It results in an explicit Q^2 dependence of the effective coupling $\overline{g}$, which is referred to as the running coupling.

$\overline{g}$ is an example for a divergent bare Green's function. However, if the coupling can be specified for a given value of $Q^2 = \mu^2$, then it can be expressed for any Q^2 in terms of the finite $\overline{g}(\mu^2)$.

$$\overline{g}(Q^2) = \overline{g}(\mu^2) - \frac{\beta_0}{32\pi^2}\overline{g}^3(\mu^2) \ln \frac{Q^2}{\mu^2} + \mathcal{O}\left(\overline{g}^5 \ln^2 \frac{Q^2}{\mu^2}\right). \tag{2.66}$$

or, using the geometric series and defining $\alpha_s(Q^2) = \frac{1}{4\pi}\overline{g}^2(Q^2)$,

$$\alpha_s(Q^2) = \frac{\alpha_s(\mu^2)}{1 + \frac{\alpha_s(\mu^2)}{4\pi}(11 - \frac{2}{3}N_f) \ln \frac{Q^2}{\mu^2}}. \tag{2.67}$$

The coupling is rendered finite (ie "renormalized") and independent from the ultra-violet cut-off κ for the price of introducing the renormalization scale μ with the dimension of a mass.

$\alpha_s(Q^2)$ is called the "running coupling constant". At high Q^2 the coupling is small, quarks and gluons behave like quasi-free particles (so-called asymptotic freedom), while at low Q^2 the coupling will become large and quarks and gluons are strongly bound into hadrons (eg. [HM84]). A scale parameter Λ_{QCD} is defined to mark the boundary between these two scenarios.

$$\Lambda^2_{QCD} = \mu^2 \exp\left[\frac{-12\pi}{(33 - 2N_f)\alpha_s(\mu^2)}\right]. \tag{2.68}$$

$$\alpha_s(Q^2) = \frac{4\pi}{(11 - \frac{2}{3}N_f)\ln\frac{Q^2}{\Lambda^2}}. \quad (2.69)$$

Λ_{QCD} is a fundamental parameter which has to be determined from experiment. It is found to be in the range of 200–300 MeV[Alt92].

Renormalization Group Equation.

The previous discussion can be generalized [Pen83]: a theory defined in terms of bare fields and couplings will have divergent Green's functions $\Gamma^{(n)}(p, g_0, \kappa)$. Renormalization scales the bare fields and couplings by appropriate factors Z and thus turns them into physical values, but at the same moment introduces the renormalization scale, μ, into the theory.

The renormalized and the bare Lagrangian describe the same physics, therefore the bare and the renormalized Green's functions are related by

$$\Gamma^{(n)}(p, g, \mu) = Z\Gamma_0^{(n)}(p, g_0, \kappa). \quad (2.70)$$

where n, the number of external fields, specifies the order of the Green's function. The Green's functions now depend on the renormalization scale μ, which is an arbitrary scale. On the other hand, the Green's functions correspond to observables, which must not depend on the choice of μ. This is stated by the renormalization group equation (RGE) [SP53, GML54, Cal70, Sym70]. In QCD, the RGE for coupling n_A gluon fields to n_F quark fields reads

$$\left[\mu\frac{\partial}{\partial\mu} + \beta(g)\frac{\partial}{\partial g} - n_A\gamma_A(g) - n_F\gamma_F(g) + \delta(g)\frac{\partial}{\partial\xi}\right]\Gamma^{(n_A,n_F)}(p, g, \mu, \xi) = 0. \quad (2.71)$$

where ξ parameterizes the gauge and

$$\beta(g) = \mu\frac{\partial}{\partial\mu}g(\mu)\Big|_{g_0,\kappa} \quad (2.72)$$

$$\gamma_{A,F}(g) = \mu\frac{\partial}{\partial\mu}[\ln Z_{A,F}]\Big|_{g_0,\kappa}. \quad (2.73)$$

The β function determines the asymptotic behaviour of the coupling, and the anomalous dimensions $\gamma_{A,F}$ determine the precise high energy behaviour of the Green's functions.

Evaluation of the RGE for four independent Green's functions yields the four functions $\beta(g)$, $\gamma_A(g)$, $\gamma_F(g)$ and $\delta(g)$ [Pen83]. Calculating the quark gluon vertex, $\Gamma^{(1,2)}$, up to leading order (one-loop diagrams) and inserting it into the RGE gives

$$\overline{g}(Q^2) = \frac{\overline{g}(\mu^2)}{\sqrt{1 + \frac{\beta_0}{16\pi^2}\overline{g}^2(\mu^2)\ln\frac{Q^2}{\mu^2}}} \quad (2.74)$$

which after expansion of the square root reproduces (2.66). The RGE has re-ordered the perturbative expansion of $\overline{g}$ such that the first term now contains contributions from an infinite set of diagrams of the former series, and it has the effect of summing the leading logarithms. Perturbative calculations in QCD are therefore in terms of the running coupling $\alpha_s(Q^2)$, and

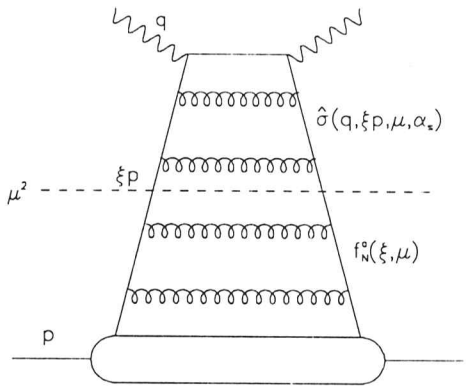

Figure 2.9: Hard-scattering cross sections are factorized into the "hard" parton-level cross-section $\hat{\sigma}$ and the "soft" parton distribution f_N^a. p is the momentum of the initial hadron, ξp is the momentum fraction carried by the parton which contributes to the hard scattering, and q is the four-momentum of the incident probe. The factorization scale μ separates short- and long-distance contributions to the cross section.

they are expected to be reliable if $\alpha_s(Q^2)$ is small, whereas expansions in terms of loops would require both $a_s(\mu^2)$ and $a_s(\mu^2)\ln\frac{Q^2}{\mu^2}$ to be small [Rob90].

$\alpha_s(Q^2)$ has been calculated next-to-leading order (NLO) by including $\mathcal{O}(g^5)$ contributions to the quark-gluon vertex, $\Gamma^{(1,2)}$ [Cas74, Jon74].

$$\alpha_s^{\mathrm{LO}}(Q^2) = \frac{4\pi}{\beta_0\ln\frac{Q^2}{\Lambda^2}}. \quad (2.75)$$

$$\alpha_s^{\mathrm{NLO}}(Q^2) = \frac{4\pi}{\beta_0\ln\frac{Q^2}{\Lambda^2}}\left[1 - \frac{\beta_1}{\beta_0}\frac{\ln\ln\frac{Q^2}{\Lambda^2}}{\ln\frac{Q^2}{\Lambda^2}}\right]. \quad (2.76)$$

where $\beta_0 = \frac{1}{3}(33 - 2N_f)$ and $\beta_1 = \frac{1}{3}(306 - 38N_f)$.

2.4.2 Perturbative Calculations

Cross sections for hard-scattering can be factorized into a "hard" cross section for the parton-level process, $\hat{\sigma}$, and a probability for finding a certain parton inside a nucleon, f. The cross section $\hat{\sigma}$ can be evaluated perturbatively, while the parton distribution functions f have to be measured experimentally. However, the f's obey an integro-differential evolution equation which can be approximated by methods of perturbative QCD. A factorization scale, μ, fixes how the finite contributions to the cross section are shared between $\hat{\sigma}$ and f (fig. 2.9). To avoid confusion, it is common to choose the factorization scale equal to the renormalization scale.

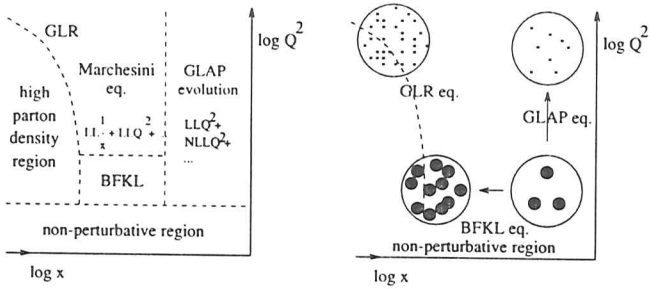

Figure 2.10: The Kwiecinski plot (left) and Martin's road-map to DIS (right) illustrate domains and effects of different evolution equations.

The generic lepton-hadron cross-section for the process $lN \to lhX$, where N is the target nucleon and h is either an identified final-state hadron or null in case of an inclusive process, is

$$\sigma_{lN \to lhX}(q, p) = \sum_a \int_x^1 d\xi f_N^a(\xi, \mu) \hat{\sigma}_{\gamma a \to h}(q, \xi p, \mu, \alpha_s). \tag{2.77}$$

where a identifies the partons inside N. This factorization theorem is valid to all orders of α_s.

The cross section, σ, is independent of the choice of renormalization scheme and factorization scale, which however are needed to define $\hat{\sigma}$. Thus, scheme and scale dependence must be compensated for in the parton distributions, f_N^a, which are therefore scheme- and scale-dependent themselves. Truncation of the perturbation series spoils the compensation and introduces arbitrary scheme and scale dependence to QCD predictions of σ [OT92].

Leading-order (LO) calculations use tree-level (parton model) $\hat{\sigma}$, one-loop α_s, and parton distribution functions (PDFs) from one-loop kernels. As $\hat{\sigma}$ has no μ dependence, σ acquires a net scale dependence through f_N^a. Next-to-leading order (NLO) calculations use NLO $\hat{\sigma}$, two-loop α_s, and two-loop evolution kernels. All three contributions now have unambiguous meanings, and the net scale dependence is greatly reduced as the variation of one factor is compensated for by the others, given all of them are specified in the same renormalization and factorization schemes.

The following sections introduce the evolution equations and review the approximations relevant to structure function measurements at HERA. A survey of the approximations together with their different domains in phase space is given in fig. 2.10.

DGLAP Equations.

By following through the different steps of a cascade, an evolution equation for the quark densities can be obtained. A quark q of momentum x can be created either from gluon pair production or from a quark reducing its momentum by radiating a gluon. In both cases the momentum of the initial parton had to be larger than x. The probabilities for both processes

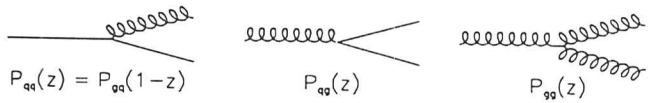

Figure 2.11: The splitting functions $P_{fi}(z)$ give the probability for an incident parton i to split into partons f and k with fractions z and $(1-z)$ of the momentum of i.

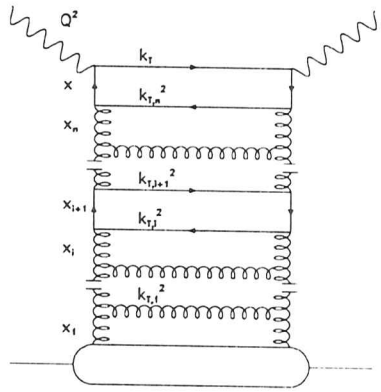

Figure 2.12: Example for the representation of a parton cascade by a ladder diagram. A low-x quark is produced via repeated gluon emission and quark-pair production. The probabilities at each vertex are calculable through the splitting functions.

should in leading order be proportional to $\alpha_s(Q^2) P_{qi}(z)$, where $P_{qi}(z)$ parameterizes the probability for an initial parton i with momentum fraction y to produce a final quark q with a fraction z of the initial momentum, ie $x = zy, 0 < z < 1$. If $q(x, Q^2)$ and $g(x, Q^2)$ specify the number of quarks and gluons, then

$$\frac{dq(x, Q^2)}{d \log Q^2} = \frac{\alpha_s(Q^2)}{2\pi} \int_x^1 \frac{dy}{y} \left[P_{qq}\left(\frac{x}{y}\right) q(y, Q^2) + P_{qg}\left(\frac{x}{y}\right) g(y, Q^2) \right]. \tag{2.78}$$

The evolution equation for the quark density is accompanied by a similar equation for the gluon density.

$$\frac{dg(x, Q^2)}{d \log Q^2} = \frac{\alpha_s(Q^2)}{2\pi} \int_x^1 \frac{dy}{y} \left[P_{gq}\left(\frac{x}{y}\right) q(y, Q^2) + \sum_q P_{qq}\left(\frac{x}{y}\right) q(y, Q^2) \right]. \tag{2.79}$$

The two equations are known as the DGLAP equations [Dok77, GL72, AP77]. The evolution kernels, P_{ij}, are the splitting functions, which in LO are

$$P_{qq}(z) = \frac{4}{3} \frac{1 + z^2}{1 - z} \tag{2.80}$$

$$P_{qq}(z) = \frac{1}{2}\left[z^2 + (1-z)^2\right]. \quad (2.81)$$

$$P_{gg}(z) = 6\left(\frac{z}{1-z} + \frac{1-z}{z} + z(1-z)\right). \quad (2.82)$$

$$P_{gq}(z) = \frac{4}{3}\frac{1+(1-z)^2}{z}. \quad (2.83)$$

Fig. 2.11 shows the diagrams which are contributing to a parton cascade and defines the splitting functions $P_{ij}(z)$. fig. 2.12 illustrates how a low-x quark is produced via a "parton ladder".

When solving the DGLAP equations, it is convenient to define singlet and non-singlet distributions.

$$q_f^{\mathrm{SI}}(x,Q^2) = q_f(x,Q^2) + \overline{q}_f(x,Q^2). \quad (2.84)$$

$$q_f^{\mathrm{NS}}(x,Q^2) = q_f(x,Q^2) - \overline{q}_f(x,Q^2). \quad (2.85)$$

The singlet distribution mixes with the gluon in two coupled integro-differential equations, while the non-singlet (or valence) distributions decouple from the gluon, each of them obeying a single evolution equation. It should be noted that the evolution equations fix only the Q^2 dependence of the parton densities, but neither their absolute value nor their x-dependence.

When calculating cross sections, ie integrating (2.78), every parton subprocess contributes by a factor

$$\int_{\Lambda^2}^{\mathcal{O}(Q^2)} \frac{dk_T^2}{k_T^2}\frac{\alpha_s(k_T^2)}{2\pi}$$

to the parton density. These integrations become nested if the phase space is required to be "strongly ordered".

$$Q^2 \gg k_{T,n}^2 \gg k_{T,n-1}^2 \gg \ldots \gg k_{T,1}^2. \quad (2.86)$$

where n counts the parton processes along the cascade (fig. 2.12).

Structure Function Formulae. Renormalization Schemes.

In LO[4]

$$F_2(x,Q^2) = x\sum_f e_f^2 q_f(x,Q^2). \quad (2.87)$$

hence LO DIS probes quark densities, and the gluon enters only through the quark evolution equation. However, in NLO the gluon enters directly into the cross-section via

$$F_2(x,Q^2) = x\sum_f e_f^2 q_f(x,Q^2) + \alpha_s(Q^2)\left[\sum_f C_2^f \otimes q_f + C_2^g \otimes g\right]. \quad (2.88)$$

[4]For brevity, anti-quarks are assumed to be included in the flavour index, f.

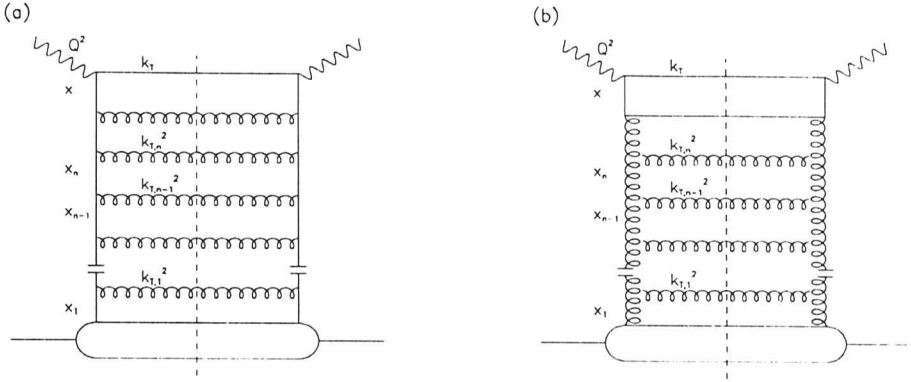

Figure 2.13: Ladder diagrams representing the LLA (a) and DLLA (b) contributions to F_2.

where $\otimes$ indicates convolution in x, and the C_2^i are coefficient functions which are calculable in QCD. Eqn. 2.88 is in the $\overline{\mathrm{MS}}$ renormalization scheme[5]. The entire NLO term can be absorbed into the LO quark term, thus modifying the meaning of q_f and maintaining eqn. 2.87 through all orders of α_s. The scheme is called the DIS scheme, and by definition $C_2^{i,\mathrm{DIS}} = 0$ [BBDM78, AEM78].

Comparison of eqns. 2.87 and 2.88 yields transformation equations for parton densities in the DIS and $\overline{\mathrm{MS}}$ scheme. Since the gluon density does not occur in F_2, $q^{\mathrm{DIS}}(x,Q^2)$ is defined to preserve the momentum sum rule.

$$q_f^{\mathrm{DIS}}(x,Q^2) = \left[1 + \alpha_s(Q^2)C_2^{f,\overline{\mathrm{MS}}}\right] \otimes q_f^{\overline{\mathrm{MS}}} + \frac{1}{2N_f^{\mathrm{eff}}}\alpha_s(Q^2)C_2^{g,\overline{\mathrm{MS}}} \otimes g^{\overline{\mathrm{MS}}} \quad (2.89)$$

$$g^{\mathrm{DIS}}(x,Q^2) = \left[1 - \alpha_s(Q^2)C_2^{g,\overline{\mathrm{MS}}}\right] \otimes g^{\overline{\mathrm{MS}}} - \alpha_s(Q^2)\sum_f C_2^{f,\overline{\mathrm{MS}}} \otimes q_f^{\overline{\mathrm{MS}}}. \quad (2.90)$$

To follow the convention, the formulae in this thesis are specified in the DIS scheme.

Leading-Log Approximation (LLA) and DLLA.

Dokshitzer has shown [Dok77] that in an axial gauge ladder-type diagrams are the source for the leading $\log Q^2$ contribution to the parton densities. The leading $\log Q^2$ approximation starts evolution from non-singlet parton distributions which decouple from the gluon. The relevant

[5]The $\overline{\mathrm{MS}}$ scheme is defined by a certain prescription to calculate perturbative matrix elements [BBDM78]

LO GLAP equation is

$$\frac{dq^{NS}(x,Q^2)}{d\log Q^2} = \frac{\alpha_s(Q^2)}{2\pi}\int_x^1 \frac{dy}{y} P_{qq}\left(\frac{x}{y}\right) q^{NS}(y,Q^2); \tag{2.91}$$

It describes the generation of a low-x quark via repeated emission of gluons (fig. 2.13).

It is useful for the analysis to take moments of eqn. (2.91), since it factorizes nested integrations over momentum fractions, and represent the quark density in terms of the Laplace-Mellin transformation [DKMT91].

$$M_n(Q^2) = \int_0^1 \frac{dx}{x} x^n q(x,Q^2). \tag{2.92}$$

$$q(x,Q^2) = \frac{1}{2\pi i}\int_{c-i\infty}^{c+i\infty} dn\, x^{-n} M_n(Q^2). \tag{2.93}$$

The differential equation for $M_n(Q^2)$ obtained from (2.91) can be solved to

$$M_n(Q^2) = c_n \left(\log\frac{Q^2}{\Lambda^2}\right)^{\frac{A_n}{b}}, \tag{2.94}$$

where A_n is the n-th moment of the splitting function $P_{qq}(z)$, $b = (11 - \frac{2}{3}N_f)/4\pi$, and c_n must be determined from experiment.

Using $\xi = \exp\log\xi$, $M_n(Q^2)$ can be expanded into a power series in $\frac{A_n}{b}\log(\log\frac{Q^2}{\Lambda^2})$, the i-th term of which can be identified with the contribution of an i-rung ladder diagram to the parton density in a region of phase space where longitudinal momenta are ordered and transverse momenta are strongly ordered [Mar93] (cf fig. 2.12a),

$$Q^2 \gg k_{T,r}^2 \gg k_{T,r-1}^2 \gg \ldots \gg k_{T,1}^2,$$
$$y > x_1 > \ldots > x_{r-1} > x,$$

ie $M_n(Q^2)$ is equivalent to a sum of the leading $\log Q^2$ contributions. The quark distributions obtained from $M_n(Q^2)$ via (2.93) are the leading-log approximation (LLA) of the GLAP evolution equations.

At small values of x quarks predominantly originate from pair production, and structure function measurements in this region are dominated by the asymptotic behaviour of the gluon density. An estimate for this behaviour at small values of x can be obtained by dropping the quark distributions and using $P_{gg}(z) \cong 6/z$. The relevant GLAP equation and its solution are

$$\frac{dg(x,Q^2)}{d\log Q^2} = \frac{3\alpha_s}{\pi}\int_x^1 \frac{dy}{y} yg(y,Q^2). \tag{2.95}$$

$$xg(x,Q^2) \sim \exp\left(2\sqrt{\frac{3\alpha_s}{\pi}\log\frac{1}{x}\log\frac{Q^2}{Q_0^2}}\right). \tag{2.96}$$

(2.95) describes the generation of low-x partons via repeated gluon pair production (fig. 2.13b) and predicts the gluon distribution, and together with it the structure function F_2, to rise faster than any power of $\log\frac{1}{x}$ with decreasing values of x.

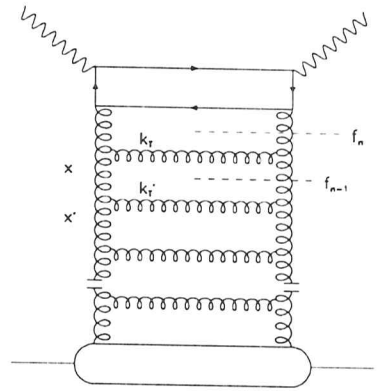

Figure 2.14: Representation of the BFKL equation through a ladder diagram.

Eqn. (2.95) gives the gluon distribution in the so-called double leading-log approximation (DLLA). $xg(x,Q^2)$ can be expanded into a power series in $\frac{3\alpha_s}{\pi} log\frac{1}{x}\log Q^2$ [Mar93], the i-th term of which corresponds to an i-rung gluon ladder in a region of phase space where both longitudinal and transverse momenta are strongly ordered (cf fig. 2.13b), ie

$$Q^2 \gg k_{T,r}^2 \gg k_{T,r-1}^2 \gg \ldots \gg k_{T,1}^2,$$
$$y \gg x_1 \gg \ldots \gg x_{r-1} \gg x.$$

BFKL evolution into the small-x regime.

In the DLLA expansion into the small-x regime, the logarithms of x are accompanied by factors of $\log Q^2$ due to the constraint of strong ordering. To evolve the parton densities into the HERA domain at small x and relatively low Q^2, the ordering of momenta within the ladder needs to be dropped, and the integration has to be performed over the entire phase space.

The integration receives contributions from a whole set of non-planar diagrams with vertical gluon lines, however it can be represented in terms of ladder diagrams (cf fig. 2.14 [Mar93]). The result is the BFKL equation [BL78, KLF77], a recursion relation in terms of the unintegrated gluon distribution $f(x,k_T^2)$.

$$f_n(x,k_T^2) = \int_x^1 \frac{dx'}{x'}\int dk_T'^2 K(k_T,k_T') f_{n-1}(x',k_T'^2). \tag{2.97}$$

$$= K \hat{\otimes} f_{n-1}. \tag{2.98}$$

$$xg(x,Q^2) = \int^{Q^2} \frac{dk_T^2}{k_T^2} f(x,k_T^2). \tag{2.99}$$

$$\text{with } f(x,k_T^2) = \sum_{n=0}^{\infty} f_n(x,k_T^2) \tag{2.100}$$

The hat in eqn. 2.98 indicates a convolution in both x and k_T^2. $K(k_T, k_T')$ is the Lipatov kernel, which includes contributions from real and virtual gluon emission.

In the BFKL approximation transverse momenta are no longer ordered along the ladder, hence inner gluon lines might contribute with values of $k_{T,i}^2 < Q_0^2$ which are below the infrared limit of perturbative QCD. This problem can be avoided by concentrating on high-Q^2 events with a high-energetic jet ("trigger jet") at $k_{T,\text{jet}}^2 \cong Q^2$, as those events have $Q^2, k_{T,1}^2 \gg Q_0^2$, ie both ends of the ladder are at a sufficient distance from the non-perturbative region [Mue90, Mue91].

The BFKL equation can be solved analytically for fixed α_s. It predicts the gluon distribution to behave at small x like

$$xg(x, Q^2) \sim x^{-\lambda}, \tag{2.101}$$

$$\lambda = \frac{12\alpha_s(Q^2)}{\pi} \ln 2. \tag{2.102}$$

For typical values of α_s the exponent is $\lambda \cong 0.4$.

Marchesini Equation.

Marchesini, Catani and Fiorani have obtained a recurrence relation in terms of a multi-gluon integrand $f_n^{(R)}(k_1 \ldots k_n)$. The integrand corresponds to a configuration R of r real and $n-r$ on-shell virtual gluons. $f_n^{(R)}$ is computed iteratively from $f_{n-1}^{(R')}$ by adding a softer real or virtual gluon k_n to R' in all possible ways. The relation can be used to derive the GLAP evolution equations for large x and the BFKL equation for small x [Mar92].

Recombination Effects. GLR Equation.

The gluon distribution $xg(x, Q^2)$ cannot rise indefinitely with decreasing x as predicted by the BFKL equation. The Froissart bound [Fro61] constrains the total photon-proton cross section to

$$\sigma_{tot}(\gamma^* p) \ll \pi R_p^2 \ln^2 s. \tag{2.103}$$

where R_p is the radius of the proton. The cross-section is given by eqn. (2.33). In the BFKL approximation, the parton density increases at small x like $x^{-\lambda_0 \alpha_s(Q^2)}$ (cf eqn 2.101). Inserting the BFKL result for F_2, the constraint from the Froissart bound becomes

$$\frac{4\pi^2 \alpha_s(Q^2)}{Q^2} x^{-\lambda_0 \alpha_s(Q^2)} \ll \pi R_p^2 (\ln s)^2. \tag{2.104}$$

where α has been replaced by $\alpha_s(Q^2)$ since the probe can also be a virtual gluon [Lev92]. It follows that the Froissart bound would be violated if x assumes values below x_{crit}, where

$$\log \frac{1}{x_{\text{crit}}} = \frac{1}{\lambda_0 \alpha_s(Q^2)} \log \frac{R_p^2 Q^2 \ln^2 s}{4\pi \alpha_s(Q^2)}. \tag{2.105}$$

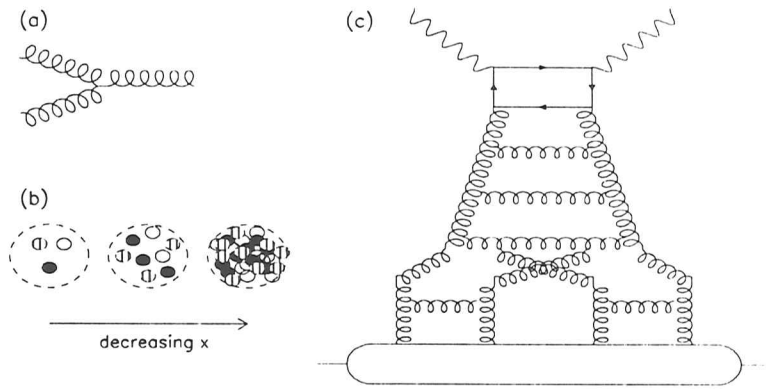

Figure 2.15: (a) Basic diagram for gluon recombination. (b) Visualization of shadowing in the nucleon (ref. text). (c) Example for a non-planar ladder diagram responsible for shadowing as described by the GLR equation.

Eqn. (2.105) can be interpreted by a classical argument: An incident photon with momentum Q^2 resolves partons at a size of $r_p = 1/Q$. With the number of partons increasing as x decreases, the proton fills up, and at some x_{crit} no more space is available for additional partons inside the proton. The partons overlap ("shadowing"), and parton recombination processes damp the growth of the parton density (fig. 2.15 a,b). As higher-Q^2 photons are probing for smaller partons, x_{crit} decreases with increasing Q^2.

It has been attempted to include recombination effects to the parton distributions by adding non-linear terms to the GLAP equations [GLR83, MQ86, BR91]. Shadowing can be ascribed to the contribution of non-planar diagrams becoming significant at small values of x (cf fig. 2.15c). [GLR83] estimated shadowing under the assumption that the coupling of n ladders is proportional to the single ladder coupling raised to the power of n and were able to describe it by an additional quadratic term in the BFKL equation which suppresses the growth of $xg(x, Q^2)$ at small values of x.

$$\frac{\partial f(x, k_T^2)}{\partial \log \frac{1}{x}} = K \otimes f - \frac{81\alpha_s^2(k_T^2)}{16R^2 k_T^2} \left[xg(x, k_T^2)\right]^2. \tag{2.106}$$

Observation of shadowing would allow to determine the parameter R from (2.106). If R assumes the value of the proton radius, the proton can be pictured as being filled with gluons, whereas smaller values of R would indicate that the gluons cluster within the proton in so-called hot spots [Mue90, Mue91, BBRK91].

2.5 Parton Parameterizations

The factorization theorem, (2.77), illustrated the importance of parameterizations of parton densities as an input for quantitative QCD calculations. The evolution equations fix the Q^2 dependence of the parton parameterizations, but absolute values and x dependence have to be determined from experiment at a given value Q_0^2.

2.5.1 Extraction of Parton Densities from Experiment

Parton parameterizations obtained from global QCD analyses have to describe any experimental data which is sensitive to parton processes. Such data include direct structure function measurements, which in LO are sensitive to valence quarks and sea quarks; measurements of F_2^n/F_2^p, which directly probe the (a)symmetry of the u and d sea; collider data on prompt photons as a measure of the gluon distribution via $gq \to q\gamma$; Drell-Yan production of lepton pairs in pN collisions, which are predominantly produced by annihilation of a valence quark with an anti-quark from the sea; or measurements of W and Z cross sections which are sensitive to individual flavour distributions.

The approximations referenced in the previous sections suggest asymptotic forms for large and small x. Taking eg sea quarks, their distributions should vanish at $x \approx 1$, while at small x the BFKL approximation may be used as an estimate for the rise of their densities. Hence

$$xq_f(x, Q_0^2) = A_f(1 - a_f x)^{n_f} x^{-\lambda_f}, \tag{2.107}$$

where f stands for the different flavours, can be used as a naive ansatz for sea quark distributions. Different parametric forms have been used to extract parton distributions from experimental data, most of them being of the type

$$xq_f(x, Q_0^2) = A_f(1 - a_f x)_f^n x^{-\lambda_f} P_f(x). \tag{2.108}$$

where $P_f(x)$ stands for a function of x. Typical choices for $P_f(x)$ are second order polynomials modified with logarithmic or $\sqrt{x}$ terms. Recent analyses, which evolve partons into the kinematic regime of HERA, are introduced in section 2.5.3.

The parton distributions are constrained by sum rules. The three most relevant sum rules are the momentum sum rule, the Gottfried sum rule, and the Gross-Llewellyn Smith sum rule.

$$I_{\text{MSR}} = \int_0^1 dx\, x(q^{\text{SI}}(x) + g(x)) = 1. \tag{2.109}$$

$$I_{\text{GSR}} = \int_0^1 \frac{dx}{x} [F_2^p(x) - F_2^n(x)] = \frac{1}{3}. \tag{2.110}$$

$$I_{\text{GLSR}} = \int_0^1 \frac{dx}{x} xF_3(x) = 3\left(1 - \frac{\alpha_s}{\pi} + \ldots\right). \tag{2.111}$$

The momentum sum rule (2.109) gives a relation between the amount of gluons and quarks in the proton. Its value has to be determined by experiment. The amount of gluons in the proton has to be determined by experiment. The other two sum rules can be obtained directly

Experiment		beam	target	measurements	x	Q^2 [GeV^2]	publication
BCDMS	NA4	μ	C	F_2	0.25...0.75	25...260	[BCD87a]
			H_2, D_2	F_2, R	0.07...0.75	7...260	[BCD90]
BEBC	WA25	ν	D_2	F_2, xF_3	0.028...0.7	0...64	[BEB85]
	WA21	ν	H_2	q^ν, $q^{\overline{\nu}}$, $\overline{q}^{\overline{\nu}}$	0.1...0.7	8.6...14.2	[BEB90]
CCFR		ν	Fe	F_2, xF_3	0.015...0.7	1.3...200	[CCF92]
CHARM	WA18	ν	$CaCO_3$	F_2, xF_3, F_L	0.02...0.4	0.8...18.9	[CHA84]
CHIO		ν	H_2, D_2	F_2, R	0.0005...0.7	0.2...80	[CHI79]
CDHS	WA1	ν	Fe	F_2, xF_3, R	0.015...0.65	0.5...200	[CDH83]
CDHSW	WA1/2	ν	Fe	F_2, xF_3, F_L, $\overline{q}^{\overline{\nu}}$	0.015...0.65	0.19...200	[CDH91]
BFP		μ	Fe	F_2	0.08...0.65	5.5...220	[BFP86]
E665		μ	H_2, D_2, A	F_2	0.0009...0.37	0.2...65	[E6694]
EMC	NA2	μ	Fe	F_2	0.03...0.8	2...250	[EMC86]
			H_2, D_2	F_2	0.03...0.75	7...170	[EMC87]
EMC	NA28	μ	D_2	F_2	0.002...0.17	0.2...8	[EMC90]
NMC	NA37	μ	H_2, D_2, A	F_2	0.006...0.6	0.8...75	[NMC91]
			H_2, D_2, A	F_2^n/F_2^p, $F_2^A/F_s^{A'}$	0.003...0.7	0.17...100	[NMC91]
SLAC		e	H_2, D_2	F_2, R	0.07...0.85	0.5...20	[WRD+92]

Table 2.2: Survey of some pre-HERA fixed-target experiments. The table lists name and type of experiment, the measurements which were performed, the maximum extension of phase space which was covered in x and Q^2, and a recent publication. A and A' stand for nuclei other than H_2 and D_2, eg He, Li, Xe, Fe.

from the QPM: the Gottfried sum rule (2.110) fixes the valence quark flavours of the nucleons, assuming $\overline{u} = \overline{d}$, and the Gross-Llewellyn Smith sum rule (2.111) evaluates the quark singlet distribution $q^{\text{SI}} = q - \overline{q}$ to determine the number of valence quarks in the nucleon.

Several sets of parton parameterizations have been created using different approaches to the input structure functions. The most recent give a good description of data available from the pre-HERA era, but show sizeable differences when extrapolated into the kinematic region which is probed by the HERA experiments. The parameterizations and the experiments on which they are based are briefly introduced in the following sections.

2.5.2 Pre-HERA Experiments

Table 2.2 gives a survey of structure function measurements which were performed before HERA data taking started. In all the experiments a lepton beam and a stationary target was used. Most of them use μ or ν beams.

The first generation of parton parameterizations has been obtained from measurements of the early 1980s. They were followed by more accurate data from the "classical" deep inelastic muon-scattering experiments (BCDMS, EMC), and by neutrino data (eg CCFR, CDHSW). Recently, the NMC collaboration has extended the measured phase-space to smaller x and provided a high-statistics measurement of the ratio F_2^n/F_2^p by comparing data from H_2 and D_2

targets. [BCKK91, Vir92] review the experimental situation before HERA data taking started.

In some experiments nucleon structure functions have also been determined from heavy-nuclei targets, (A). It was generally expected that such structure functions would differ only slightly from those measured with hydrogen targets, (D), because structure functions describe small distance scales. However, the EMC collaboration [EMC88b, EMC88a] and later BCDMS [BCD87b] and SLAC experiments [WRD+92] found the ratio

$$r = \frac{F_2^{(A)}(x, Q^2)}{F_2^{(D)}(x, Q^2)}$$

to vary between 0.8 and 1.1, depending on x. The ratio reaches its minimum for $x \cong 0.3 \ldots 0.8$, implying the relative importance of valence quarks being degraded in a nucleus compared to the free nucleon [Rob90]. This result became known as the "EMC effect".

2.5.3 Some Recent Parton Parameterizations

Three groups have emerged which obtained parton parameterizations from global NLO QCD analyses and made predictions for the parton densities in the HERA regime. The analyses of the CTEQ collaboration [CTE93] and Martin, Roberts and Stirling (MRS) [MRS93b] start from phenomenological ansatzes for the x dependence of the different valence and sea quark distributions and the gluon distribution at a given Q_0^2, which are then evolved in Q^2 using the NLO DGLAP equations. Glück, Reya and Vogt (GRV) [GRV92] fix boundary conditions for anti-quarks and gluons at a very low $Q^2 = \mu^2 = 0.3\,\mathrm{GeV}^2$, use an MRS parameterization for the valence quarks at $Q_0^2 = 4\,\mathrm{GeV}^2$, and "radiatively generate" parton distributions through the RGE. In addition to the NLO analyses, CTEQ and GRV provide LO PDFs to reduce computing power requirements when making estimates for future experiments.

The following sections briefly introduce the analyses of the different groups. The parameterizations which are used for the analysis of the 1993 HERA measurements are characterized in table 2.3. Up-to-date parton distribution functions (PDFs) are kept in a database at CERN and can be accessed through the PDFlib programme package [PB93].

CTEQ Collaboration.

The CTEQ collaboration[6] obtains parton distributions through a global NLO QCD analysis of data for various hard scattering processes. The hard cross-sections of all processes included in the analysis are calculated in pQCD to NLO in α_s [CTE94]. The individual partons are parameterized at $Q_0 = 1.6\,\mathrm{GeV}$, which is taken to be the charm threshold, and are evolved in Q^2 using the GLAP equations with two-loop expressions for the splitting functions and the running coupling. The calculations are performed in the $\overline{\mathrm{MS}}$ scheme.

The CTEQ PDFs are updated whenever new data become available. CTEQ PDFs are labeled CTEQnX, where n denotes the generation of the PDF and X identifies the constraints and

[6] The work of the CTEQ collaboration continues previous analyses from Duke and Owens [DDR83, DO84] and Morfin and Tung [MT91].

	CTEQ	MRS	GRV
INPUT DATA			
DIS	BCDMS $F_2^{\mu p}, F_2^{\mu d}$	BCDMS $F_2^{\mu p}, F_2^{\mu d}, F_2^{\mu n}/F_2^{\mu p}$	
		EMC $F_2^{\mu n}/F_2^{\mu p}$	EMC $F_2^{\mu p}$ (x¡0.07)
	NMC $F_2^{\mu p}, F_2^{\mu d}, F_2^{\mu n}/F_2^{\mu p}$	NMC $F_2^{\mu p}, F_2^{\mu d}, F_2^{\mu n}/F_2^{\mu p}$	
	H1,ZEUS F_2^{ep} (1992)		SLAC F_2^{ep}, F_2^{ed}
	CCFR $F_2^{\nu N}, xF_3^{\nu N}$	CCFR $F_2^{\nu N}, xF_3^{\nu N}$	
		CDHSW $F_2^{\nu N}, xF_3^{\nu N}$	
prompt γ	WA70	WA70	
	E706		
	UA6		
Drell-Yan	E605	E605	E605
	CDF		
W/Z prod.		CDF	
		UA2	
BOUNDARY CONDITIONS AT μ^2			
$\mu^2[\mathrm{GeV}^2]$	2.56	4	0.3 ($\cong 2\Lambda^2_{\mathrm{QCD}}$)
$xg(x,\mu^2)$			$Ax^{\alpha}(1-x)^{\beta}$
$x\overline{u}(x,\mu^2)$			$A'x^{\alpha'}(1-x)^{\beta'}$
$x\overline{d}(x,\mu^2)$			$x\overline{u}(x,\mu^2)$
$xs(x,\mu^2)$	$\frac{1}{4}(x\overline{u}(x,\mu^2)+x\overline{d}(x,\mu^2))$	$\frac{1}{4}(x\overline{u}(x,\mu^2)+x\overline{d}(x,\mu^2))$	0
$xc(x,\mu^2)$	0	0	0
INPUT PARAMETERIZATIONS AT Q_0^2			
$Q_0^2[\mathrm{GeV}^2]$	2.56	4	4
$xf(x,Q_0^2)$	$A_0^f x^{A_1^f}(1-x)^{A_2^f}\times$	$A_f x^{\delta_f}(1-x)^{\eta_f}\times$	$A_f x^{\delta_f}(1-x)^{\eta_f}\times$
	$(1+A_3^f x^{A_4^f})$	$(1+\varepsilon_f\sqrt{x}+\gamma_f x)$	$(1+\varepsilon_f\sqrt{x}+\gamma_f x)$
	$f = u_v, d_v, \frac{1}{2}(\overline{u}+\overline{d}), s$	$f = u_v + d_v, d_v, S$	$f = u_v + d_v, d_v$
$xg(x,Q_0^2)$	$A_0^g x^{A_1^g}(1-x)^{A_2^g}\times$	$A_g x^{\delta_g}(1-x)^{\eta_g}\times$	
	$(1+A_3^g x^{A_4^g})$	$(1+\gamma_g x)$	
$x\Delta(x,Q_0^2)$	$A_0^- x^{A_1^-}(1-x)^{A_2^-}$	$A_\Delta x^{\eta_\Delta}(1-x)^{\eta_S}$	
	$(1+A_3^-\sqrt{x}+A_4^- x)$		
CONSTRAINTS			
		$2\overline{d} = 0.4S + \Delta$	
		$2\overline{u} = 0.4S - \Delta$	
		$\delta_S = \delta_g$	
RESULTING SETS OF PDFs			
	2M: best fit, $A_1^f = -0.26$	$\mathrm{S}^0 : \delta_g = 0, \overline{u} = \overline{d}$	HO: NLO QCD evolution
	2MS: $A_1^f = -\frac{1}{2}$	$\mathrm{D}^0 : \delta_g = 0, \overline{u} \neq \overline{d}$	LO: HO terms dropped
	2MF: $A_1^f = 0$	$\mathrm{D}^- : \delta_g = -\frac{1}{2}, \overline{u} \neq \overline{d}$	
	2ML: $\Lambda^{(5)}_{\mathrm{QCD}} = 220\mathrm{MeV}$	$\mathrm{D}^-_{\mathrm{shadowed}} R = 5.2\mathrm{GeV}^{-1}$	
$\Lambda^{(N_f)}_{\mathrm{QCD}}$			
$\Lambda^{(4)}_{\mathrm{QCD}}[\mathrm{MeV}]$	235	215 ± 60	200*
$\Lambda^{(5)}_{\mathrm{QCD}}[\mathrm{MeV}]$	139		153*
$\Lambda^{(6)}_{\mathrm{QCD}}[\mathrm{MeV}]$			83*

Table 2.3: Overview of parton distributions used for the 1993 analysis of HERA data (cf text). Δ parameterizes the flavour-SU(2) asymmetry of the sea, $\Delta = \overline{d} - \overline{u}$. Parameters marked with an asterisk (*) were fixed for the analysis.

assumptions which have been imposed on the distributions. So far, CTEQ has performed three global analysis. The CTEQ1 analysis [CTE93] was based on structure functions and cross-sections for Drell-Yan and prompt-γ production obtained by pre-HERA experiments. The CTEQ2 analysis was made available after the initial structure function measurements at HERA had been published [H1 93a, ZEU93d]. It was widely used for the analysis of the 1993 HERA data and is characterized in table 2.3.

The CTEQ2 analysis has been published together with the most recent CTEQ3 analysis [CTE94], which also incorporates novel data on the asymmetry of Drell-Yan production from proton and neutron targets from NA51 and on the lepton-asymmetry in W production from CDF. The CTEQ3 analysis requires 15 independent shape parameters

Martin, Roberts and Stirling.

MRS PDFs are obtained in much the same way as those from CTEQ, however the analyses differ in the type of input parameterization, the selected input data, and the relative normalization of the different input data sets. MRS parameterize the partons at $Q_0 = 2\,\mathrm{GeV}$, which is expected to be sufficiently large for the pQCD evolution to be valid. Again, the Q^2 dependence is established through the NLO DGLAP equations, and the PDFs are fit to experimental data on hard scattering processes.

Before HERA data taking started, MRS PDFs [MRS93b] were based on structure function measurements from fixed-target muon and (anti-)neutrino scattering and on cross-sections for Drell-Yan, prompt-γ, W and Z production. The sets D^0 and D^- label PDFs with a flavour-SU(2) asymmetric sea (ie $\overline{u}$ and $\overline{d}$ "D"ifferent) and flat (Regge-type) or singular (BFKL-like) gluon distribution at small x, respectively. The set S^0 indicates Regge-type gluons and an SU(2) symmetric sea (ie $\overline{u}$ and $\overline{d}$ the "S"ame). For studies of DIS at HERA, additional D^- sets are provided assuming GLR-like shadowing for $R = 2\mathrm{GeV}^{-1}$ and $R = 5\mathrm{GeV}^{-1}$. The MRS PDFs have been updated once [MRS93a] ($\mathrm{S}^{0'}$, $\mathrm{D}^{0'}$, and $\mathrm{D}^{-'}$) when more precise data from CCFR and NMC became available. The analysis is characterized in table 2.3.

The initial F_2^{ep} results from HERA measurements have been incorporated into the unpublished set MRS(H). The most recent analysis, MRS(A) [MS94], is tuned to include the asymmetry measurements from NA51 and CDF, and an EMC F_2^c measurement from the process $\mu N \rightarrow c\overline{c}X$. The latter leads to a modified treatment of charm compared to the previous analyses. It is now assumed that the charm distribution $c(x, Q^2) = 0$ for $Q^2 < m_c^2$. Massless NLO GLAP evolution then results in $c \approx 0.1s$ at Q_0^2, where s is the strange distribution.

Glück, Reya and Vogt.

Contrary to the other two analyses, GRV make assumptions on the nature of the valence quarks, gluons and sea quarks in the proton at very low $Q^2 = \mu^2$, thus they only need to fix the valence quark distribution at a given Q_0^2 to uniquely determine individual parton distributions.

GRV assume that the proton consists at $Q^2 = \mu^2 = 0.3\,\mathrm{GeV}^2 \cong 2\Lambda^2_{\mathrm{QCD}}$ entirely of valence

quarks and "valence-like" gluons [GRV90], ie they postulate

$$xg(x,\mu^2) = \frac{n_g}{3}\left(xu_v(x,\mu^2) + xd_v(x,\mu^2)\right) \quad (2.112)$$

$$x\overline{q}(x,\mu^2) = 0. \quad (2.113)$$

The index v indicates valence quarks, $q_v = q - \overline{q}$, and $n_g = 2$ counts the number of gluons. Thus the nucleon can be pictured to consist of three valence quarks and two constituent gluons. Two gluons can combine into a colour and spin singlet, as required for the nucleon. In a more recent publication [GRV92], GRV relaxed the boundary condition to account for the NMC measurement of $F_2^{\mu n}/F_2^{\mu p}$ by allowing finite light sea densities at $Q^2 = \mu^2$, and they now parameterize

$$xg(x,\mu^2) = Ax^{\alpha}(1-x)^{\beta} \quad (2.114)$$

$$x\overline{u}(x,\mu^2) = A'x^{\alpha'}(1-x)^{\beta'} = x\overline{d}(x,\mu^2). \quad (2.115)$$

Once the boundary conditions at μ^2 are fixed, only the valence quark distributions have to be parameterized and fit to experimental data. The gluon and sea quarks can be uniquely determined from QCD evolution through the RGE. GRV use KMRS-B$^-$ [KMRS90] partons to parameterize the valence quarks at $Q_0^2 = 4\,\mathrm{GeV}^2$. Since the contribution of the valence quarks becomes small with decreasing x, GRV partons are uniquely determined although the experimentally measured phase space is rather limited towards small values of x. GRV provides PDFs in the kinematic range $10^{-5} < x < 1$, $0.3\,\mathrm{GeV}^2 < Q^2 < 10^8\,\mathrm{GeV}^2$.

2.5.4 Results and Expectations from HERA

Phase Space Covered by 1993 HERA Measurements.

With the beginning of HERA data taking the kinematic region of structure function measurements has been extended by more than two orders of magnitude towards both lower values of x and higher values of Q^2. The HERA experiments have for the first time seen an increase of the structure functions with decreasing x. By shifting the nominal collision vertex the accessible kinematic domain has been further extended to overlap with fixed-target data of pre-HERA experiments.

With an integrated luminosity of $0.54\,\mathrm{pb}^{-1}$ during the 1993 data taking period, the ZEUS collaboration published 56 data points for $F_2(x, Q^2)$ in the region $0.0003 < x < 0.1$ and $8.5 < Q^2 < 2000$ [ZEU95c]. Similar results have been presented by the H1 collaboration [H1 95]. Fig. 2.16 shows how the measured phase space is extended by the present HERA experiments.

Small-x Behaviour of F_2

At very low values of x, shadowing effects are expected to dampen the rise of the structure function. GLR-type shadowing is estimated to become significant for x values below $x_{\mathrm{crit}} \cong$

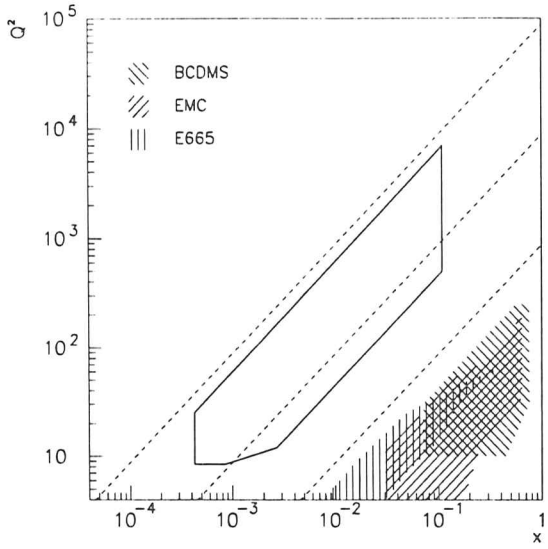

Figure 2.16: Phase space so far accessed by HERA experiments (solid line). The lower limit is due to the beam-pipe opening in the detectors, the upper limit results from the cross-sections becoming too small. The shaded areas show the kinematic regime covered by pre-HERA fixed target experiments. The dashed lines are lines of constant y (1, 0.1, and 0.01).

$\mathcal{O}(10^{-4})$, assuming $R = 3 \ldots 5\,\mathrm{GeV}^{-1}$. A MC study [GKR94] investigated whether such effects will observable by the HERA experiments. It turned out that recombination effects can be ruled out if they do not exist in the HERA x domain, however their presence will not be quantifiable if they exist.

Shape of the Gluon Distribution.

The small-x behaviour of the structure function is directly linked to the gluon density at small x. So far, the gluon density has been extracted at $Q^2 = 20\,\mathrm{GeV}$ by using (N)LO approximations of the evolution equation for the structure function [Pry93, Pry94, EKL94] and by performing a full NLO QCD simultaneous fit of the ZEUS and NMC data [ZEU95a].

For increased statistics corresponding to an integrated luminosity of $\mathcal{L} = 20\,\mathrm{pb}^{-1}$, it has been proposed to measure the longitudinal structure function F_L from radiative events, and to use F_L to extract the gluon density [CSDL91].

Flavour-Asymmetric Sea-Quarks. Valence-Quarks.

It has been pointed out that valence and sea quark PDFs can be unfolded from HERA measurements if the machine is run in e^-p and e^+p mode and both NC and CC cross sections are used [IR89]. Currently, valence quark distributions are obtained by measurements of the W production cross-section in $p\overline{p}$ collisions (u, d) and from the difference of structure functions from neutrino and muon scattering (s).

Assuming massless quarks, the light sea is expected to be flavour-SU(3) symmetric. Neutrino di-muon data, however, indicate that the strange sea, $\overline{s}$, is suppressed by a factor of $\frac{1}{2}$ compared to $\overline{u}$ and $\overline{d}$. Recent measurements of the asymmetry in W-boson production and difference in Drell-Yan cross-sections for protons and neutrons indicate that also flavour-SU(2) symmetry of $\overline{u}$ and $\overline{d}$ is broken. The most recent PDF analyses impose $\overline{s} = (\overline{u} + \overline{d})/4$ and parameterize $(\overline{d} - \overline{u})$.

Chapter 3

HERA and ZEUS

3.1 HERA

HERA[1], the world's first electron-proton colliding facility, is located at DESY in Hamburg, Germany. HERA provides electron-proton collisions at a design CM energy of $\sqrt{s}$=314 GeV. The first collisions were observed on October 19^{th}, 1991, at $\sqrt{s}$=152 GeV. Operation for physics measurements started in spring 1992 at a proton beam energy of 820 GeV and an electron beam energy of 27 GeV, yielding $\sqrt{s}$=298 GeV.

The HERA accelerator is accommodated in a 6.3 km long underground tunnel. About one fourth of the tunnel runs under a populated area, the remainder surrounds a large recreation area. Four large halls are constructed around HERA's four interaction points, offering room for HEP experiments. Two halls are occupied by the experiments H1 (north hall, [H1 93b]) and ZEUS (south hall, [ZEU93a]), which are running since HERA first delivered luminosity. The remaining two halls are allocated to the experiments HERMES (east hall, [HER90]) and HERA-B ([HER94]).

Fig. 3.1 shows a bird eye's view of DESY (with the airport in the background). Dashed lines show the locations of the HERA tunnel (10 m-30 m underground) and the older PETRA accelerator, which surrounds the site of DESY, capital letters indicate the location of the experiments.

3.1.1 Machine Layout

Figure 3.2 shows a schematic view of DESY's accelerator complex. Linear accelerators (linacs) are used for the initial acceleration of electrons, positrons[2] and protons. A positron intensity accumulator (PIA) helps to increase positron beam currents. The beams are further accelerated

[1]abbr. for "Hadronen-Elektronen Ring Anlage", hadron electron ring accelerator

[2]Positrons have been used in pre-HERA e^+e^--colliding experiments at DESY and were used at HERA instead of electrons during the second half of the 1994 data taking period.

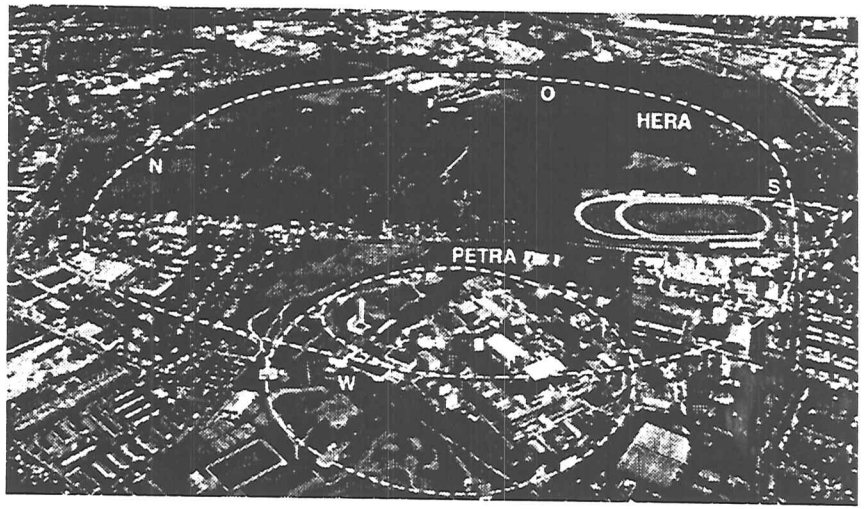

Figure 3.1: Aerial view of DESY in Hamburg. The dashed lines show the location of the PETRA and HERA colliders. The ZEUS experiment is located in the HERA south hall (S).

in the synchrotrons DESY-II ($e^{\pm}$) and DESY-III (p) and the PETRA[3] accelerator, which was used for e^+e^- collisions till 1988 and then modified to become a pre-accelerator for HERA.

PETRA accelerates electrons and protons to an energy of 14 GeV (12 GeV in 1993) and 40 GeV.

[3]abbr. for "Positronen-Elektronen Tandem Ring Anlage", positron electron tandem ring accelerator

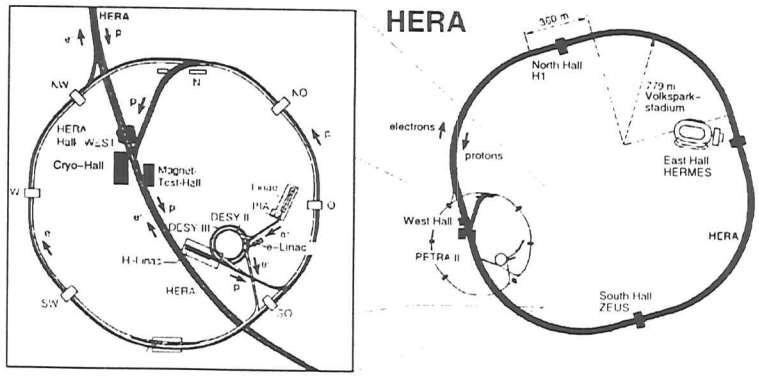

Figure 3.2: Schematic view of DESY's accelerator complex (cf text)

	electron ring	proton ring
circumference	6336 m	
filling time	15 min	20 min
injection energy	14 GeV	40 GeV
beam energy	30 GeV	820 GeV
energy in CMS	314 GeV	
magnetic bending field	0.164 T	4.682 T
no. buckets	220	220
no. bunches	210	210
no. particles/bunch	$0.8 \cdot 10^{13}$	$2.1 \cdot 10^{13}$
beam current	60 mA	160 mA
current/bunch	0.3 mA	0.8 mA
σ_z	30 mm	440 mm
σ_x	0.264 mm	0.300 mm
σ_y	0.017 mm	0.095 mm
beam crossing interval	96 ns	
beam crossing angle	0 rad	
luminosity	$1.5 \cdot 10^{31}\,\mathrm{cm}^{-2}\mathrm{s}^{-1}$	
specific luminosity	$3.3 \cdot 10^{29}\,\mathrm{cm}^{-2}\mathrm{s}^{-1}\mathrm{mA}^{-2}$	
polarization time	25 min	

Table 3.1: HERA design parameters.

respectively. To achieve optimum luminosity in the HERA collider, first the proton beam is injected, ramped to its nominal energy of 820 GeV, and stored in an orbit which is well-separated from the interaction points (IP). Then the electrons are injected and ramped to their nominal energy. The electron orbit is fixed, and the proton beam is directed into the orbit of the electrons at the IPs.

While circulating, the electron beam may become transversely polarized as the electron spins predominantly adjust anti-parallel to the magnetic bending fields [ST64]. Specially developed spin rotators are foreseen to turn the electron spins to become (anti-)parallel to the orbit at the interaction points. The theoretical limit for the degree of polarization is $P_0 = 92\%$, so far 70% have been reached. Table 3.1 summarizes the design parameters of HERA.

3.1.2 Physics Potential

Lepton-quark collisions at high energies involve a variety of processes which are suitable to probe different physics aspects within the Standard Model (cf eg [Ros94, Par94]) or beyond. The physics which can be studied at HERA is extensively discussed in [HER87, HER91] and is briefly reviewed in eg [Wol94]. Some topics are highlighted in the following paragraphs.

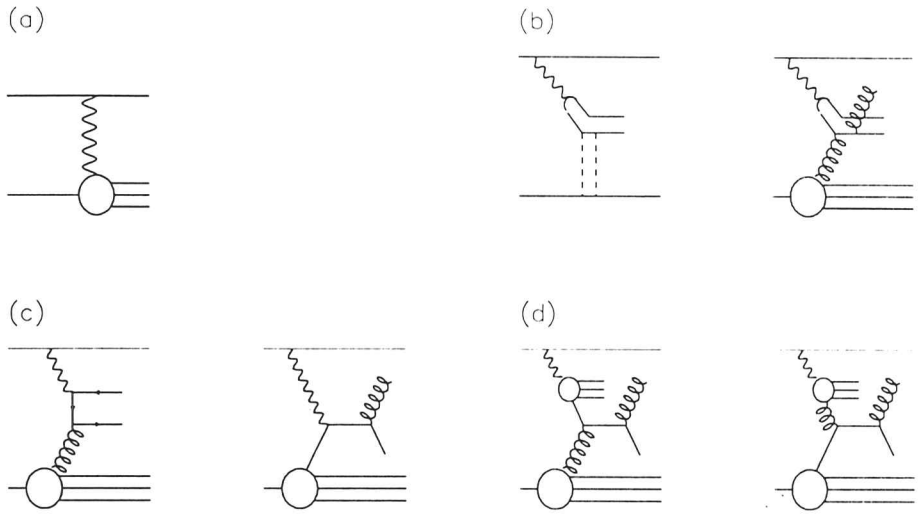

Figure 3.3: Examples for processes which contribute to the photoproduction cross section: (a) basic diagram, (b) VDM: basic diagram, elastic scattering and hard interaction within VDM, (c) direct processes: BGF (left) and QCD-compton (right), (d) quark or gluon from a resolved photon.

Deep Inelastic Scattering.

Deep inelastic scattering and the opportunities it offers to study QCD at low x have already been discussed in the previous chapter, although the discussion was limited to unpolarized beams and neutral current exchange. Since the experiments measure the entire final state, other fields of research include jet studies and hadronic energy flows, which can be used to test QCD and derive the running coupling constant, α_s, and to test fragmentation models. Other topics are the study of diffraction and measurements of heavy-flavour production in DIS.

Charged currents lead to the production of a final state neutrino and allow a measurement of the electroweak parameters of the SM. The first measurements [H1 94, ZEU95b] demonstrated the influence of the W propagator on the cross section. The HERMES collaboration [HER90] will measure the scattering of polarized electrons from the HERA electron beam off a polarized ^{3}He target.

Photoproduction.

ep collisions can be related to (virtual) photon-proton interactions, where the electron beam is simply responsible for the presence of the virtual photons (fig. 3.3a). The total photon-proton

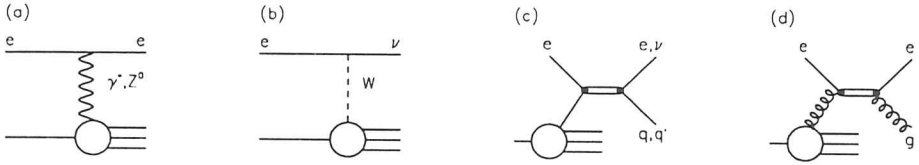

Figure 3.4: Lowest order diagrams for NC (a) and CC (b) interactions compared to s-channel production of lepto-quarks (c) and lepto-gluons (d).

cross section, $\sigma_{\rm tot}^{\gamma^* p}$, can be extrapolated from the structure function, F_2, for $Q^2 \to 0$ [Lev95]

$$\sigma_{\rm tot}^{\gamma^* p}(W) = \frac{4\pi^2\alpha}{Q^4}\frac{4m_p^2x^2+Q^2}{1-x}F_2(x,Q^2). \qquad (3.1)$$

using $W^2 = (\frac{1}{x}-1)Q^2 + m_p^2$.

The bulk of interactions at $Q^2 \approx 0$ can be described by the vector-meson dominance model (VDM). The VDM assumes the photon to fluctuate into a vector meson (ρ, ω, ϕ), which then interacts with the proton. It thus relates photoproduction to hadro-production cross sections (eg $\pi^{\pm}p, K^{\pm}p, \rho p$). Consequently, the VDM predicts the total photon-proton cross section to be almost independent of W.

Contrary to vector mesons, photons also have a point-like coupling to quarks, which leads to diagrams beyond the VDM. QCD Compton (QCDC) and photon-gluon fusion (BGF) are called direct processes (fig. 3.3c), since they are due to the direct coupling of the photon to a quark. Fig. 3.3d shows examples of resolved processes, in which partons emerging from the photon couple to partons in the proton.

Initial measurements of photon-proton reactions at HERA energies [H1 93c, ZEU92a] indicate that the cross section receives both VDM-like and hard contributions. Studies of final-state transverse momentum distributions and observation of di-jet events established the presence of hard processes and identified both direct and resolved processes.

Measurement of photoproduction of jets is sensitive to the photon structure function. Exclusive measurements of heavy flavour production, which proceeds predominantly via the BGF process, are sensitive to the gluon density in the proton, and allow to search for rare decays as a possible indication for physics beyond the SM.

Searches for Exotic Particles.

Extensions which have been proposed for the SM include lepto-quark (or lepto-gluon) resonances resulting from a new interaction of a lepton and a quark (gluon). Compared to other experiments, HERA offers a complementary search possibility for lepto-quark (LQ) production in the s-channel, $eq \to LQ \to l'q'$, cf fig. 3.4.

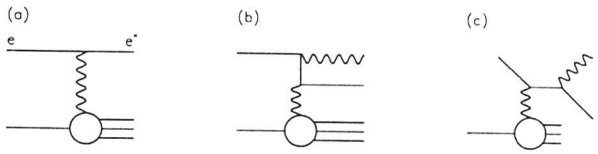

Figure 3.5: Some diagrams for the production of excited electrons at HERA: (a) basic diagram for $ep \to e^*X$, (b) t-channel contribution of e^*, (c) s-channel contribution.

Lepto-quarks would be signaled by a peak in the distribution of the invariant mass of the final electron-quark system, M_{eq}, or equivalently, in the x distribution at $x_0 = m_{\rm LQ}^2/s$, where $m_{\rm LQ}$ is the mass of the lepto-quark.

The cross section for lepto-quark production is given by

$$\sigma(eq \to {\rm LQ}) = \frac{\pi}{4s}g^2 q(x_0, m_{\rm LQ}^2). \qquad (3.2)$$

where $g = \sqrt{g_L^2 + g_R^2}$, $g_{L,R}$ are the left- and right-handed couplings, and q is the quark density. The cross section is of the order 100 pb for lepto-quarks of $m_{\rm LQ}$=100 GeV and g of the order of the standard gauge coupling. HERA is expected to be sensitive to leptoquarks of masses up to 200 GeV and couplings as small as $g \cong \mathcal{O}(10^{-3}\alpha_{\rm em})$ [BRW87].

Excited fermions, f^*, would indicate a new substructure in leptons. At HERA, they could be produced via $ep \to e^*X$ (fig. 3.5). They would decay into $e\gamma$, eZ, or νW. The cleanest signal can be expected from the $e\gamma$ decay channel, corresponding to a relatively quiet event with a wide-angle electron-photon pair [BDK93].

A signal for e^*-production would be observed in the distribution of the invariant mass of the electron-photon pair, $M_{e\gamma}$. The major background from wide-angle QED Compton events can be suppressed by requiring $M_{e\gamma} > 90$ GeV, the mass limits for excited electrons obtained by LEP.

The cross section for e^*-production would be of the order of 1 pb or less [HKZ85] for excited electrons with masses above 50 GeV. Requiring at least ten observed events, for a compositeness scale of $\mathcal{O}$(1 TeV) HERA would be sensitive to e^* with masses up to 160 GeV at an integrated luminosity of $\mathcal{L}$=200 pb^{-1} [BDK93].

3.1.3 Operation in 1993

In 1993, HERA delivered luminosity for physics measurements from the end of June till the end of October. Not all of HERA's design values have already been reached during this period. The electron beam energy was limited to 26.67 GeV since some super-conducting cavities were not yet installed. The achieved maximum luminosity was $\mathcal{L} = 0.7 \cdot 10^{30}$ cm^{-2}s^{-1} with typical beam currents of 10-15 mA, however the maximum specific luminosity of $\mathcal{L}_{\rm spec}$ =

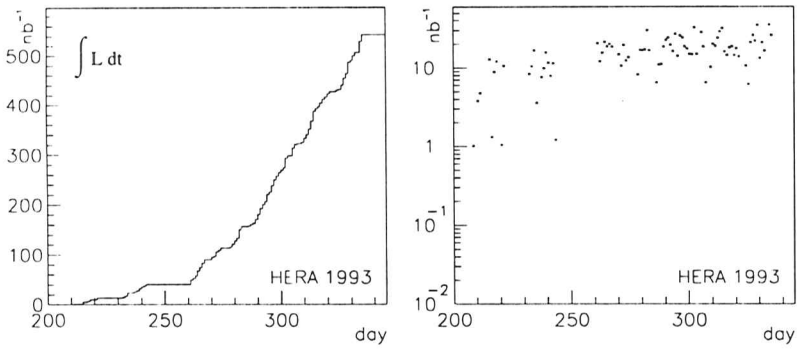

Figure 3.6: Integrated luminosity (left) and luminosity per day (right) for 1993 HERA data taking period.

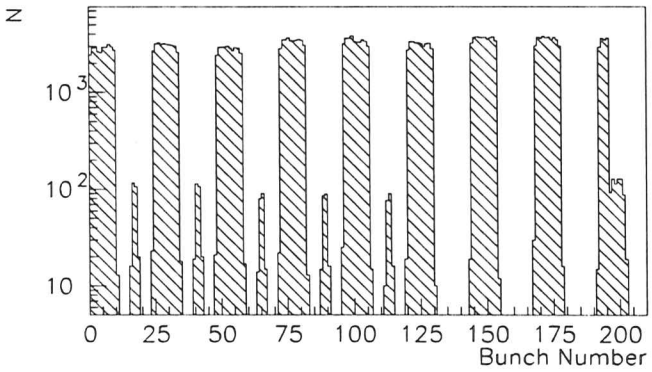

Figure 3.7: Bunch filling scheme for 1993 HERA data taking period. The histogram plots the number of DIS candidate events observed by ZEUS versus the bunch number. Bins with more than 10^3 entries correspond to colliding bunches, while bins with about 10^2 entries indicate pilot bunches (cf text).

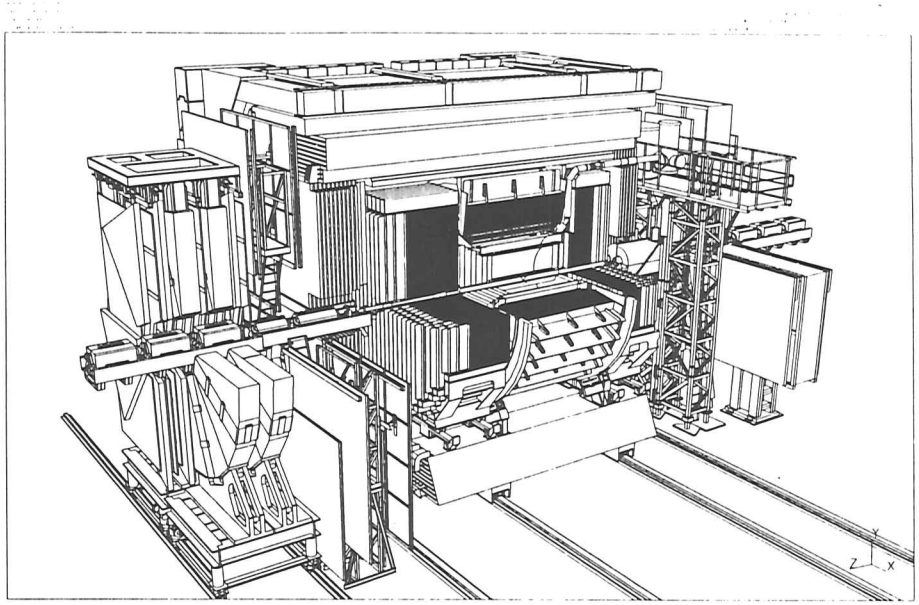

Figure 3.8: Three-dimensional view of the ZEUS detector (cf text).

$7.5 \cdot 10^{29}\,\mathrm{cm}^{-2}\mathrm{s}^{-1}\mathrm{mA}^{-2}$ exceeded the expectation by more than a factor of two. The integrated luminosity observed by ZEUS was $550\,\mathrm{nb}^{-1}$ (cf fig. 3.6), which is about twenty times higher than the luminosity collected in 1992.

Fig. 3.7 shows the bunch configuration of 1993. The machine collided 84 electron bunches on 84 proton bunches, with an additional 10 (6) unpaired electron (proton) bunches for background studies (so-called pilot bunches). The colliding bunches traveled in groups of ten, being separated by gaps of 14 buckets. The electron pilot bunches were placed in two subsequent buckets in the center of the first five of these gaps, while the proton pilots traveled as a train following the last four colliding bunches.

3.2 ZEUS

ZEUS [ZEU93a] is a collaboration of more than 450 physicists, engineers, and technicians, coming from 51 different institutes of 12 nations. The ZEUS collaboration constructed a multipurpose magnetic detector for one of HERA's interaction regions.

Fig. 3.8 shows a three-dimensional view of the detector. The electron beam enters the detector

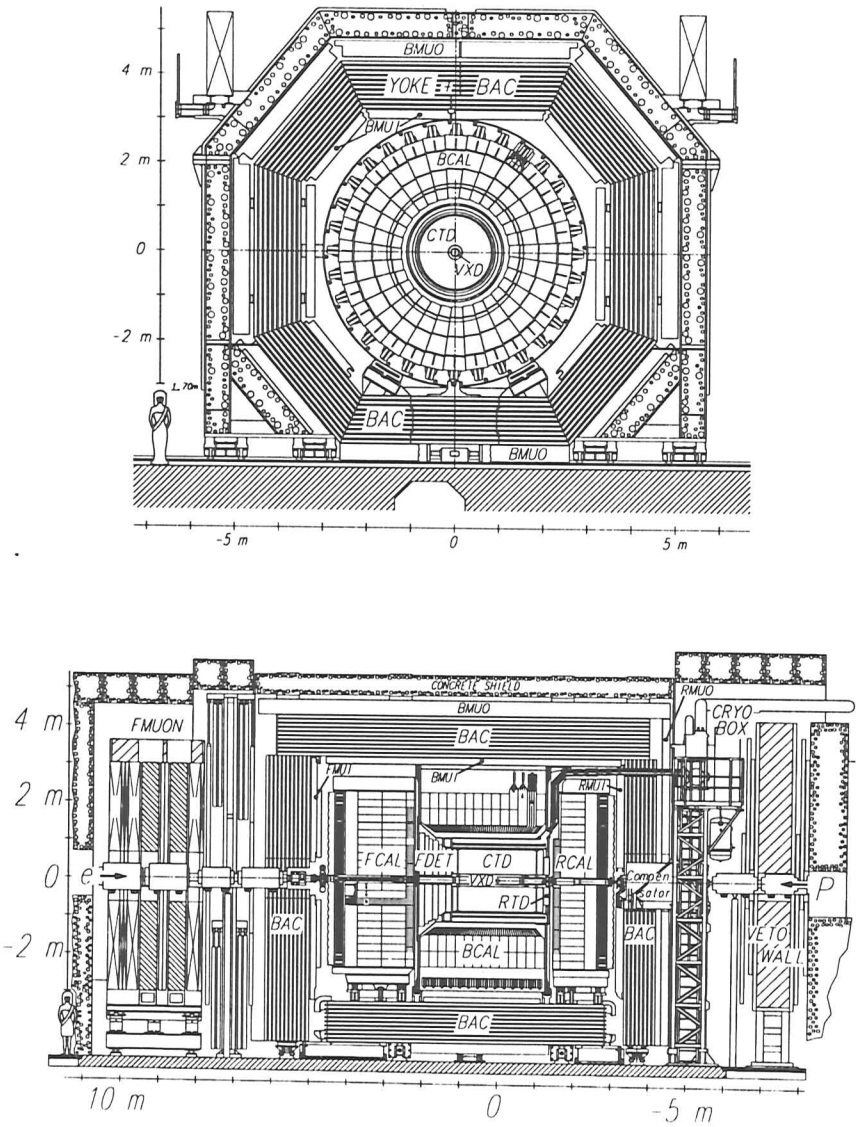

Figure 3.9: Schematic views of the ZEUS detector: Cross section (top) and longitudinal cut (bottom). The different detector components are explained in the text.

from the left, the proton beam from the right. The interaction point is surrounded by a tracking system, which sits inside a thin super-conducting solenoid producing a magnetic field of up to 1.54 T to deflect charged particles. A high-resolution uranium-scintillator sandwich calorimeter absorbs the final state particles. The detector is encapsulated in an iron return yoke for the magnetic field, which contains a backing calorimeter and has chambers for muon detection mounted on its inner and outer sides. The setup is completed by a forward[1] muon spectrometer, a veto-wall which indicates that particles which were produced upstream of the interaction point enter the detector from the back, and some detector components close to the beam axis to catch particles which escaped the main detector through the beam-pipe openings.

The following section gives a brief overview of the major detector components. Fig. 3.9 shows a longitudinal cut and a cross section of the detector and indicates the location of the different detector components. The major characteristics of the detector are summarized in table 3.2. The trigger and data acquisition system is described in a separate section.

3.2.1 Detector Components

Calorimeter.

The ZEUS calorimeter is designed to give the best possible resolution in the measurement of hadronic jets, to have a good resolution for electromagnetic showers, and to give a uniform response over as much of the solid angle as can be covered by detector material. It consists of a high-resolution inner calorimeter (CAL), and a lower-resolution outer backing calorimeter (BAC). The high-resolution calorimeter is described in detail in [D+91, ZEU91a, ZEU93a]

The backing calorimeter consists of proportional tubes, which are interleafed with 73mm thick iron plates of the return yoke for the magnetic field. The ten layers of iron correspond to a thickness of $4.3\lambda_0$, where λ_0 is the hadronic interaction length. The purpose of BAC is to tag jets which leak out of the high-resolution calorimeter. Its hadronic energy resolution is $\sigma_E^{\mathrm{hadr}}/E \approx 100\%/\sqrt{E\,[\mathrm{GeV}]}$.

The high-resolution calorimeter is realized as a uranium-scintillator sampling calorimeter. It is mechanically divided into three sections: the forward calorimeter (FCAL), the barrel calorimeter (BCAL), and the rear calorimeter (RCAL). The barrel calorimeter surrounds the central detector region and the solenoid and consists of 32 wedge-shaped modules with typical dimensions of 3 m×0.5 m×1.7 m. FCAL and RCAL are made from quadric modules of 20 cm width, which are arranged to form walls perpendicular to the beam axis at both ends of the BCAL. The heights of the FCAL and RCAL modules are varying from 220 cm to 460 cm depending on the module's distance to the beam axis, module depths vary accordingly from 117 cm to 153 cm in the FCAL, and 69 cm to 87 cm in the RCAL. Fig. 3.10 shows the largest FCAL module.

The solid angle coverage is 99.8% in the forward hemisphere, and 99.5% in the rear. The polar

[1] The coordinate system aligns the z-axis with the proton beam direction. The x axis points to the center of HERA, the y axis points upward.

Vertex Detector (VXD)			
active radius		106.5-142.5	mm
active length		1590	mm
polar angle coverage		$8.6^0 - 165^0$	
Lorentz angle		5^0	
position resolution		35	μm
Central Tracking Detector (CTD)			
active radius		190-785	mm
active length		2024	mm
polar angle coverage		$15^0 - 164^0$	
max. drift time		500	ns
Lorentz angle		45^0	
position resolution		100-200	μm
z resolution (stereo)		1.2	mm
z resolution (timing)		3	cm
two-track resolution		1.6	mm
dE/dx resolution		$\approx 5\%$	(e^-)
$\sigma(p)/p$ at 90^0		$0.0021p\,[\mathrm{GeV/c^{-1}}] \oplus 0.0029$	
Forward/Rear Tracking Detectors (FTD1-3.RTD)			
active radius	(FTD)	180-1085	mm
	(RTD)	220-495	mm
polar angle coverage	(FTD)	$6^0 - 28^0$	
	(RTD)	$160^0 - 170^0$	
single wire efficiency		97	%
position resolution		120	μm
double track resolution		2	mm
Superconducting Solenoid (COIL)			
radius (coil/cryostat)		925-957.1 (860-1110)	mm
length (coil/cryostat)		2460 (2800)	mm
nominal current		4987	A
max. B field		1.54	T
High-Resolution Calorimeter (CAL)			
active radius	(BCAL)	1232-2296	mm
maximum depth	(FCAL)	1525 (7.1)	mm (λ_0)
	(BCAL)	1059 (4.9)	mm (λ_0)
	(RCAL)	870 (4.0)	mm (λ_0)
polar angle coverage	(FCAL)	$2.2^0 - 39.9^0$	
	(BCAL)	$36.7^0 - 129.1^0$	
	(RCAL)	$128.1^0 - 176.5^0$	
energy resolution (hadrons)		$35/\sqrt{E\,[\mathrm{GeV}]} \oplus 2$	%
energy resolution (electrons)		$18/\sqrt{E\,[\mathrm{GeV}]} \oplus 2$	%
time resolution		$1.5/\sqrt{E\,[\mathrm{GeV}]} \oplus 0.5$	ns
x-position resolution (hadrons)		$6.5/\sqrt{E\,[\mathrm{GeV}]}$	cm
y-position resolution (hadrons)		$6.7/\sqrt{E\,[\mathrm{GeV}]}$	cm
x-position resolution (electrons)		$5.4/\sqrt{E\,[\mathrm{GeV}]}$	cm
y-position resolution (electrons)		$1.4/\sqrt{E\,[\mathrm{GeV}]}$	cm
Backing Calorimeter (BAC)			
energy resolution (hadrons)		$100/\sqrt{E\,[\mathrm{GeV}]}$	%

Table 3.2: Major characteristics of the tracking system and calorimeter of the ZEUS detector. The values are taken from the references quoted in the text and from [ZEU93a].

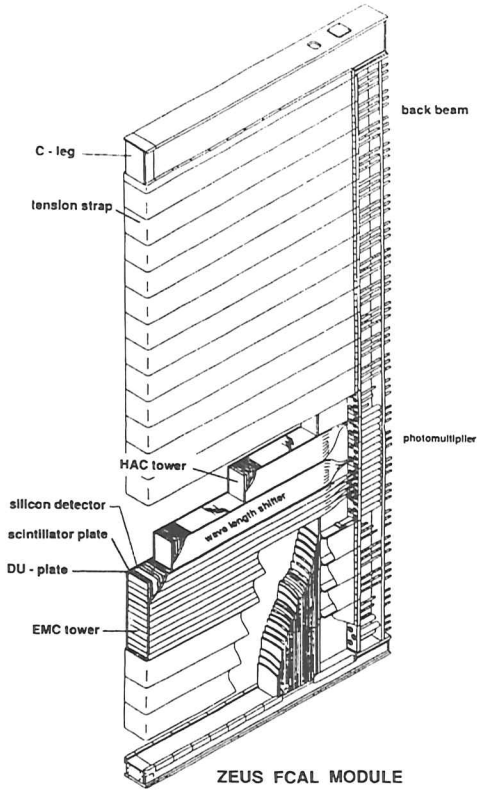

Figure 3.10: Largest FCAL module.

angle coverage of the different calorimeter sections is

$$\begin{aligned} \text{FCAL: } \theta &= 2.2^0 \ldots 39.9^0. \\ \text{BCAL: } \theta &= 36.7^0 \ldots 129.1^0. \\ \text{RCAL: } \theta &= 128.1^0 \ldots 176.5^0. \end{aligned}$$

The depth of the calorimeter is chosen to contain at least 95% of the energy for more than 90% of the hadronic jets having the highest energy which is kinematically possible. This energy varies from 800 GeV in the very forward region to 200 GeV in the barrel and 30 GeV in the rear calorimeters. The corresponding calorimeter depths are $7\lambda_0$, $5\lambda_0$, and $4\lambda_0$ in FCAL, BCAL, and RCAL, respectively.

The CAL modules consist of alternate layers of depleted uranium (DU) and scintillator (Sci) with $1X_0$ sampling. A unit cell of $\approx$8 mm depth is common to the entire CAL to ensure a

homogeneous response. It contains a 3.3 mm ($1X_0$) DU plate, a 2.6 mm Sci plate, and an air gap to avoid pressure on the scintillator tiles. The unit cell dimensions achieve compensation[5] above 1 GeV, ie equal signals from electromagnetic and hadronic particles of the same energy ($e/h = 1$). Compensation yields optimal energy resolution for hadronic jets, in case of ZEUS [D+91, ZEU91a]

$$\sigma_E^{\mathrm{hadr}}/E = 35\%/\sqrt{E\,[\mathrm{GeV}]}. \quad (3.3)$$

$$\sigma_E^{\mathrm{em}}/E = 18\%/\sqrt{E\,[\mathrm{GeV}]}. \quad (3.4)$$

These resolutions have been demonstrated in test beam measurements [Kla88].

The calorimeter is read out by the standard technique of wavelength shifting and light guiding using wavelength shifter (WLS) plates. The light is then collected by photo-multiplier tubes (PMT), the signals of which are passed to the electronic read-out. The readout via PMTs enables an accurate time measurement with a resolution of

$$\sigma_t = \left(1.5/\sqrt{E\,[\mathrm{GeV}]} \oplus 0.5\right)\ \mathrm{ns}. \quad (3.5)$$

The basic readout cell is called a tower and has a typical cross-section of 20 cm×20 cm. Each tower is longitudinally segmented into an electromagnetic (EMC) and hadronic (HAC) sections. FCAL and BCAL have two HACs, while the RCAL, which is hit by lower energy particles, has only one HAC section. The EMC is further segmented into strips of 5(10) cm×20 cm in the FCAL and BCAL (RCAL).

The active area of each WLS tile is clad in a reflective aluminum foil. An individual pattern of black stripes is printed on each foil to correct for different light yields of the scintillator plates in a given tower, for variations in the thickness of the DU plates, and for variations in the light collection efficiency within a scintillator plate.

The DU plates are clad in stainless steel of 0.2 mm (0.4 mm) thickness in the EMC (HAC) sections. The stainless steel cladding is used to reduce the signal from uranium decays (uranium noise), and at the same time provides a fire protection.

The calorimeter has been calibrated in test beam measurements at CERN prior to installation in the detector. Several calibration tools have been developed for an in-situ calibration:

- The DU activity gives rise to a constant level of light in the scintillators. The signal is integrated over a few ms (so-called dark current). The dark current is used to adjust the PMT gains to specific currents (156 nA, 838 nA and 1106 nA in the EMC, HAC1 and HAC2 sections). Monitoring the dark current is accurate to 1%, the rms value from the uranium noise corresponds to 15 MeV (25 MeV) in the EMC (HAC) towers.

[5] Typically, calorimeters are under-compensating, ie $e/h \gtrsim 1.5$, and both the hadronic signal has to be enhanced and the electromagnetic signal needs to be suppressed to obtain compensation. Enhancement of the hadronic signal can be achieved by over-efficient detection of the neutron signal in a hadronic shower, or by detecting photons from nuclear de-excitation processes [Wig88, BAB88]. The electromagnetic signal is suppressed by choosing a heavy absorber material.

- Stainless steel tubes with an outer diameter of 2 mm are attached to each side of each tower. A ^{60}Co-source fixed at the tip of a piano wire can be moved within the tubes to survey the calorimeter response.
- A fiber-optical system allows to inject light from a dye laser or from distributed LEDs into the transition pieces in front of each PMT to calibrate the PMT response. The light pulse gives a PMT response similar to a signal generated by a particle in the calorimeter [M+93].
- The front-end and digital electronics can be calibrated independently of the optical read-out by a charge injection system which allows the injection of specific charges into the inputs of the analog cards.

Two (one) layers of 3 cm×3 cm silicon diodes are foreseen to be inserted into the FCAL (B/RCAL) after $6X_0$ and $3X_0$ ($3X_0$) to improve electron and hadron identification (hadron-electron separator, HES). The RHES is already instrumented and has been successfully used for the study of NC-DIS [Fle94, Ohr96].

Tracking System.

The tracking system consists of a forward tracking detector (FTD), the central tracking detector (CTD), the rear tracking detector (RTD), and the vertex detector (VXD). A transition radiation detector (TRD) is interleafed with the FTD. FTD and TRD together are referred to as the forward detector, FDET. The tracking system has been developed for track reconstruction, particle identification, and event triggering. It provides charged particle tracking for polar angles in the range of $7.5^0 < \theta < 170^0$.

The FTD consists of three sets of 18-layer wire chambers (FTD1,2,3) with 6+6+6 sense layers arranged at 120^0 stereo. They are interleafed with four layers TRD for electron identification. The RTD is a similar 18-layer chamber at the rear. Both FTD and RTD were not fully instrumented and hence unavailable for the 1993 data taking period.

The CTD covers a polar angle range of $15^0 < \theta < 164^0$. It reconstructs tracks, delivers dE/dx information to improve particle identification, and locates the interaction vertex along the beam axis as part of the trigger. The major tasks of the CTD are [ZEU89]

- to measure charged tracks,
- to measure the charge of muons unambiguously for p_t up to 150 GeV/c,
- to provide good tracking in dense jets,
- to offer a good double-track resolution,
- to allow an easy resolution of left/right ambiguities,
- and to deliver fast signals to avoid confusion between subsequent bunch crossings.

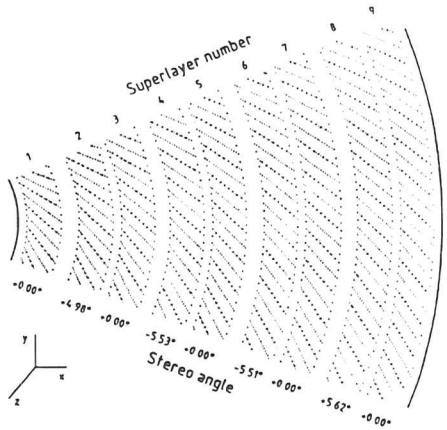

Figure 3.11: Cross section of an octant of the CTD (cf text).

The CTD has been realized as a multi-cell stereo superlayer chamber [Sax88]. Its wires are organized in nine superlayers, which are constructed from cells of eight sense wires each, with alternate superlayers being rotated with stereo angles of $\pm 5^0$. Superlayers 1, 3 and 5 are equipped with special electronics to measure the longitudinal coordinate along a wire by the time difference of signals at the two ends of the sense wires. An accuracy of 200 ps corresponds to a resolution of 3 cm in space [F+93]. Fast signals are obtained by choosing a fast drift gas (50 μm/ns) and a short maximum drift length of 25 mm. A double hit resolution of 1.6 mm is achieved by using digital filtering techniques. Fig. 3.11 shows the layout of one octant of the chamber.

The vertex detector (VXD) is a 1.59 m long cylindrical drift chamber which consists of 120 radial cells of 12 sense wires each. The cells are pointing to the beam pipe center. The VXD is operated with dimethyl ether at atmospheric pressure. It has an active radial area of 106.5 mm $< r <$ 142.5 mm and covers the polar angle $8.6^0 < \theta < 165^0$. It is designed to achieve a spatial resolution of up to 35 μm [A+91].

Luminosity Monitor.

The luminosity measurement is based on the Bethe-Heitler Bremsstrahlung process, $ep \rightarrow ep\gamma$. The Bremsstrahlung photon is captured in a lead-scintillator calorimeter placed in the electron beam direction at a distance of z=-106 m from the IP [ZEU92b, PZ94]. An additional electron calorimeter at z=-35 m tags electrons from photoproduction. Fig. 3.12 shows the setup of the luminosity monitor.

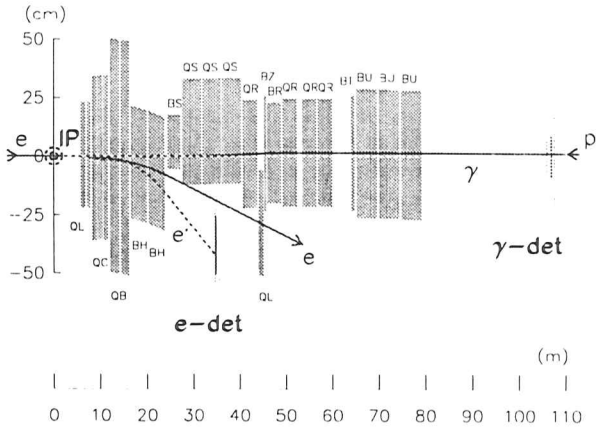

Figure 3.12: Setup of luminosity monitor [ZEU92b]. The γ-calorimeter (γ-det) tags Bremsstrahlung-photons from the Bethe-Heitler process $ep \rightarrow ep\gamma$, the electron calorimeter (e-det) tags photo-produced electrons (e'). Q and B label quadrupole and bending magnets of the collider. The solid lines show the nominal e and p orbits. The Čerenkov counter in front of γ-det (open box) has been removed after the 1992 data taking period.

Other Components.

A detailed description of the ZEUS detector covering layout and performance of all its components can be found in [ZEU93a]. Components which are not introduced above (eg the different muon detection systems) are of minor relevance to this analysis.

Two components which were incorporated in the trigger are the veto wall (VETO) and the C5 counters. The veto wall is located behind the RCAL and is used to tag showers originating from upstream beam-gas interactions which enter the detector from the back. The C5 counters are scintillator ring counters which are mounted on the beam pipe and resolve the beam structure and other beam properties.

3.2.2 Online Data Acquisition

The trigger and data acquisition (DAQ) system of the ZEUS experiment is a highly parallel distributed real-time system. It consists of several independent readout systems and three trigger levels for online data selection. Collider performance, detector layout, and off-line computing capacities define the conditions under which the trigger and data acquisition system has to operate:

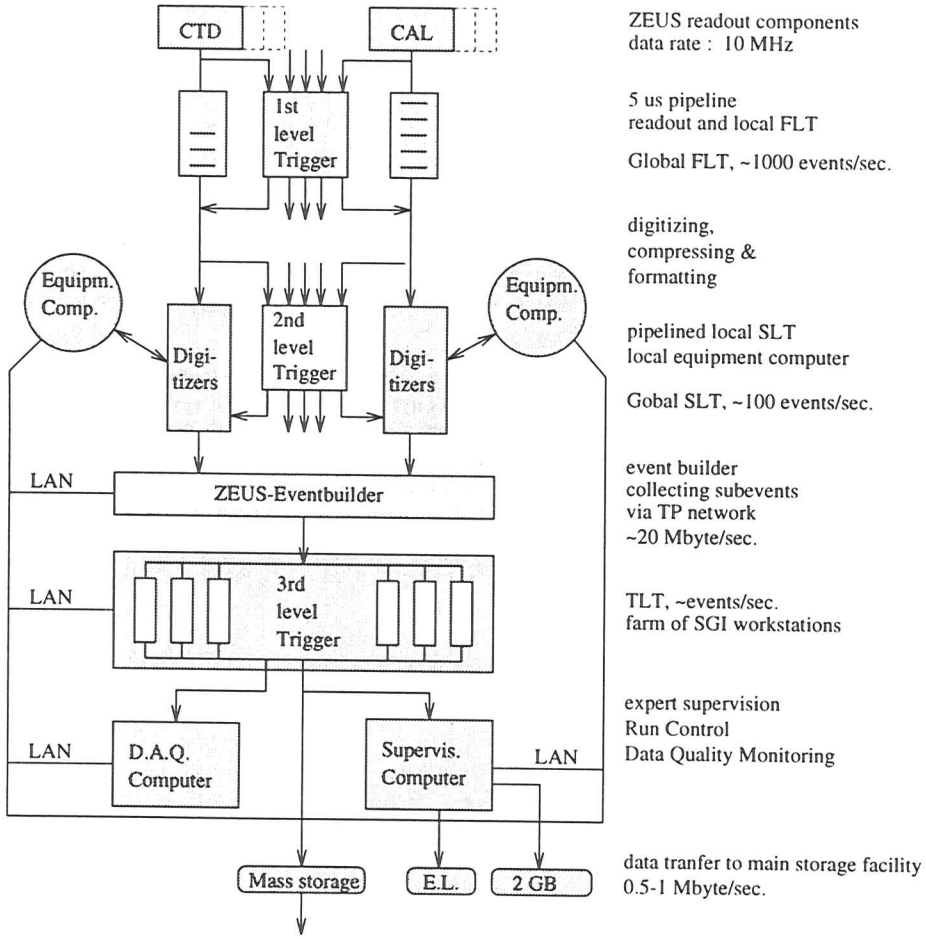

Figure 3.13: Layout of the Trigger and Data Acquisition System of the ZEUS experiment: on the right side, the data throughput at the different components of the system are shown.

- The short interval between beam crossings of only 96 ns requires a front-end trigger data input rate of 10.5 MHz.
- More than 250.000 readout channels produce an initial raw data rate exceeding 10 GB/s.
- The readout data rate has to be reduced by a factor of at least 10^4 for data recording, reconstruction and analysis.

The subsequent sections describe DAQ system operation and shortly introduce its major components. The layout of the trigger and data acquisition system and the nominal data throughput at its components are shown in figure 3.13. It is global strategy to store all the threshold values and algorithms which are required for trigger decisions in software processes to keep them exchangeable. This way, triggers can be developed and simulated off-line, before they are incorporated into the trigger system and may be even migrated down to the first level.

DAQ System Operation.

The ZEUS detector comprises several independently operating detector components, each of them equipped with their own so-called component subsystem (CSS). Component subsystems contain the "front-end" electronics required for the component control and readout. They interface to two levels of global trigger processors and the Eventbuilder. Most CSS are based on custom built VME-compatible transputer boards [Gin93, BHV94].

Once a detector component has been read out, the data are stored in a 5.5 μs first level trigger analog pipeline and analyzed by a local first level trigger processor. The results of the different component subsystems referring to the same beam crossing are input to the global first level trigger (GFLT), which computes an overall first level trigger decision. The maximum rate of GFLT accept decisions is designed to be 1 kHz. Up to the GFLT both the trigger and readout are dead-time free.

On GFLT accept, data accepted for further analysis are copied to a second level trigger pipeline. A GFLT accept rate of 1 kHz and a "copy" time of 30 μs result in 3% dead-time. This is the only source of dead-time provided no buffer full states occur. A second level trigger processor local to the component subsystem computes a trigger sub-decision, which is forwarded to the global second level trigger (GSLT) and used to compute an overall second level trigger decision. The GSLT is designed to accept about 10% of all GSLT accepted triggers.

In case a component subsystem receives a positive GSLT decision, the corresponding data are assigned a "GSLT decision number" and transferred to the Eventbuilder. The Eventbuilder combines and formats all the component data carrying the same GSLT decision number into one data set. This data set is called an "event", and its GSLT decision number is also referred to as the "event number".

Once an event is complete, it is input to the third level trigger (TLT). The TLT is a processor farm consisting of six branches of a total of 36 processor nodes. It performs the global event reconstruction and a final filtering and is designed to accept up to 5 events/s.

Global First Level Trigger (GFLT).

The GFLT receives for each bunch crossing fifty-one 16bit data words from the FLT processors which are local to the components. The data is subdivided into eight categories (eg energy, tracks) and correlated within each category to obtain yes/no bits. Logical operations are performed on these bits to obtain a subtrigger decision for each category. A logical "or" of the

individual subtriggers yields the final trigger decision.

The GFLT implementation is based on memory lookup tables (MLTs) and Xilinx-chips. The MLTs are used for comparison of the incoming component data with threshold values to obtain the yes/no bits. The Xilinx chips perform the logical operations on these bits, thus allowing to easily update or modify the trigger logic.

Global Second Level Trigger (GSLT).

The GSLT is based on transputer hardware in a VME environment. It consists of eight input modules, up to eight subtrigger modules, a central trigger module, and a control and switch box [Uij92]. The trigger modules are implemented with a custom made VME module housing two transputers and a 512kB triple-ported memory (TPM), which can be accessed simultaneously via both transputers and the VME bus [NIK90].

The input modules obtain data from the component SLT processors and distribute it to all subtriggers participating in the GSLT. The subtriggers can run independent trigger algorithms; their results are combined and evaluated by the central trigger module. The data transfer from the input modules to the subtriggers uses transputer links, the subtrigger decisions are forwarded to the central trigger module via the VMEbus, while the final GSLT decision is again made available on transputer links.

Eventbuilder (EVB).

The Eventbuilder [BFHV92, BHV93, BHV94] merges and formats the data flows originating from the various detector components into a single event record. It is implemented as an asynchronous real-time parallel packet-switching transputer network. The EVB is subject to the highest data rate within the ZEUS data acquisition system and can handle a bandwidth of 24 MB/s. It has been modeled, verified and documented with structured development tools.

Due to its connections to almost all parts of the data acquisition system, the Eventbuilder is also an important tool for system analysis and diagnosis. The monitoring capabilities of the Eventbuilder were especially beneficial during the commissioning phase of the data acquisition system [Sch92c], resulting in the proposal for the construction of an expert system to evaluate the monitoring information and support the operators which are running the experiment [BFH92, BFHO94].

Third Level Trigger (TLT).

The third level trigger is built of a farm of RISC workstations which run a subset of the off-line reconstruction software.

3.2.3 Event Reconstruction and Off-line Analysis

Event reconstruction and physics analyses are performed in a distributed UNIX-based client-server environment which incorporates desktop computing facilities (workstations and X-Terminal), central computing services, and hierarchical mass storage. About 300 user end-stations are connected via several Ethernet segments to an Ethernet/FDDI/HIPPI network backbone. Two multiprocessor UNIX machines are used for event reconstruction and as a central batch facility. The data is stored in tape silos and tape robots, which are supported by about 100GB of permanent disks for fast data accesses [Man94].

Chapter 4

Extraction of F2

It is a capital mistake
to theorize before one has data.
Insensibly one begins to twist facts to suit theories,
instead of theories to suit facts.

Arthur Conan Doyle, *A Scandal in Bohemia*

4.1 Event Signatures

4.1.1 DIS Event Characteristics

DIS events are uniquely characterized by the scattered beam electron in the final state. In the QPM picture the hadronic final state consists of the current jet and the proton remnant. Fig. 4.1 (top) shows such a "typical" DIS event. Q^2 is large, and the electron is scattered under such a large angle that it can be detected in both the tracking system and the barrel calorimeter. At lower values of Q^2 the scattering angle decreases, and eventually the electron can no longer be spotted by the tracking system and has to be reconstructed from calorimeter information only (fig. 4.1, bottom).

Since gluon radiation in the hadronic final state produces more than just the one jet which is expected from the QPM, and interactions between jets soften the structure of the hadronic final state, it is difficult to derive a unique signature for DIS from the hadronic final state.

A useful quantity for discriminating DIS events against background is δ. It is obtained from conservation of energy and longitudinal momentum. Writing the four-momenta of the initial and final state electron and hadron(s),

$$k_e = (A, 0, 0, -A), \qquad k'_e = (E_e, P_{x,e}, P_{y,e}, P_{z,e}). \tag{4.1}$$

$$p_h = (P, 0, 0, P), \qquad p'_h = (E_h, P_{x,h}, P_{y,h}, P_{z,h}). \tag{4.2}$$

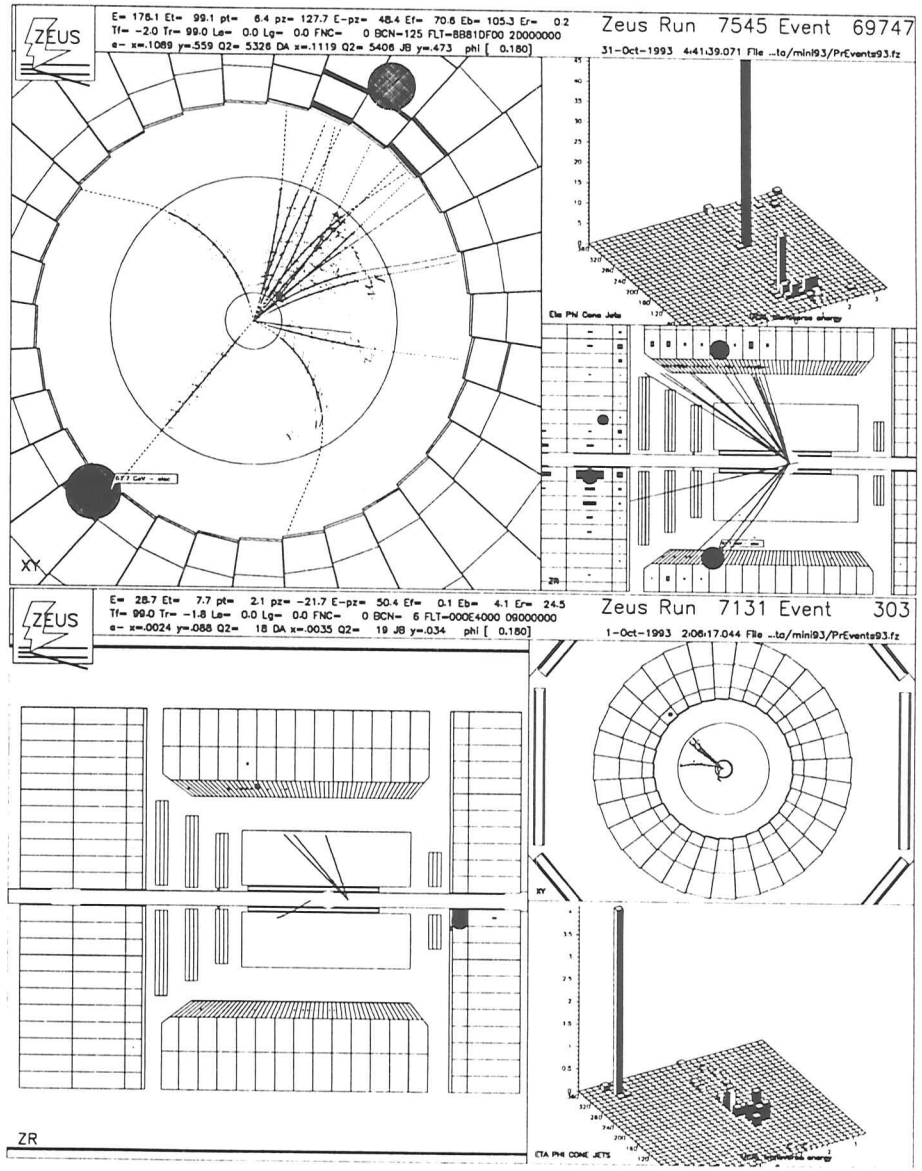

Figure 4.1: Neutral current DIS candidate events. Top: Event as it is expected from the QPM. The scattered electron can be identified from both the calorimeter and the tracking system. Bottom: The electron is scattered under an angle too small to cross the tracking system.

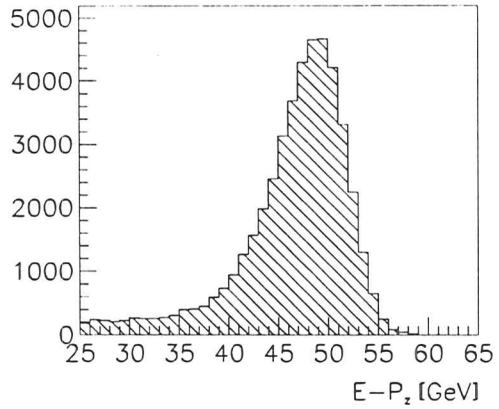

Figure 4.2: $\delta = \sum_i E_i - P_{z,i}$ for MC DIS events. The distribution is expected to peak at twice the electron beam energy (explanation in the text).

yields from

$$\text{energies}: \quad P + A = E_e + \sum_h E_h, \tag{4.3}$$

$$\text{longitudinal momentum}: \quad P - A = P_{z,e} + \sum_h P_{z,h}, \tag{4.4}$$

where the sums run over all final state hadrons h, or

$$\begin{aligned} \delta &= \sum_i E_i - P_{z,i} \\ &= 2A. \end{aligned} \tag{4.5}$$

The sum runs over all final state particles i, including the scattered electron. A and P are the electron and proton beam energies. In case of initial state radiation (ISR) the expression modifies to $\delta = 2(A - E_\gamma)$, where E_γ is the energy of the radiated photon. Hence for genuine DIS events the δ-distribution is a Gaussian centered at $2A$ which has a width of twice the energy resolution at A and a radiative tail towards lower energies.

Fig. 4.2 shows the δ distribution for a sample of MC DIS events which have been subject to the full detector simulation. Fits of a Gaussian to the high-energetic edge of the spectrum and a Gaussian plus an exponential to the lower edge give 49.1 GeV for the central value and 2.6 GeV (7.8 GeV) for the width towards higher (lower) energies. The shift of the peak is due to inactive material in front of the calorimeter.

4.1.2 Events with a Large Rapidity Gap

Among the DIS candidate events, a class of events has been observed in which no hadronic activity is detected in the forward region [ZEU93e]. The polar angle θ of a final state hadron

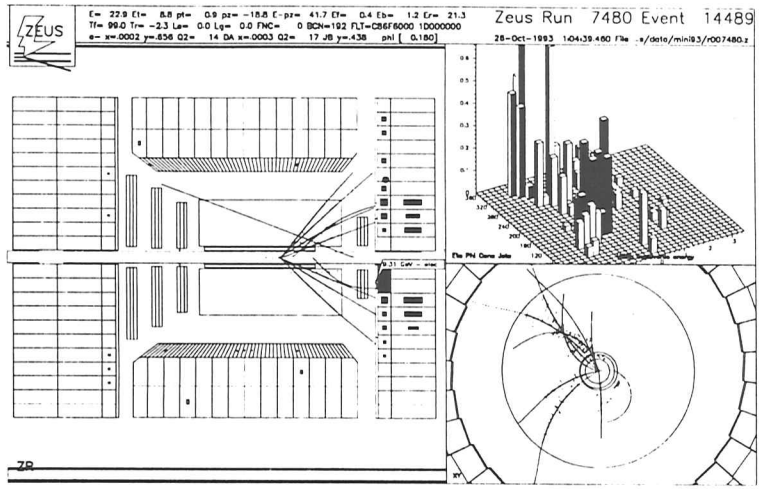

Figure 4.3: Neutral current DIS event with a large rapidity gap (LRG). The event is due to diffractive scattering where the proton escapes undetected down the beam-pipe.

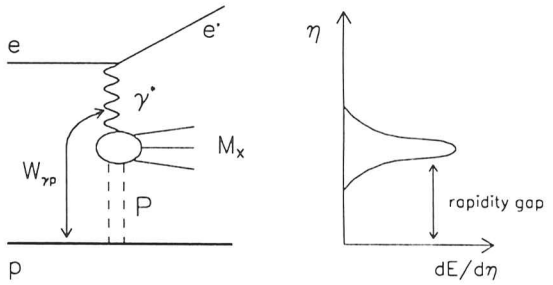

Figure 4.4: Schematic diagram for NC DIS events with a large rapidity gab. Diffractive dissociative scattering is assumed to be due to the exchange of a pomeron carrying the quantum numbers of the vacuum. The right side shows the energy flow in the final state of LRG events

is measured in terms of the pseudo-rapidity η.

$$\eta = -\ln \tan \frac{\theta}{2}. \tag{4.6}$$

Events with no activity in the forward region have an unpopulated area in their rapidity distribution and are hence known as large-rapidity-gap (LRG) events. The events are due to diffractive dissociative scattering, which is assumed to be mediated via pomeron exchange. Fig. 4.3 shows an example for an LRG event. fig. 4.4 sketches the scattering mechanism and

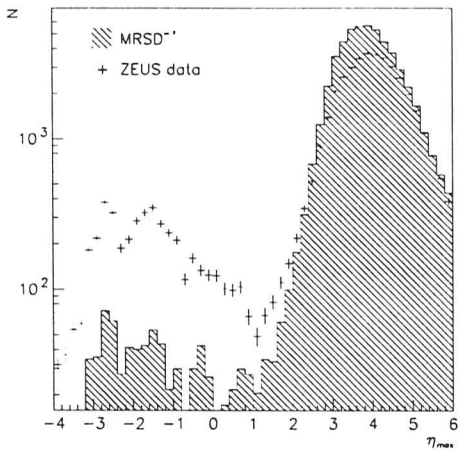

Figure 4.5: The η_{max} distribution shows a clear excess of DIS data events with large rapidity gaps compared to a CDMBGF-MC sample. Data and MC have been normalized to the same luminosity.

illustrates how pomeron exchange is linked to a large rapidity gap in the energy flow of the hadronic final state[1].

An event is considered to be an LRG event if the pseudo-rapidity of the most-forward energy deposit in the calorimeter is $\eta_{\max} < 1.5$. The fraction of DIS events with a LRG exceeds the prediction from MC simulation. This is illustrated in fig. 4.5 which compares the $\eta_{\max}$ distribution from data with a CDMBGF MC simulation. A clear excess of data events with $\eta_{\max} < 1.5$ can be seen. Properties of DIS LRG events are being studied [ZEU94c].

The rapidity gap is a property of the hadronic final state only. hence DIS LRG events can be treated like ordinary DIS events as long as they are reconstructed from the electron only. Formulae including the hadronic final state remain valid only if they are constructed in such a way that they are independent of fragmentation processes. In this respect. DIS LRG events offer a unique possibility to investigate the model dependence of an analysis.

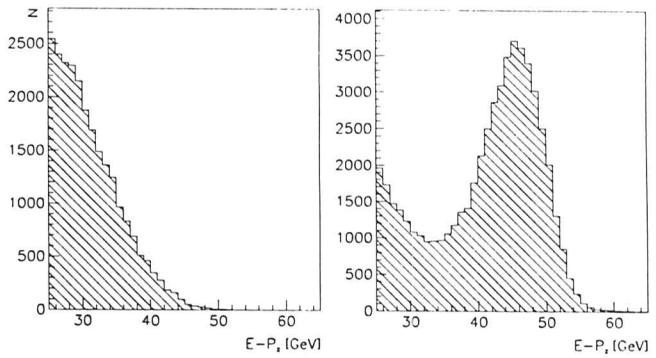

Figure 4.6: $\delta = \sum_i E_i - P_{z,i}$ for photoproduction (MC. left) and DIS (data. right) events. The peak at twice the electron beam energy is due to DIS. the rise towards low energies is due to (misidentified) photoproduction events (explanation in the text).

4.1.3 Background from Photoproduction

Photoproduction events are characterized by values of Q^2 close to zero. For such events. the scattered beam electron escapes undetected down the beam-pipe. However in some of these events. soft pions are misidentified as the scattered beam electron.

Background from photoproduction events can be suppressed via the δ distribution. In photoproduction. the contribution from the undetected beam electron is missing. hence δ assumes values below $2A$. Fig. 4.6 shows the δ-distribution from a photoproduction MC sample (left) and the δ distribution obtained from data (right). Photoproduction events are seen to peak below 30 GeV. In the distribution of data events. the peak at 45 GeV is due to DIS. and the rise towards lower energies is due to photoproduction background. The majority of photoproduction events can be suppressed by requiring that a DIS event has $\delta > 35$ GeV.

It should be noted that a selection cut on δ also removes radiative events from the sample (cf sect. 4.4.3). From eqn. (4.5) follows that requiring $\delta > 35$ GeV implicitly removes events where the initially radiated photon has an energy above $E_\gamma > 9$ GeV.

4.1.4 Beam-Induced Background

Events from beam-gas or beam-wall interactions are accepted due to their high energy deposits in the calorimeter. where isolated deposits in the vicinity of the beam pipe are taken to be the scattered beam electron. Beam-induced background events are characterized by high activity of both the calorimeter and the tracking system. An example for a beam-gas event is shown in fig. 4.7.

[1] The proton escapes undetected down the beam-pipe

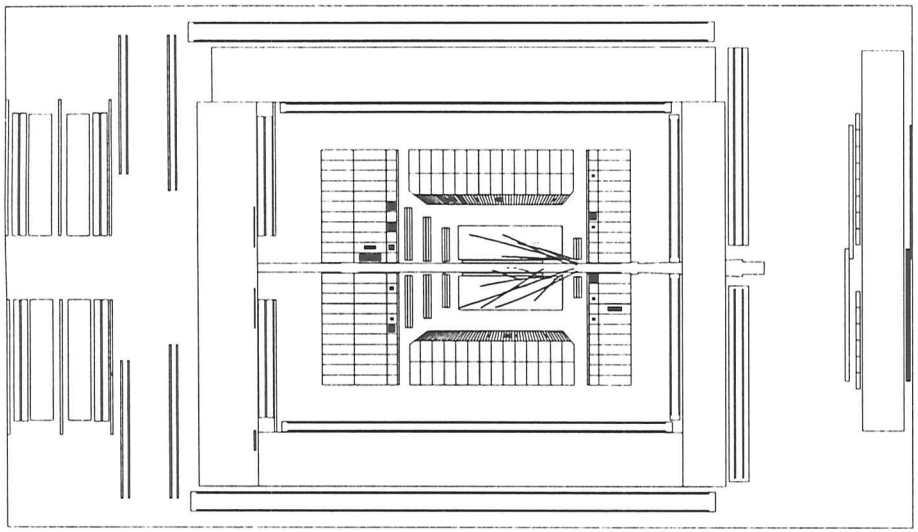

Figure 4.7: Beam-Gas interaction: the incoming proton collided upstream of the nominal interaction vertex with a gas nucleus inside the beam pipe.

Beam-gas events can be identified from the calorimeter timing. While in an ep collision final state particles are emitted from the IP and arrive at the calorimeter at time $t = 0$ ns, beam-gas events which occured upstream of the detector deposit their energy about 10 ns early in the RCAL. In the FCAL these events are again in time, but plotting t_{RCAL} versus $t_{\mathrm{FCAL}} - t_{\mathrm{RCAL}}$ clearly separates beam-gas events from genuine ep collisions.

4.1.5 Other Backgrounds

Cosmic and Halo Muons.

Cosmic muons or muons from the beam halo may cause calorimeter signals which resemble those of an electron, however most of these events are characterized by a relatively quiet (ie few GeV) calorimeter and a correspondingly small value of d. Topological algorithms have been developed to identify muon events (ALHALO [Pri93], MUTRIG [Ban93]). They explore the property of cosmic muons to cause calorimeter signals which align with hits in the muon chambers, or of halo muons to traverse several adjacent cells of the barrel calorimeter.

Fig. 4.8 shows a cosmic muon. High energetic cosmic muons can trigger the detector, if they pass close to the forward region. They can produce complicated events by high-energy knock-on

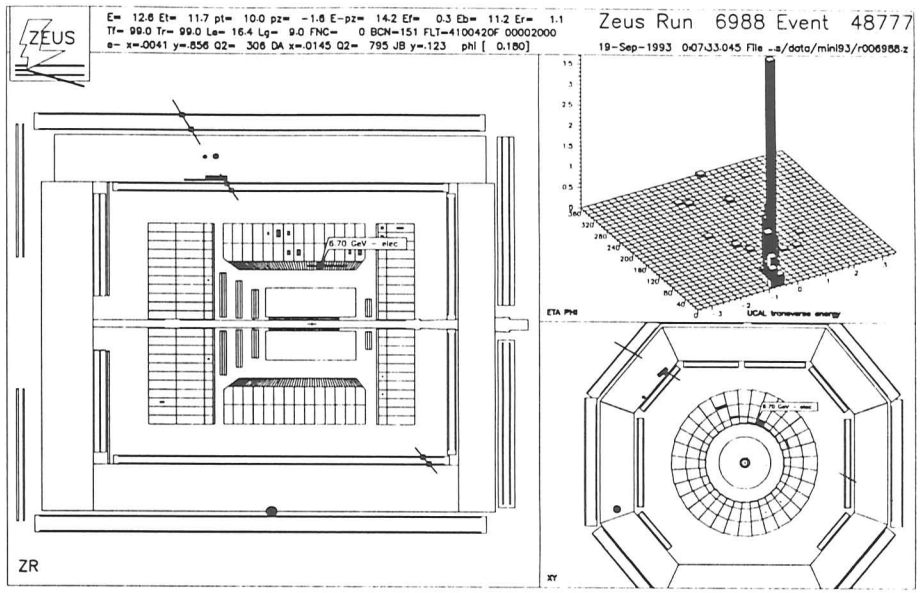

Figure 4.8: Cosmic muon in the RCAL.

electrons, bremsstrahlung, or direct pair production with subsequent showering. Fig. 4.9 shows a muon running parallel to the proton beam, which traverses the calorimeter.

Sparks.

Occasionally events are observed in which a single calorimeter cell detects a large energy deposit. These events are due to a sudden discharge of the static charge between the respective photo-multiplier and its shielding. The events are referred to as sparks.

Sparks occur mostly in the BCAL EMC section, as in the forward and rear calorimeters the PMT shieldings are put on high voltage. Spark events are characterized by a large imbalance in the readout of the respective calorimeter cell as only one of its photo-multipliers produces a signal. They occur at random times wrt the beam crossings and are easily recognized from their event topology.

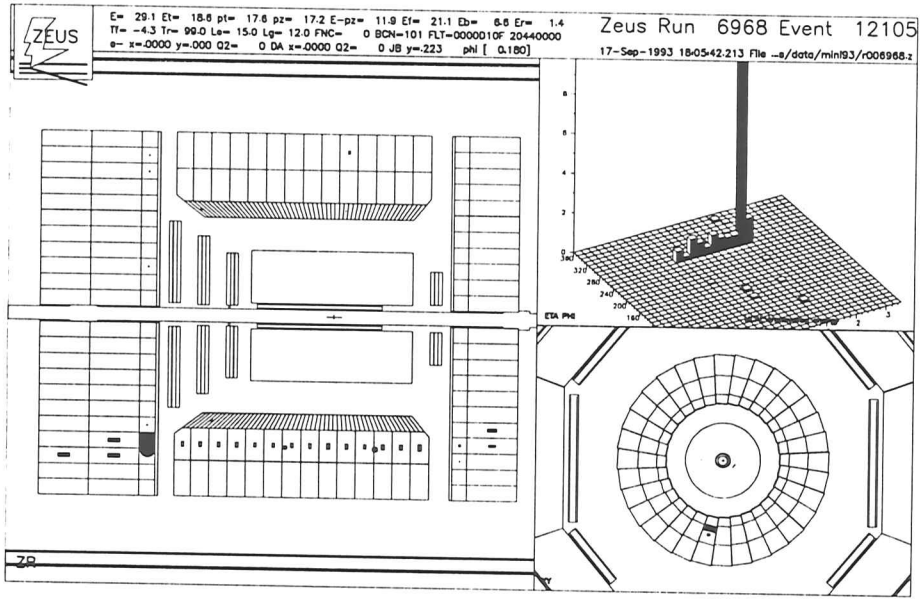

Figure 4.9: Halo-μ traversing the barrel calorimeter.

4.2 Electron Identification

Several algorithms for electron identification have been developed by members of the ZEUS collaboration. For the analysis of the 1993 data, all of them are based exclusively on calorimeter information, however they implement different methods to isolate the signature of an electron. The following gives a brief overview of different approaches to electron identification and compares their performance.

4.2.1 Overview of Algorithms

Algorithms for electron identification are characterized by the variables they use. Simple algorithms rely on variables which are obtained directly from the detector readout, while more sophisticated algorithms compute so-called features, which combine several readout variables to only few quantities from which the electron signature can be isolated. Some of the algorithms introduced below are also described in [ZEU93f].

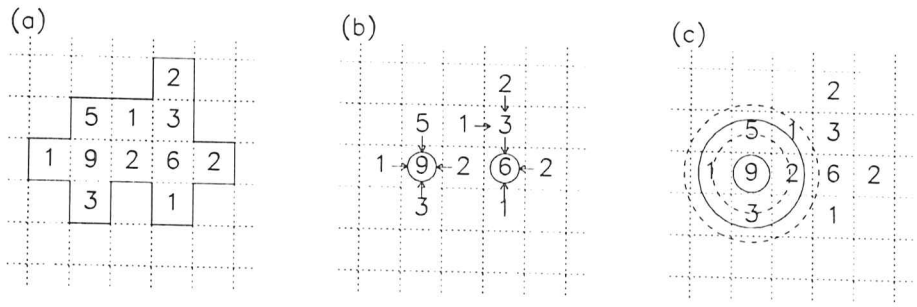

Figure 4.10: Methods used for electron identification: condensates (a), islands (b), and cones (c). The grid shows the tower structure of a part of the calorimeter, the numbers give energy deposits in arbitrary units.

Cell-Based Calorimeter Objects: Condensates and Islands.

Adjacent cells with an energy deposit above a given threshold are combined into so-called condensates, where two cells are called adjacent if they share one of their sides (fig. 4.10a). Purely electromagnetic condensates have to exceed 100 MeV, while purely hadronic condensates or condensates of mixed energies have to have at least 200 MeV.

The first algorithms which became available for electron identification (LXELID [Whi92], HEBBES [dJ92], BEAMELEC [Doc92]) were simply looking for calorimeter condensates which could be ascribed to an electron, where the decision whether a condensate is due to an electron is computed from the number and types of cells contributing to the condensate, and from the fraction of electromagnetic to total energy for the condensate or part of it.

If more than one condensate in an event is found to originate from an electron, some physics argument is used to pick the scattered beam electron (eg the highest energetic condensate, highest P_t condensate).

A similar algorithm has been developed for the HES [Fle94]. It first creates condensate-like objects from HES diodes having signals above a given threshold. Then, it computes the energy deposits (in mips) and positions for each of these objects and correlates them with energies and positions obtained from calorimeter signals to decide whether a given HES object is due to an electron.

The ISLAND [Wai93] algorithm assigns a pointer to each cell which specifies its highest-energetic neighbour having a higher energy deposit than the cell; if no such neighbour is found, the pointer aims at the cell itself (fig. 4.10b). All the cells which lie on paths leading to the same self-pointing cell can then be merged into an island. Islands can be used for electron identification similar to condensates. They have the advantage of being able to separate overlapping objects.

Islands and Cones.

More sophisticated algorithms than those described before create variables which are independent of the calorimeter geometry to identify the scattered electron.

The cone algorithm (fig. 4.10c) maps the calorimeter cells on a sphere. It starts by identifying seed cells, which are EMC cells with energy deposits above 1 GeV. If two such cells are separated by less than 12^0, only the higher-energetic of the two cells is considered further. The electromagnetic and hadronic energies and their ratios are calculated for (inner and outer) cones surrounding the seed, and a probability for the seed being due to an electron hit is calculated from these variables and some properties of the seed cell.

The first cone-based algorithm was ELEC5 [Rep92], using cones of 5^0 and 17.2^0 for EMC cells, and 11.5^0 and 22.9^0 for HAC cells. If more than one electron candidate was found, the algorithm selected the highest-P_t candidate as the scattered beam electron. The algorithm was slightly modified and tuned to improve angular resolution and the quality of the selected sample (EEXOTIC [CR92]).

The performance of the cone-based finders made those based on the calorimeter geometry obsolete, except for the HES finder which is a valuable tool for systematic studies as it is considered to be independent of the calorimeter-based finders.

Neural-Network Approach.

The cone-based algorithms follow the classical approach of pattern recognition, which transforms the measurement space containing all available raw data into a relatively low-dimensional feature space on which the actual recognition is performed (eg [BFH92]). The feature extraction, however, is theoretically not yet well-developed, and it embodies the danger of dropping relevant input data when computing the features.

A possibility to avoid such dangers is offered by feed-forward neural networks (NN). NNs can be trained on the entire measurement space and subsequently be either used for the pattern recognition process, or be evaluated to extract the relevant features. An electron identification algorithm (SINISTRA, [ACS95]) has been developed following the first approach, using a software implementation of a NN.

4.2.2 Comparison of Performance

The performance of an electron finder is measured by its efficiency in identifying a scattered beam electron, ε, and by the purity of an identified event sample, p. Both ε and p are determined from MC events. The efficiency is simply the fraction of DIS MC events in which an electron

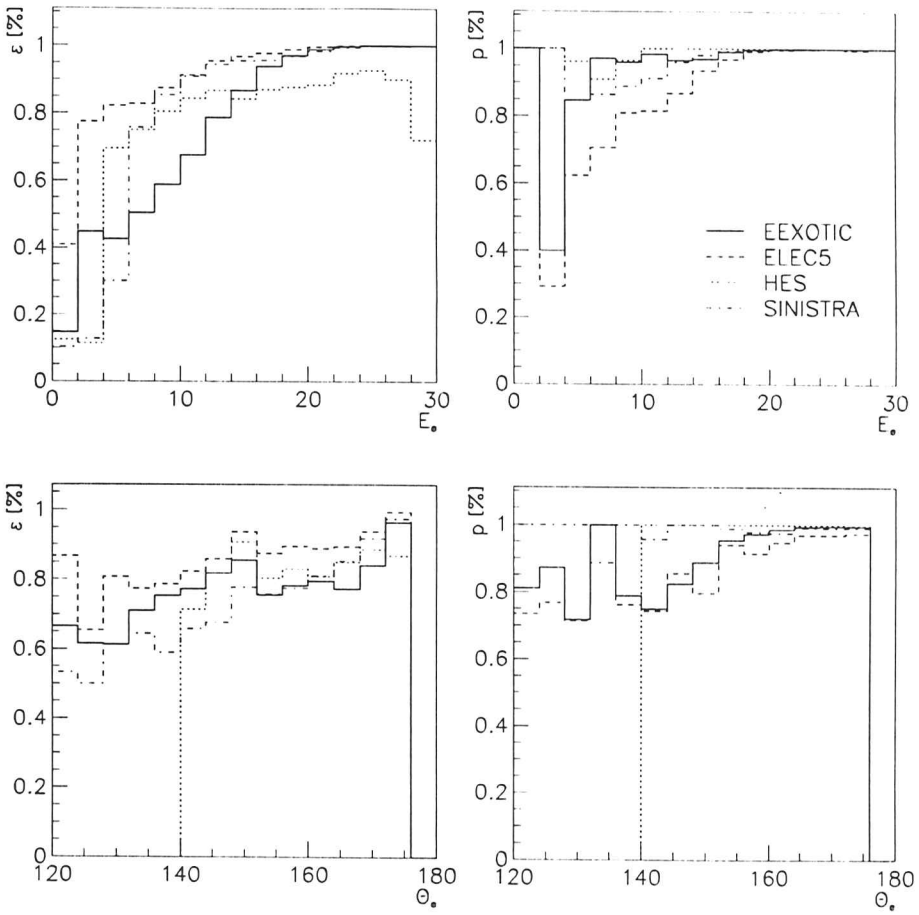

Figure 4.11: Efficiency (ε) and purity (p) of different electron identification algorithms. The values on the abscissas were taken at MC generator level. The HES curves drop at $\theta = 140^0$ as 1993 the HES was installed only in a part of the RCAL.

has been identified[2].

$$\varepsilon = \frac{\text{no. identified } e^-}{\text{no. generated DIS events}}. \tag{4.7}$$

For the purity, the algorithm is run on a photoproduction MC of the same luminosity to calculate the fraction of genuine DIS events among the events which were selected from both

[2]For the HES finder, the generated electron was required to pass through the active area of the HES

samples.

$$p = \frac{\text{no. identified } e^-}{\text{no. identified DIS events + no. mis-identified } \gamma^* p \text{ events}}. \quad (4.8)$$

Fig. 4.11 plots the efficiencies and purities against energy and angle of the scattered electron for the four different electron finders which were introduced in the previous sections. Only events with 35 GeV< δ <60 GeV were selected, as this cut is imposed on the data prior to electron identification. It should be noted that ε and p can be further improved by additional selection cuts.

Efficiency and purity are close to 100% for electrons above 20 GeV. At lower energies, ε and p decrease due to selection cuts internal to the finders which are needed to discriminate against soft pions. The NN-based finder, SINISTRA, lies with both ε and p between the cone-based finders EEXOTIC and ELEC5. In θ, ε and p approach 100% in the vicinity of the beam-pipe with a slight decrease towards larger scattering angles[3]. The decrease can be explained with the non-projective RCAL geometry. The HES finder operates only in that part of the RCAL where the HES was installed.

4.3 Event Selection

Events which are observed with the ZEUS detector are filtered by a three-level online trigger system before being written to disk (cf sect. 3.2.2). After complete reconstruction, the data are subject to an additional DST[4] filter, which identifies global event properties and stores them in a keyword to ease data access. Events passing the TLT are written to cartridges, while events which pass the DST selection are held on fast disks. Trigger rates are designed to meet with bandwidth and disk space limits.

For the 1993 data taking period, the TLT output data rate for NC DIS candidate events was designed to be 1 Hz for a specific luminosity of $10^{30}\,\mathrm{cm^2 s^{-1}}$. The disk space allocated to NC events amounted to 600 events per nb^{-1}. The ZEUS experiment collected a total of 6.1 million events, corresponding to a luminosity of 554 nb^{-1}. About 1.1 million of the events were recorded for structure function analysis, about 330k events were kept after the DST filtering.

4.3.1 Online Filters

First Level (FLT).

The first level trigger consists of trigger processors which are local to the individual detector components (subtriggers), and of a global processor (GFLT) which evaluates the different subtriggers. A total of 64 subtriggers contribute to the GFLT decision. For NC DIS, however, only those from the calorimeter (CAL-FLT) are relevant.

[3] Electrons emerging down the rear beamline have a scattering angle of $\theta = 180°$.
[4] DST: Data Summary Tape

Quantity		E_{tot}	E_t	P_t^{miss}	E_{EMC}	E_{BEMC}	E_{REMC}	E_{REMCth}
Threshold	[GeV]	15	11.5	10	10	3	2	3.7

Table 4.1: CAL-FLT thresholds for 1993 data taking period. Not all the triggers were active for the entire data taking period. The P_t^{miss} trigger contains an upper limit and was changed during data taking [Tok93].

At CAL-FLT level, the calorimeter is organized into so-called trigger towers. A trigger tower provides the sum of the PMT signals of an entire EMC or HAC section of a given calorimeter tower. The signals are used to compute the total energy in the calorimeter, E_{tot}, the transverse energy, E_t, the missing transverse momentum, P_t^{miss}, and the total energies of the BCAL EMC, E_{BEMC}, the RCAL EMC, E_{REMC}, and the RCAL EMC except for the towers next to the beam-pipe, E_{REMCth}.

After suppressing noise by excluding trigger towers with less than 464 MeV, events were accepted if one of the above quantities exceeded a pre-defined threshold (cf table 4.1). While an excess over the EMC thresholds suggest the presence of an electron, the E_t threshold selects events with a high Q^2. The P_t^{miss} is actually an upper limit; exceeding it indicates a CC-event. A concise definition of all subtriggers, their thresholds, and their activation periods can be found in [Tok93].

Second Level (SLT).

During 1993, the SLT was used to suppress obvious background events. It ran a spark identification algorithm, and it used calorimeter timing information to suppress background from beam-gas events by accepting only events with $|t_{FCAL}| < 8$ ns and $|t_{RCAL}| < 8$ ns, or events for which no timing information was available.

Third Level (TLT).

The TLT is a global trigger processor which applies the same selection algorithms to all events. Events were accepted for structure function studies if the FLT found an electron-type energy deposit in the RCAL or the BCAL, or if the transverse energy of the event, E_T, exceeded 40 GeV, however they were rejected as background if they had an extreme value of $\delta = E - P_z$. At the TLT, both δ and E_T were calculated from calorimeter deposits, assuming the event vertex to be at $z = 0$ cm. In particular, the TLT accepted events according to one or both of the following two selection mechanisms [GNS94]:

1
- the BEMC, REMC or REMC threshold bits were set by the FLT (see above);
- $\delta + 2E_\gamma^{Lumi} > 20$ GeV, where E_γ^{Lumi} is the energy measured in the photon calorimeter of the luminosity monitor, which ensures radiative events being included in the selection; and

- $\delta < 100$ GeV, where $E_\gamma^{\rm Lumi}$ has been excluded to not reject NC DIS events with bremsstrahlung overlays.

2. - $E_T > 40$ GeV, and
   - δ has the same properties as in 1.

Events which were selected by the first criteria have the scattered beam electron in the RCAL or the BCAL and are referred to as normal events, while the second criteria identify very-high-Q^2 events.

4.3.2 DST algorithms

The DST filters are part of the ZEUS off-line reconstruction programme ZEPHYR. They are applied when the reconstructed vertex and calibrated calorimeter energies are available. The result of the DST algorithms is encoded into the bits of a dedicated keyword[5] which is later used for easy access to events. For brevity, the different selection algorithms are referred to as DST bits.

Events suitable for structure function studies can be identified by bits 9 to 15 [GNS94]. DST bits #9 and #10 are global bits which are used to tag an electron or a reconstructed vertex in the event.

#9 Scattered beam electron identified
Any of the four electron finding algorithms ELEC5, EEXOTIC, LOCAL and SINISTRA has identified at least one electron with $E_e > 4$ GeV.

#10 Reconstructed vertex available
An event vertex has been reconstructed from the VXD.

DST bits #11-15 are reserved for NC DIS candidates and require an event to have been accepted as normal or very-high-Q^2 event by the TLT. Bit #11 is set after some stricter background rejection.

#11 NC DIS candidate

- the TLT has accepted the event as NC DIS candidate, and
- the timing obtained from the calorimeter is within the bounds

$$\begin{aligned} |t_R| &< 6\text{ns}, \\ |t_F| &< 8\text{ns}, \\ |t_F - t_R| &< 8\text{ns}, \\ |t_G| &< 8\text{ns}, \end{aligned}$$

and

[5] The result of the DST selection is stored in the word `ZDSKEY_tstam11`, ref [ZEU93b].

Quantity	Definition
A	energy of electron beam
P	energy of proton beam
E'_e	energy of scattered beam electron
θ	angle of scattered beam electron
F	energy of hadronic final state
γ	energy-weighted hadronic angle (angle of struck quark in QPM)

Table 4.2: Definitions used for reconstruction of kinematics.

- the topological algorithms MUTRIG [Ban93] and ALHALO [Pri93] have not found any cosmic muons or muons from the beam halo, and
- the algorithm RMSPARK [Sch92b] did not identify the energy deposit in the calorimeter to be due to a bad channel in the calorimeter or a sparking photo-multiplier, and
- $\delta + 2E_\gamma^{\rm Lumi} > 25$ GeV, where the event vertex is forced to $z = 0$ cm.

The timing cut is used to reject beam-gas background events, while the δ-cut reduces contributions from photoproduction (ref sect. 4.1). Bits #12 to #14 require bit #11 to be set and implement increasingly stricter cuts against background, selecting 1.1, 0.8, 0.4 and 0.2 events/μb^{-1}, respectively. Bit #15 flags LRG events by requiring the FCAL energy to be less than 10 GeV.

Events which have both DST bit #9 and bit #11 set were kept on a fast disk. The event sample amounts to approximately 320 000 events and is referred to as the miniDST. The events in the miniDST were scanned and stored in a column-wise ntuple data structure [App92]. Further background rejection was imposed on the data using the algorithms ISITAMU [Abr92] and COMCOS [Tsu92] to reject cosmic and halo muons and QED Compton events. The routine EVTAKE [Sch92a] vetoed events which were recorded when the detector was not fully operational. 308 796 events were stored in the ntuple.

4.4 Kinematic Reconstruction

4.4.1 Observables in DIS

DIS can be described by four primary measured variables, the energies and angles of the scattered lepton and the hadronic final state (E'_e, θ, F and γ_h, cf table 4.2). Measurement of the electron variables is straight forward as they are obtained from a single particle, whereas the hadronic variables have to be taken from the complex hadronic final state.

In principle, F and γ_h can be obtained from a jet-finding algorithm. The energy flow of the hadronic final state however depends on the fragmentation process. For an inclusive measurement it is unacceptable for the kinematic variables to depend on the hadronization, hence

it is necessary to construct model-independent hadronic variables for the use for kinematic reconstruction.

F and γ_h can be shown to be fragmentation-model independent and insensitive to the loss of particles down the beam-pipe [Ben94] if they are calculated from $P_{t,h}$ and $\delta_h = E_h - P_{z,h}$.

$$F = \frac{P_{t,h}^2 + (E_h - P_{z,h})^2}{2(E_h - P_{z,h})}. \tag{4.9}$$

$$\cos\gamma_h = \frac{P_{t,h}^2 - (E_h - P_{z,h})^2}{P_{t,h}^2 + (E_h - P_{z,h})^2}. \tag{4.10}$$

The subscript h implies summation over all final state hadrons.

The observed variables are constrained by energy and longitudinal and transverse momentum conservation.

$$xP + A = E + F. \tag{4.11}$$

$$xP - A = E\cos\theta + F\cos\gamma_h. \tag{4.12}$$

$$E\sin\theta = -F\sin\gamma_h. \tag{4.13}$$

Using the conservation laws and the definitions of x, y and Q^2 in terms of the lepton and nucleon four vectors, it is possible to write the kinematic variables in terms of any two observables. Generating the explicit expressions for x, y and Q^2 is an algebraic problem which has been solved using the program MATHEMATICA [Ben91].

4.4.2 Reconstruction Methods

Reconstruction methods calculate the event kinematics from primary measured quantities. Fig. 4.12 shows the isolines of the four primary measured quantities of DIS. In regions where the isolines are narrowly separated the respective quantity is especially well suited for kinematic reconstruction since small variations in the kinematic variables correspond to large changes of the measured quantity.

Several approaches exist to kinematic reconstruction. Energy and momentum conservation yield six generic reconstruction methods which combine any two of the primary measured variables. They include the two classical methods which rely on the electron or hadronic variables only. Regarding the over-constraintness of the measurement, a third quantity can be introduced into the reconstruction to calculate the energy of the initial beam electron and thus become insensitive to initial state radiation. Additionally, fig. 4.12 suggests that combinations of kinematic variables which were reconstructed from different methods can improve the kinematic resolution.

The following sections introduce different reconstruction methods. Equations are given for two kinematic variables, the third is to be determined through the relation $Q^2 = 4APxy$. Fig. 4.13 illustrates resolution and bias of the reconstruction methods.

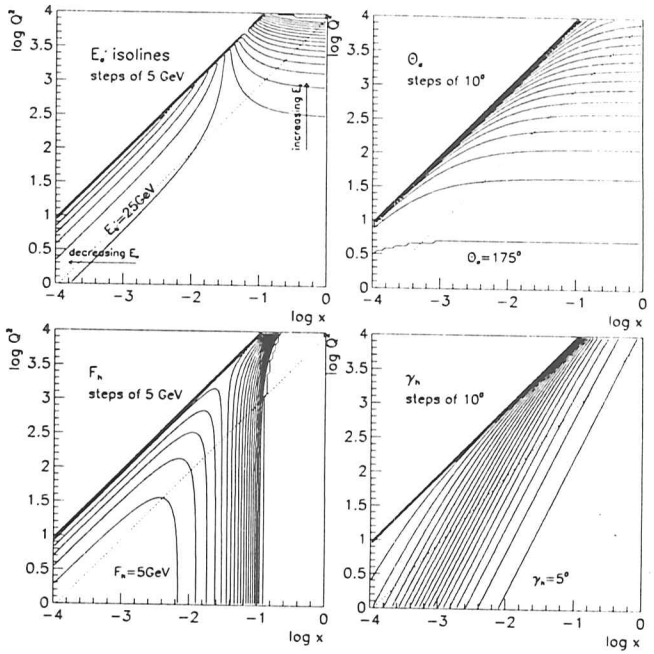

Figure 4.12: Isolines for the four primary measured variables E'_e, θ, F and γ_h. In regions where the isolines are widely separated the respective variable is well suited for kinematic reconstruction.

Electron-Only Method.

Reconstruction of kinematics from the electron only has already been mentioned in table 2.1. At HERA.

$$y_{el} = 1 - \frac{E'_e}{2A}(1 - \cos\theta). \tag{4.14}$$

$$Q^2_{el} = 2AE'_e(1 + \cos\theta). \tag{4.15}$$

The resolutions of y_{el} and Q^2_{el} can be written explicitly.

$$\frac{\delta Q^2}{Q^2} = \frac{\delta E}{E} \oplus \tan\frac{\theta}{2}\delta\theta \tag{4.16}$$

$$\frac{\delta y}{y} = \left(1 - \frac{1}{y}\right)\left(\frac{\delta E}{E} \oplus \cot\frac{\theta}{2}\delta\theta\right). \tag{4.17}$$

The resolution in Q^2 is of the order of energy and angular resolution of the apparatus, while

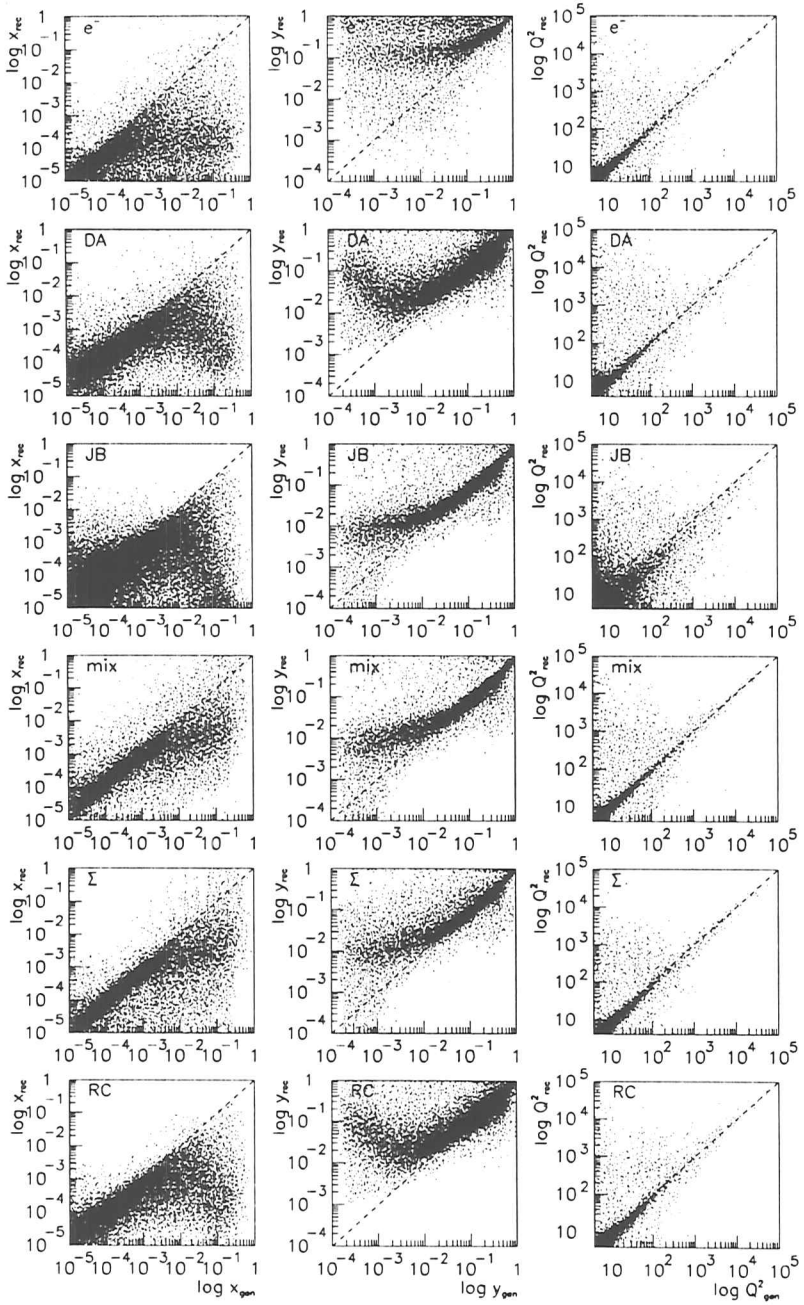

the resolution in y is only for high values of y of similar quality and deteriorates towards lower y due to the factor of y^{-1}.

Hadron-Only Method (Jacquet-Blondel Method [JB79]).

Jacquet and Blondel have developed a reconstruction method which exploits only the hadronic final state. It relies on the assumptions that the transverse momentum of forward hadrons and the energy and the momentum of backward hadrons are negligible. The kinematic variables are calculated by summing energy and momenta of all final state particles h.

$$\begin{aligned} y_{\mathrm{JB}} &= \frac{\sum_h (E - P_z)_h}{2A} \\ &= \frac{F}{2A}(1 - \cos\gamma_h)\,. \end{aligned} \tag{4.18}$$

$$\begin{aligned} Q^2_{\mathrm{JB}} &= \frac{(\sum_h P_{T,h})^2}{1 - y_{\mathrm{JB}}} \\ &= \frac{F^2}{1 - y_{\mathrm{JB}}} \sin^2\gamma_h\,. \end{aligned} \tag{4.19}$$

where $(\sum_h P_{T,h})^2 = (\sum_h P_{x,h})^2 + (\sum_h P_{y,h})^2$. The expressions in terms of F and γ_h show that the Jacquet-Blondel reconstruction method is independent of the fragmentation processes in the hadronic final state. The Jacquet-Blondel method is the only reconstruction method which is also applicable for CC DIS events.

The resolution in y shows that y_{JB} is a particularly good estimator for y since the resolution is of the order of energy and angular resolution of the apparatus independent of y.

$$\frac{\delta y}{y} = \frac{\delta F}{F} \oplus \cot\frac{\gamma_h}{2}\,\delta\gamma_h\,. \tag{4.20}$$

The hadronic angle, γ_h, can be expressed in terms of y_{JB}, which links the resolution of γ_h to the resolution of y_{JB}.

$$\cos\gamma_h = \frac{(\sum_h P_{T,h})^2 - 4A^2 y^2_{\mathrm{JB}}}{(\sum_h P_{T,h})^2 + 4A^2 y^2_{\mathrm{JB}}}\,. \tag{4.21}$$

Double-Angle Method.

The DA method relies on θ and γ_h to reconstruct event kinematics. Both angles are obtained from the impact positions of the electron and the final state hadrons on the face of the calorimeter. Impact positions of particles are measured by determining the center of energy deposit from the calorimeter cells which were hit by the particle, so they are insensitive to inactive material in front of the calorimeter.

$$x_{\mathrm{DA}} = \frac{A\sin\gamma_h + \sin\theta + \sin(\theta+\gamma)}{P\sin\gamma_h + \sin\theta - \sin(\theta+\gamma)}\,. \tag{4.22}$$

$$Q^2_{\mathrm{DA}} = 4A^2 \frac{\sin\gamma_h(1+\cos\theta)}{\sin\gamma_h + \sin\theta - \sin(\theta+\gamma)}\,. \tag{4.23}$$

The energy of the scattered beam electron can be calculated from the angles.

$$E_{\mathrm{DA}} = \frac{Q^2_{\mathrm{DA}}}{2A(1+\cos\theta)} = 2A\frac{\sin\gamma_h}{\sin\gamma_h + \sin\theta - \sin(\theta+\gamma)}. \quad (4.24)$$

It should be noted that $E_{\mathrm{DA}} \geq E'_e$ since the angles are insensitive to inactive material in front of the calorimeter, and E_{DA} therefore reconstructs the entire energy of the scattered electron while the measured E_e is smaller due to energy losses of the electron before entering the calorimeter.

Mixed Method.

The previous paragraphs have shown Q^2_{el} and y_{JB} reconstruction to be limited only by the resolution of the detector, hence it is tempting to obtain the kinematics from

$$y_{\mathrm{mix}} = y_{\mathrm{JB}}, \quad (4.25)$$
$$Q^2_{\mathrm{mix}} = Q^2_{\mathrm{el}}. \quad (4.26)$$

Σ Method [BB94].

The Σ method[6] is to first order independent of initial state radiation (ISR). It is constructed by exploiting energy and momentum conservation, eqn. (4.5), to eliminate $2A$ from the denominator of (4.18). Q^2 is then calculated from the expressions for y and Q^2 at the electron vertex.

$$y_\Sigma = \frac{y_{\mathrm{JB}}}{1 - y_{\mathrm{el}} + y_{\mathrm{JB}}}. \quad (4.27)$$
$$Q^2_\Sigma = \frac{E'^2_e \sin^2\theta}{1 - y_\Sigma}. \quad (4.28)$$

Initial State Radiation Corrected Method.

Since the measurement is over-constrained, two kinematic variables and the energy of the incident beam electron can be calculated from any three measured variables. The measurement of the hadronic energy has the broadest resolution, hence E'_e, θ and γ_h are chosen, yielding

$$y_{\mathrm{RC}} = y_{\mathrm{DA}}, \quad (4.29)$$
$$Q^2_{\mathrm{RC}} = E'^2_e \frac{(\sin\theta + \sin\gamma_h - \sin(\theta+\gamma))(1+\cos\theta)}{\sin\gamma_h}. \quad (4.30)$$

The method is insensitive to initial state radiation (see below).

[6] The quantity δ was labeled Σ by the authors of the Σ method

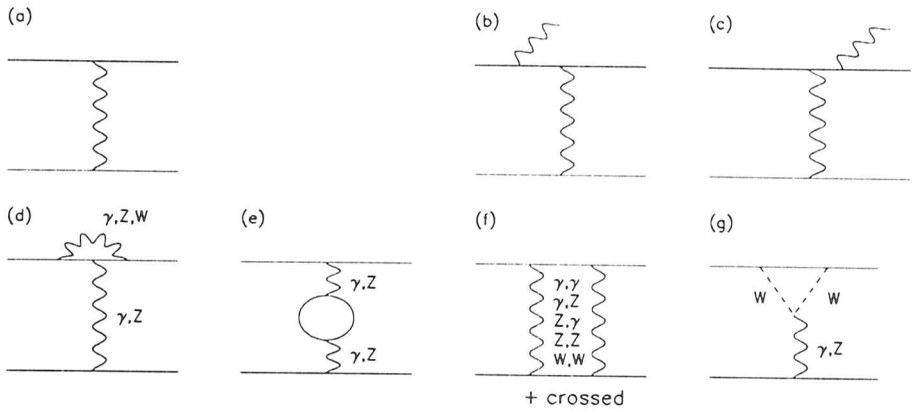

Figure 4.14: Radiative corrections to the Born diagram (a): photon bremsstrahlung, ie initial state radiation (ISR, b) and final state radiation (FSR, c), vertex correction (d), self energy terms (e), two-boson exchange (f), and gauge self-coupling (g). Corrections originating from the lepton line can occur at the parton line as well, which is not separately shown (b,c,d,g).

4.4.3 Radiative Corrections.

Radiative Contributions to the Cross Section.

Fig. 4.14 gives an overview of radiative corrections in lowest order. Their contributions to the cross section are classified according to their type as weak or purely photonic. Photonic contributions are labeled wrt their origin as leptonic, partonic, or lepton-parton interference terms.

The weak contribution is small and can be neglected for this analysis. Its dominant term is the fermion-loop contribution to vacuum polarization which reaches 6% at $Q^2 \cong M^2_Z$; the other contributions stay below the 1% level [Hol87].

Photonic contributions are discussed extensively in [MT69]. For leptonic radiation, they can reach 200% and more in the high-y region if the kinematics are reconstructed from the final-state electron [S+91]. An incident beam electron can lose energy due to photon radiation prior to the interaction, thus decreasing its initial energy, $A \to A' = A - E_\gamma$. Since the photon is emitted almost collinear with the electron, it escapes undetected through the beam-pipe opening, and the initial beam energy, A, is used to reconstruct the event kinematics. The obtained Q^2 is larger than the Q^2_h at the hadronic vertex, and since the differential cross section is proportional to Q^{-4}_h, radiation off the initial beam electron enhances the observed cross section at high values of Q^2.

Partonic contributions are suppressed wrt the electron due to the higher masses of the quarks[7] [Blü90] and lepton-quark interference terms stay below the 5% limit [Hol87]. Therefore, the discussion is limited to leptonic photon radiation.

Radiative Correction Factor $\delta_{\rm RC}$.

The effect on the observed cross section is quantified in terms of a radiative correction, $\delta_{\rm RC}$, which is defined by

$$\frac{d^2\sigma}{dxdy} = \frac{d^2\sigma_{\rm Born}}{dxdy}(1+\delta_{\rm RC}(x,y)). \tag{4.31}$$

where the Born term labels the cross section in the one photon exchange picture. Since the effects of radiation are different for the different measured quantities, $\delta_{\rm RC}$ is a function of which variables are chosen for the kinematic reconstruction of the event.

Leptonic Radiation.

Photon radiation is described by two splitting functions P_{ff} and $P_{\gamma f}$, which give the probabilities for photon bremsstrahlung from a fermion ($f = e, \ldots, u, d, \ldots$), and for the fragmentation of an initial fermion f into a photon [Blü90]. They contribute to $\delta_{\rm RC}$ by bremsstrahlung from the electron line, and by collinear fragmentation of an initial quark into a quasi-real intermediate photon, which then Compton-scatters off the electron. The contribution from bremsstrahlung is $\propto e_f^2 \ln(Q^2/m_f^2)$, where e_f and m_f are the fermion charge and mass. The contribution from Compton scattering gets significant in the phase space region of low x and high y.

Unless the radiated photon is experimentally separated from the final state, the differential cross section has to be integrated over the phase space which is available to the photon. In the LLA, the above contributions to $\delta_{\rm RC}$ can be identified with different regions of phase space. Bremsstrahlung comes from regions where photon emission is nearly collinear with the initial of final state lepton. The corresponding diagrams are called initial state radiation (ISR, fig. 4.14b) and final state radiation (FSR, fig. 4.14c). The contribution from Compton scattering gets large in the region $Q_h^2 \to 0$ [S+91].

Compton scattering is a dominant source of uncertainty in calculations of radiative corrections since it requires knowledge of the structure functions at $Q^2 \to 0$, a region which is not covered by most of the available PDFs. However, it has a clean experimental signature, hence its magnitude might be directly accessible to measurement at HERA.

[7] Since quark masses are not experimentally accessible parameters, no attempt is made to isolate the partonic contribution to $\delta_{\rm RC}$. Commonly, they are absorbed in the quark densities, $q(x,Q^2)$, leading to a modification in the splitting functions (2.80) (2.82) [Hol87]. The contribution due to radiation from the outgoing parton vanishes [Blü90].

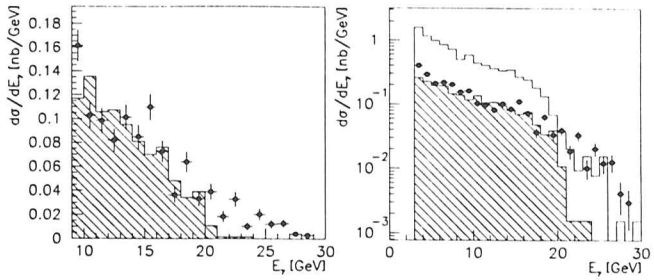

Figure 4.15: Left: Differential cross section for ISR which is observed (solid circles) in the luminosity monitor compared to an absolute prediction from the HERACLES MC (shaded histogram). Right: Comparison with the cross section at generator level (open histogram) illustrates the acceptance of the luminosity monitor.

Magnitude of Radiative Corrections.

Several analytical programs exist for calculating the magnitude of radiative corrections for the different reconstruction methods. They are reviewed and their results are summarized in [S+91]. It follows that radiative corrections can become huge for the lepton variables, but remain at the level of 10% for hadron variables. For the electron-only method, $\delta_{\rm RC}$ exceeds 50% at low x and high y and reaches even more than 200% for $x < 10^{-4}, y > 0.9$. The correction can, however, be drastically reduced to below $\mathcal{O}(40\%)$ by imposing a selection cut on $\delta = E - P_z$.

Simulating Radiative Corrections.

In most cases the final state photon of a radiative event is not experimentally observed. In case of ISR, it escapes undetected down the beampipe opening, while for FSR so far no special attempt is made to identify the photon, hence it is either absorbed in the electron signal or ascribed to the hadronic final state. The extraction of F_2 therefore depends on radiation being accurately simulated in the MC.

A possibility to check the simulation of radiative events is offered by the luminosity monitor, which has a limited acceptance for bremsstrahlung photons. Fig. 4.15 (left) compares the observed photon spectrum with an absolute prediction from the HERACLES MC and the full detector simulation. The spectra are in good agreement, justifying the confidence in the MC simulation. Fig. 4.15 (right) compares the measured spectrum with the spectrum of the generated ISR photons to illustrate the acceptance region of the luminosity counters.

Two quantities are used to estimate and control radiative effects in the data sample. The initial electron energy, A, is reconstructed from measured quantities, $A \to A(E'_e, \theta, \gamma_h)$, to reduce the mismatch of the reconstructed kinematics, and momentum conservation, δ, is used to suppress events with very energetic initial state radiation. Both quantities allow to reconstruct the

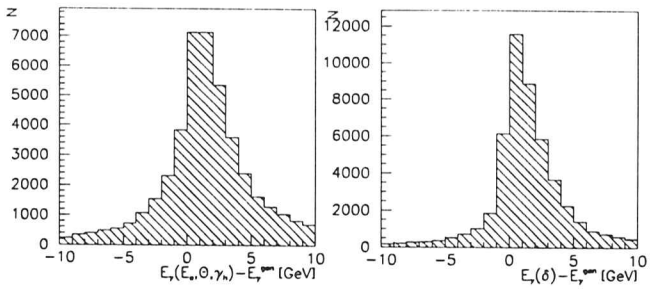

Figure 4.16: Generated energy of ISR photon, E_γ, compared to E_γ reconstructed from measured quantities (left) and E_γ reconstructed from δ (right).

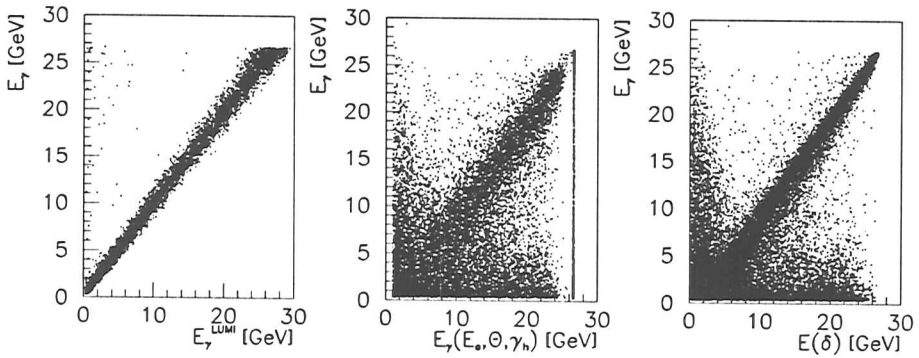

Figure 4.17: Generated energy of ISR photon, E_γ, plotted versus the observed energy in the luminosity monitor (left, only events with $E_\gamma^{\mathrm{LUMI}} > 0.35\,\mathrm{GeV}$ are considered) and versus E_γ reconstructed from measured quantities (middle) and from δ (right).

energy E_γ of the ISR photon.

$$E_\gamma(E'_e, \theta, \gamma_h) = A - A(E'_e, \theta, \gamma_h). \tag{4.32}$$

$$\text{and } E_\gamma(\delta) = A - \frac{1}{2}\delta. \tag{4.33}$$

Figs. 4.16 and 4.17 illustrate by the MC simulation how accurately the initial state photon can be reconstructed from those quantities. The reconstructed γ energy is seen to be slightly larger than the generated energy. This is due to final state particles depositing some of their energy in inactive material before entering the calorimeter, leading to both E'_e and δ being measured slightly too low. The correlation between $E_\gamma(\delta)$ and E_γ, however, is accurate for $E_\gamma(\delta) > 9\,\mathrm{GeV}$, which is used as a criterion to suppress background events from the DIS sample.

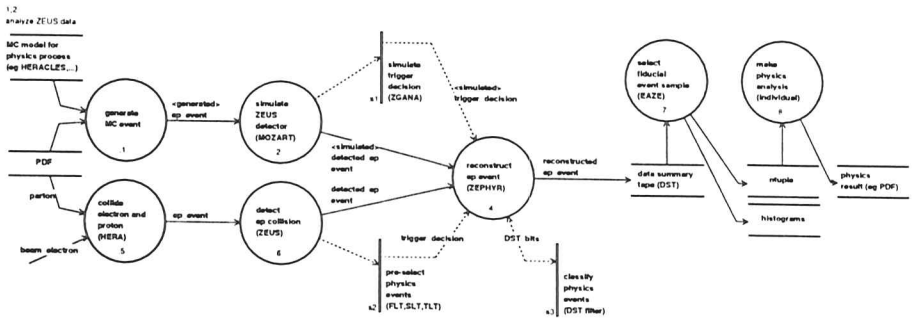

Figure 4.18: Monte Carlo simulation of the ZEUS experiment. Events are generated according to a MC model and subjected to the full detector simulation. MC and data events are then passed through the same event reconstruction software.

4.4.4 Monte Carlo Validation

Resolutions, biases and kinematic acceptances for the reconstruction methods can be obtained from MC simulation only, hence the MC needs to be validated before the structure function is extracted. The following sections introduce the MC generators which were used for event generation, compare spectra and scales from data and MC for the primary measured quantities, and determine their resolution. Special attention is paid to the electron energy scale, which is discussed in a separate section.

Event Generators and Detector Simulation.

To investigate migration and resolution effects and to determine the kinematic acceptance, NC DIS events were generated with a lower limit of $Q^2 > 4\,\mathrm{GeV}$ using the HERACLES MC program [KSM91b, KSM91a] with the parton parameterization MRSD-'. HERACLES includes electroweak radiative corrections to first order. The hadronic final state was simulated using the color dipole model (CDM) [AGLP89] including boson-gluon fusion (BGF) as implemented in ARIADNE [Lön92] for the QCD cascade, and JETSET [Sjö86, SB87] for the hadronization. The events are referred to as the MC sample and correspond to an integrated luminosity of $738\,\mathrm{nb}^{-1}$.

It has previously been established that the ARIADNE model gives the best available overall description of the hadronic final state as it is observed in DIS [ZEU93c, ZEU94a]. Effects of variations in the structure function have been investigated by reweighting the MC events to the MRSD0', GRV(HO) and CTEQ-2D' sets of partons. To study the effects of large rapidity gap (LRG) events on acceptance and event migration, the POMPYT [BI93] and NZ [NZ92] models have been used, both of which give reasonable descriptions of the data [ZEU94b]. The photoproduction background at high values of y has been investigated using the PYTHIA MC program.

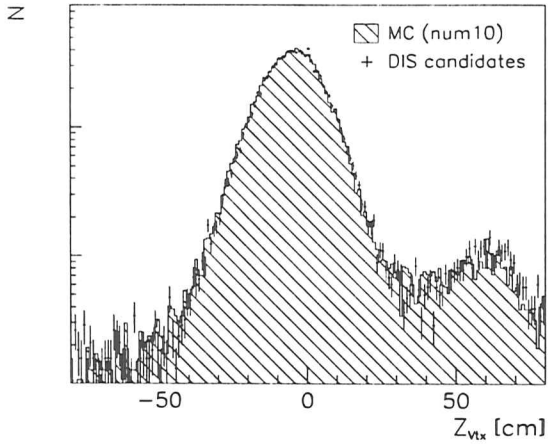

Figure 4.19: Distribution of the interaction vertex for 1993 data taking period. The MC vertex (shaded histogram) has been reweighted with the observed distribution (crosses). Some early runs (#< 6300) with a slightly wider vertex distribution have been removed from the sample.

The MC events were subjected to the full detector simulation and then reconstructed exactly like the measured data. The MC simulation of the ZEUS detector is based on the GEANT [B+87] program package. The detector simulation program, MOZART [ZEU93a], incorporates the best knowledge of the apparatus and is tuned to reproduce test beam measurements. The trigger is simulated by the program ZGANA [ZEU93a]. Fig. 4.18 summarizes the MC simulation of the ZEUS experiment.

Primary measured Quantities used for Kinematic Reconstruction.

Fig. 4.19 shows the vertex distribution of the data and the MC DIS candidate events. The vertex has been determined from the tracks reconstructed in the CTD and the VXD. If no tracking information is available, the event vertex is estimated from FCAL timing. If both tracking and FCAL timing are unavailable, the event vertex is set to the nominal interaction point (IP), z_0.

Vertices are reconstructed from the tracking detectors by first fitting the individual hits to tracks, which are then fitted to a common vertex. Cuts on the χ^2 of the individual tracks ensure that only well-reconstructed tracks contribute to the vertex fit. Fig. 4.20 (left) shows the resolution of the vertex fitting package.

In some events the particles emerge under very small angles and hence hardly cross the tracking system. In such cases the event vertex is estimated from the FCAL timing (cf fig. 4.21). The timing of the PMT signals is adjusted such that for events which occur at the IP the signal

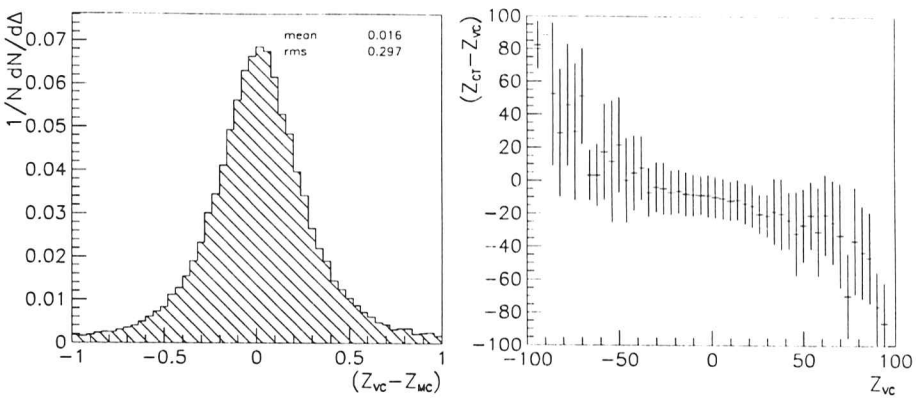

Figure 4.20: Resolution of the tracking (VC, left) and calorimeter timing (CT, right) vertex finding packages. The left histogram compares reconstructed and generated vertices (MC), the right histogram compares vertex positions from calorimeter timing and tracking, both obtained from data since the MC simulation of calorimeter timing was not satisfactory for the 1993 data taking period.

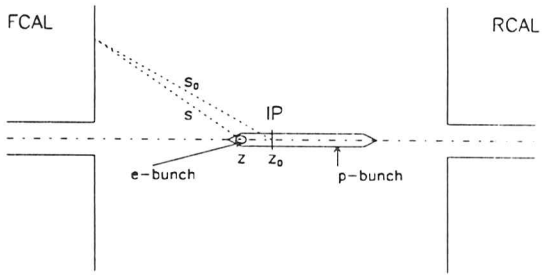

Figure 4.21: Vertex determination from timing measurements with the calorimeter. The nominal interaction point (IP) is at z_0. Particles from interactions occuring upstream of the IP arrive at the calorimeter by $\Delta t = \frac{1}{c}(z - z_0 + s - s_0)$ earlier than those from the IP (cf text)

arrives at $\theta_{\mathrm{FCAL}} = 0$. For events which occur at a distance $(z - z_0)$ upstream of the IP, the signals arrive earlier by a time difference Δt.

$$\Delta t = \frac{z - z_0}{c} + \frac{s - s_0}{c}. \tag{4.34}$$

The first term accounts for the interaction occuring earlier than interactions at the IP, the second term is due to the shorter travel distance of the emitted particles (cf fig. 4.21). For particles which hit the RCAL close to the beam-pipe both contributions cancel. The resolution

Vertexing Package	Efficiency (in %) Data	MC
Tracking	97.5%	99.4%
CAL timing	99.6%	99.7%
none		

Table 4.3: Efficiencies of the vertex finding packages.

of the vertex from calorimeter timing is shown in fig. 4.20 (right). Table 4.3 summarizes the efficiencies of the different vertex finding packages.

The MC vertex distribution has been generated using a parameterization of the event vertices observed in non-diffractive photo-production. Some early runs (before 6300) had to be excluded from the data sample as at that time the 208 MHz system in the HERA p-ring was not operating and the p-bunches had a different rms. The figure shows that data and MC simulation are in good agreement. The secondary peak at +60 cm originates from proton satellite bunches.

Fig. 4.22 compares the electron and hadron variables from the data sample which are used for reconstructing the event kinematics with different MC samples. The MC simulated electron energy has been corrected to match the observed energy spectrum (see below). Data and MC have been normalized to the same luminosity and are shown at an arbitrary scale. The data is bracketed by the MRSD0′ and MRSD−′ samples and is in good agreement with a MC sample that has been reweighted to the structure function which is obtained in this thesis.

Fig. 4.23 quantifies the capability of the MC to reproduce the observed data. Since the measurements are over-constrained, each observed quantity can be reconstructed from any other two. Thus plotting the ratios $E'_e/E_{\rm DA}$, $\theta/\theta_{\rm JB}$, $\gamma_h/\gamma_{\rm el}$ and $F/F_{\rm DA}$ allows to compare the energy scales and the inter-calibration of the calorimeter modules of data and in the MC. The figure shows that the MC reproduces the data with an accuracy of better than 1% except for the hadronic energy where the difference amounts to 6%. For the purposes of this thesis, this difference can be ignored, as F is required only for the Jacquet-Blondel reconstruction method, which is used only as a cross-check to the other methods.

Electron Energy Scale.

The distribution of the electron energy obtained from the detector simulation program[8] used for the analysis of the 1993 data does not agree with the data. The MC simulation of the calorimeter has been tuned to reproduce calibration data which were recorded at test beams at the CERN PS and SPS [ZEU91b] prior to calorimeter installation. Therefore differences in the energy scales of data and MC have to originate from differences in the experimental setup at CERN and at HERA. Possible reasons which were considered for the mismatch include miscalibration, under-estimation of the amount of inactive material in the MC, effects from the

[8]The ZEUS data which was taken during the 1993 running period is analyzed with the versions NUM10V3 and NUM10V4 of the ZEUS detector simulation program MOZART.

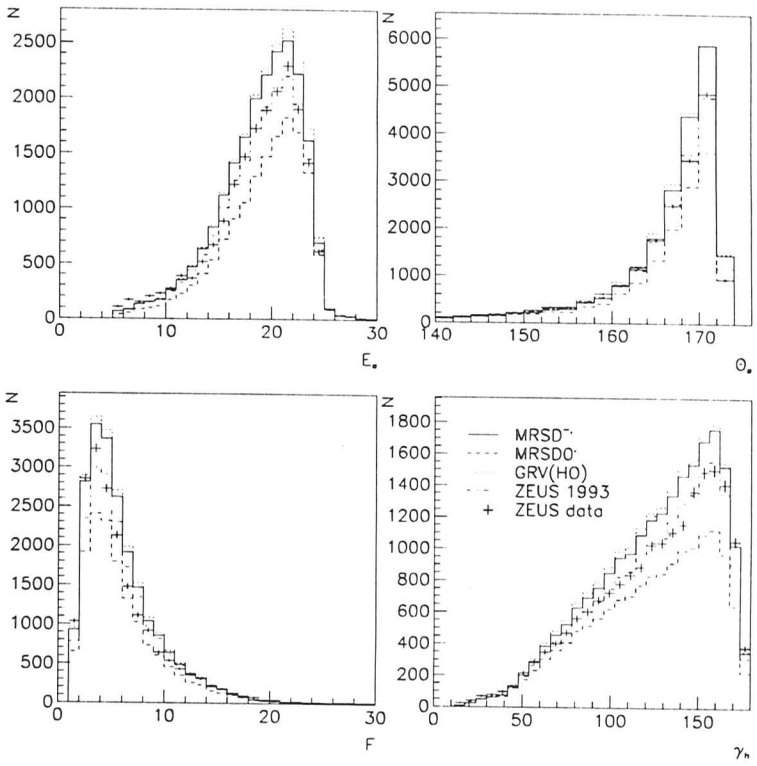

Figure 4.22: Distributions of electron and hadronic variables which are used for kinematic reconstruction. Data (crosses) are compared to a MC which has been reweighted with the MRSD-', MRSD0' and GRV(HO) parton parameterizations (cf chapter 2) and to the structure function extracted in this thesis (ZEUS1993).

magnetic field or from adjacent modules, which were both not present at the beam tests, or an erroneous geometry description of the calorimeter [CCG+94].

Monte Carlo studies indicated and recent updates of the program confirmed that the description of inactive material in front of the calorimeter close to the beam-pipe was still incomplete in the MC versions used for the 1993 analyses. The effect becomes visible when comparing the measured energy of the scattered electron, E'_e, to the same quantity reconstructed from the double-angle reconstruction method, $E_{\rm DA}$.

The ratio of the two quantities,

$$r_{\rm DA} = \frac{E'_e}{E_{\rm DA}} \qquad (4.35)$$

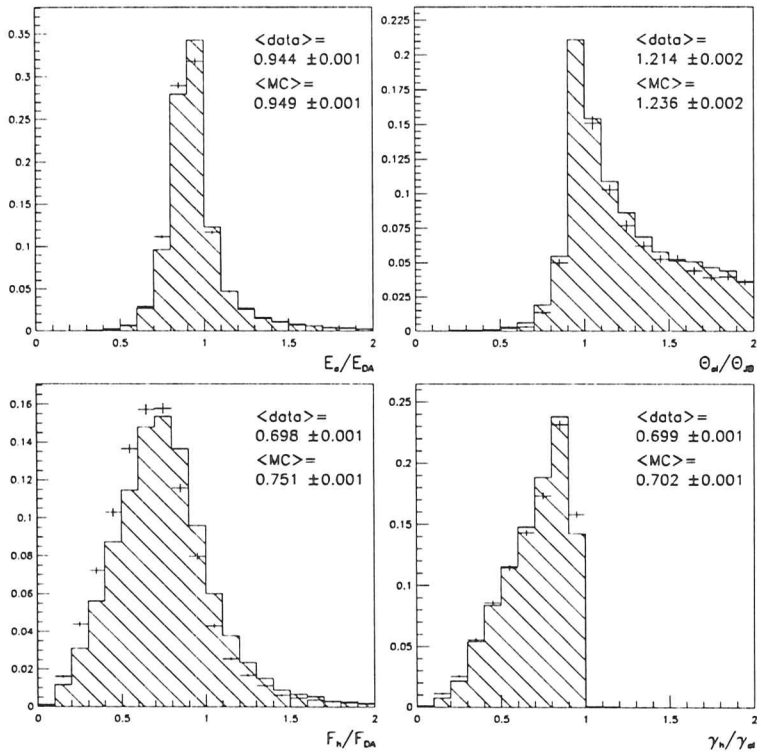

Figure 4.23: Ratios of measured and kinematically reconstructed values of the four primary measured quantities (cf text). The MC has been reweighted to the structure function which is obtained by this analysis.

can be used as an estimator for the amount of inactive material in front of the calorimeter. As E_e and $E_{\rm DA}$ can be obtained for both data and MC events. $r_{\rm DA}$ allows to cross-check the detector description used for the simulation program. Plotting $r_{\rm DA}$ versus the scattering angle of the electron, θ_e, reveals that the energy scale mismatch of data and MC is significant at large values of θ_e, ie in the vicinity of the beam pipe (fig. 4.24, left). Thus the MC-predicted values of E_e have to be modified by a correction function depending on θ_e.

Assuming missing inactive material in the MC description to be the only reason for the discrepancy, the energy dependence of the energy correction can be obtained from calorimeter calibration measurements performed at CERN prior to installation of the calorimeter in the ZEUS detector. Fig. 4.25 (upper left) shows the decrease of the calorimeter response.

$$r^n_{X_0} = \frac{E_{\rm meas}}{E_{\rm true}}. \tag{4.36}$$

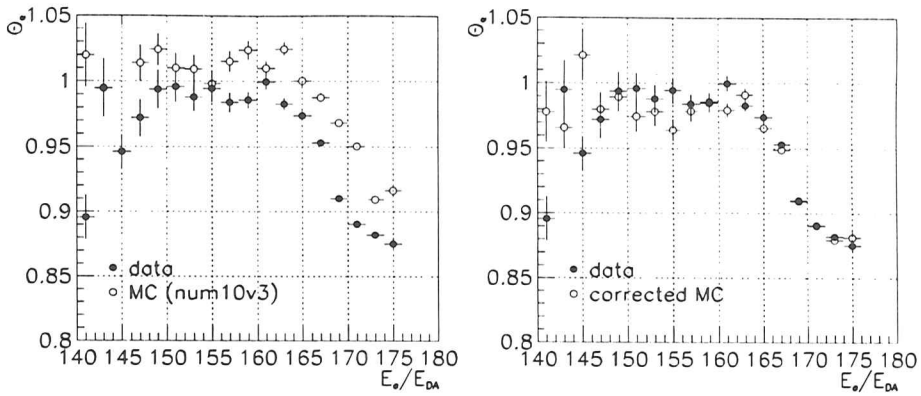

Figure 4.24: The ratio of the electron energy as obtained from measurement (E_e) and double-angle reconstruction (E_{DA}), plotted versus the electron scattering angle Θ_e. (Left: no energy scale corrections have been used. Right: The MC simulated measured energy has been rescaled to the data.).

for electrons which traversed $n = 1, 2$ or 3 radiation lengths of inactive material before entering the calorimeter. The solid lines show a linear approximation of $r^n_{X_0}$ for electron energies between 5 GeV and 30 GeV, which describe the data reasonably well.

The lower left plot of fig. 4.25 shows the ratio $r^m_{X_0}/r^n_{X_0}$ for $m > n$, which can be used to correct MC simulated energies for missing inactive material in the detector description. It is parameterized empirically by

$$\frac{r^m_{X_0}}{r^n_{X_0}} = a_1^{(m,n)} E^n_{X_0} + a_2^{(m,n)} + \frac{a_3^{(m,n)}}{E^n_{X_0}}. \tag{4.37}$$

Fig. 4.25 (right) shows the spectrum of E_e for different parameterizations of the nucleon structure function. Only events with a reconstructed electron which was found outside a box of 16cm radius around the beam-pipe and with a value of δ between 35 GeV and 60 GeV were taken[9]. After imposing an additional cut of $20{\rm GeV}^2 < Q^2_{\rm DA} < 100{\rm GeV}^2$, within one FWHM the spectrum hardly depends on the structure function chosen for the nucleon.

The MC simulated electron energy E'_e can be adapted to the data by multiplying it with a function of the form specified in (4.37). Since additional material in front of the calorimeter deteriorates the energy resolution, an additional term $a_4/\sqrt{E^n_{X_0}}$ multiplied by a Gaussian random number has to be added to eqn. (4.37).

The parameters a_i can be determined from a fit of the MC spectrum to the data. Fig. 4.24 indicates that the fit has to be performed for separate intervals of θ, where the choice of the

[9]The selection criteria are discussed in section 4.3.

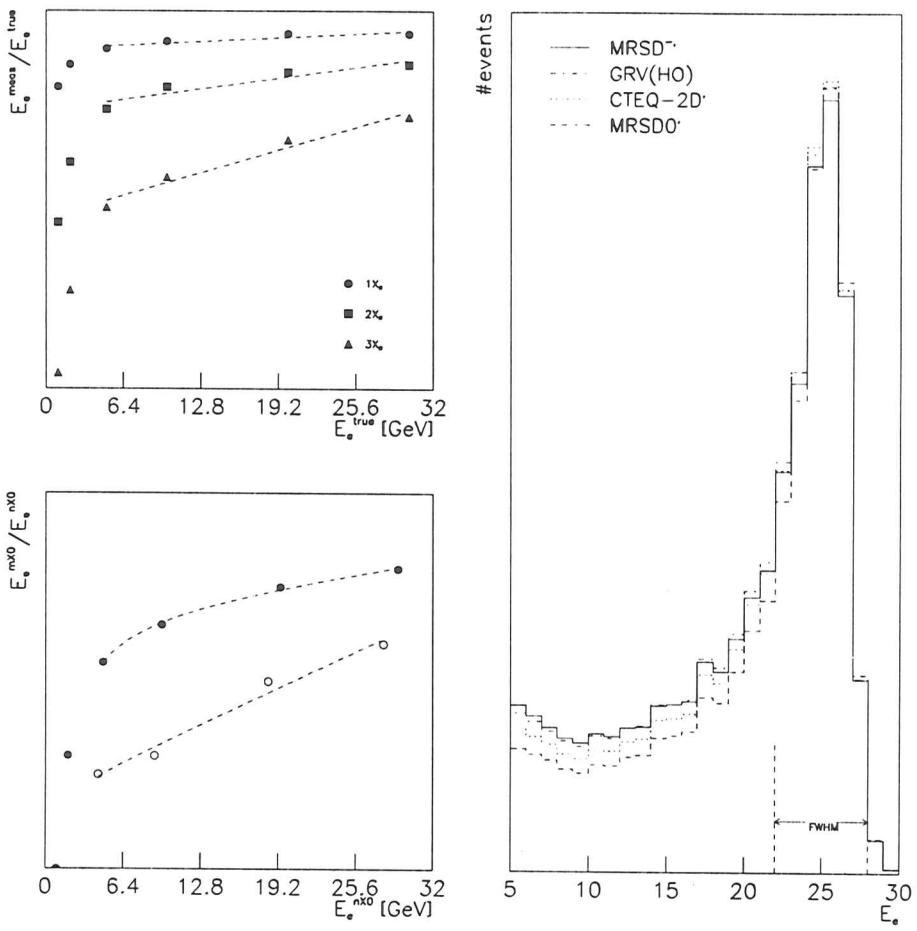

Figure 4.25: Upper left: Influence of inactive material in front of the calorimeter on the energy deposit of electrons in the calorimeter. The data points have been obtained in test beam measurements at CERN (cf [ZEU91b, Krü92]). The abscissa shows the energy of the incident electron (beam energy), the ordinate the ratio of measured and incident electron energy. The lines are linear fits to the data for incident electron energies of 5 GeV< E_e <30 GeV. Lower left: The ratio of the measured energies from locations with different amounts of inactive material in front of the calorimeter with an empirical parameterization (cf text). Right: MC predictions for the measured energy of the scattered electron, E_e. Different structure functions have been simulated by reweighting the MC events. The spectra are normalized to the same luminosity. Location and shape of the kinematic peak (within vertical lines) are independent of the nucleon structure function.

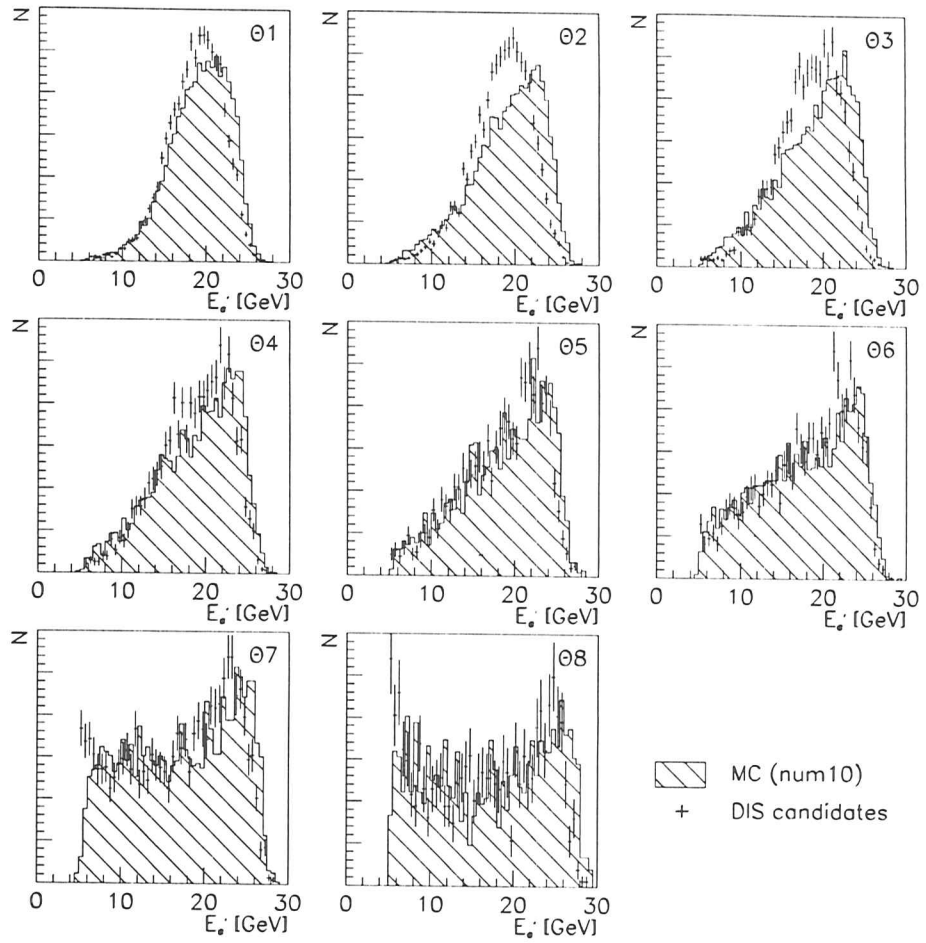

Figure 4.26: Energy spectra of scattered beam electron for DIS candidate and MC generated events. The labels Θi refer to bins in theta (explanation see text).

intervals is limited by the statistics of the data sample.

The intervals chosen for this analysis are defined in table 4.4, which also lists the result of the fit. According to fig. 4.25, the χ^2 for the fit has been calculated only within one FWHM. Fig. 4.26 shows the E'_e spectra from data and MC for the different θ intervals, fig. 4.27 shows the same spectra after the MC has been adapted to the data. The right plot in fig. 4.24 shows the ratio r_{DA} after the MC energy has been modified. Data and MC agree within 2%.

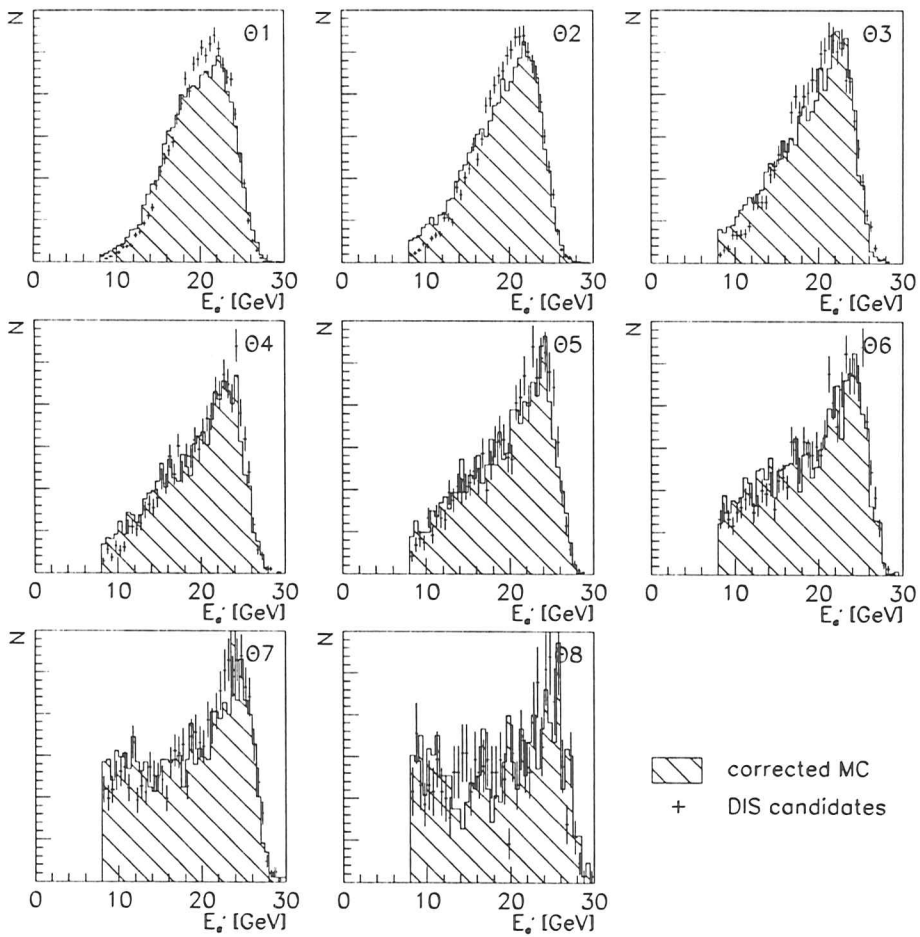

Figure 4.27: Energy spectra of scattered beam electron for DIS candidate and MC generated events. The energy of the MC events has been corrected using a second order polynomial in E_e with Θi dependent coefficients.

Energy and angular dependence of the correction function are plotted in fig. 4.28. Comparison of the energy dependence with the test beam measurement (fig. 4.25) shows that the shape of the correction function is compatible with the assumption of missing inactive material in the MC description of the detector. The angular dependence of the energy correction reveals the areas in which the description is incomplete.

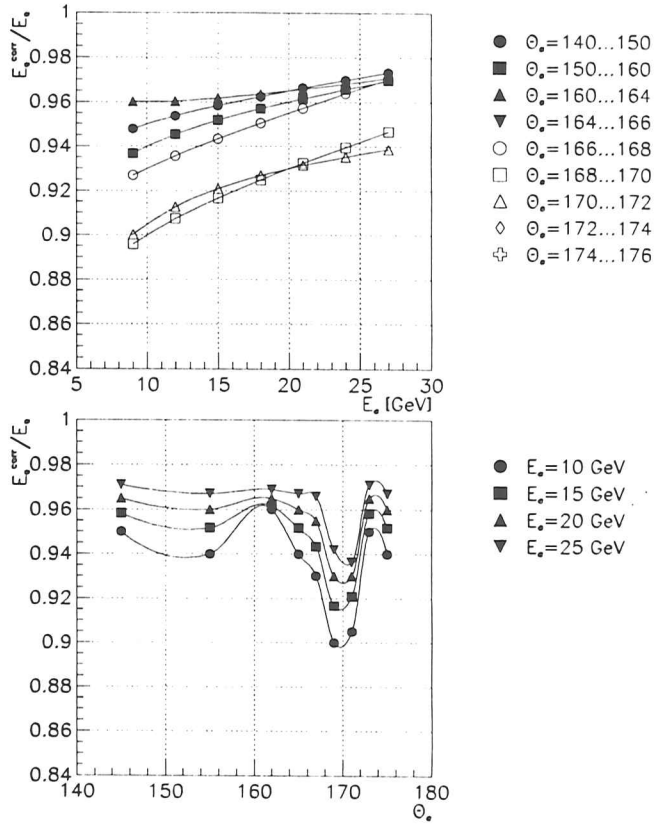

Figure 4.28: Energy dependence (top) and angular dependence (bottom) of the electron energy correction. The solid lines are splines which are drawn to guide the eye.

Figs. 4.29 and 4.30 verify the MC energy corrections. Fig. 4.29 compares the energy scales of data and MC by plotting for each kinematic variable the ratio of the values reconstructed from E'_e and θ (subscript e) and from θ and γ_h (subscript DA). The energy scales agree within two percent. Fig. 4.30 shows the reconstructed x and Q^2 spectra for data and MC. The MC sample has been reweighted to the MRSD0' and MRSD-' parameterizations and to the structure function which is obtained by this analysis. For the latter, data and MC agree within 1%.

An alternative approach corrects the measured energy of the scattered beam electron back to its true value [CCG+94]. Data and MC events from the kinematic peak are compared in different regions of the RCAL, and the position of the mean value in the measured distribution is used to estimate the amount of inactive material in front of the RCAL face at the respective location. In this way the inactive material in both the detector and the MC description of the detector

ID	θ_{min}	θ_{max}	a_1	a_2	a_3	a_4	χ^2
Θ_1	174	176	0.001	0.95	-0.2	0.28	0.416
Θ_2	172	174	0.001	0.95	-0.1	0.21	2.51
Θ_3	170	172	0.0005	0.94	-0.4	0.21	1.41
Θ_4	168	170	0.002	0.9	-0.2	0.14	0.632
Θ_5	166	168	0.002	0.92	-0.1	0.14	0.84
Θ_6	164	166	0.001	0.95	-0.2	0.14	0.338
Θ_7	160	164	0.001	0.94	0.1	0.14	0.756
Θ_8	150	160	0.001	0.95	-0.2	0.21	0.552
Θ_9	140	150	0.001	0.95	-0.1	0.07	0.405

Table 4.4: Parameters of the correction function for the MC simulated electron energy of scattered beam electron (explanation in the text).

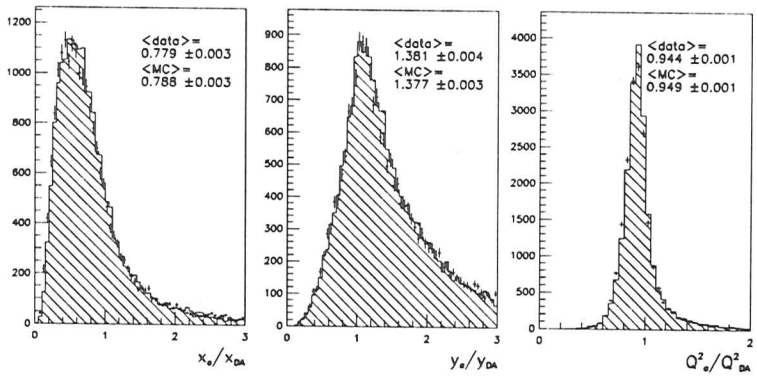

Figure 4.29: Comparison of ratios of E_e, x, y and Q^2 obtained from electron-only and double angle reconstruction for data (solid circles) and MC (histograms). Only events which are in both the electron-only and the double-angle sample were taken (cf text). Monte Carlo events have been reweighted to the measured structure function (dotted line), and the MRSD$^-$ (solid) and MRSD0 (dashed) parameterizations. Data and MC agree within 2%.

can be catalogued.

The observed energy of the scattered beam electron is now modified for both MC and data events according to this map and the impact position of the electron on the RCAL in the following way: The energy loss of the electron before entering the calorimeter is calculated from a parameterization of the energy loss of electrons in dead material which was recorded during the calorimeter calibration at CERN.

Compared to the previous method, this approach has the advantage that its absolute values can be verified from data events only [ZEU95c]. For comparison, fig. 4.31 shows the data and

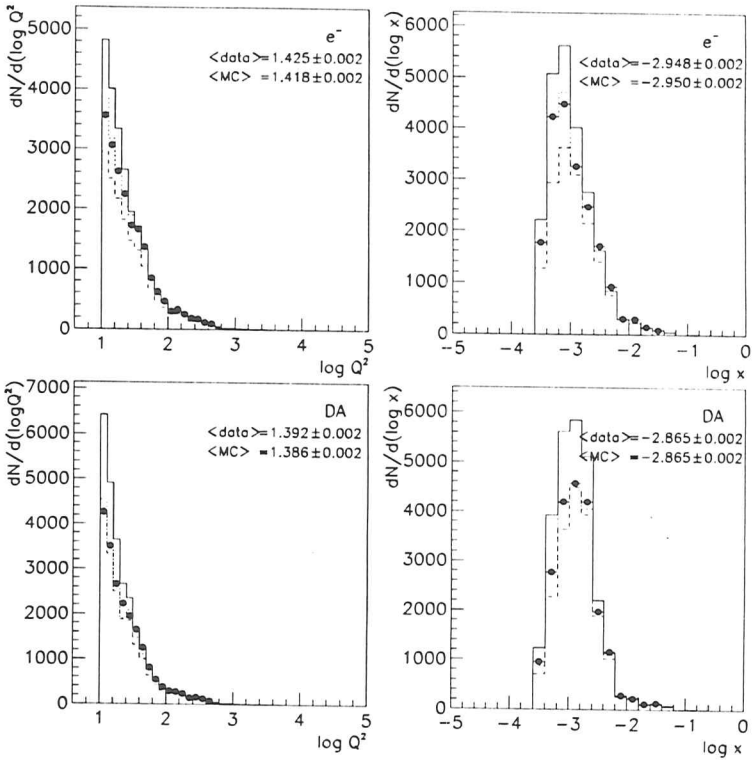

Figure 4.30: Comparison of x and Q^2 spectra obtained from electron-only and double angle reconstruction for data (solid circles) and MC (histograms). Only events which are reconstructed within the bins for which F_2 was extracted were taken (cf text). Monte Carlo events have been reweighted with the measured structure function.

MC energy spectra corrected with this method in the bins of the previous correction method.

4.4.5 Kinematic Acceptance

The phase space which is accessible to DIS measurements is limited by the resolution and the acceptance of the detector. Detection of the scattered beam electron is limited towards low values of Q^2 by the rear beam-pipe opening, which prohibits measurements above[10] $\theta = 177.4^0$. Due to the forward beam-pipe opening final state hadrons which are emitted below $\gamma_h = 1.6^0$ escape undetected. Towards low values of y the acceptance is limited due to the resolution

[10] The angles stated are wrt the nominal interaction point (IP).

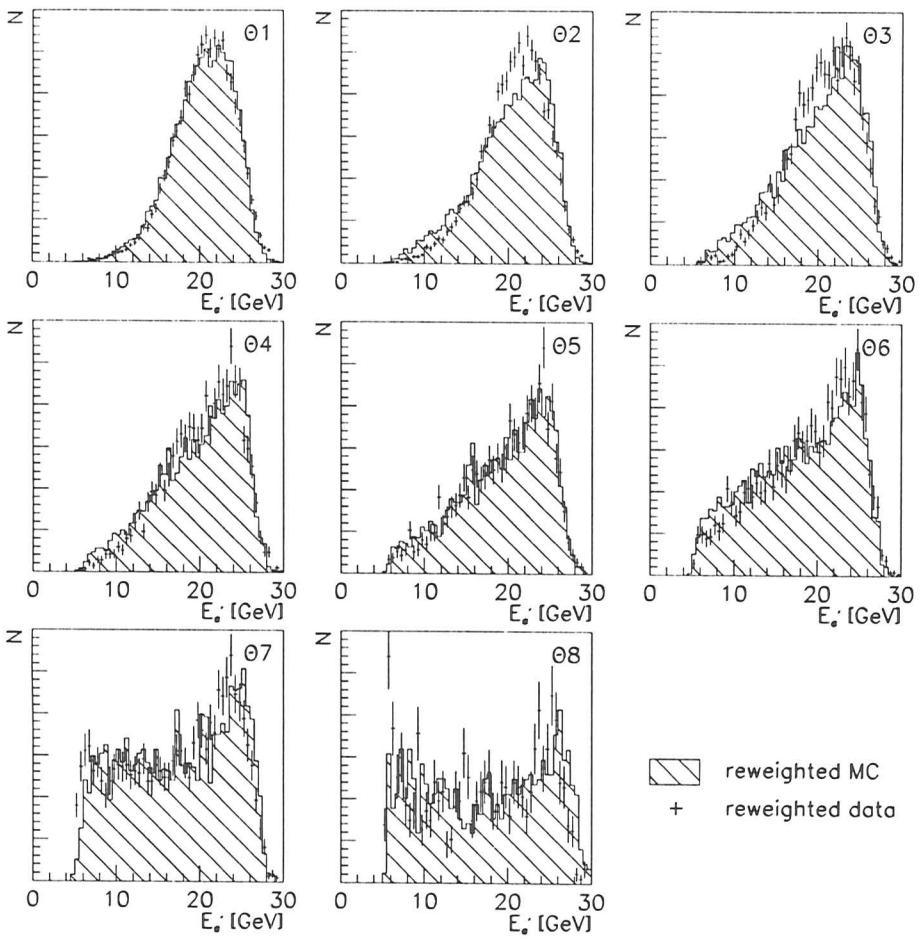

Figure 4.31: Energy spectra of scattered beam electron for DIS candidate and MC generated events. The energy of both MC and data events has been modified according to a map of the inactive material in front of the calorimeter.

in x, which is in many cases proportional to y^{-1}. At high y the measurement is distorted by background from photoproduction, which "fakes" electrons in the forward region of the detector.

A set of selection cuts is imposed on the data to retain only well-measured events for the analysis. In particular the aims and the corresponding requirements are

Variable	Lower Limit	Upper Limit	Aim	Target
suppress background from $\gamma^* p$				
$E - P_z$	35 GeV	60 GeV	suppress $\gamma * p$ and ISR	any event
$y_{\rm el}$	0.95		remove events with fake FCAL electron	any event
ensure reliable electron identification				
$x_{\rm CAL}, y_{\rm CAL}$	-16 cm	16 cm	containment of em shower in CAL	any event
E'_e	5 GeV		reasonable purity of electron finder	any event
ensure applicability of electron energy corrections				
$z_{\rm Vertex}$	-20 cm	20 cm	correctness of θ dependence	E'_e
E'_e	8 GeV		correctness of E'_e dependence	E'_e
θ		140^0	availability of energy corrections	E'_e
suppress effects from calorimeter noise				
$y_{\rm JB}$	0.04		exclude events with low hadronic activity	γh

Table 4.5: Selection cuts which are imposed on the data to retain only well-measured events. Some of the cuts are globally applied to any event, while others are specific to certain reconstruction methods. In the latter case, the "target" column specifies which variables are improved by the cut.

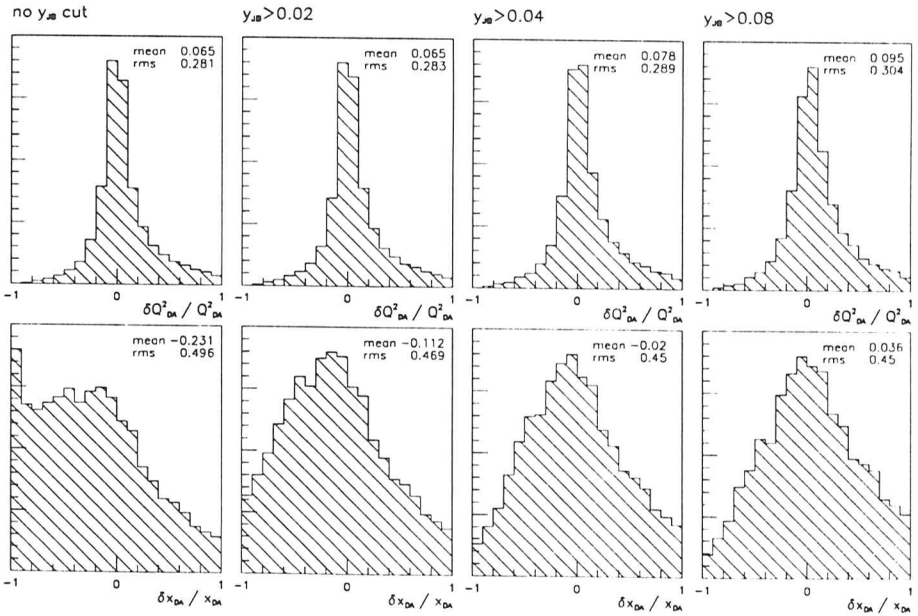

Figure 4.32: Influence of a selection cut in $y_{\rm JB}$ on the reconstruction of kinematic variables via the double-angle method (cf text).

- **Suppress background from photoproduction**
  The majority of photoproduction events can be suppressed by requiring $\delta = E - P_z$ to be in the range of 35 GeV to 60 GeV (cf sect. 4.1.3). For some events, fake electrons are identified by the electron finding algorithms in the vicinity of the forward beam pipe opening. These events are removed by requiring $y_{el} < 0.95$.

- **Ensure reliable identification of scattered beam electron**
  Electron identification is considered reliable if the electromagnetic shower which is due to the electron is fully contained in the calorimeter, and if the purity of the electron identification is of $\mathcal{O}(50\%)$ or better. Containment is achieved by requiring the impact position of backward electrons on the face of the RCAL, $(x_{\mathrm{RCAL}}, y_{\mathrm{RCAL}})$, to lie outside a box of 32 cm width which is centered around the beam-pipe opening. The purity of the electron finders is established by a fiducial cut on the electron energy, requiring $E'_e > 5\,GeV$ (cf sect. 4.2).

- **Ensure applicability of electron energy corrections**
  If reconstruction of the event kinematics makes use of the measured energy of the scattered beam electron, E'_e, special care needs to be taken to ensure that the energy correction for the MC simulation can be used. The energy corrections were obtained in bins of θ. A fiducial cut requiring the interaction vertex to be within 20 cm of the IP ensures that the measured electron angle θ is compatible with the binning. Since the energy corrections are obtained only for $\theta > 140^0$, electrons below this angle are not considered for the analysis. As the fitting of the energy spectra was limited to one FWHM of the spectra, a fiducial cut of $E'_e > 10\,GeV$ is imposed on the data.

- **Reduce effects which are due to calorimeter noise**
  At low values y_{JB} the resolution of y_{JB} deteriorates because the signal from the hadronic activity becomes comparable to the uranium noise (cf fig. 4.13). Since the hadronic angle γ_h is directly linked to y_{JB} via eqn. (4.21), a cut requiring $y_{\mathrm{JB}} > 0.04$ is imposed on the data if the event kinematics are reconstructed using γ_h. Fig. 4.32 illustrates the effect of this cut on the resolution of the double-angle variables.

The selection cuts are summarized in table 4.5.

4.5 Unfolding the Data

Reconstructed event distributions are smeared due to initial state radiation (ISR), limited detector resolution, energy losses in inactive material, and particles which escape undetected. Figs. 4.33 and 4.34 illustrate the migration effects for the different reconstruction methods before and after the kinematic selection cuts have been applied. It can be seen that migration effects are still present in the selected data sample, although they have been drastically reduced by the selection cuts.

An extraction of F_2 requires unsmeared event distributions, hence the data have to be unfolded first. The problem of unfolding can be generalized to an integral equation,

$$M(x, Q^2) = \int dx'\, dQ^{2\prime}\, T(x, Q^2, x', Q^{2\prime}) N(x', Q^{2\prime}). \qquad (4.38)$$

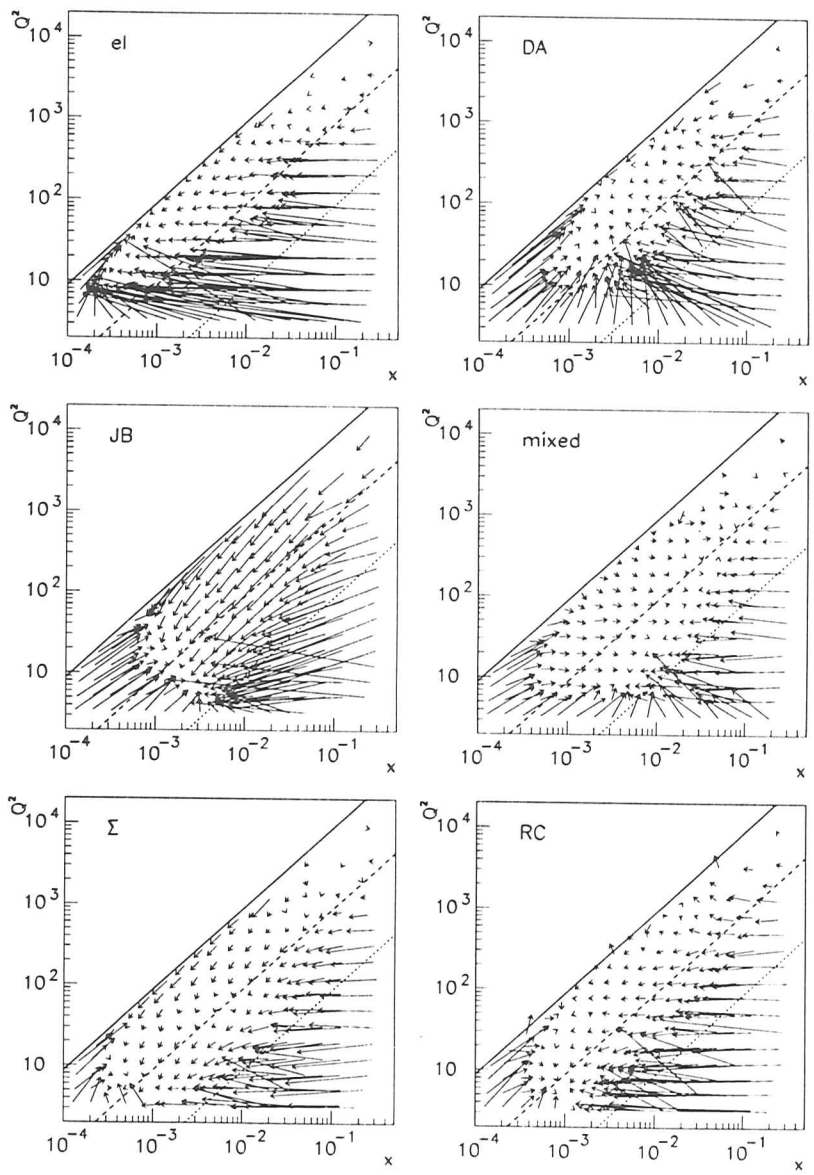

Figure 4.33: Migration of events due to kinematic reconstruction for different reconstruction methods. The arrows point from the generated to the reconstructed (x, Q^2). No selection cuts have been applied.

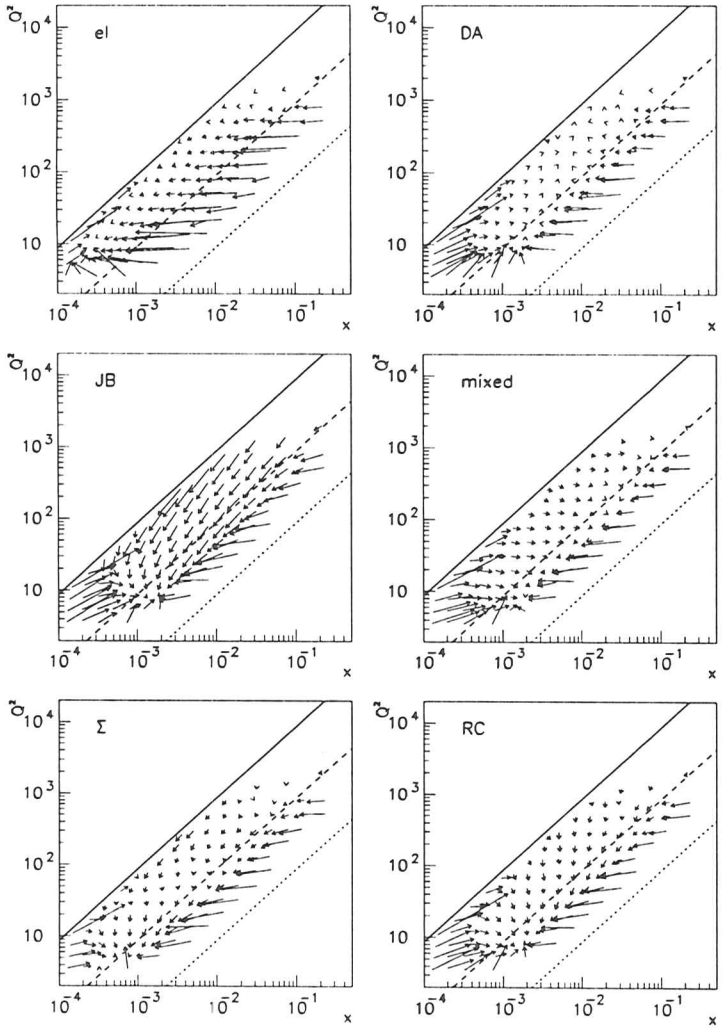

Figure 4.34: Migration of accepted DIS events due to kinematic reconstruction for different reconstruction methods. The arrows point from the generated to the reconstructed (x, Q^2).

range		c	δc	$\Delta^{\min}$	Δ
Bins in Q^2					
10	25	15	0.27	8.1	15
25	55	35	0.34	23.8	30
55	120	65	0.30	39.0	65
120	240	160	0.32	102.4	120
240	500	320	0.27	172.8	260
500	2000	1000	0.20	400.0	1500
2000	10000	5000	0.20	2000.0	8000
Bins in x					
0.00030	0.00085	0.0007	0.36	0.00051	0.00055
0.00085	0.00268	0.001	0.39	0.00078	0.00183
0.00268	0.00536	0.004	0.35	0.00280	0.00268
0.00536	0.01414	0.008	0.34	0.00544	0.00536
0.01414	0.05656	0.04	0.30	0.02400	0.04242
0.05656	0.22620	0.1	0.22	0.04400	0.16964

Table 4.6: Binning used for systematic studies. The table lists for each bin the lower and the upper limit, the central value at which F_2 is extracted (c), the resolution at the central value (δc), the width of the bin (Δ), and the minimum bin width corresponding to twice the detector resolution ($\Delta^{\min}$).

M counts the number of events which are reconstructed at x and Q^2, and N is the theoretical distribution, ie the number of events originating from x', $Q^{2'}$. T is the transfer function which describes the detector response[11] as the probability for an event originating from $(x', Q^{2'})$ to be reconstructed at (x, Q^2). T combines kinematic acceptance and migration probabilities. In practice, an additional term $\varepsilon(x, Q^2)$ has to be added to the rhs of eqn. (4.38) to account for the statistical uncertainties of the measurement [Blo84].

If the data are binned in a total of n bins in x and Q^2, the arguments of eqn. (4.38) assume only n different discrete values. In this case, M and N become vectors of dimension n, and T becomes an $n \times n$ matrix (transfer matrix). The unsmeared distribution is obtained from eqn (4.38) via inversion or iteratively. In case of convergence, both methods can be shown to yield the same result [Blo84].

4.5.1 Bin Selection

Figs. 4.35 and 4.36 show the resolutions in x and Q^2 for electron-only and double-angle reconstruction. The x-resolution is of the order of 30% (37%) for the electron-only (double-angle) reconstruction at low values of Q^2 and improves by 5% (10%) towards higher Q^2. The Q^2 resolution is about 20% (27%) at low Q^2 and improves to 9% (14%) towards high Q^2 and high

[11] M, N and T depend of course also on the primary measured quantities, collider and detector operation conditions etc. For the practical purposes of this thesis, however, it is sufficient to take the distributions to depend only on the kinematic variables, ie $M(x, Q^2)$, or $M(y, Q^2)$.

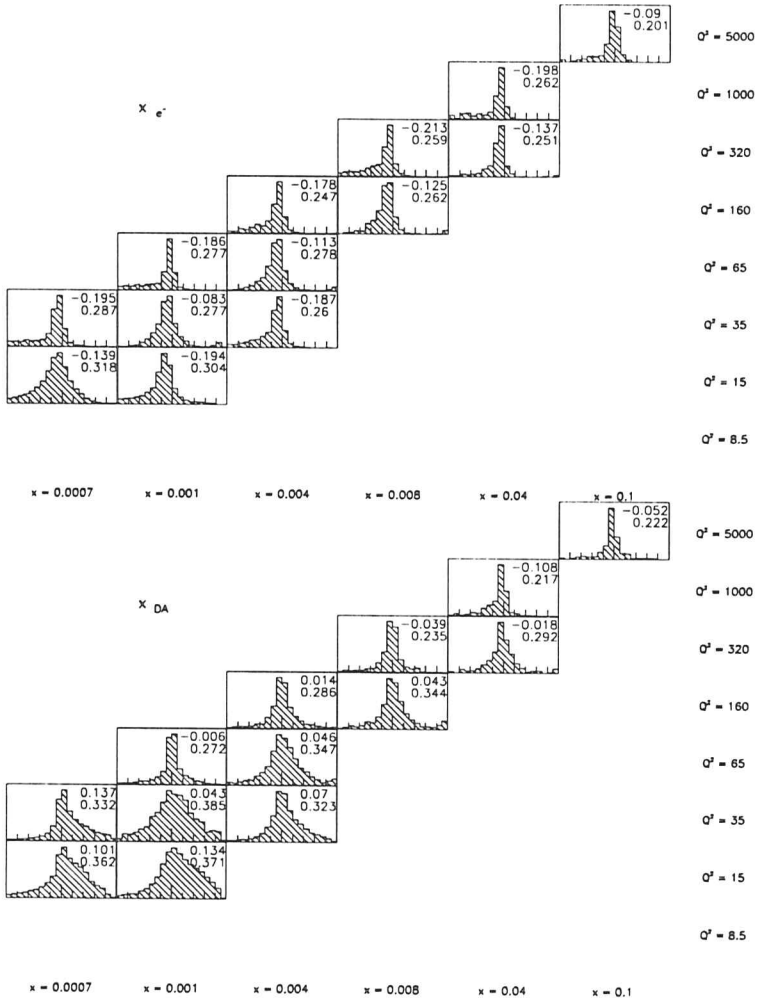

Figure 4.35: Resolution of x reconstructed from the electron-only and the double angle method. The histograms plot $(x_{\rm d} - x_{\rm MC})/x_{\rm MC}$, where subscript MC refers to the kinematic values at generator level. The two numbers in each histogram specify the mean (upper) and rms (lower).

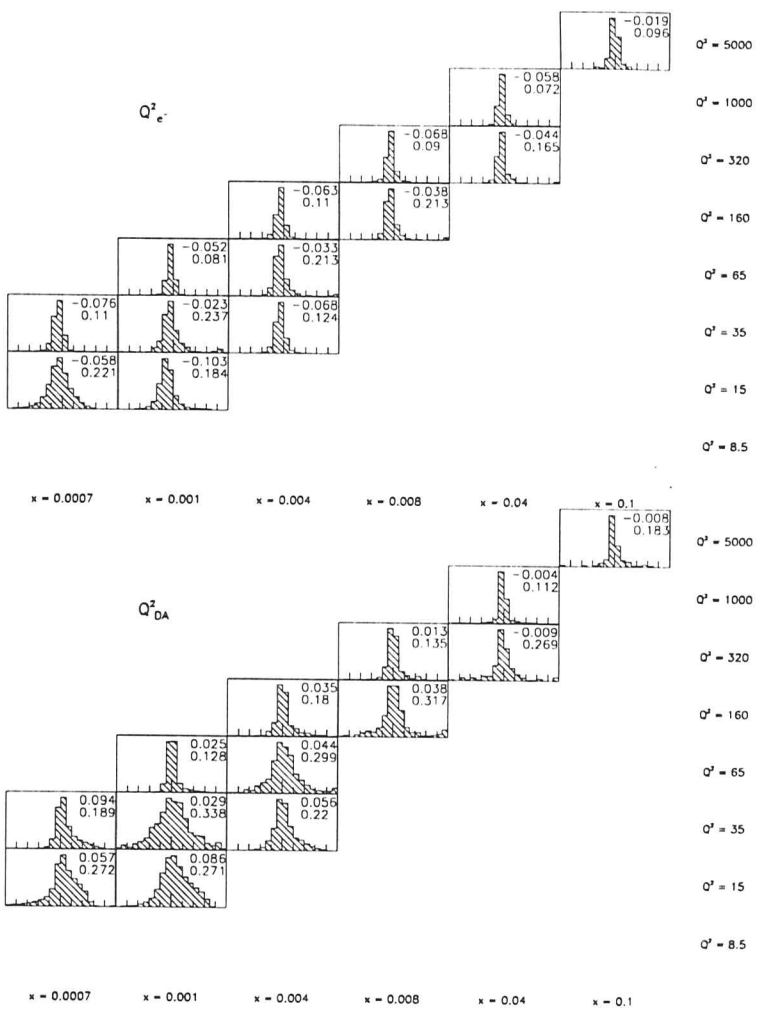

Figure 4.36: Resolution of Q^2 reconstructed from the electron-only and the double-angle method. The histograms plot $(Q^2_{\rm DA} - Q^2_{\rm MC})/Q^2_{\rm MC}$, where the subscript MC refers to the kinematic values at generator level. The two numbers in each histogram specify the mean (upper) and rms (lower).

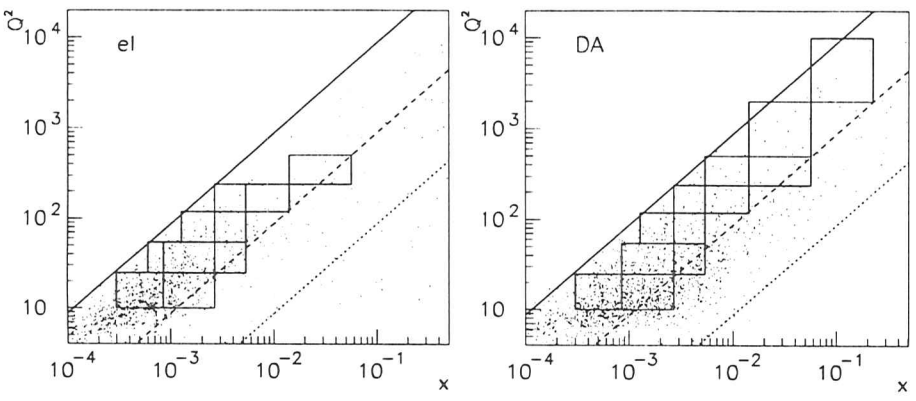

Figure 4.37: Distribution of reconstructed events and bins suitable for an extraction of the structure function for the electron-only and double-angle reconstruction methods. The solid, dashed and dotted line show values of $y = 1$, 0.1 and 0.01.

y.

Neighbouring bins are negatively correlated due to migrations. To avoid numerical problems while unfolding, the size of a bin in a kinematic variable should be larger than twice its resolution at the center of the bin. If smaller bins are chosen, the unfolded distribution shows oscillatory behaviour. Such distributions seem unphysical, and they are difficult to present and to discuss as they can be interpreted only together with the full error matrix.

Table 4.5.1 defines a binning which is suitable to investigate the systematics of the extraction of the structure function. The bins are chosen according to the above rule and are enlarged at high Q^2 to obtain sufficient statistics per bin. The table compares the chosen bin size to the minimum bin size required by the detector resolution. For this purpose, the resolution has been worst-case estimated by the maximum double-angle resolution at the central value of each bin.

Four quantities are defined as a measure for the quality of a bin. The smearing s is the probability for an event to be reconstructed in the bin where it originates. The purity p is the fraction which specifies how many the of events which are measured in a bin originate from that bin. The correction factor c gives the ratio of the events originating from a bin and the events measured in that bin, and the acceptance A is the probability for an event which originates from a bin to be reconstructed within the kinematic region used for the analysis. The bin quality can be calculated from the quantities of eqn. 4.38.

$$s(x,Q^2) = T(x,Q^2,x,Q^2). \tag{4.39}$$

$$p(x,Q^2) = \frac{N(x,Q^2)T(x,Q^2,x,Q^2)}{M(x,Q^2)}. \tag{4.40}$$

$$c(x,Q^2) = \frac{N(x,Q^2)}{M(x,Q^2)} = \frac{p}{s}. \tag{4.41}$$

$$A(x,Q^2) = \int dx'\,dQ^{2\prime}\,T(x',Q^{2\prime},x,Q^2). \tag{4.42}$$

In practice the bin quality has to be obtained from MC as all of the quantities depend on N or T. The MC sample has to be sufficiently large to keep the statistical uncertainties of s, p c and A small. Since s and A depend only on the transfer matrix, they are insensitive to the MC input structure function.

Bins with a small value of s smear their contents over adjacent bins, while bins with a high correction factor are flooded with events from neighbouring bins. In both cases the unfolding procedures become numerically instable. In bins with a low acceptance even small uncertainties in the acceptance can lead to large fluctuations when rescaling the unfolded distribution. Hence bins were only kept in the analysis if

$$\begin{array}{rcl} & s & > 0.1, \\ 3.5 > & c & > 0.4, \\ & A & > 0.1, \end{array} \tag{4.43}$$

and if at least 10 events were observed in the bin. Fig 4.37 shows the distribution of the reconstructed events over the phase space and the bins suitable for electron-only and double-angle reconstruction. The bins resulting for the other reconstruction methods are similar to these two methods.

The migration plot, fig. 4.33, shows that migrations are dominantly in the direction of y, hence binning the data in y and Q^2 should reduce migration effects and thus improve the bin quality. Compared to the binning in x and Q^2, it turns out that the region of kinematic acceptance extends for most reconstruction methods towards lower y, ie higher x. Fig. 4.38 shows the resolutions in y for the electron-only and the double-angle reconstruction. Fig. 4.39 shows the (y,Q^2) bins suitable for kinematic reconstruction for the different reconstruction methods.

4.5.2 Background Subtraction

Only few non-DIS events remain in the data sample after all selection cuts have been applied. Tags of the luminosity monitor identify photoproduction events, however the luminosity monitor cannot be used to quantify the amount of remaining photoproduction events due to its limited acceptance. Events originating from unpaired electron or proton bunches indicate beam-gas background in the DIS sample.

The remaining background from photoproduction has to be estimated from a fit to the observed and MC-simulated δ-distributions. The shape of the MC simulated δ-distribution can be empirically parameterized by a Gaussian with a radiative tail towards lower energies. The contribution from photoproduction background, which is present in the observed δ-distribution, can be parameterized by an additional Gaussian tail. Δ^{MC} and Δ^{data} specify the simulated and observed distributions.

$$\Delta^{\mathrm{MC}}(\delta) = \begin{cases} \delta > \delta_0^{\mathrm{MC}}: & A\exp\left(-\frac{(\delta-\delta_0^{\mathrm{MC}})^2}{2\sigma_{\mathrm{rad}}^{\mathrm{MC}\,2}}\right) \\ \delta \le \delta_0^{\mathrm{MC}}: & C+(A-C)\exp\left(-\frac{(\delta-\delta_0^{\mathrm{MC}})^2}{2(\sigma_{\mathrm{rad}}^{\mathrm{MC}\,2}+\sigma_{\mathrm{rad}}^{\mathrm{MC}\,2})}\right) \end{cases} \tag{4.44}$$

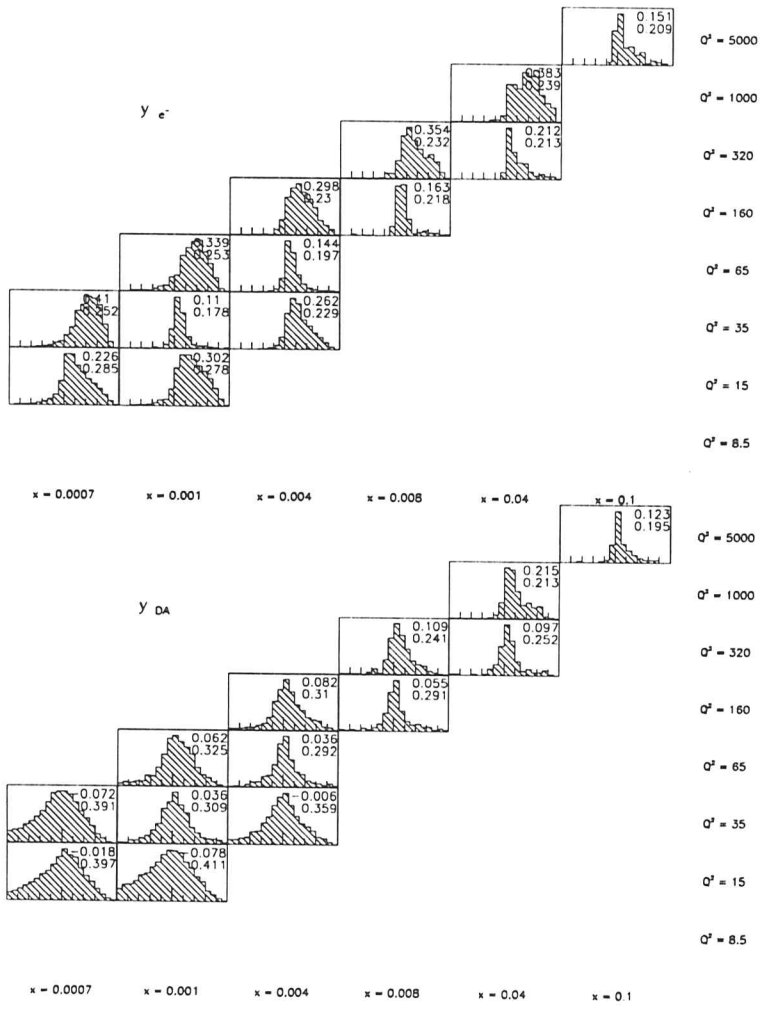

Figure 4.38: Resolution of y reconstructed from the electron-only and the double angle method. The histograms plot $(y_A - y_{MC})/y_{MC}$, where subscript MC refers to the kinematic values at generator level. The two numbers in each histogram specify the mean (upper) and rms (lower).

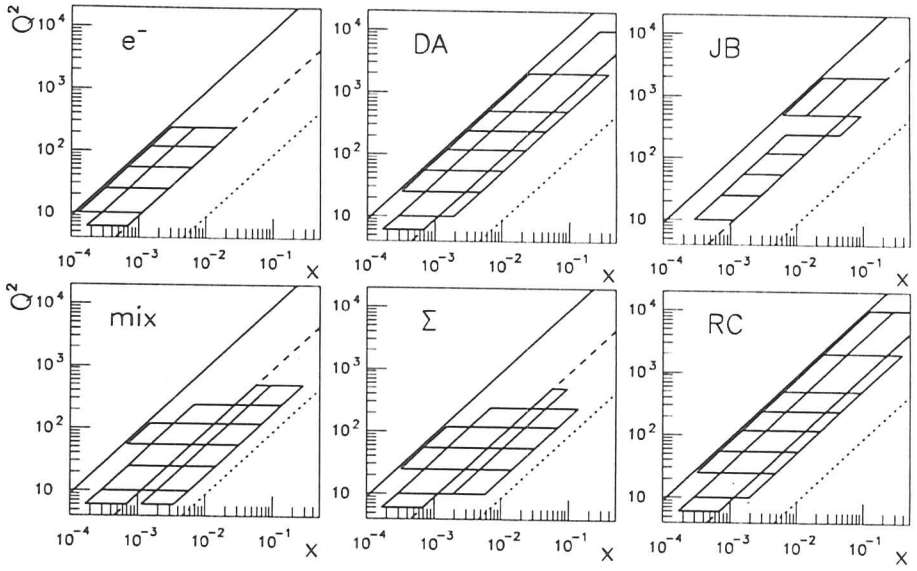

Figure 4.39: Bins in which the structure function can be extracted from different reconstruction methods. The upper limit on Q^2 for the electron-only, the mixed and the Σ methods is due to the electron energy corrections being available only in a limited range in θ

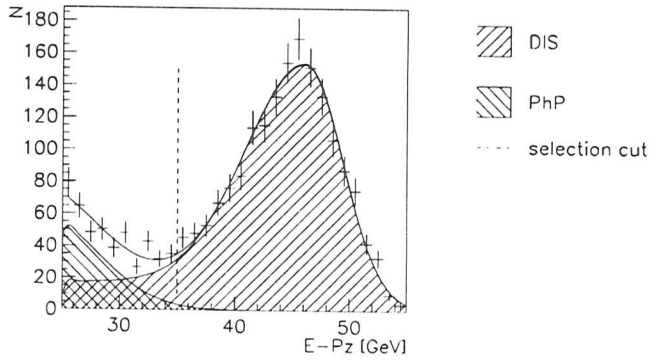

Figure 4.40: Estimating photoproduction background from the $E - P_Z$ distribution (cf text).

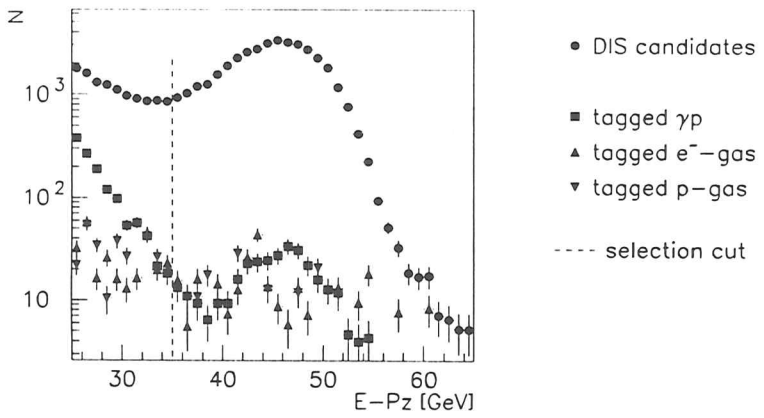

Figure 4.41: $E - P_Z$ distribution for tagged photoproduction events and beam-gas collisions from pilot bunches remaining in the DIS sample.

$$\Delta^{\text{data}}(\delta) = \Delta_1^{\text{data}}(\delta) + \Delta_2^{\text{data}}(\delta) \tag{4.45}$$

$$\Delta_1^{\text{data}}(\delta) = \begin{cases} \delta > \delta_0^{\text{data}}: & BA \exp\left(-\frac{(\delta-\delta_0^{\text{data}})^2}{2\sigma_{\text{d}}^{\text{data}\,2}}\right) \\ \delta \le \delta_0^{\text{data}}: & BC + B(A-C)\exp\left(-\frac{(\delta-\delta_0^{\text{data}})^2}{2\left(\sigma_{\text{d}}^{\text{data}\,2}+\sigma_{\text{rad}}^{\text{MC}\,2}\right)}\right) \end{cases} \tag{4.46}$$

$$\Delta_2^{\text{data}}(\delta) = D \exp\left(-\frac{(\delta-\delta_0^{\text{PHP}})^2}{2\sigma_{\text{d}}^{\text{PHP}\,2}}\right). \tag{4.47}$$

δ_0 is the central value of the peak due to DIS. σ_{d} and σ_{rad} are contributions to the width from detector resolution and radiation. The superscripts MC and data indicate from which distribution the parameters have been determined. A, B, C and D are used for normalization. The contribution from ISR events to the δ distribution is taken to be equal for data and MC and is parametrized by C (magnitude) and $\sigma_{\text{d}}^{\text{PHP}}$ (width). The result of the fit is shown in fig. 4.40.

The number of remaining background events, N_{BG}, is obtained by integrating the parameterization of photoproduction events over the δ range which is accepted for DIS candidates.

$$N_{\text{BG}} = \int_{35\,GeV}^{60\,GeV} d\delta\ \Delta_2^{\text{data}}. \tag{4.48}$$

However, due to the energy scale mismatch between data and MC, N_{BG} overestimates the remaining background by

$$dN_{\text{BG}} = \int_{35\,GeV-(\delta_0^{\text{MC}}-\delta_0^{\text{data}})}^{35\,GeV} d\delta\ \Delta_1^{\text{data}}. \tag{4.49}$$

The remaining beam-gas background is estimated from the pilot bunches. So far, the bunch number has been ignored when events were selected for the DIS sample. Now, it can be used

Quantity		Definition
N	$N_i = N(x, Q^2)$	true distribution of events
M	$M_i = M(x, Q^2)$	experimentally observed distribution of events
T	$T_{ij} = T(x, Q^2, x', Q^{2\prime})$	transfer matrix, ie probability of an event originating from bin $(x', Q^{2\prime})$ to be reconstructed in bin (x, Q^2)
N^{MC}	$N_i^{\text{MC}} = N(x, Q^2)$	MC generated distribution of events
M^{MC}	$M_i^{\text{MC}} = M(x, Q^2)$	MC predicted distribution using full detector simulation
T^{MC}	$T_{ij}^{\text{MC}} = T(x, Q^2, x', Q^{2\prime})$	transfer matrix constructed from MC simulation (cf text)

Table 4.7: Definitions used for unfolding.

to determine how many events originate from unpaired electron or proton bunches. The weight of these events is determined by the ratio of the beam currents in the pilot and the colliding bunches.

Fig. 4.41 illustrates the amount of the different types of background which is present in the DIS sample after all the selection cuts have been imposed.

4.5.3 Unfolding by Matrix Inversion

Definitions.

If M labels[12] an observed distribution of events and N is the corresponding true distribution, then a transfer matrix T can be constructed such that

$$M^T = N^T T \iff M_j = N_i T_{ij}. \tag{4.50}$$

where the subscript i refers to the i-th component (bin) of the respective quantity. Quantities from MC-simulation are identified by an additional superscript $^{\text{MC}}$. N^{MC} is the generated distribution. M^{MC} is the MC-prediction after the full detector simulation has been used, and T^{MC} is the transfer matrix obtained from MC simulation. The definitions are summarized in table 4.7.

If T_{ij} is non-singular, eqn. (4.50) can be inverted to obtain the unsmeared distribution from the experimentally observed distribution.

$$N = \left(T^{-1}\right)^T M \iff N_i = \left(T_{ij}^{-1}\right)^T M_j. \tag{4.51}$$

The detector simulation reproduces the spectra of the primary measured quantities, so it can be postulated that

$$T_{ij}^{\text{MC}} = T_{ij}. \tag{4.52}$$

[12] The dependencies on the kinematic variables are listed in table 4.7, but have been omitted in the equations for brevity.

and eqn. (4.51) becomes

$$N = \left(\left(T^{\mathrm{MC}}\right)^{-1}\right)^{T} M \iff N_i = \left(T^{\mathrm{MC}}_{ji}\right)^{-1} M_j. \tag{4.53}$$

Hence an unsmeared distribution can be obtained from an experimentally observed distribution by inversion of the MC-constructed transfer matrix.

The covariance matrices C^M and C^N are obtained by error propagation. Their diagonal elements specify the absolute errors of M and N, the non-diagonal elements measure the correlation of the corresponding components[13] in M and N. C^N can be calculated from the transfer matrix, T, and the errors of the measured distribution, M, using

$$C^M = \mathbf{1} \cdot M \iff C^M_{ij} = M_i \delta_{ij} \tag{4.54}$$

$$C^N = \left(T^{-1}\right)^T C^M T^{-1} \iff C^N_{ij} = T^{-1}_{ki} M_k T^{-1}_{kj}, \tag{4.55}$$

and assuming negligible background. The correlation of two bins becomes better visible in the correlation matrix, R, which contains the elements of the covariance matrix normalized such that $-1 < R_{ij} < 1$.

$$\left(R^N_{ij}\right) = \frac{C^N_{ij}}{\sqrt{M_i M_j}}. \tag{4.56}$$

R_{ij} vanishes if the two bins i and j are uncorrelated and becomes 1 (-1) for fully (anti-) correlated bins.

Construction of the Transfer Matrix.

The transfer matrix is constructed from the MC simulation. First, a binning of n "physics bins" is defined. The bins are numbered consecutively from 0 to n, where the n-th bin (background bin) accommodates events which do not fall into one of the physics bins. Next, the MC events are scanned, and each event is stored in the one-dimensional histogram N_i, where i labels the bin in which the event was generated, and in the two-dimensional histogram T_{ij}, where j identifies the bin in which the event has been reconstructed. Events which fail the selection criteria are treated like background events.

After scanning, the bin properties are calculated from eqns. (4.39) to (4.42)[14], and the selection criteria (4.43) are imposed on the transfer matrix. Bins k which fail the selection are removed from the transfer matrix and added to the background bin via

$$N_n \leftarrow N_n + N_k. \tag{4.57}$$

$$T_{nn} \leftarrow T_{nn} + T_{kk}. \tag{4.58}$$

$$T_{in} \leftarrow T_{in} + T_{ik}, \; i \neq k \tag{4.59}$$

$$T_{ni} \leftarrow T_{ni} + T_{ki}, \; i \neq k. \tag{4.60}$$

[13] Hence covariance matrices are symmetric.

[14] At this stage, the histogram T_{ij} is not yet normalized, ie its elements still contain $N_i T_{ij}$.

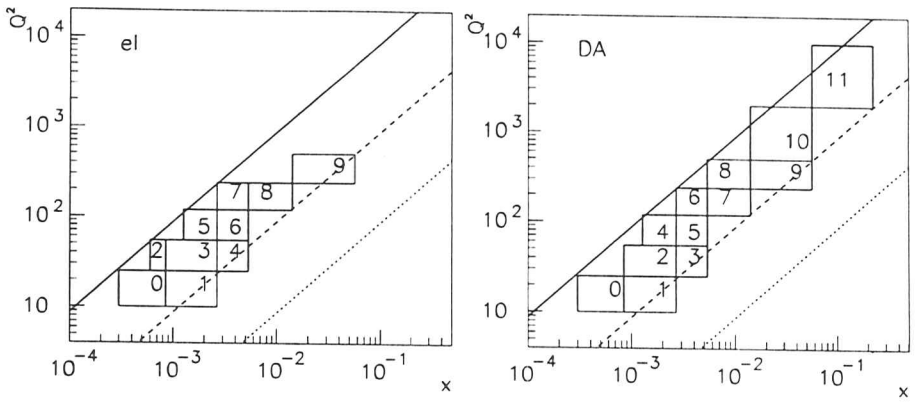

Figure 4.42: Numbering scheme for (x, Q^2) bins

The equations state that events in bad bins are treated like background events, and that migrations to and from a bad bin become migrations to and from the background. After reduction the bins can be re-numbered, and finally the transfer matrix is normalized via

$$T_{ij} \leftarrow \frac{1}{N_i} T_{ij}. \tag{4.61}$$

Removing bad bins properly from the transfer matrix is essential for the unfolding procedure. Bad bins must not be simply dropped as they can be sources for migrations to the measured phase space, but keeping them in the transfer matrix usually leads to the matrix becoming singular.

Detector effects are unfolded via the inverse transfer matrix, $(T^{-1})_{ji}$, which somehow encodes the probability P_{ji} for an event which is measured in bin j to have originated from bin i. The algorithm described above can be used to construct such a probability matrix P_{ji} from a MC sample, but the resulting matrix depends strongly on the MC input structure function. It is therefore different from the unique inverse transfer matrix and suitable for unfolding only if the MC model correctly describes the measured distribution.

Example for Weakly Correlated Bins.

The bins which were defined in the previous section (table 4.5.1) are used to unfold the ZEUS data taken during the 1993 HERA running period. Fig. 4.42 defines the bin numbering scheme for reconstruction via the electron-only and the double-angle method after having imposed the bin selection criteria. Other reconstruction methods have been used as well, but are not discussed in detail for brevity.

The transfer and correlation matrices for the two methods are shown in fig. 4.43. The abscissa

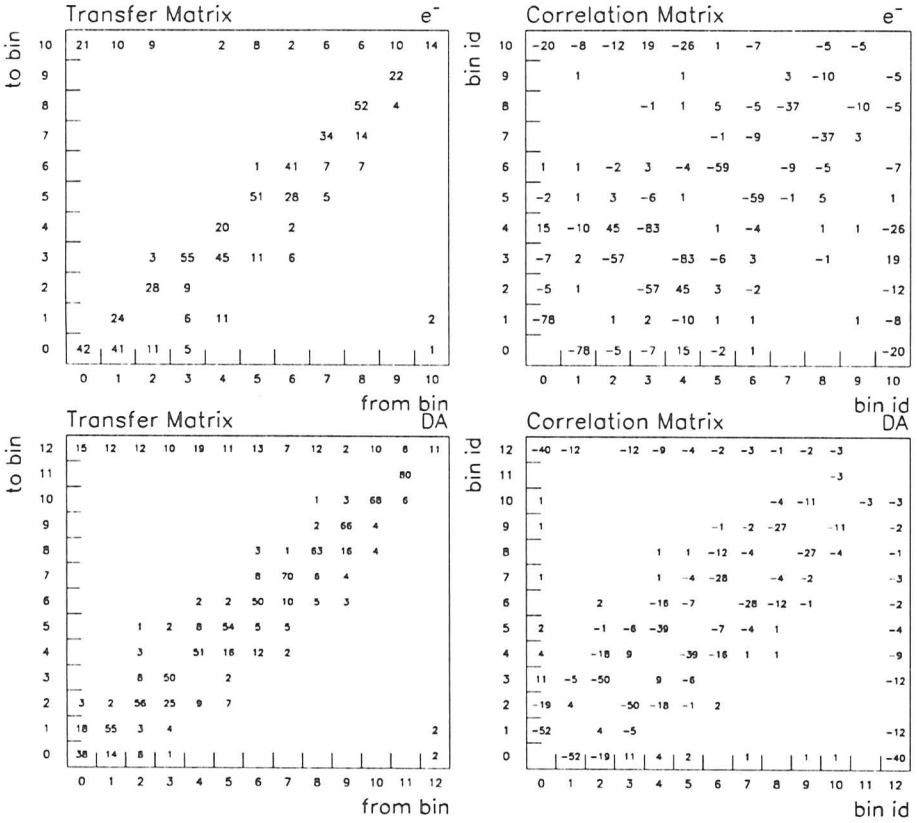

Figure 4.43: Transfer and correlation matrix for bins in (x, Q^2), for the electron-only (top) and double-angle (bottom) reconstruction methods. The transfer matrices contain the migration probabilities from one bin to another, the correlation matrices show the correlation coefficients (both given in %). The diagonal elements of the correlation matrix have been suppressed: they contain the number of events corresponding to the statistical uncertainty.

specifies the bin (i) in which an event was generated, the ordinate holds the bin (j) where the event has been reconstructed. The transfer matrices show that most events are reconstructed in their proper bins, $T_{ii} = \mathcal{O}(60\%)$, except for low values of Q^2 where despite the large bin size migrations are still strong. The latter is also seen from the correlation matrix, which shows negative correlations of down to $\mathcal{O}(-70\%)$ for adjacent bins in the lower Q^2 ($\leq 65\,\mathrm{GeV}^2$) region.

The resulting unfolded distributions are shown in fig. 4.44. The unsmeared distribution, N_i,

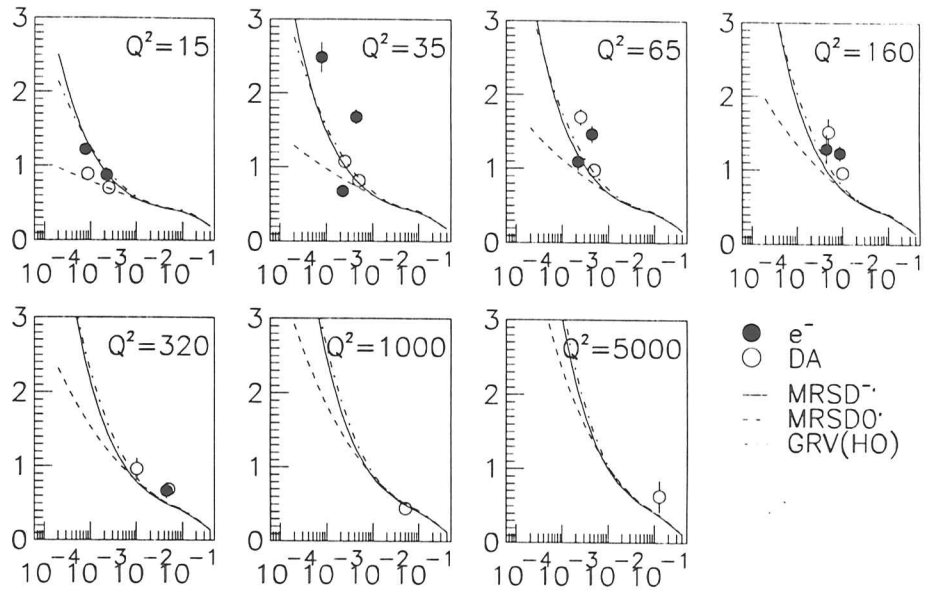

Figure 4.44: $F_2(x, Q^2)$ unfolded via matrix inversion, bins of (x, Q^2).

has been converted to F_2 to be comparable with other analyses[15]. The error bars show the statistical uncertainties as obtained from error propagation, eqn. (4.55).

At first glance, the structure functions obtained from the two reconstruction methods seem to disagree. A closer look, however, reveals that the double-angle data points follow a smooth curve, while the data points from the electron-only method are strongly fluctuating around the parameterizations. The fluctuations occur in the three lowest Q^2 bins and are alternating wrt the parameterizations, in accordance with the negative correlations of adjacent bins stated in the correlation matrix. In this sense, the fluctuating result obtained from the electron-only method in correlated bins is compatible with the smoother result obtained from the double-angle method in less correlated bins.

A similar analysis has been carried out in bins of y and Q^2. The bin boundaries in y are at $y_i = 0.02, 0.06, 0.1, 0.4$ and 0.9. They have been chosen to yield bins of a width larger than 2σ and with sizes similar to the bins in x and Q^2. Fig. 4.45 defines the numbering scheme for the selected electron-only and double-angle bins, fig. 4.46 shows the corresponding transfer and correlation matrices. Compared to the previous analysis, the accessible phase-space extends to lower y for the double-angle method, and the bin quality at low Q^2 has improved for both methods.

[15] Conversion of an unsmeared distribution to a structure function is discussed in the next section.

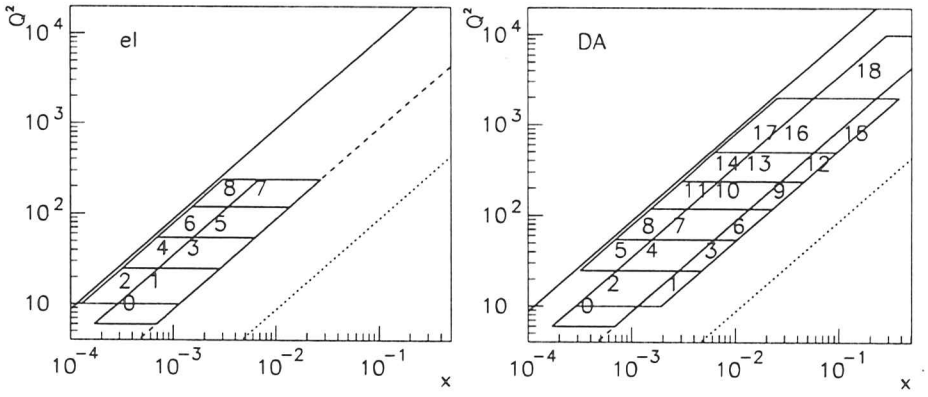

Figure 4.45: Numbering scheme for bins in (y, Q^2).

Fig. 4.47 plots the unsmeared event distribution, as before already converted to the structure function F_2. The electron data still seems to be wildly fluctuating similar to the (x, Q^2)-bins. However, fig. 4.48, which plots $F_2(x, y)$ in bins of fixed y, reveals that the shapes of the structure function are similar for both reconstruction methods within each bin of y. The electron data simply has picked up global fluctuation over entire bins of y.

4.5.4 Iterative Methods

The Iteration Procedure.

As an alternative, an iterative procedure can be tried to solve eqn. (4.51) (eg [Blo84, d'A94a]). An initial MC-generated distribution is used to produce a prediction for the measured distribution. The prediction is compared to the experimental data and a $\chi 2$ is calculated for the two distributions. If the MC-generated distribution succeeds in reproducing the measurement it can be taken to be equal to the unsmeared physical distribution. Otherwise it has to be iterated.

If the statistics is low, the procedure can be distorted by bin-to-bin fluctuations, and the resulting unfolded distribution receives unphysical oscillatory structures. An entropy H^2 can be defined as a measure for the smoothness of the unfolded data and can be used to suppress fluctuations in the resulting distribution by aborting the iteration for the price of a higher χ^2. Alternatively, the solution can be forced to remain smooth by either imposing constraints on the function which updates the MC, or by requiring the resulting distribution to satisfy an a-priori defined functional form. The latter two techniques are commonly referred to as smoothing or regularization (eg [Blo84, d'A94a]).

Using the definitions of the previous section with additional superscripts $^{(n)}$ to indicate the n-th

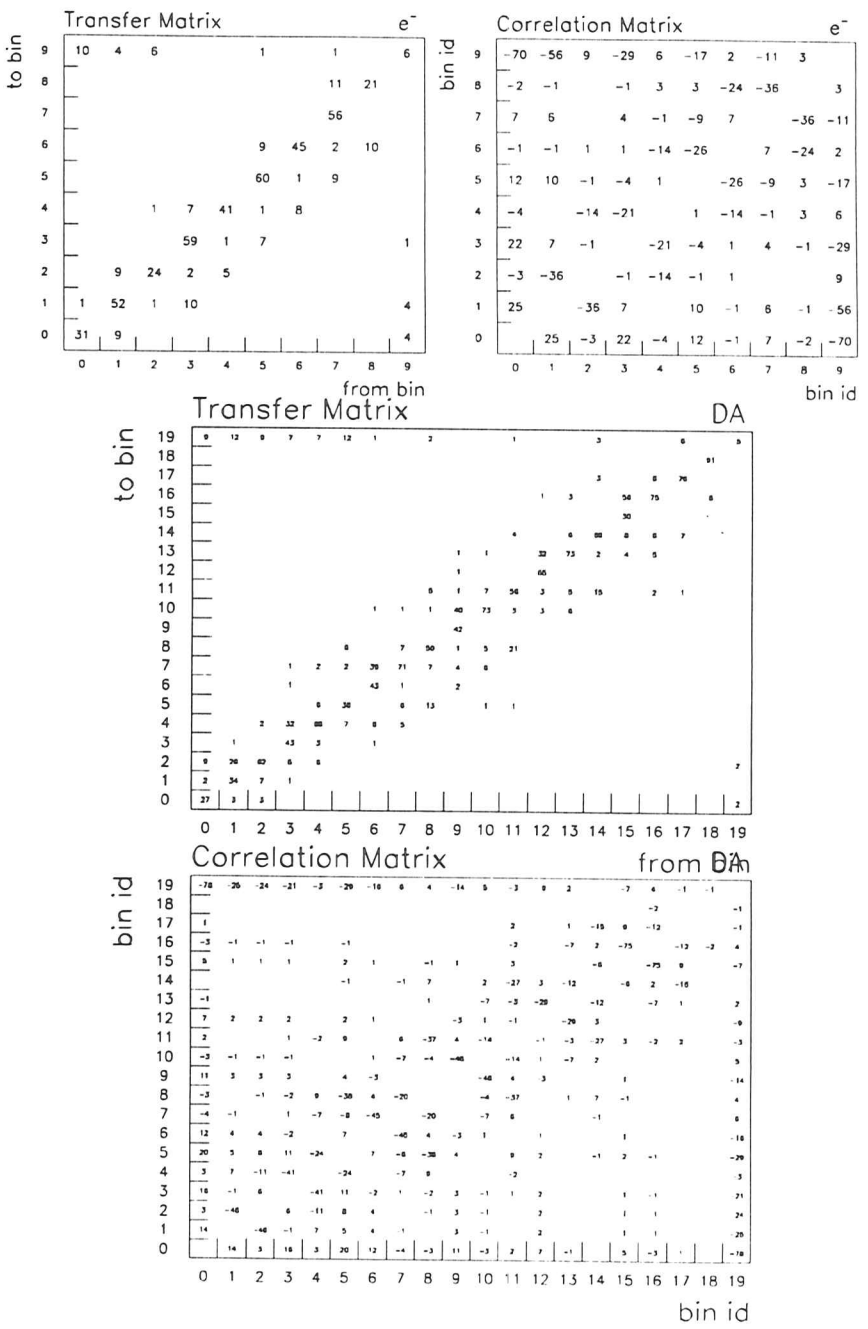

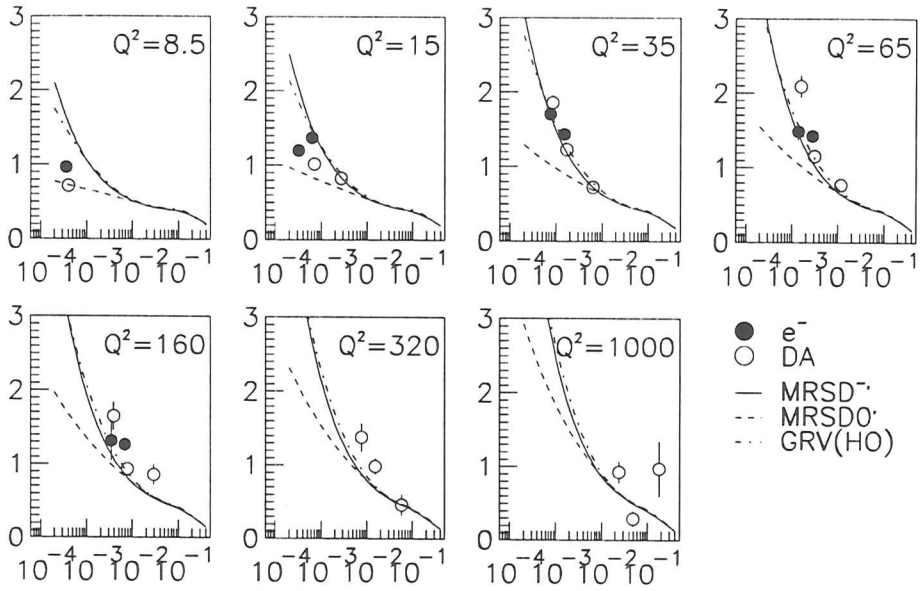

Figure 4.47: $F_2(x, Q^2)$ obtained via matrix inversion in bins of (y, Q^2).

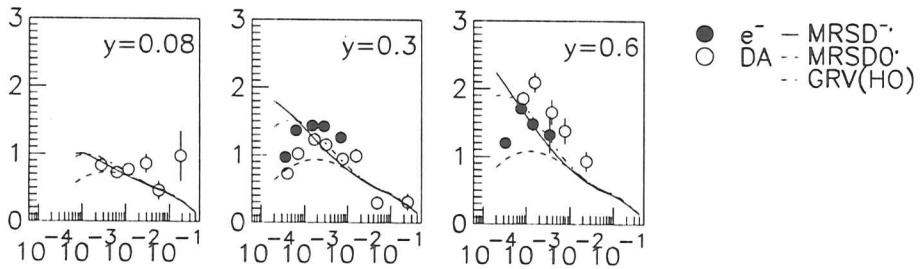

Figure 4.48: $F_2(x, y)$ obtained via matrix inversion in bins of (y, Q^2), plotted for three values of y.

iteration, the procedure can be expressed formally.

$$\left(M^{\mathrm{MC},(n)}\right)^T = \left(N^{\mathrm{MC},(n)}\right)^T T^T. \tag{4.62}$$

$$\chi^{(n)2} = \sum_i \frac{\left(M_i^{\mathrm{MC},(n)} - M_i\right)^2}{M_i^{\mathrm{MC},(n)} + M_i}. \tag{4.63}$$

$$H^{(n)2} = \sum_i \sum_j \mathrm{neigh}(i,j) \left(N_i^{\mathrm{MC},(n)} - N_j^{\mathrm{MC},(n)}\right)^2. \tag{4.64}$$

$$N^{\mathrm{MC},(n+1)} = f\left(N^{\mathrm{MC},(n)}, M^{\mathrm{MC},(n)}, M\right). \tag{4.65}$$

where $\mathrm{neigh}(i,j)$ is a function which is one if bins i and j share a common boundary and zero otherwise.

Different iterative procedures have been proposed with different recurrence relations f for the updated theoretical distribution. In an intuitive approach [ZEU93f] which has already been used for [ZEU93d] the theoretical input distribution is reweighted with the ratio of the experimentally observed and the MC-predicted distribution of measured events.

$$N_i^{\mathrm{MC},(n+1)} = \frac{M_i}{M_i^{\mathrm{MC},(n)}} N_i^{\mathrm{MC},(n)}. \tag{4.66}$$

Error propagation relies on the covariance matrix which is not calculated in this method. Hence the statistical error of the unsmeared physical distribution has to be estimated from the statistical errors of the theoretical input distribution, $N^{\mathrm{MC},(0)}$, the corresponding MC-prediction for the measured distribution, $M^{\mathrm{MC},(0)}$, and the experimentally observed distribution, M. Assuming the three distributions to be statistically independent[16], the error on the unsmeared distribution is

$$\frac{\delta N_i^{\mathrm{MC},(n)}}{N_i^{\mathrm{MC},(n)}} = \frac{1}{N_i^{\mathrm{MC},(n)}} + \frac{1}{M_i^{\mathrm{MC},(n)}} + \frac{1}{M_i}. \tag{4.67}$$

Example for Weakly Correlated Bins.

The analysis of the 1993 ZEUS data which was presented in the previous section has been repeated using the iterative unfolding instead of matrix inversion. The result is shown in fig. 4.49, which plots the unfolded distributions in terms of F_2. When unfolding, the χ^2 decreases with every iteration and converges to unphysically low values, while the entropy, which measures the smoothness of the resulting structure function, remains roughly constant. In this analysis, the iteration has been stopped if

$$\begin{aligned} \chi^2 &< 1.1. \\ \text{or } \Delta\chi^2 &< 0. \\ \text{or } \frac{\Delta H^2}{H^2} &< -0.02 \text{ and } \frac{\Delta\chi^2}{\chi^2} < 0.10. \\ \text{or } \frac{\Delta H^2}{H^2} &< -0.10. \end{aligned} \tag{4.68}$$

The conditions correspond to χ^2 assuming an acceptable value, χ^2 increasing in subsequent iterations, or the resulting distribution picking up oscillations which are large compared to the gain in χ^2, or which are simply too large. Typically, it takes two to three iterations to achieve an acceptable value of χ^2.

[16] which is not really true, but should be sufficient for this purpose

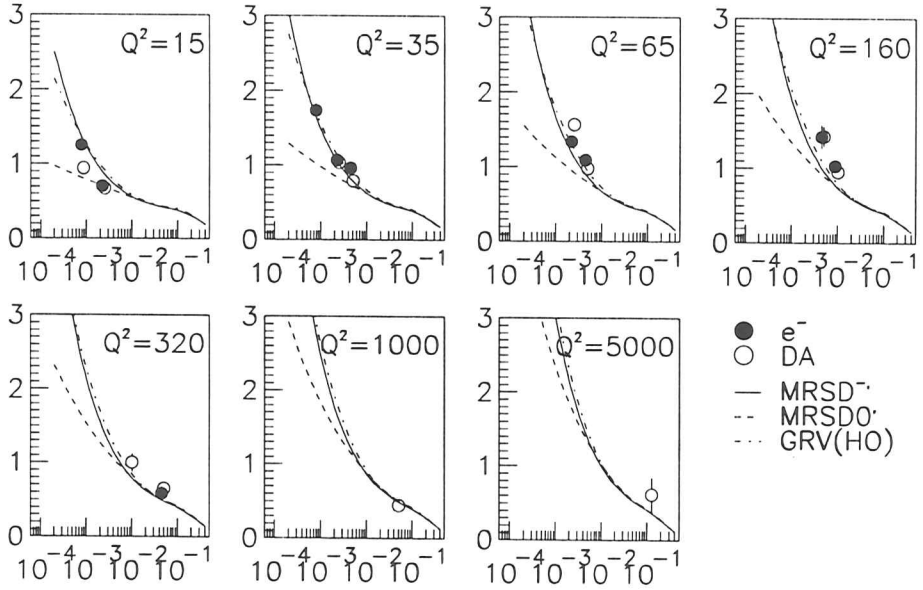

Figure 4.49: $F_2(x, Q^2)$ obtained via an iterative unfolding method in bins of (x, Q^2). The unfolding has been stopped after five (two) iterations for the electron-only (double-angle) reconstruction with $\chi^2_{\rm el}/{\rm ndf} = 0.8110$ and $\chi^2_{\rm DA}/{\rm ndf} = 0.7321$.

Figs. 4.50 and 4.51 plot the result of an iterative unfolding in bins of (y, Q^2). Again, the plots show the extension of the accessible phase space towards lower values of y compared to the binning in (x, Q^2).

4.5.5 Comparison of Methods

This section quantifies the similarity of unfolding via matrix inversion and iterative unfolding. First, two special cases are discussed in which unfolding reduces to multiplication with a correction factor. Then, the results of the unfolding in weakly correlated bins are compared, and finally some consequences of choosing bins of the order of the detector resolution are discussed.

Special Cases.

In an ideal experiment migrations are absent, leading to the transfer matrix being diagonal. The diagonal elements contain the acceptance, which in this case is equal to the smearing.

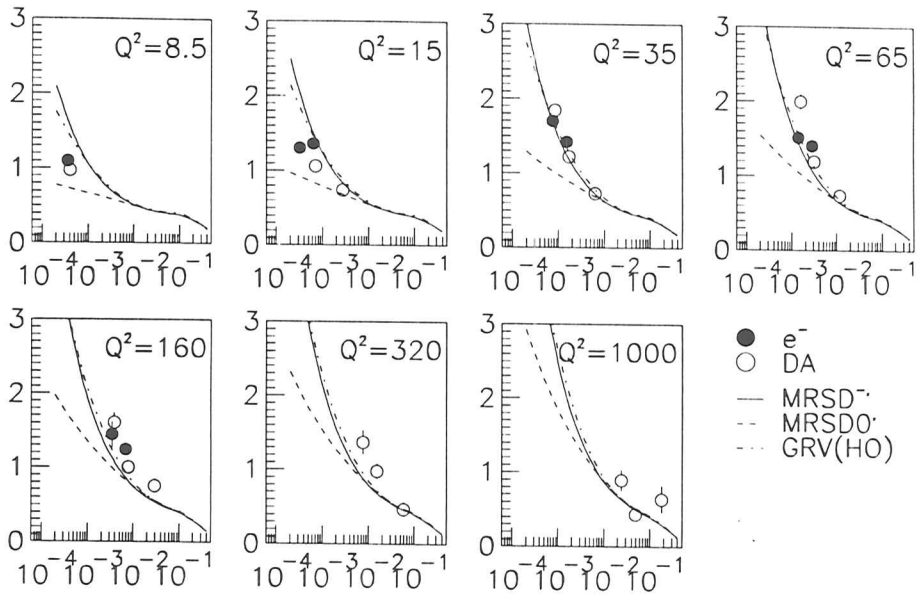

Figure 4.50: $F_2(x, Q^2)$ obtained via an iterative unfolding method in bins of (y, Q^2). The unfolding has been stopped after three (two) iterations for the electron-only (double-angle) reconstruction with $\chi^2_{\rm el}/{\rm ndf} = 0.9723$ and $\chi^2_{\rm DA}/{\rm ndf} = 0.9008$.

$A_i = s_i = T_{ii}$, and from eqn. (4.50) follows

$$N_i = \frac{M_i}{A_i}. \tag{4.69}$$

Insertion into the iteration prescription, (4.66), yields $N_i^{(n+1)} = N_i^{(n)}$, ie the iteration converges after one step as expected. Practically, a simple acceptance correction can be used whenever migrations are negligible, ie $A_i \cong s_i$, but will be insufficient in any other case.

If the MC input structure function equals the data, the correction factors, c_i (eqn. (4.41)), are the same for data and MC, and unfolding simplifies to

$$N_i = c_i M_i. \tag{4.70}$$

The iteration prescription, (4.66), becomes $N_i^{(n)} = c_i M_i$, again converging at first step.

Eqn. (4.70) does not require the transfer matrix to be diagonal, but on the contrary properly accounts for migrations. For practical purposes, however, it has to be noted that also events originating outside the observed phase space can migrate and thus contribute to the measured region, hence eqn. (4.70) can be applied safely only if the equality of data and MC structure

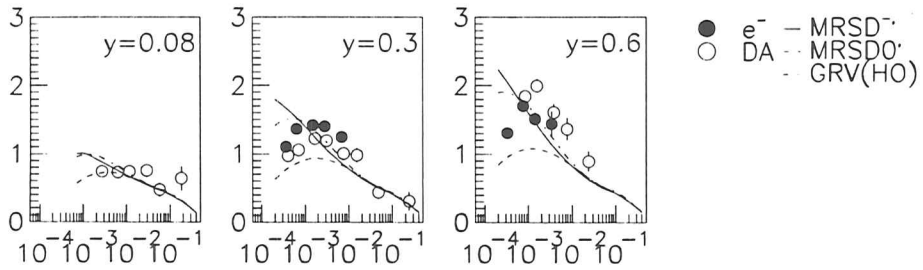

Figure 4.51: $F_2(x, y)$ obtained via an iterative unfolding method in bins of (y, Q^2)

functions is guaranteed even beyond the actual range of measurements, or if migrations from those regions can been excluded.

The equality of a simulated and an observed structure function can be established only after the measurement has been analyzed. Thus eqn. (4.70) seems especially unsuitable if previously unexplored regions of phase space are probed. For this reason, the factor method is not investigated in this thesis, even though the CTEQ-2D˙ and the unpublished MRS(H) parton parameterizations are in good agreement with the observed data. Generally, the inappropriate use of factor methods biases the result towards the MC input (eg [Blo84]).

Weakly Correlated Bins.

The previous section presented the proton structure function as obtained in weakly correlated bins from different reconstruction and unfolding methods. Figs. 4.52 and 4.53 show a bin-by-bin comparison of the results for the binning in (x, Q^2) and (y, Q^2), respectively. Some of the bins are not accessible by all reconstruction methods and hence have less entries. Obviously, the mixed and the Σ method extend to the lowest values of y.

In both cases the results of the different analyses are statistically compatible. At low Q^2, some of the data points which were obtained by matrix inversion seem to be incompatible with their counterparts from the iterative unfolding, however those fluctuations are compensated for by a corresponding deviation into the other direction in an adjacent negatively-correlated bin. At high Q^2, the results agree within the errors (only statistical errors are shown).

The analysis in bins of (y, Q^2) covers a larger phase space and yields significantly more bins than the analysis in bins of (x, Q^2). It reaches lower values of x and Q^2, provides a higher-x bin at high Q^2, and generally extends to lower y. At first glance, both analyses seem to be of similar quality regarding bin-by-bin fluctuations of the result. It has to be noted, however, that both analyses are presented in bins of (x, Q^2), whereas figs. 4.48 and 4.51 have shown before that the solution in (y, Q^2)-bins is smooth within each bin of y.

The results obtained by matrix inversion are stronger fluctuating than those from the iterative

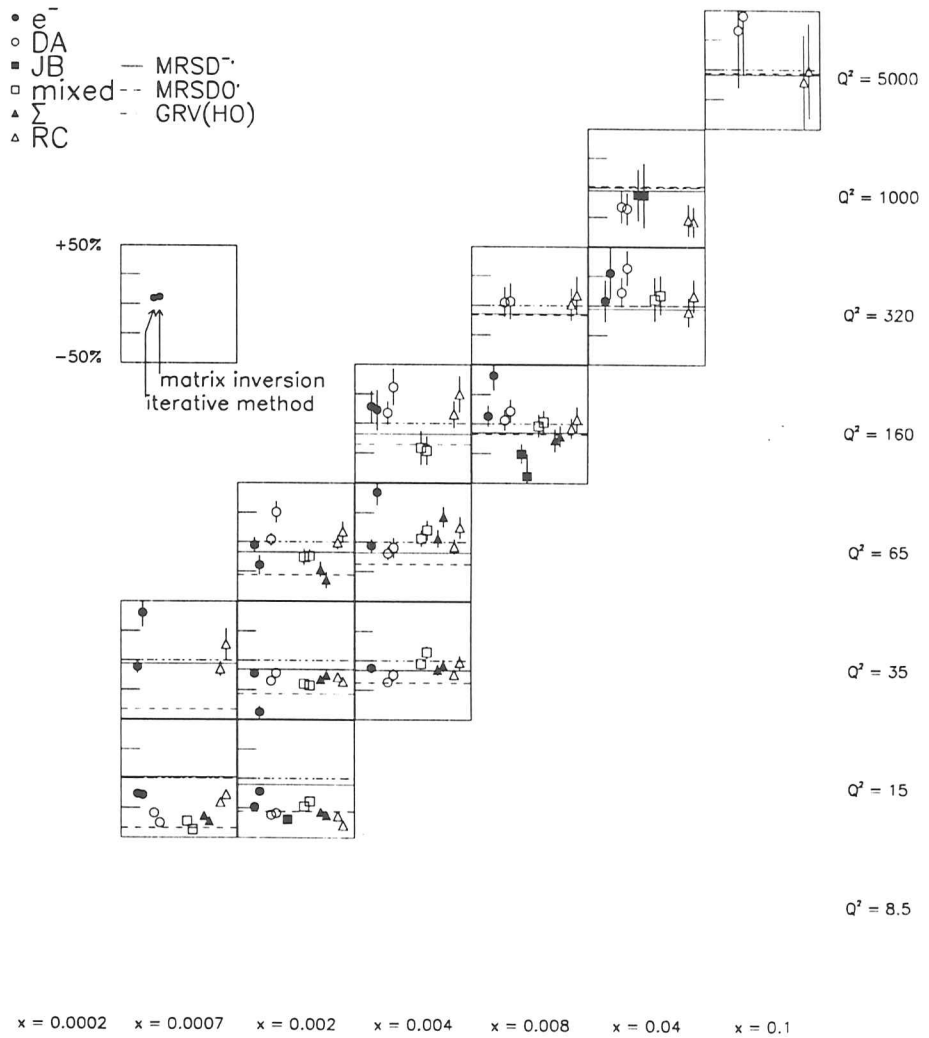

Figure 4.52: Comparison of $F_2(x, Q^2)$ from different reconstruction and unfolding methods. The data points show the deviation from the GRV parameterization. Only statistical uncertainties are shown.

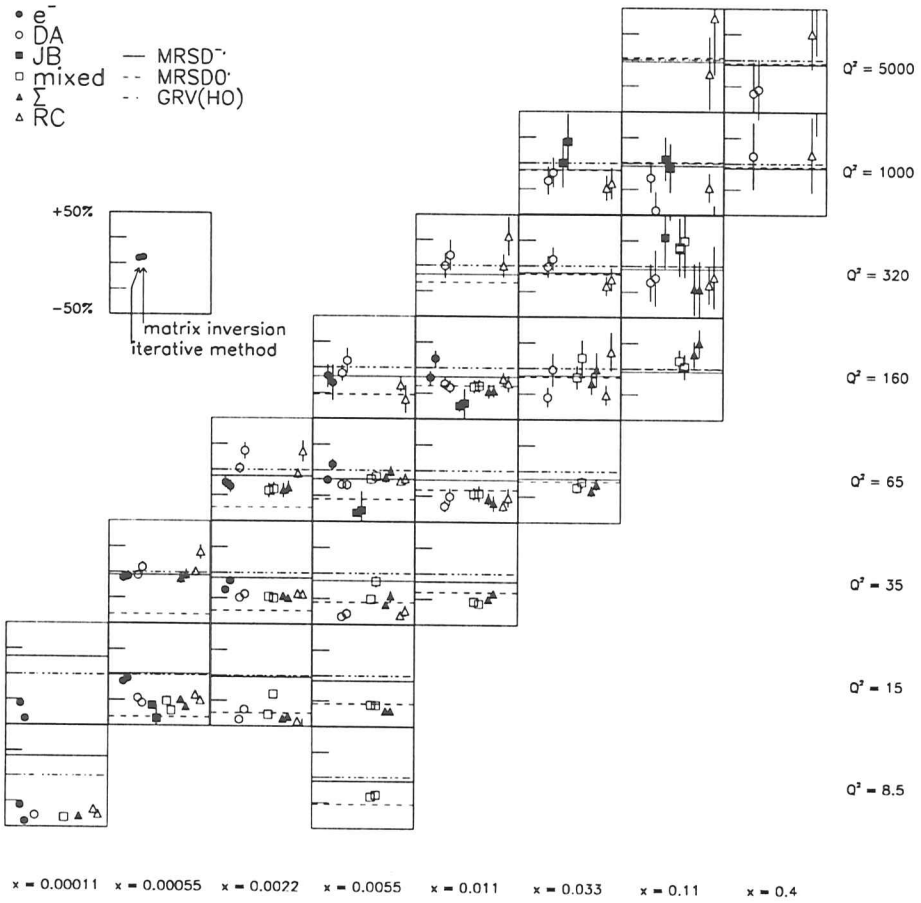

Figure 4.53: Comparison of $F_2(y, Q^2)$ from different reconstruction and unfolding methods. The data points show the deviation from the GRV parameterization. Only statistical uncertainties are shown.

method. This is due to the fact that the iteration procedure has not been stopped only after it converged, but rather when the χ^2 was already acceptable. The iteration procedure eventually transforms the (smooth) input distribution to the exact (and maybe fluctuating) unfolded solution; thus stopping the iteration before convergence has been obtained can be interpreted as still incorporating properties (eg smoothness) of the MC input distribution.

Fluctuating solutions have to be analyzed using the correlation matrix or have to be avoided by further increasing the bin size. On the other hand, it seems plausible for a "physical" structure

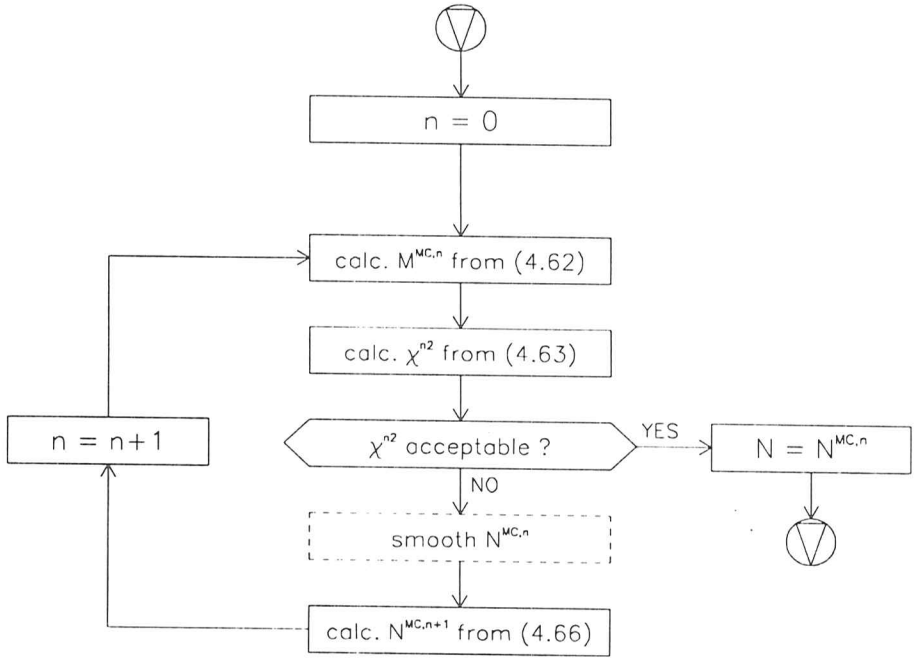

Figure 4.54: Flow chart for iterative unfolding procedures. The optional smoothing can be used to suppress fluctuations in the unfolded distribution (cf text).

function to be smooth, and for bins to be of the size of the detector resolution. Stopping an iterative unfolding before fluctuations start dominating the result can yield a solution which has those properties. The effect can be pronounced by "smoothing" the input distribution before each iteration. In any case the validity of the solution has to be ensured by its χ^2/dof being of $\mathcal{O}(1)$.

Fig. 4.54 shows a flow chart for iterative unfolding with optional smoothing. Smoothing involves fitting the distribution to a theoretical expression (eg [Ben94, d'A94b]), thus the unfolded distribution becomes in fact a theoretical curve smeared with the statistical fluctuations of the measurement, and it has to be checked from the absolute value of the χ^2 whether the expression chosen for the fit is adequate to describe the data. Another caveat lies in bins with low statistics: as those bins give only small contributions to the total χ^2, it has to be made sure that physics signals occuring in those bins are not "smoothed away".

For the above reasons, smoothing algorithms are not used in this thesis. Fluctuations are controlled by the entropy criteria for stopping the iterative unfolding.

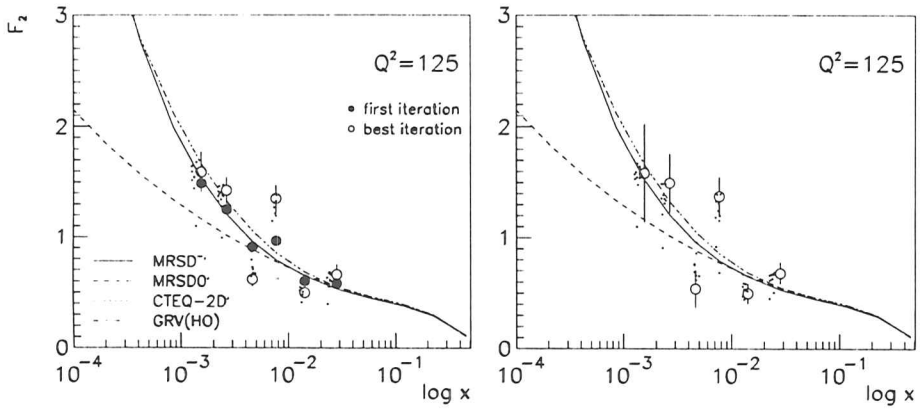

Figure 4.55: Example for unfolding the structure function in correlated bins. The left plot shows unfolding by an iterative method. The initial solution is smooth and picks up oscillations as the iteration continues. It converges to the solution obtained by matrix inversion (right), although it underestimates the statistical uncertainties.

Bins According to Detector Resolution.

If the bin size is reduced, migrations increase and the correlations between the bins grow, leading to even more fluctuating results. An example for an analysis where the data was binned according to the detector resolution[17] is shown in fig. 4.55, which compares structure functions from the electron-only method which were unfolded iteratively and by matrix inversion, respectively.

The plots show how the iterative method method (left) picks up fluctuations while converging towards the result from matrix inversion (right). The initial χ^2 is 2.9938/dof. After one iteration (black dots on the left plot), the solution is still smooth, and χ^2 = 1.1863/dof is already acceptable. After convergence (open circles, left plot), the solution is wildly oscillating with χ^2 = 0.2518/dof. Both methods finally yield the same result, although the iterative method tends to underestimate the statistical uncertainties.

4.6 Determination of F2

This section describes how the structure function is extracted from the unfolded event distribution. First, formulae are specified which relate the structure function to observed quantities. Then the analysis software which implements the extraction is briefly discussed, and a coarse data model is used to identify and quantify the systematic uncertainties of the method.

[17] The analysis is described in the next chapter. The bins were chosen according to [ZEU95c].

4.6.1 Formulae

Two different approaches have been developed to extract the structure function from the measured event distribution. The first approach determines for each bin the observed cross-section and then isolates the structure function by explicitly removing the contributions from F_L, F_3 and QED radiation. The second approach uses the unfolded event distribution to reweight the MC input distribution. F_L, F_3 and radiative corrections are thus performed implicitly as they were included in the MC simulation, ie are covered by the generated distribution.

The differential cross section for NC DIS has been given in eqn. (2.38). It can be separated into contributions from F_2, F_L and Z exchange.

$$\frac{d^2\sigma}{dxdQ^2} =: \tilde{\sigma} = \sigma(F_2) + \sigma(F_L) + \sigma(F_3) \tag{4.71}$$

$$= \frac{2\pi\alpha^2}{xQ^4} Y_+ \left(F_2 - \frac{y^2}{Y_+} F_L + \frac{Y_-}{Y_+} xF_3 \right). \tag{4.72}$$

$$Y_\pm = 1 \pm (1-y)^2. \tag{4.73}$$

The tilde (~) indicates that the cross section is directly related to the measured event distribution,

$$\tilde{\sigma} = \frac{N}{\mathcal{L}A}. \tag{4.74}$$

where $\mathcal{L}$ is the integrated luminosity of the data sample, and A is the acceptance[18]. An observed structure function $\tilde{F}_2$ is defined by

$$\tilde{F}_2 = \frac{xQ^4}{2\pi\alpha^2} \frac{1}{Y_+} \tilde{\sigma}. \tag{4.75}$$

F_2 can be derived from the observed structure function $\tilde{F}_2$ via

$$\tilde{F}_2 = F_2 (1 - \delta_{F_L} + \delta_Z)(1 + \delta_{\rm RC})(1 + \delta_{\rm bin}). \tag{4.76}$$

The δ_i are correction factors which separate the contributions due to F_L, Z-exchange, QED radiation, and bin centering.

δ_{F_L} and δ_Z are obtained from comparison of eqns. (4.72) and (4.75), by integrating the corresponding cross sections over the bin, ie

$$\delta_{F_L} = \frac{\sigma(F_L)}{\sigma(F_2)}. \tag{4.77}$$

$$\delta_Z = \frac{\sigma(F_3)}{\sigma(F_2)}. \tag{4.78}$$

where

$$\sigma(F_2) = \int\int_{\rm bin} dxdQ^2 \, \frac{2\pi\alpha^2}{xQ^4} Y_+ F_2(x, Q^2). \tag{4.79}$$

[18] If the transfer matrix has been constructed as described above, the acceptance has already been corrected for with the unfolding and A has to be set to one.

$$\sigma(F_L) = \int\int_{\text{bin}} dxdQ^2 \frac{2\pi\alpha^2}{xQ^4} Y_+ \frac{y^2}{Y_+} F_L(x,Q^2). \quad (4.80)$$

$$\sigma(F_3) = \int\int_{\text{bin}} dxdQ^2 \frac{2\pi\alpha^2}{xQ^4} Y_+ \frac{Y_-}{Y_+} F_3(x,Q^2). \quad (4.81)$$

Neither F_L nor F_3 have been measured in the HERA regime so far, hence both correction factors have to be determined theoretically. F_L can be separated into three terms which arise from QCD effects, target mass corrections and higher-twist contributions. The latter two terms can be ignored for this analysis since they decrease as Q^2 increases and are negligible in the Q^2 region which contributes to the measurement [ZEU93f]. The QCD contribution to F_L is [Rob90]

$$F_L^{\text{QCD}}(x,Q^2) = \frac{4\alpha_s}{3\pi}x^2\int_x^1 \frac{d\xi}{\xi^3}F_2(\xi,Q^2) + \frac{2\alpha_s}{\pi}\sum_f e_f^2 x^2 \int_x^1 \frac{d\xi}{\xi}\left(1-\frac{x}{\xi}\right)\xi g(\xi,Q^2). \quad (4.82)$$

F_3 can be calculated from eqn. (2.53).

δ_{RC} is the correction due to QED radiation which has been discussed in section 4.4.3.

$$\delta_{\text{RC}} = \frac{\tilde{\sigma}}{\sigma_{\text{Born}}} - 1. \quad (4.83)$$

and δ_{bin} arises since the center of gravity of the data in a bin, $(x_{\text{meas}}, Q^2_{\text{meas}})$, differs from the central value of the bin, $(x_{\text{ctr}}, Q^2_{\text{ctr}})$, at which F_2 is extracted,

$$\delta_{\text{bin}} = \frac{\sigma(x_{\text{ctr}}, Q^2_{\text{ctr}})}{<\sigma(x,Q^2)>_{\text{bin}}} - 1. \quad (4.84)$$

For this thesis, the correction factors are computed from the MRSD-' set of PDFs.

Instead of computing all the individual correction factors, the structure function can be obtained by reweighting the MC input structure function with the unfolded distribution of measured events,

$$F_2(x,Q^2) = \frac{N^{\text{data}}/\mathcal{L}^{\text{data}}}{N^{\text{MC}}/\mathcal{L}^{\text{MC}}} F_2^{\text{MC}}(x,Q^2). \quad (4.85)$$

The different corrections are now hidden in the generated distribution, N^{MC}. This can be seen by inserting eqn. (4.74) into (4.85) and then expanding the cross sections using (4.76).

$$F_2(x,Q^2) = \frac{\tilde{\sigma}}{\sigma^{\text{MC}}} F_2^{\text{MC}} \quad (4.86)$$

$$= \frac{\frac{2\pi\alpha^2}{xQ^4}Y_+ F_2 (1-\delta_{F_L}+\delta_Z)(1+\delta_{\text{RC}})(1+\delta_{\text{bin}})}{\frac{2\pi\alpha^2}{xQ^4}Y_+ F_2^{\text{MC}}\left(1-\delta_{F_L}^{\text{MC}}+\delta_Z^{\text{MC}}\right)(1+\delta_{\text{RC}}^{\text{MC}})(1+\delta_{\text{bin}}^{\text{MC}})} F_2^{\text{MC}}. \quad (4.87)$$

which solves for $\delta_i = \delta_i^{\text{MC}}$. As in the first approach, the correction factors are determined by the input set of PDFs, which again is MRSD-'.

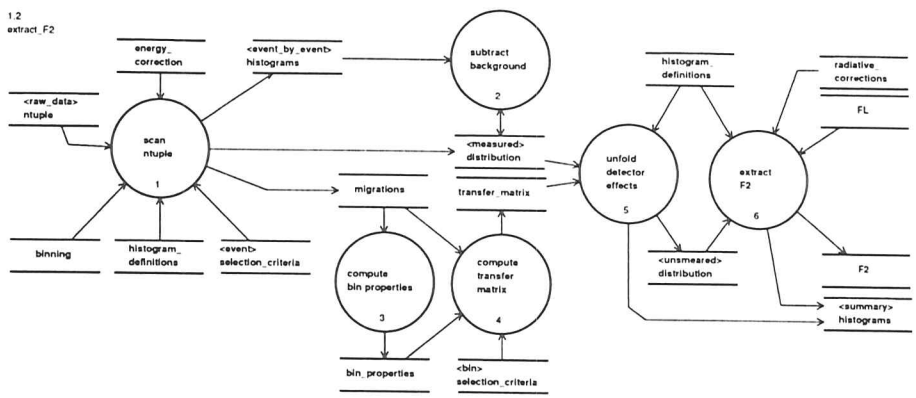

Figure 4.56: Analysis procedure for extracting F_2 (Data Flow Diagram, DFD). Double bars indicate data stores, bubbles symbolize processes which transform the data. Arrows define the data flow, ie the direction of processing.

4.6.2 Analysis Tools

A brief description of the analysis procedure suits to summarize the extraction of F_2 and identifies the systematic uncertainties of the analysis.

The data flow diagram (DFD[19]) 4.56 summarizes the extraction F_2. The double bars symbolize stores which hold the input, intermediate and output data, the bubbles identify the processes which transform the data according to the previous sections. The arrows define the data flow, ie the direction of processing. Stores which sit at the root of an arrow contain input data for the analysis and are thus sources of potential uncertainties. Stores at arrow tips contain results from processing and thus inherit the uncertainties of their predecessors. Sources of systematic uncertainties are identified from the data model in the next section.

Raw data from both experiment and MC simulation are stored in column-wise HBOOK ntuples [App92]. First, the ntuples are scanned (process .1). At this stage, the energy corrections are applied, the events are filtered and binned, the measured event distribution is accumulated, and the migrations are traced. A set of histograms is filled to validate the MC and accumulate different spectra.

After scanning, the δ-distributions are used to subtract photoproduction background from the measured event distribution (process .2). The migrations are evaluated to obtain the bin properties (process .3), and are used to construct the transfer matrix for the good bins (process .4). Obviously, process .2 is executed on the observed data only, while processes .3 and .4 apply only to the MC simulation.

[19] The diagram follows the notations of [HP87, You89]

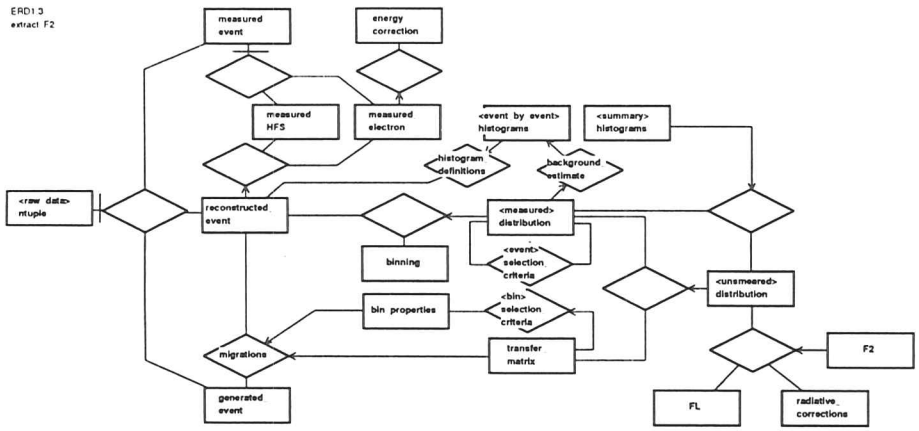

Figure 4.57: Data involved in extracting F_2 (Entity-Relationship Diagram, ERD). Boxes represent (factual) data objects, diamonds (dynamical) relationships among the data. Arrows can be read as "is derived from" (in reverse direction), orthogonal bars as "consists of".

Transfer matrix and measured distribution are needed to unfold the data (process .5), before finally the structure function can be extracted (process .6). Summary histograms are filled during the last two stages with contain the bin properties, the observed distributions, etc.

For this thesis, fig. 4.56 was implemented in a stand-alone C-program which is capable of reading HBOOK-ntuples and provides PAW-compatible output [App92, App93][20].

4.6.3 Systematic Uncertainties

Sources for Systematic Uncertainties.

Fig. 4.57 shows a coarse data model of the F_2 extraction procedure, which can be used to identify sources of systematic uncertainties. The figure is in the syntax of an entity-relationship diagram (ERD, cf eg [Fla81]).

Boxes symbolize data objects, which contain the factual data. Diamonds define relationships among objects, ie they are dynamically established. If establishing a relationship results in factual data, a so-called associative object is linked via an arrow to the relationship from which it originates. Thus the arrow can in reverse direction be interpreted as "is derived from".

[20]Unfortunately, physics analyses usually only agree on input and output data formats. From a software engineer's point of view, most of the above processes are of general purpose, and once they are organized properly, ie the customization (eg bin or histogram definitions, selection criteria) is moved to external tables, they could be re-usable if the data format of the intermediate data (event distributions, transfer matrix) were fixed.

parent object		impact on	determined by
generated events	.1	computation of migrations	statistics, input structure function
	.3	computation of bin properties	dto.
	.4	computation of transfer matrix	dto.
measured events	.1	computation of migrations	statistics, scales of primmicas, quant.
	.3	computation of bin properties	statistics, scales of primmicas, quant.
	.2	background subtraction	scales of primary measured quantities
	.5	unfolding	statistics
energy correction	.1	computation of migrations	applicability in E'_γ, θ
binning	.1	convergence of unfolding	bin size
	.6	bin center correction	input structure function
event selection criteria	.1	computation of migration	fiducial cuts against background
	.1	computation of acceptance	fiducial cuts for better resolution, electron identification.
F_L	.6	F_L correction	input structure function
radiative corrections	.6	correction for QED radiation	input structure function

Table 4.8: Sources of systematic uncertainties.

An example clarifies the definitions:

A generated event migrates to the position in phase space where it is reconstructed. Therefore, generated and reconstructed events are related via migrations (bottom left in fig. 4.57). Migrations have to be stored to derive the bin properties and the transfer matrix, which are therefore both associative objects to the migrations. The bin properties are (dynamically) matched to the bin selection criteria, and only good bins are considered in the transfer matrix. In this sense, the transfer matrix is also derived from the bin selection criteria, which at the same time specify the relation between the bin properties and the transfer matrix.

The benefit of an ERD is that it identifies the dependencies of the different data objects, and therefore — since associative objects inherit their properties from their "parent" objects — an ERD allows to trace back any possible uncertainty in a result to objects which appear only in the rôle of a parent. This can be illustrated with the same example as before:

The unfolded distribution will only be correct if the transfer matrix is correct. The elements of the transfer matrix are constructed from the accumulated migrations, which are calculated from the generated and the reconstructed events. Generated events are only parent object and thus are a possible source for errors in the transfer matrix. The reconstructed event depends on the measured[21] event and the energy corrections, which both are also parents only. Therefore, any problem with the transfer matrix is either due to problems with the generated events (limited statistics, input model dependence), with the measured events (invalid simulation of the measured quantities), or with the energy corrections (applied outside valid range).

Fig. 4.57 contains a total of seven parent-only objects: the generated events, the measured events, the energy corrections, the binning, the event selection criteria, the longitudinal structure function, and the radiative corrections. The impact of these objects on the analysis and

[21]in this case MC simulated

purpose	quantity	nominal	variation
suppress γp background	y_{el}	< 0.95	< 0.90
	δ	$35\text{GeV} < \delta < 60\text{GeV}$	$32\text{GeV} < \delta < 60\text{GeV}$,
			$40\text{GeV} < \delta < 60\text{GeV}$
validity of E'_e correction	E'_e	el: $> 8\text{GeV}$	$> 10\text{GeV}$
		DA: $> 5\text{GeV}$	$> 10\text{GeV}$, $> 8\text{GeV}$
containment of DIS electron	$\lvert x_{\text{CAL}}, y_{\text{CAL}}\rvert$	$> 16\text{cm}$	$> 14\text{cm}$, $> 18\text{cm}$
reliable vertex measurement	z_{Vertex}	el: $\pm 20\text{cm}$	$\pm 20\text{cm}$
improve γ_h resolution	y_{JB}	> 0.04	> 0.03, > 0.05

Table 4.9: Systematic checks performed to estimate the sensitivity of the analysis to the fiducial selection cuts. The table lists the purpose of the cuts, the quantity on which the cut is performed, the nominal cut parameters, and the range in which the parameters have been varied (cf text).

the input parameters which determine the properties of each of object are identified in table 4.8. The sensitivity of the analysis to the choice of these input parameters is briefly investigated in the following sections.

Fiducial Selection Cuts.

Selection cuts are applied to suppress background events, to improve the kinematic resolution, or to ensure the validity of the energy corrections. The sensitivity of the analysis to the choice of a specific cut parameter is checked by varying the parameter and then repeating the analysis.

To estimate the total uncertainty arising from the selection cuts, the cuts are grouped according to their purpose. For each group, the maximum increase and decrease of the structure function is identified which is due to a variation of one of the cuts of the group. The maximum deviations are then added in quadrature to give upper and lower limits for the resulting structure function.

Table 4.9 lists which cuts have been varied in what range and how they were grouped. Varying the cuts against γp background is the dominant uncertainty and can amount to changes in the structure function of up to 20% in the highest-y bins; in the other bins, however, the effect is of $\mathcal{O}(10\%)$ at low values Q^2, decreasing to the percent level above Q^2 of $65\,\text{GeV}^2$. If the selection cut on E'_e is raised, the structure function is lowered by a few percent, however this effect might also be due to the reduced statistics and deteriorating bin properties in the low y bins as a cut in E'_e is similar to a cut on y in this region (cf fig. 4.12).

Modification of the box cut effects F_2 at the few percent level, similar to the stricter vertex requirement. Both modifications do not introduce a systematic shift of the structure function. Lowering the cut on y_{JB} increases F_2 by up to 50% in the lowest-y at high Q^2, while raising the cut has no observable effect on F_2.

Generally, tightening or loosing the cuts leads to a small increase or decrease of F_2 in the region of phase space which is touched by the cut. Tables listing the variations in F_2 due to

the different variations are listed in the appendix.

Uncertainties in the MC Simulation.

The MC simulation of the experiment has been extensively discussed in a previous section, which verified that simulated and observed scales and spectra of the primary measured quantities agree to better than 1%.

In principle, the sensitivity of the analysis to the energy scales can be tested by imposing small scale shifts on either the data or the simulated events. For this analysis, however, effects of the MC simulation are not included to the systematic uncertainty because of excellent agreement between data and MC.

Dependence on the MC input structure function.

The MC calculations required for this analysis — bin properties, transfer matrix, correction factors — have been performed using the MRSD-' set of PDFs. The MRSD-' parameterization agrees with the data above $Q^2 \cong 25\,\text{GeV}^2$, but overshoots the measurement at lower values of Q^2. Since in this region the data are bracketed by the MRSD-' and MRSD0' PDFs, the analysis has been repeated using MRSD0' partons to test the sensitivity of the analysis to the choice of the MC input structure function.

It has been argued (and can be directly verified) that the bin properties s and A and the transfer matrix are independent of the selected set of input PDFs[22], hence the dependence on the PDFs enters through the correction factors, δ_i. The uncertainty arising from the δ_i is estimated by

$$\Delta_{\text{MC}} = \frac{1-\delta^0_{F_L}+\delta^0_Z}{1-\delta^-_{F_L}+\delta^-_Z}\,\frac{1+\delta^0_{\text{RC}}}{1+\delta^-_{\text{RC}}}\,\frac{1+\delta^0_{\text{bin}}}{1+\delta^-_{\text{bin}}}. \tag{4.88}$$

where the superscripts ^{0} and $^-$ identify correction factors which are calculated from MRSD0' and MRSD-' partons, respectively.

Methodological Uncertainties.

The sources of systematic uncertainties which were identified from the ERD cover data quality aspects, but ignore possible inefficiencies of the analysis procedure itself.

The major steps in the analysis are identified in the data-flow diagram 4.56. The crucial analysis tools used in the different processing stages are the electron finder (process .1), fits to δ-distributions (process .2), and kinematic reconstruction and unfolding algorithms (process .5)[23].

[22] In principle they could also depend on the fragmentation model since the kinematic is reconstructed form parts of the hadronic final state (cf discussion below).

[23] Formally, the DFD has to be decomposed into a set of sub-diagrams which define the internal structure

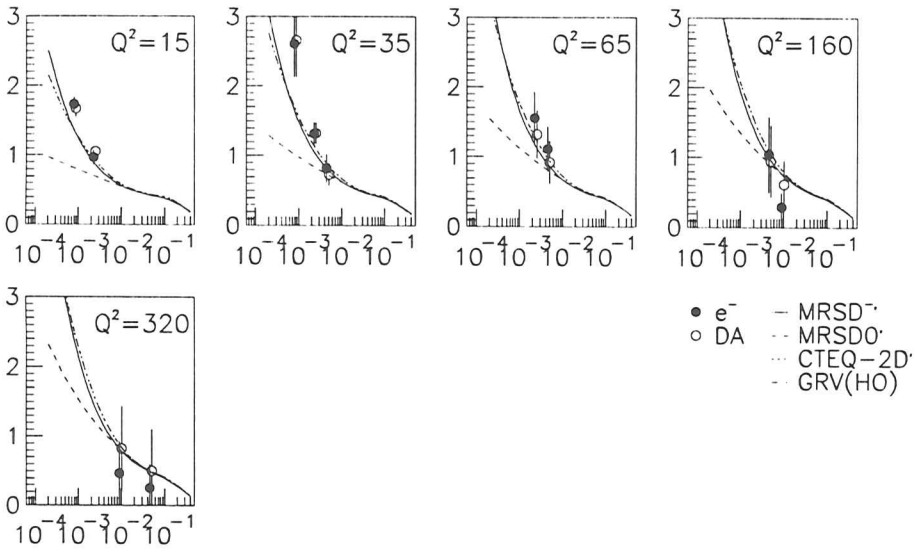

Figure 4.58: $F_2(x, Q^2)$ from LRG DIS events. The data points have been divided by r, the ration of LRG events in the DIS sample (cf text).

The sensitivity of the structure function to the different analysis tools is checked by replacing individual tools by equivalent algorithms. However, since replacing one analysis tool by another affects the correlations among the bins, it seems unfair to perform a bin-by-bin comparison of the resulting structure functions. It has therefore only been checked that the results are statistically compatible, but observed variations in the structure function are not included in the estimate of the systematic uncertainty.

The different electron finding algorithms which are available were introduced in sect. 4.2. They have been exchanged and were found to yield compatible results. The amount of γp-background in the remaining event sample has been cross-checked with a minimum-bias photoproduction MC. The effects of different reconstruction and unfolding procedures have been extensively discussed in the previous section.

4.6.4 Dependence on the Hadronic Final State

F and γ_h have been constructed with the aim that the reconstruction of kinematics from hadronic variables becomes insensitive to the fragmentation processes of the hadronic final state. The requirement is mandatory if detector acceptance and resolution corrections are determined from MC, and it has been verified that different MC samples produce similar transfer matrices [ZEU95c].

In an intuitive approach, the sensitivity of reconstruction and unfolding to the hadronic final state can be estimated directly from the data. The idea is to compare DIS events with a large rapidity gap (LRG) with normal DIS events. The two classes of events are markedly different in the hadronic final state. In an analysis limited to LRG DIS events, F_2 is extracted from electron-only and double-angle variables using the transfer matrix constructed from the CDMBGF MC sample. The transfer matrix for the electron variables should be valid without any restriction since the rapidity gap is a property of the hadronic system alone, and hence should not affect the simulation of the electron vertex. The DA transfer matrix, however, depends on the hadronic final state through the angle γ_h, hence the matrix from the CDMBGF is strictly not applicable. It will nevertheless reproduce the result obtained from the electron variables if γ_h is indeed insensitive to the fragmentation process.

LRG events have been selected from the DIS data sample by requiring $\eta_{\max} > 1.5$. The fraction of LRG events in the DIS sample, r, has been measured for events with $W_{\mathrm{DA}} > 140\,\mathrm{GeV}$ and $Q^2_{\mathrm{DA}} > 10\,\mathrm{GeV}^2$ in three bins of x [ZEU94c].

The structure function which is obtained from the LRG DIS events, F_2^{LRG}, is shown in fig. 4.58. To guide the eye, the data points have been scaled up by the ratio r from [ZEU94c] and are overlayed with the usual F_2^p parameterizations. The figure shows that the data points obtained from electron-only and double angle reconstruction agree within the statistical uncertainty, hence γ_h is indeed independent of the properties of the hadronic final state.

of each of its processes. This procedure of decomposition is repeated until the processes on the lowest level diagrams correspond to simple algorithms which can be implemented as such. The lowest level set of diagrams allows to distinguish I/O and data formatting processes from data transforming or filtering processes, the latter of which are sources for methodological uncertainties.

Chapter 5

Results

This it is
and nothing more.
Edgar Allan Poe, *The Raven*

This section presents the structure functions which were obtained from the different analyses which were introduced in the previous section. The structure function has been measured in two different sets of bins: first, it has been extracted in the weakly correlated bins which were defined in section 4.5.1, then an analysis has been performed in narrower bins, which have been used in [ZEU95c]. The detailed listings of the results obtained from the electron-only and the double-angle reconstruction methods can be found in the appendix.

5.1 Weakly Correlated Bins

The extraction of $F_2(x, Q^2)$ in weakly correlated bins has been extensively discussed in the previous section. Figs. 5.1 and 5.2 show the results for the analyses where the data was binned in (x, Q^2) and (y, Q^2), respectively. The systematic uncertainties were added in quadrature to the statistical uncertainties, which are shown as the inner error bars on the plots.

It has been argued before that the structure function shows fluctuating behaviour when plotted against x. Plotting F_2 for fixed Q^2 or fixed y, however, yields smooth solutions for bins of (x, Q^2) or (y, Q^2), as the fluctuations are common to the entire bin (figs. 5.1-5.4).

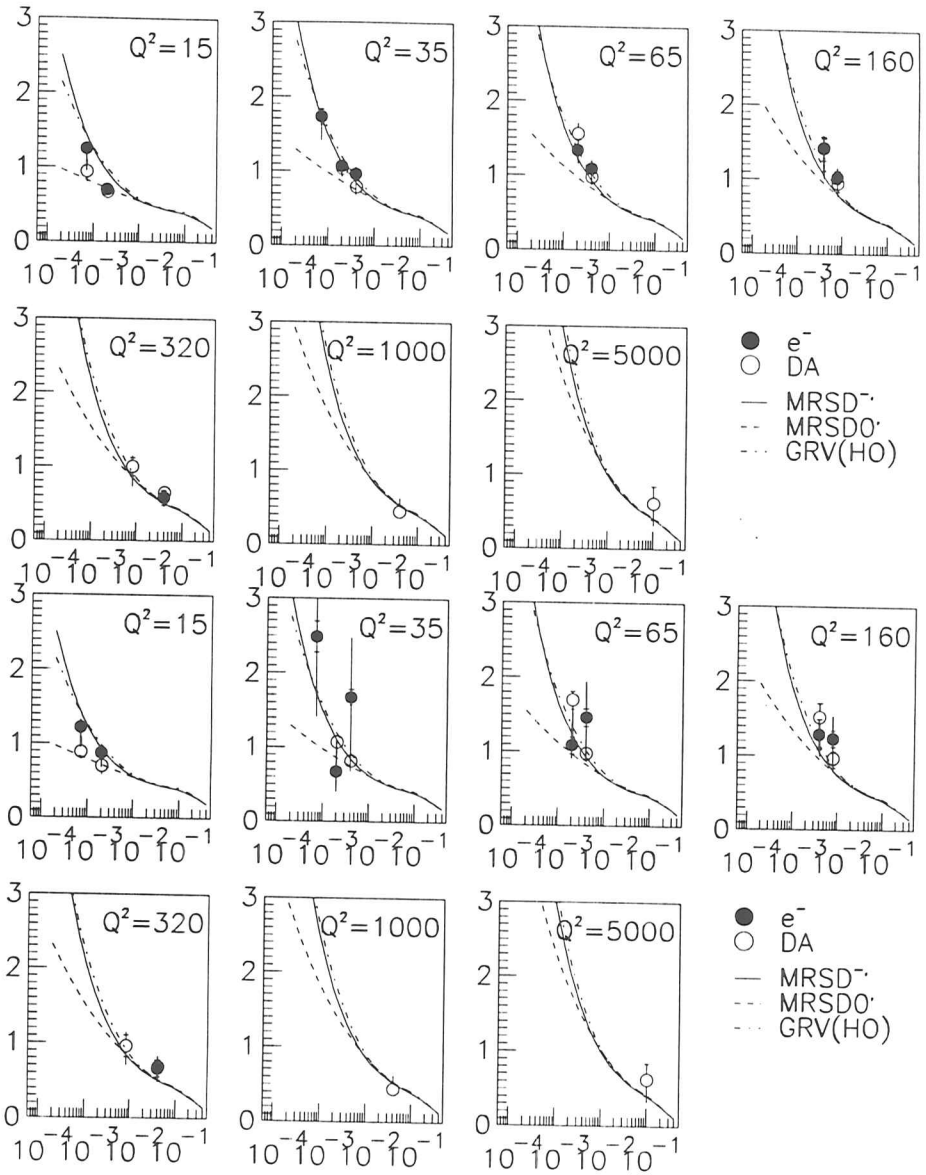

Figure 5.1: $F_2(x, Q^2)$ in weakly correlated bins. The error bars show statistical and systematic uncertainties added in quadrature. The inner errors are the statistical uncertainties only. The data was binned in (x, Q^2) and has been unfolded iteratively (top) and via matrix inversion (bottom).

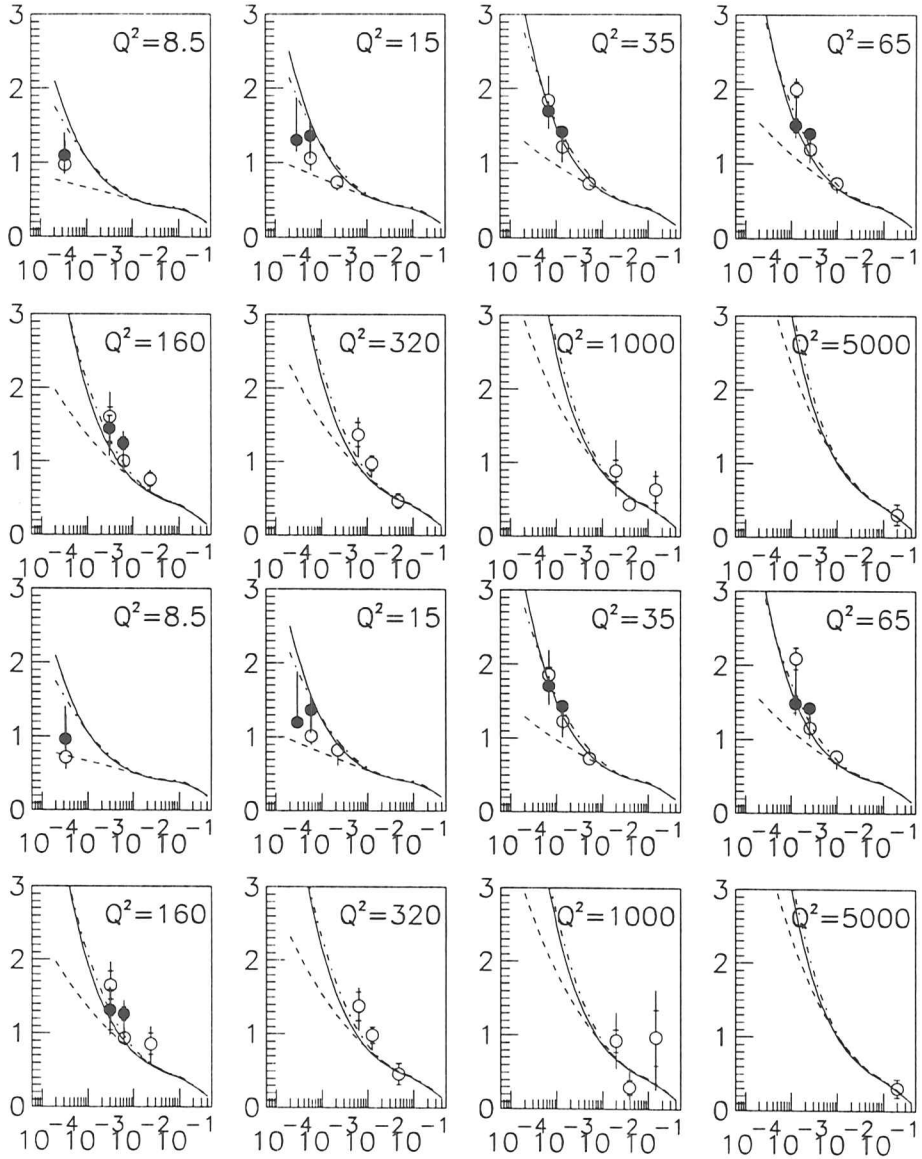

Figure 5.2: $F_2(x, Q^2)$ in weakly correlated bins. The error bars show statistical and systematic uncertainties added in quadrature. The inner errors are the statistical uncertainties only. The data was binned in (y, Q^2) and has been unfolded iteratively (top) and via matrix inversion (bottom).The symbols are the same as those in the previous figure.

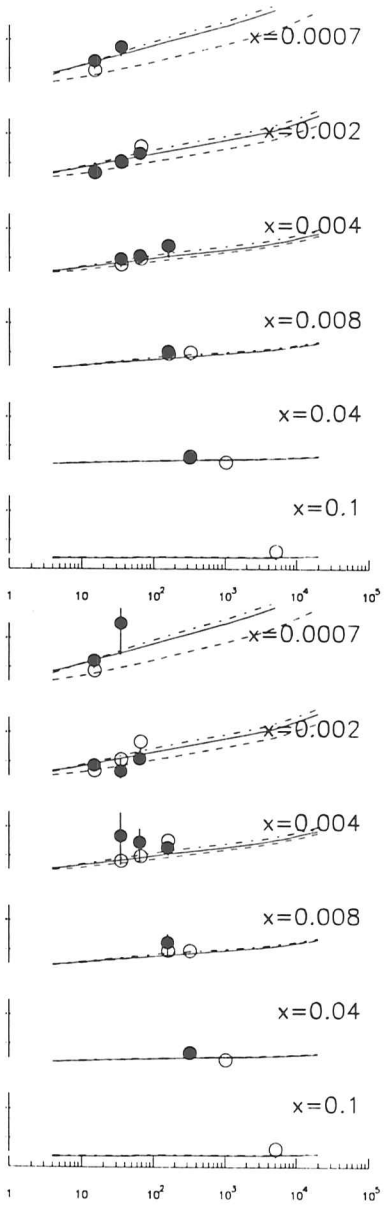

Figure 5.3: $F_2(x, Q^2)$ in weakly correlated bins. The error bars show statistical and systematic uncertainties added in quadrature. The inner errors are the statistical uncertainties only. The data was binned in (y, Q^2) and has been unfolded iteratively (top) and via matrix inversion (bottom). The symbols are similar to the previous figures.

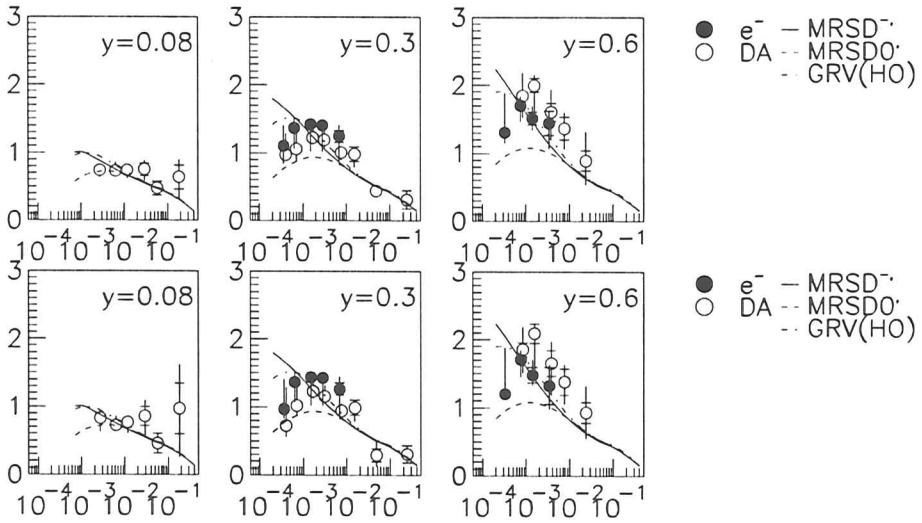

Figure 5.4: $F_2(x, Q^2)$ in weakly correlated bins. The error bars show statistical and systematic uncertainties added in quadrature. The inner errors are the statistical uncertainties only. The data was binned in (y, Q^2) and has been unfolded iteratively (top) and via matrix inversion (bottom).

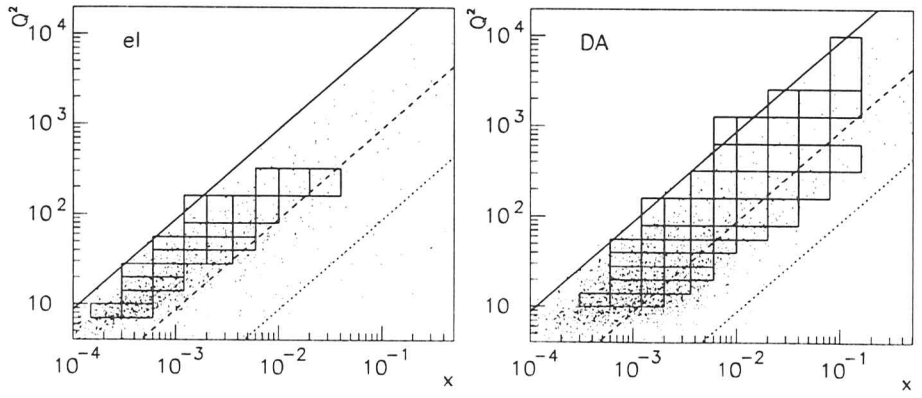

Figure 5.5: Bins in which F_2 has been extracted.

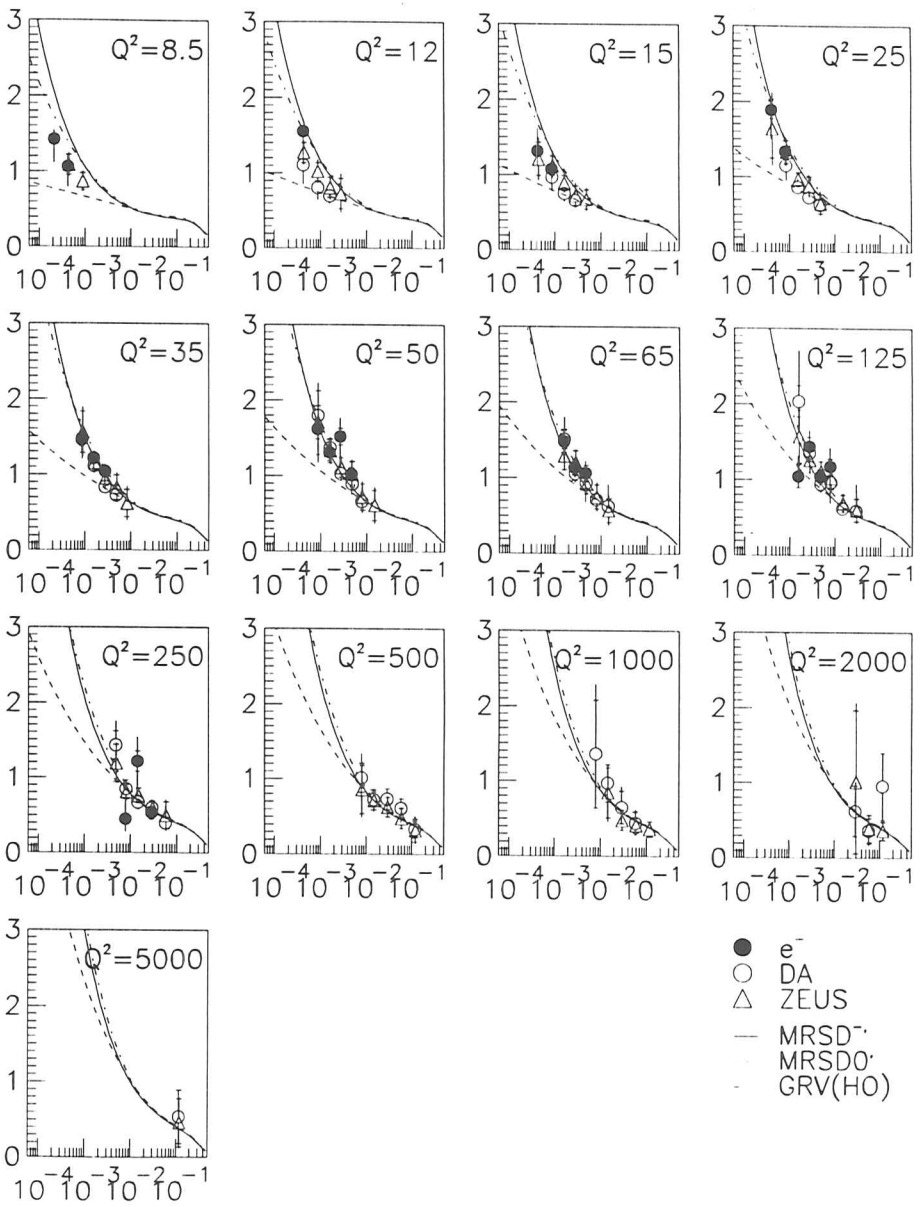

Figure 5.6: Results of an F_2 analysis performed in the (x, Q^2) bins which were chosen in [ZEU95c]. The data has been unfolded iteratively. The inner error bars show the statistical uncertainty, the full error bars show statistical and systematical uncertainty added in quadrature.

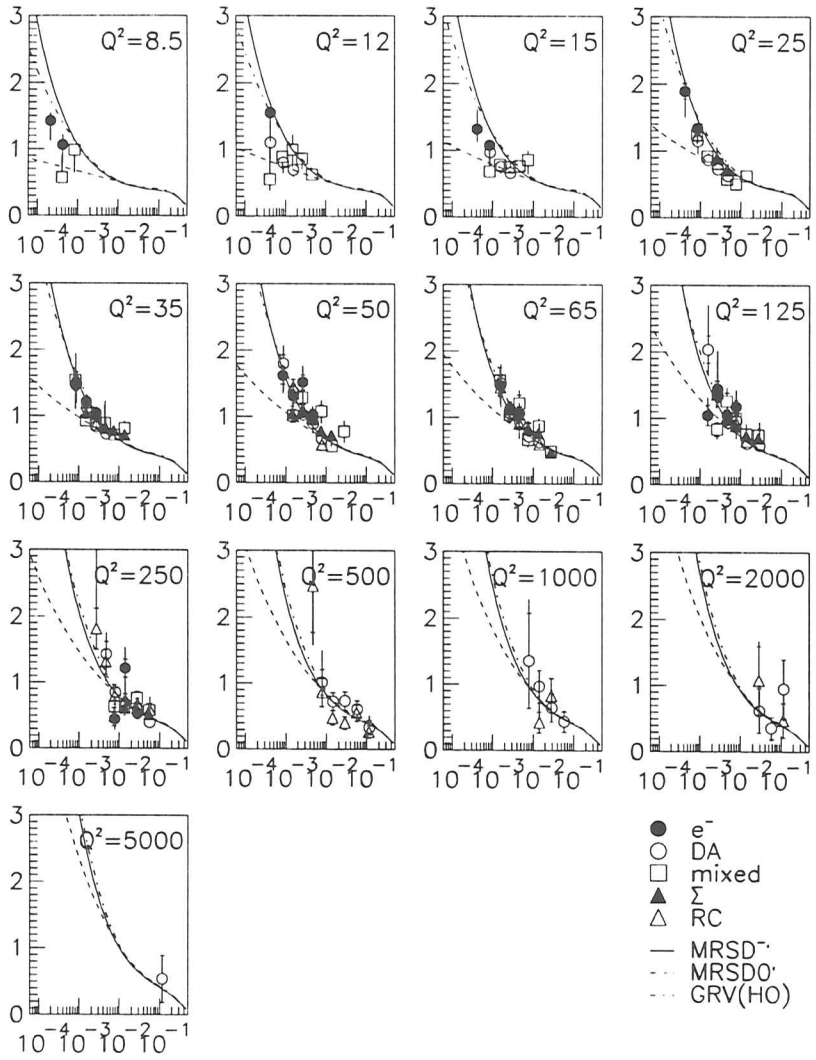

Figure 5.7: $F_2(x, Q^2)$ for all the reconstruction methods which were introduced in the previous chapter.

Reconst. Meth.	el	DA	JB	mixed	Σ	RC
χ^2/dof (initial)	2.8941	1.5029		3.7620	0.6882	1.0480
χ^2/dof (final)	1.7626	0.5968		1.0926	./.	./.

Table 5.1: χ^2/dof after the initial and the final iteration. The Σ method and the method insensitive to ISR converged after the initial iteration. The Jacquet-Blondel method has been removed from the analysis (cf text).

5.2 Bins According to Detector Resolution

5.2.1 Analysis in bins of x and Q^2

Fig. 5.5 shows the bins in which this analysis has been performed. The bins are defined in [ZEU95c] and are chosen such that the bin widths are of the order of the detector resolution. At high values of Q^2, the bins are larger to account for reduced statistics in this kinematic region.

The analysis described in the previous section has been repeated for the narrower bins. Solutions obtained via inversion of the transfer matrix are heavily fluctuating (cf fig. 4.55) and are no longer pursued. The result which is obtained from the iterative unfolding procedure is shown in fig. 5.6 for the electron-only and double-angle reconstruction methods, and in fig. 5.7 for all the reconstruction methods which were introduced in the previous chapter. It should be stressed again that no smoothing algorithm has been used.

All the analyses confirm the rise of the structure function towards the small-x region. The electron-only and double-angle analysis are in agreement with the published work of the ZEUS collaboration [ZEU95c] within the errors: The data points of the two analyses agree within the errors in the medium-Q^2 region, which is accessible to both reconstruction methods. Below, the electron-only method can reach lower values of x and Q^2 (ie higher values of y) than the double-angle method, and the data points obtained from the two methods are lining up.

The iteration procedure has been stopped after one ore two iterations, yielding values of χ^2/dof of $\mathcal{O}(1)$. Table 5.1 lists the values of the χ^2/dof for the first iteration and for the final result. After Jacquet-Blondel reconstruction, most of the bins had smearings $s = \mathcal{O}(0.13)$, thus the Jacquet-Blondel method has been removed from the analysis.

Fig. 5.8 plots the resulting structure function against Q^2 for fixed values of x. At high-x, the data is in agreement with the PDFs. In this region, the PDFs have been obtained from structure functions which were measured by pre-HERA experiments and have then been GLAP-evolved towards higher Q^2. At lower values of x, the PDFs disagree due to different assumptions on the x-evolution of the gluon density. The data clearly favour the parameterizations based on a Lipatov-like gluon distribution.

Reconstruction via the mixed method, the Σ method, or the radiatively corrected method can extend the accessible phase space in the medium-Q^2 region towards higher values of x, thus

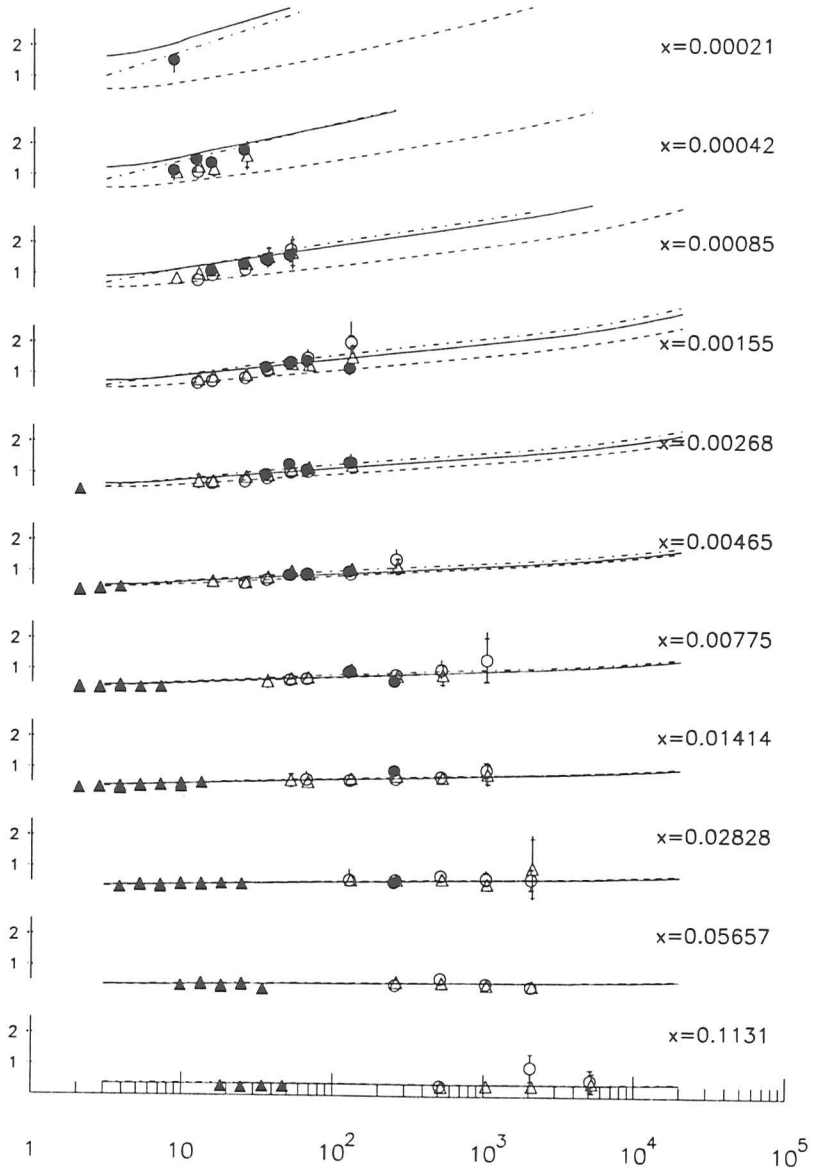

Figure 5.8: Same analysis as in fig. 5.6, plotted for fixed values of x. The open (closed) circles refer to the electron-only (double-angle) method, the open and closed triangles plot the data from ZEUS [ZEU95c] and the preliminary data from E665 [E6694] for comparison.

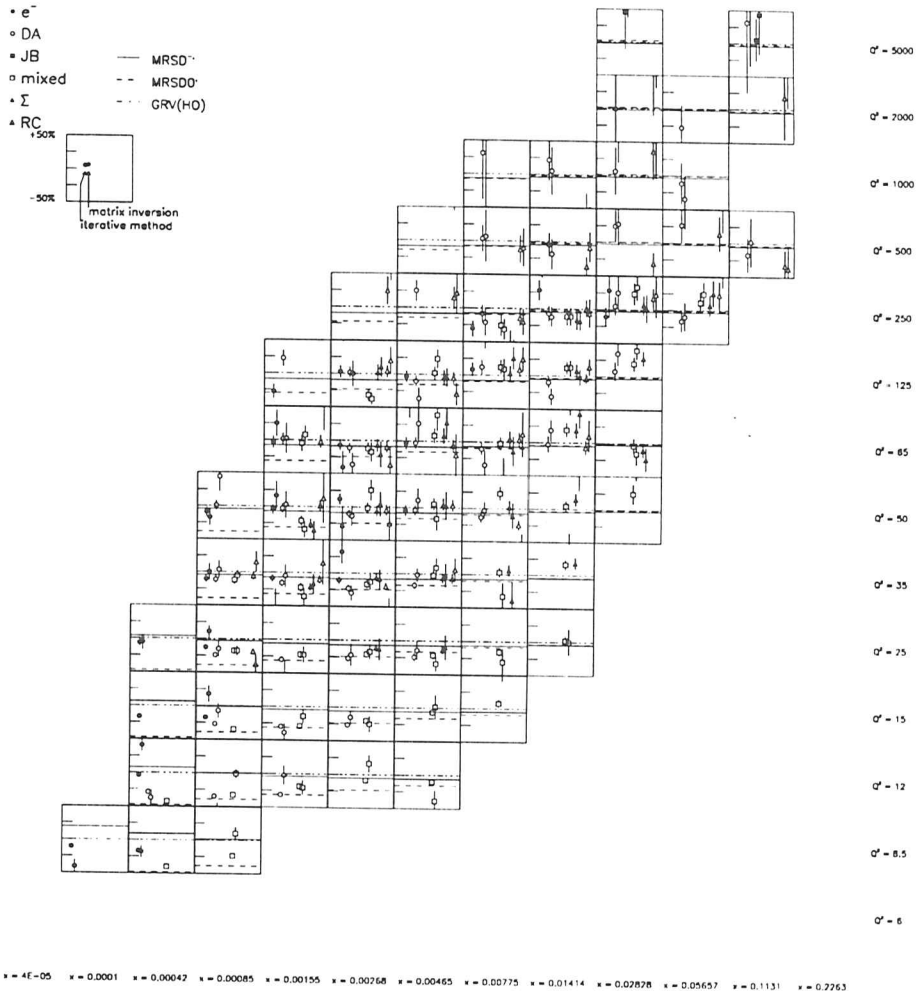

Figure 5.9: Bin-by-bin comparison of $F_2(x, Q^2)$ obtained from different reconstruction and unfolding methods in the bins of [ZEU95c].

connecting the ZEUS data with the pre-HERA experiments. This is emphasized by fig. 5.9, which repeats the bin-by-bin comparison which was already introduced for the weakly correlated bins (cf sect. 4.5.5). The figure shows that the central region of phase space is accessible to all reconstruction methods, and that all the methods yield similar results, while the asymptotic regions are measured by few methods: the mixed method can be seen to extend to the lowest values of y.

It should be noted that fig. 5.9 contains also the data points which were obtained by matrix inversion, although they are in several bins fluctuating out of the range of the ordinate.

Reconst. Meth.	el	DA	JB	mixed	Σ	RC
χ^2/dof (initial)	3.6466	1.7677		2.3104	0.9959	0.6576
χ^2/dof (final)	1.2289	0.8098		1.3739	./.	./.

Table 5.2: χ^2/dof after the initial and the final iteration. The Σ method and the method insensitive to ISR converged after the initial iteration. The Jacquet-Blondel method has been removed from the analysis for the same reasons as in the previous section.

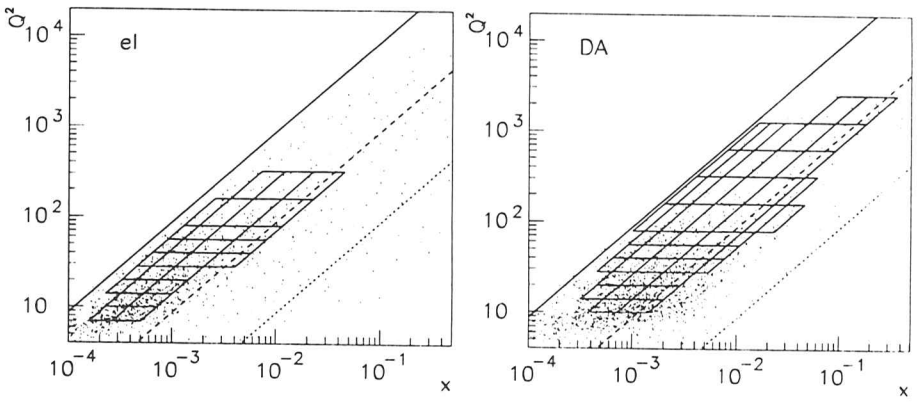

Figure 5.10: Bins in which F_2 has been extracted.

5.2.2 Analysis in bins of y and Q^2

It has been argued in the previous section that binning the data in (y, Q^2) reduces the correlations among the bins and thus yields both more data points and a smoother result as can be obtained from bins of (x, Q^2) of similar size. Furthermore, it has been pointed out in [BCF91] that it could be advantageous to extrapolate results from the region of phase space which has been probed by fixed target experiments to the region which is probed by HERA with a QCD evolution in y, which would require a structure function measurement in terms of y and Q^2.

Fig. 5.10 shows a binning scheme in y and Q^2, which has been used for a structure function extraction. The bins are chosen to be of similar size as the bins defined in [ZEU95c], which were used in the previous section.

Figs. 5.11 and 5.12 summarize the result for the electron-only and double-angle reconstruction method, and for all reconstruction methods used in this thesis, respectively. For the same reasons as before, only the iterative unfolding procedure was considered. The procedure stopped after one or two iterations with the χ^2/dof's listed in table 5.2. The result is qualitatively similar to that of the previous section, except for the electron-only method yielding some additional data points in the low-Q^2 region.

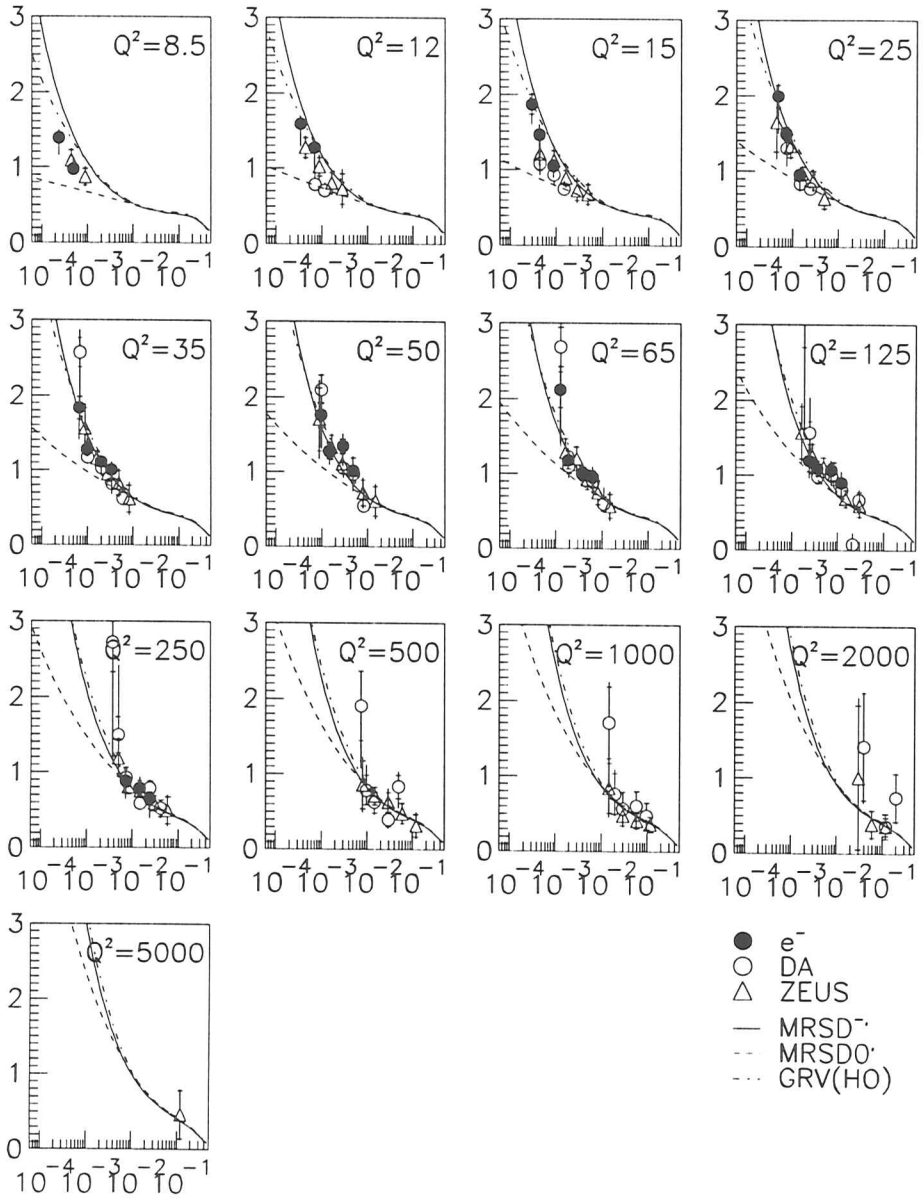

Figure 5.11: Results of an F_2 analysis performed in bins of y and Q. The bins were chosen to be of similar size as the (x, Q^2) bins defined in [ZEU95c]. The data has been unfolded iteratively.

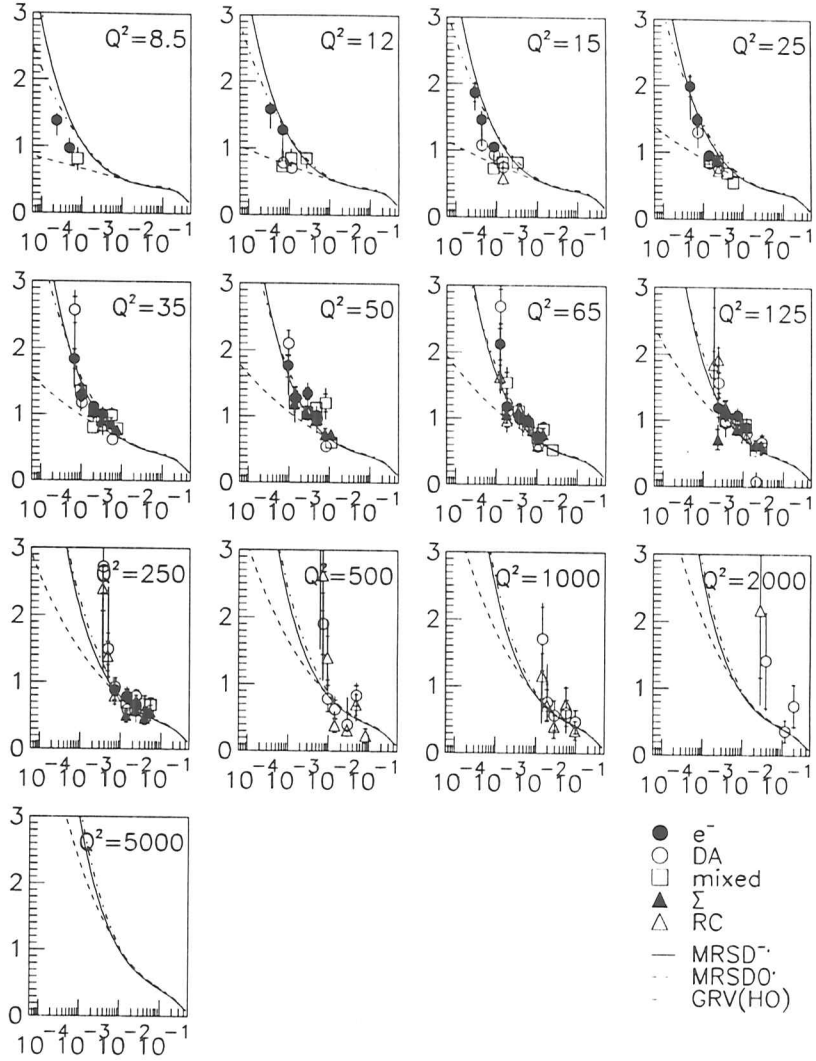

Figure 5.12: Comparison of the results obtained from different reconstruction methods. The data has been unfolded iteratively.

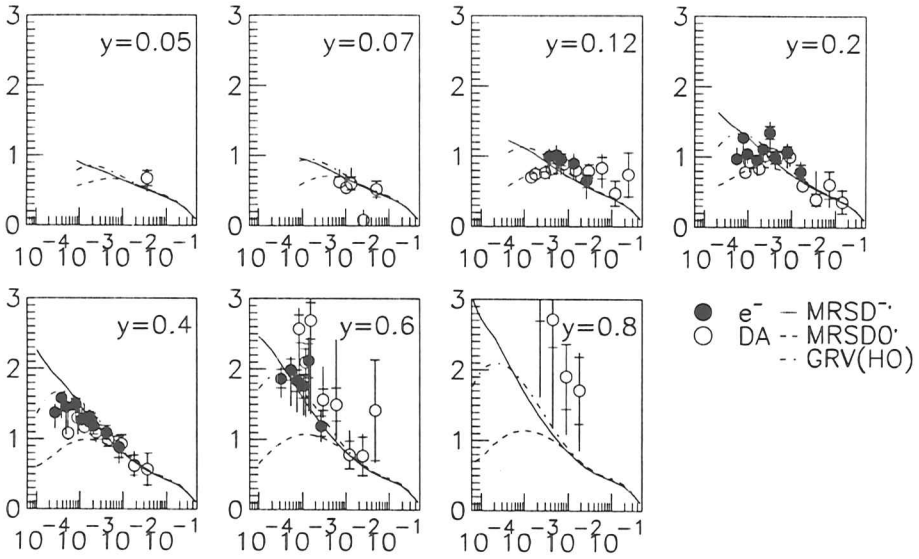

Figure 5.13: $F_2(x, y)$ plotted for fixed y after iterative unfolding.

Fig. 5.13 plots the structure function in bins of fixed y, as it would be required for comparison with a QCD evolution in y. The data points are lining up smoothly for both reconstruction methods, again clearly favouring the PDFs based on a Lipatov-like gluon distribution.

5.3 Connection to fixed target data

Fig. 5.9 has already shown that the mixed reconstruction method enables access to the lowest y bins. This becomes obvious when looking at the migration plots (fig. 4.34): for the Jacquet-Blondel method, the dominant drift in the low-y region is along lines of fixed y, while for the electron-only method migrations occur in the direction of fixed Q^2, and accordingly migration effects can be expected to be very small for kinematics obtained from y_{JB} and Q^2_{e}.

Fig. 5.14 shows the structure function as obtained from the mixed reconstruction method in comparison with the data from ZEUS [ZEU95c] and E665 [E6694]. It can be seen that the gap between the two experiments is accessible via mixed reconstruction.

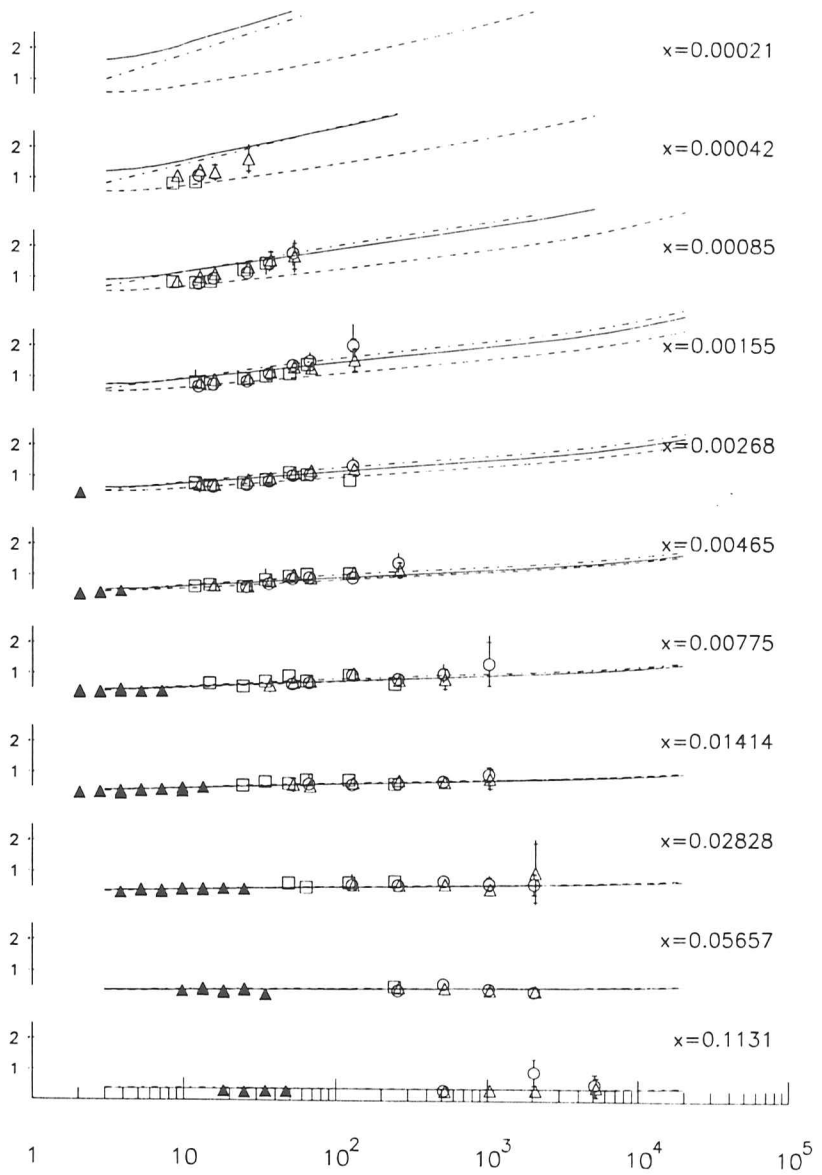

Figure 5.14: $F_2(x, Q^2)$ reconstructed from the mixed method (open squares) in comparison with the data from ZEUS (open triangles) and E665 (closed triangles).

Chapter 6

Conclusion

The structure function F_2 of the proton has been measured from the data which was taken during 1993 with the ZEUS experiment at HERA. Event kinematics have been reconstructed from the scattered electron only, the double-angle method, the Jacquet-Blondel method, a mixed method ($y_{\mathrm{JB}}, Q^2_{\mathrm{el}}$), the Σ-method, and from a method which corrects for initial state radiation. The data was binned in (x, Q^2) and (y, Q^2), and detector effects have been unfolded via inversion of the transfer matrix, and with an iterative method. The results from the different methods were compared with special focus on the electron-only and the double-angle reconstruction and are found to be in agreement. They confirm the rise of F_2 with decreasing x.

Different reconstruction methods provide access to different regions of the phase space, depending on the resolution and the migrations of the method. Reconstruction from the mixed method reaches the lowest values of y and allows to connect HERA measurements to the data obtained from pre-HERA fixed target experiments. For the electron-only reconstruction, bins in y and Q^2 are less correlated than bins in x and Q^2, thus yielding more data points and a smoother solution.

Both unfolding procedures obtained similar results if the bins were chosen to have a width of at least twice the detector resolution. If smaller bins are chosen, unfolding via matrix inversion introduces oscillations into the resulting structure function as adjacent bins become strongly negatively correlated. The solution from the iterative unfolding is generally smoother: the iterative procedure slowly adapts a smooth Monte Carlo input structure function to the measurement and is aborted as soon as the measurement is reproduced at an acceptable level.

The electron-only and the double-angle methods have been used to reconstruct events with a large rapidity gap. The events were then unfolded with a transfer matrix obtained from a CDM-BGF Monte Carlo. The results for both methods were in good agreement, which is taken as an evidence that the double-angle reconstruction is indeed independent of the properties of the hadronic final state.

Acknowledgement

I highly enjoyed being a member of the ZEUS collaboration for the past years, and I like to thank all my colleagues for the many stimulating discussions and the inspiring atmosphere they created.

I owe a special thanks to my supervisor, Prof. Dr. Erich Lohrmann, for offering me the opportunity to write this thesis, and for his guidance through the past years. I enjoyed the freedom he gave me to explore some of the many fields which are involved in setting up an experiment like ZEUS, and I benefited from his insisting at the right time that I should focus on this work again. He provided useful advice and ideas whenever asked for, and fascinating lectures on how to judge both science and scientists.

Another special thanks goes to Dr. Wolfgang Vogel, with whom I worked when constructing the Eventbuilder; he is responsible for my interest in and positive experience with Real-Time systems. It made work very interesting, but also a bit difficult, to be confronted daily with exciting projects going on next door.

Over the whole period I worked closely together with Dr. Ulf Behrens, Johannes Mainusch, and Kars Ohrenberg. I enjoyed their friendship and the open and spontaneous atmosphere in this group, which allowed to share frustrations as well as successes. It was an invaluable help to be able to discuss my work whenever I got stuck, and to discuss something other than my work when I got really stuck. Furthermore, Kars Ohrenberg allowed me to share his Ntuples, and thus prevented me from spoiling my education by being forced to finally learn Fortran.

Dr. Nikolai Pavel carefully read the second chapter of this thesis and provided many helpful comments and suggestions.

Finally, I like to thank all my friends who made sure that I did not get lost in the fundamental structures of nature, but also came to enjoy some of its beauties.

Appendix A

Tables

A.1 Weakly Correlated Bins

x	Q^2	$F2$ ±stat ±syst	$N_{\rm obs}$	$N_{\rm php}$	σ ±stat
0.00070	15	$1.252\pm0.024\pm^{0.061}_{0.296}$	8826	289	24.698±0.468
0.00200	15	$0.701\pm0.016\pm^{0.072}_{0.018}$	5753	0	17.154±0.380
0.00070	35	$1.731\pm0.106\pm^{0.039}_{0.308}$	747	17	3.842 ±0.235
0.00200	35	$1.069\pm0.032\pm^{0.020}_{0.138}$	3317	22	7.843 ±0.237
0.00400	35	$0.968\pm0.043\pm^{0.088}_{0.289}$	1436	0	4.696 ±0.208
0.00200	65	$1.341\pm0.082\pm^{0.030}_{0.108}$	767	11	2.353 ±0.145
0.00400	65	$1.090\pm0.067\pm^{0.092}_{0.205}$	832	0	1.899 ±0.116
0.00400	160	$1.420\pm0.160\pm^{0.085}_{0.285}$	202	0	1.251 ±0.141
0.00800	160	$1.035\pm0.087\pm^{0.094}_{0.233}$	416	0	1.121 ±0.094
0.04000	320	$0.584\pm0.099\pm^{0.037}_{0.065}$	84	0	1.175 ±0.199

Table A.1: $F_2(x, Q^2)$ as obtained from an analysis where the data was binned in x and Q^2, reconstructed using the electron only method, and unfolded via an iterative method.

x	Q^2	$F2$ ±stat ±syst	$N_{\rm obs}$	$N_{\rm php}$	σ ±stat
0.00070	15	$0.948\pm0.021\pm^{0.139}_{0.149}$	6529	193	16.470±0.357
0.00200	15	$0.672\pm0.014\pm^{0.061}_{0.094}$	7366	35	14.816±0.308
0.00200	35	$1.038\pm0.032\pm^{0.079}_{0.119}$	3409	132	6.489 ±0.200
0.00400	35	$0.790\pm0.035\pm^{0.085}_{0.036}$	1580	43	3.252 ±0.144
0.00200	65	$1.562\pm0.085\pm^{0.116}_{0.393}$	1123	48	2.253 ±0.122
0.00400	65	$0.979\pm0.062\pm^{0.012}_{0.079}$	789	19	1.451 ±0.092
0.00400	160	$1.426\pm0.132\pm^{0.068}_{0.397}$	386	17	0.758 ±0.070
0.00800	160	$0.954\pm0.079\pm^{0.042}_{0.102}$	443	2	0.862 ±0.072
0.00800	320	$0.999\pm0.122\pm^{0.093}_{0.248}$	218	6	0.406 ±0.050
0.04000	320	$0.653\pm0.072\pm^{0.035}_{0.125}$	245	0	0.526 ±0.058
0.04000	1000	$0.451\pm0.074\pm^{0.166}_{0.033}$	116	5	0.240 ±0.040
0.10000	5000	$0.619\pm0.222\pm^{0.043}_{0.202}$	22	0	0.054 ±0.020

Table A.2: $F_2(x, Q^2)$ as obtained from an analysis where the data was binned in x and Q^2, reconstructed using the double angle method, and unfolded via an iterative method.

x	Q^2	A	c	s	p	$\delta_{\rm RC}$	$\delta^{\rm acc}_{\rm RC}$	$\delta_{\rm F_L}$	$\delta_{\rm ctr}$	$\delta_{\rm F_3}$	$\delta_{\rm weak}$
0.00030 0.00085	10 25	0.66	0.96	0.43	0.41	1.076	0.953	0.014	-0.076	0.000	1.000
0.00085 0.00268	10 25	0.76	1.24	0.24	0.30	2.120	0.749	0.001	-0.160	0.000	1.000
0.00060 0.00085	25 55	0.53	1.38	0.29	0.40	-0.417	-0.463	0.084	0.017	0.000	1.000
0.00085 0.00268	25 55	0.80	0.96	0.56	0.54	1.477	1.077	0.008	-0.083	0.000	1.000
0.00268 0.00536	25 55	0.82	1.22	0.20	0.25	0.567	0.023	0.002	-0.042	0.000	1.000
0.00127 0.00268	55 120	0.73	1.13	0.51	0.58	0.069	-0.205	0.027	-0.028	0.000	1.000
0.00268 0.00536	55 120	0.82	0.87	0.42	0.36	0.100	-0.096	0.006	-0.034	0.000	1.000
0.00268 0.00536	120 240	0.55	1.60	0.35	0.56	0.434	0.044	0.043	0.023	0.000	1.000
0.00536 0.01414	120 240	0.81	0.99	0.53	0.52	0.369	0.040	0.009	0.049	0.000	1.000
0.01414 0.05656	240 500	0.39	2.56	0.23	0.59	0.862	0.237	0.001	-0.120	0.000	1.000

Table A.3: Bin properties for analyses in (x, Q^2) bins, using the electron only reconstruction method.

x		Q^2		A	c	s	p	$\delta_{\rm RC}$	$\delta_{\rm RC}^{\rm acc}$	$\delta_{\rm F_L}$	$\delta_{\rm ctr}$	$\delta_{\rm F_3}$	$\delta_{\rm weak}$
0.00030	0.00085	10	25	0.77	1.08	0.39	0.42	0.618	0.484	0.014	-0.089	0.000	1.000
0.00085	0.00268	10	25	0.84	0.89	0.55	0.49	2.707	1.205	0.001	-0.114	0.000	1.000
0.00085	0.00268	25	55	0.94	0.91	0.57	0.52	1.631	0.882	0.008	-0.087	0.000	1.000
0.00268	0.00536	25	55	0.95	0.98	0.50	0.49	0.921	0.091	0.002	-0.019	0.000	1.000
0.00127	0.00268	55	120	0.92	0.90	0.52	0.46	0.248	-0.204	0.027	-0.070	0.000	1.000
0.00268	0.00536	55	120	0.96	0.87	0.54	0.47	0.236	-0.230	0.006	-0.025	0.000	1.000
0.00268	0.00536	120	240	0.94	0.91	0.51	0.46	0.779	0.069	0.043	-0.043	0.000	1.000
0.00536	0.01414	120	240	0.98	0.92	0.70	0.64	0.566	-0.078	0.009	0.039	0.000	1.000
0.00536	0.01414	240	500	0.94	0.90	0.64	0.58	0.718	-0.063	0.039	0.017	0.000	1.000
0.01414	0.05656	240	500	0.97	0.95	0.67	0.63	1.511	0.318	0.001	-0.087	0.000	1.000
0.01414	0.05656	500	2000	0.90	1.00	0.69	0.69	2.721	0.677	0.009	-0.083	0.001	0.996
0.05656	0.22620	2000	10000	0.93	1.07	0.80	0.86	2.723	-0.099	0.016	0.051	0.022	0.961

Table A.4: Bin properties for analyses in $(x.Q^2)$ bins. using the double angle reconstruction method.

x	Q^2	F_2	$y_{\rm el}\downarrow$	$\delta_{\rm lo}$	$\delta^{\rm hi}$	$E_e\uparrow$	$E_e\Uparrow$	Box$\downarrow$	Box$\uparrow$	Vtx	$y_{\rm JB}\downarrow$	$y_{\rm JB}\uparrow$
0.00070	15	1.25	0.01	0.04	-0.13	0.00	0.03	0.01	0.00	0.00	0.00	0.00
0.00200	15	0.70	0.05	0.05	0.07	0.00	0.05	0.04	0.07	0.00	0.00	0.00
0.00070	35	1.73	-0.07	0.04	-0.30	0.00	-0.09	-0.07	-0.06	0.00	0.00	0.00
0.00200	35	1.07	0.01	0.01	-0.02	0.00	0.01	0.01	0.01	0.00	0.00	0.00
0.00400	35	0.97	-0.10	-0.10	-0.09	0.00	-0.10	-0.10	-0.10	0.00	0.00	0.00
0.00200	65	1.34	-0.02	0.02	-0.11	0.00	0.01	-0.02	-0.02	0.00	0.00	0.00
0.00400	65	1.09	-0.10	-0.11	-0.09	0.00	-0.10	-0.10	-0.10	0.00	0.00	0.00
0.00400	160	1.42	-0.14	-0.10	-0.26	0.00	-0.14	-0.14	-0.14	0.00	0.00	0.00
0.00800	160	1.03	-0.12	-0.12	-0.13	0.00	-0.12	-0.12	-0.11	0.00	0.00	0.00
0.04000	320	0.58	-0.04	-0.04	-0.04	0.00	-0.04	-0.04	-0.04	0.00	0.00	0.00

Table A.5: Systematic checks for the analysis in $(x.Q^2)$ bins. using the electron only reconstruction method.

x	Q^2	F_2	$y_{\rm el}\downarrow$	$\delta_{\rm lo}$	$\delta^{\rm hi}$	$E_e\uparrow$	$E_e\Uparrow$	Box$\downarrow$	Box$\uparrow$	Vtx	$y_{\rm JB}\downarrow$	$y_{\rm JB}\uparrow$
0.00070	15	0.95	0.05	0.14	-0.12	0.02	-0.01	0.06	0.04	0.05	0.07	0.04
0.00200	15	0.67	0.00	0.02	-0.07	0.00	-0.00	0.01	-0.02	0.00	0.06	0.03
0.00200	35	1.04	-0.01	0.05	-0.10	-0.04	-0.06	-0.01	-0.01	0.01	0.00	-0.03
0.00400	35	0.79	-0.01	-0.00	-0.04	-0.01	-0.01	-0.01	-0.01	0.00	0.07	-0.03
0.00200	65	1.56	-0.11	0.08	-0.31	-0.26	-0.35	-0.09	-0.12	-0.14	-0.10	-0.11
0.00400	65	0.98	-0.03	-0.02	-0.08	-0.03	-0.03	-0.03	-0.03	-0.03	-0.01	-0.05
0.00400	160	1.43	-0.10	0.04	-0.38	-0.25	-0.16	-0.08	-0.11	-0.16	-0.10	-0.10
0.00800	160	0.95	-0.06	-0.05	-0.10	-0.07	-0.07	-0.06	-0.06	-0.05	-0.05	-0.07
0.00800	320	1.00	-0.04	0.07	-0.15	-0.14	-0.22	-0.02	-0.02	0.02	-0.02	-0.02
0.04000	320	0.65	-0.08	-0.08	-0.12	-0.08	-0.08	-0.08	-0.08	-0.05	-0.04	-0.08
0.04000	1000	0.45	0.01	0.16	-0.03	0.00	-0.00	0.01	0.01	0.04	0.01	0.00
0.10000	5000	0.62	-0.13	-0.09	-0.08	-0.13	-0.13	-0.09	-0.09	-0.12	-0.09	-0.09

Table A.6: Systematic checks for the analysis in $(x.Q^2)$ bins. using the double angle reconstruction method.

x	Q^2	$F2$ ±stat ±syst	$N_{\rm obs}$	$N_{\rm php}$	σ ±stat
0.00032	8	$1.101\pm0.020\pm^{0.306}_{0.259}$	8658	0	42.179±0.771
0.00057	15	$1.364\pm0.022\pm^{0.135}_{0.308}$	11822	0	27.484±0.448
0.00029	15	$1.303\pm0.042\pm^{0.577}_{0.151}$	2749	299	25.137±0.806
0.00134	35	$1.421\pm0.039\pm^{0.027}_{0.408}$	4017	0	10.190±0.278
0.00067	35	$1.698\pm0.073\pm^{0.116}_{0.232}$	1459	46	9.080 ±0.392
0.00248	65	$1.406\pm0.060\pm^{0.030}_{0.391}$	1657	0	4.084 ±0.174
0.00124	65	$1.513\pm0.097\pm^{0.162}_{0.145}$	674	14	3.162 ±0.203
0.00610	160	$1.242\pm0.086\pm^{0.144}_{0.351}$	591	0	1.722 ±0.120
0.00305	160	$1.446\pm0.179\pm^{0.027}_{0.335}$	159	0	2.077 ±0.257

Table A.7: $F_2(x.Q^2)$ as obtained from an analysis where the data was binned in y and Q^2, reconstructed using the electron only method. and unfolded via an iterative method.

x	Q^2	$F2$ ±stat ±syst	$N_{\rm obs}$	$N_{\rm php}$	σ ±stat
0.00032	8	$0.973\pm0.021\pm^{0.320}_{0.088}$	6031	171	33.854±0.723
0.00215	15	$0.739\pm0.025\pm^{0.068}_{0.115}$	2722	14	7.019 ±0.233
0.00057	15	$1.059\pm0.019\pm^{0.223}_{0.166}$	9956	140	18.382±0.333
0.00501	35	$0.731\pm0.041\pm^{0.119}_{0.052}$	962	10	2.234 ±0.124
0.00134	35	$1.223\pm0.035\pm^{0.151}_{0.092}$	3926	112	7.414 ±0.211
0.00067	35	$1.839\pm0.071\pm^{0.335}_{0.311}$	2043	198	6.980 ±0.271
0.00930	65	$0.743\pm0.062\pm^{0.062}_{0.119}$	424	0	1.014 ±0.084
0.00248	65	$1.190\pm0.053\pm^{0.122}_{0.094}$	1607	6	2.915 ±0.129
0.00124	65	$1.994\pm0.102\pm^{0.122}_{0.525}$	1185	31	3.045 ±0.156
0.02289	160	$0.752\pm0.094\pm^{0.090}_{0.142}$	197	0	0.421 ±0.053
0.00610	160	$1.002\pm0.070\pm^{0.025}_{0.083}$	613	1	1.193 ±0.084
0.00305	160	$1.606\pm0.134\pm^{0.307}_{0.391}$	526	27	0.913 ±0.076
0.04578	320	$0.473\pm0.101\pm^{0.021}_{0.062}$	75	1	0.115 ±0.025
0.01221	320	$0.980\pm0.105\pm^{0.025}_{0.166}$	259	0	0.555 ±0.059
0.00610	320	$1.369\pm0.165\pm^{0.168}_{0.258}$	233	4	0.421 ±0.051
0.14305	1000	$0.639\pm0.179\pm^{0.188}_{0.278}$	41	0	0.085 ±0.024
0.03815	1000	$0.435\pm0.074\pm^{0.057}_{0.012}$	107	2	0.198 ±0.034
0.01907	1000	$0.894\pm0.147\pm^{0.395}_{0.323}$	115	4	0.248 ±0.041
0.19074	5000	$0.308\pm0.139\pm^{0.011}_{0.035}$	15	0	0.028 ±0.013

Table A.8: $F_2(x.Q^2)$ as obtained from an analysis where the data was binned in y and Q^2, reconstructed using the double angle method. and unfolded via an iterative method.

y	Q^2	A	c	s	p	$\delta_{\rm RC}$	$\delta^{\rm acc}_{\rm RC}$	$\delta_{\rm F_L}$	$\delta_{\rm cut}$	$\delta_{\rm F_2}$	$\delta_{\rm weak}$
0.10000 0.40000	6 10	0.44	1.25	0.32	0.40	2.022	1.351	0.025	0.137	0.000	1.000
0.10000 0.40000	10 25	0.76	0.87	0.52	0.46	1.727	1.010	0.022	0.190	0.000	1.000
0.40000 0.90000	10 25	0.35	2.14	0.25	0.53	0.145	0.472	0.132	0.110	0.000	1.000
0.10000 0.40000	25 55	0.81	0.96	0.59	0.57	1.204	0.767	0.019	0.218	0.000	1.000
0.40000 0.90000	25 55	0.48	1.56	0.41	0.64	0.251	0.126	0.094	0.053	0.000	1.000
0.10000 0.40000	55 120	0.82	0.90	0.61	0.55	1.303	0.751	0.017	0.265	0.000	1.000
0.40000 0.90000	55 120	0.56	1.42	0.46	0.65	1.279	0.682	0.084	0.096	0.000	1.000
0.10000 0.40000	120 240	0.81	1.02	0.57	0.58	0.530	0.170	0.016	0.209	0.000	1.000
0.40000 0.90000	120 240	0.33	2.17	0.22	0.47	0.590	0.200	0.082	0.079	0.000	1.000

Table A.9: Bin properties for analyses in $(y.Q^2)$ bins. using the electron only reconstruction method.

y	Q^2	A	c	s	p	$\delta_{\rm RC}$	$\delta^{\rm acc}_{\rm RC}$	$\delta_{\rm F_L}$	$\delta_{\rm cut}$	$\delta_{\rm F_2}$	$\delta_{\rm w}$
0.10000 0.40000	6 10	0.49	1.64	0.28	0.46	1.222	0.607	0.025	0.209	0.000	1.0
0.06000 0.10000	10 25	0.81	1.03	0.35	0.36	0.739	-0.148	0.001	0.010	0.000	1.0
0.10000 0.40000	10 25	0.87	0.86	0.62	0.54	1.365	0.779	0.022	0.243	0.000	1.0
0.06000 0.10000	25 55	0.94	1.07	0.43	0.46	0.640	-0.158	0.001	0.016	0.000	1.0
0.10000 0.40000	25 55	0.95	0.92	0.69	0.63	1.328	0.575	0.019	0.224	0.000	1.0
0.40000 0.90000	25 55	0.70	1.26	0.39	0.49	0.197	-0.036	0.094	0.022	0.000	1.0
0.06000 0.10000	55 120	0.97	1.07	0.43	0.46	-0.203	-0.654	0.001	0.054	0.000	1.0
0.10000 0.40000	55 120	0.96	0.88	0.71	0.63	1.499	0.522	0.017	0.268	0.000	1.0
0.40000 0.90000	55 120	0.80	1.01	0.50	0.50	1.778	0.661	0.084	0.032	0.000	1.0
0.06000 0.10000	120 240	0.97	0.88	0.42	0.37	-0.340	-0.613	0.001	0.024	0.000	1.0
0.10000 0.40000	120 240	0.97	0.94	0.73	0.69	0.781	0.056	0.016	0.184	0.000	1.0
0.40000 0.90000	120 240	0.89	0.86	0.57	0.49	1.085	0.116	0.082	-0.034	0.000	1.0
0.06000 0.10000	240 500	0.96	0.72	0.55	0.40	-0.029	-0.418	0.001	0.016	0.000	1.0
0.10000 0.40000	240 500	0.97	1.00	0.74	0.74	1.682	0.420	0.015	0.210	0.000	1.0
0.40000 0.90000	240 500	0.95	0.89	0.69	0.62	0.198	-0.358	0.075	-0.039	0.000	1.0
0.06000 0.10000	500 2000	1.00	0.74	0.30	0.23	-0.237	-0.625	0.000	-0.095	0.001	0.9
0.10000 0.40000	500 2000	0.95	0.98	0.75	0.74	1.859	0.501	0.009	0.131	0.001	0.9
0.40000 0.90000	500 2000	0.91	0.99	0.76	0.75	0.371	-0.312	0.049	-0.085	0.001	0.9
0.10000 0.40000	2000 10000	1.00	0.92	0.92	0.85	2.456	0.182	0.003	-0.110	0.020	0.9

Table A.10: Bin properties for analyses in $(y.Q^2)$ bins. using the double angle reconstruction method.

y	Q^2	F_2	$y_{\rm el}\downarrow$	$\delta_{\rm lo}$	$\delta^{\rm hi}$	$E_e\uparrow$	$E_e\Uparrow$	Box$\downarrow$	Box$\uparrow$	Vtx	$y_{\rm JB}\downarrow$	$y_{\rm JB}\uparrow$
0.00032	8	1.10	0.13	0.12	0.06	0.00	0.13	0.25	0.14	0.00	0.00	0.00
0.00057	15	1.36	-0.04	-0.04	-0.09	0.00	-0.04	-0.04	-0.05	0.00	0.00	0.00
0.00029	15	1.30	0.29	0.49	-0.15	0.00	0.35	0.28	0.31	0.00	0.00	0.00
0.00134	35	1.42	-0.13	-0.13	-0.14	0.00	-0.13	-0.13	-0.13	0.00	0.00	0.00
0.00067	35	1.70	-0.02	0.11	-0.23	0.00	-0.08	-0.02	-0.02	0.00	0.00	0.00
0.00248	65	1.41	-0.18	-0.19	-0.17	0.00	-0.18	-0.18	-0.18	0.00	0.00	0.00
0.00124	65	1.51	0.03	0.10	-0.14	0.00	0.00	0.03	0.03	0.00	0.00	0.00
0.00610	160	1.24	-0.20	-0.20	-0.21	0.00	-0.20	-0.20	-0.20	0.00	0.00	0.00
0.00305	160	1.45	-0.10	-0.05	-0.30	0.00	0.00	-0.10	-0.10	0.00	0.00	0.00

Table A.11: Systematic checks for the analysis in $(y.Q^2)$ bins, using the electron only reconstruction method.

y	Q^2	F_2	$y_{\rm el}\downarrow$	$\delta_{\rm lo}$	$\delta^{\rm hi}$	$E_e\uparrow$	$E_e\Uparrow$	Box$\downarrow$	Box$\uparrow$	Vtx	$y_{\rm JB}\downarrow$	$y_{\rm JB}\uparrow$
0.00032	8	0.97	0.10	0.19	-0.08	0.09	0.08	0.21	0.10	0.13	0.12	0.08
0.00215	15	0.74	-0.04	-0.03	-0.10	-0.04	-0.05	-0.04	-0.08	-0.04	0.07	-0.03
0.00057	15	1.06	0.02	0.08	-0.15	0.01	-0.01	0.02	-0.00	0.01	0.05	-0.01
0.00501	35	0.73	-0.03	-0.03	-0.05	-0.03	-0.03	-0.03	-0.03	-0.03	0.12	0.01
0.00134	35	1.22	-0.01	0.04	-0.09	-0.02	-0.04	-0.01	-0.01	0.02	0.02	-0.04
0.00067	35	1.84	0.02	0.26	-0.29	-0.20	-0.12	0.04	0.01	0.02	0.03	0.02
0.00930	65	0.74	-0.07	-0.07	-0.07	-0.07	-0.07	-0.07	-0.07	-0.03	0.06	-0.12
0.00248	65	1.19	-0.03	-0.01	-0.08	-0.03	-0.04	-0.03	-0.03	-0.01	0.01	-0.06
0.00124	65	1.99	-0.17	0.11	-0.43	-0.43	-0.20	-0.15	-0.19	-0.25	-0.17	-0.17
0.02289	160	0.75	-0.14	-0.13	-0.13	-0.14	-0.14	-0.14	-0.14	-0.10	-0.10	-0.13
0.00610	160	1.00	-0.03	-0.02	-0.07	-0.04	-0.05	-0.03	-0.03	-0.01	-0.01	-0.05
0.00305	160	1.61	0.02	0.23	-0.34	-0.28	-0.14	0.05	-0.02	-0.19	0.02	0.01
0.04578	320	0.47	-0.04	-0.03	-0.06	-0.04	-0.04	-0.04	-0.04	-0.00	0.01	-0.03
0.01221	320	0.98	-0.08	-0.06	-0.16	-0.07	-0.08	-0.08	-0.08	-0.03	-0.06	-0.09
0.00610	320	1.37	-0.04	0.11	-0.18	-0.24	-0.12	-0.03	-0.04	0.01	-0.03	-0.03
0.14305	1000	0.64	-0.21	-0.20	-0.23	-0.21	-0.21	-0.21	-0.21	-0.23	-0.21	-0.25
0.03815	1000	0.43	0.02	0.06	-0.00	0.02	0.02	0.02	0.02	0.02	0.03	0.02
0.01907	1000	0.89	-0.08	0.39	-0.21	-0.18	-0.27	-0.01	-0.06	-0.06	-0.06	-0.06
0.19074	5000	0.31	0.02	-0.02	-0.03	-0.02	-0.02	-0.02	-0.02	0.01	-0.02	-0.02

Table A.12: Systematic checks for the analysis in $(y.Q^2)$ bins, using the double angle reconstruction method.

x	Q^2	$F2$ $\pm$stat. $\pm$syst.	$N_{\rm obs}$	$N_{\rm php}$	σ $\pm$stat.
0.00021	8	$1.426\pm0.043\pm^{0.112}_{0.307}$	3282	16	14.930±0.446
0.00042	8	$1.064\pm0.030\pm^{0.147}_{0.273}$	4045	0	12.231±0.342
0.00042	12	$1.551\pm0.048\pm^{0.009}_{0.429}$	3330	8	8.158 ±0.254
0.00042	15	$1.315\pm0.057\pm^{0.295}_{0.182}$	1672	125	5.499 ±0.238
0.00085	15	$1.082\pm0.041\pm^{0.039}_{0.169}$	2352	0	4.486 ±0.169
0.00042	25	$1.893\pm0.121\pm^{0.094}_{0.373}$	629	17	6.351 ±0.407
0.00085	25	$1.341\pm0.063\pm^{0.013}_{0.183}$	1382	2	3.395 ±0.160
0.00085	35	$1.458\pm0.086\pm^{0.106}_{0.128}$	867	19	2.639 ±0.155
0.00155	35	$1.217\pm0.076\pm^{0.001}_{0.139}$	790	0	1.661 ±0.104
0.00268	35	$1.040\pm0.064\pm^{0.076}_{0.232}$	836	0	1.916 ±0.117
0.00085	50	$1.618\pm0.130\pm^{0.106}_{0.240}$	427	12	2.392 ±0.192
0.00155	50	$1.307\pm0.103\pm^{0.065}_{0.055}$	464	0	1.181 ±0.093
0.00268	50	$1.518\pm0.107\pm^{0.218}_{0.386}$	581	0	1.713 ±0.121
0.00465	50	$1.022\pm0.086\pm^{0.107}_{0.259}$	427	0	1.128 ±0.095
0.00155	65	$1.483\pm0.142\pm^{0.021}_{0.203}$	325	5	0.900 ±0.086
0.00268	65	$1.135\pm0.101\pm^{0.004}_{0.094}$	386	0	0.819 ±0.073
0.00465	65	$1.064\pm0.103\pm^{0.122}_{0.369}$	328	0	0.829 ±0.080
0.00155	125	$1.045\pm0.154\pm^{0.220}_{0.018}$	118	2	1.066 ±0.157
0.00268	125	$1.436\pm0.125\pm^{0.022}_{0.210}$	374	3	1.246 ±0.109
0.00465	125	$1.047\pm0.093\pm^{0.024}_{0.094}$	382	0	0.841 ±0.075
0.00775	125	$1.170\pm0.105\pm^{0.227}_{0.466}$	392	0	0.965 ±0.086
0.00775	250	$0.445\pm0.081\pm^{0.235}_{0.149}$	91	5	0.247 ±0.045
0.01414	250	$1.217\pm0.137\pm^{0.289}_{0.441}$	223	0	0.983 ±0.111
0.02828	250	$0.531\pm0.085\pm^{0.017}_{0.054}$	111	0	0.363 ±0.058

Table A.13: $F_2(x.Q^2)$ as obtained from an analysis where the data was binned in x and Q^2, reconstructed using the electron only method, and unfolded via an iterative method.

A.2 Bins According to Detector Resolution

A.2.1 Analysis in bins of (x, Q^2)

x	Q^2	$F2$ ±stat ±syst	$N_{\rm obs}$	$N_{\rm php}$	σ ±stat
0.00042	12	$1.110\pm0.042\pm^{0.074}_{0.257}$	2012	43	5.210±0.198
0.00085	12	$0.807\pm0.029\pm^{0.032}_{0.161}$	2500	29	4.409±0.159
0.00155	12	$0.699\pm0.032\pm^{0.076}_{0.106}$	1458	3	3.267±0.151
0.00085	15	$0.969\pm0.040\pm^{0.045}_{0.181}$	1865	25	3.452±0.143
0.00155	15	$0.757\pm0.038\pm^{0.040}_{0.109}$	1276	2	2.228±0.112
0.00268	15	$0.660\pm0.036\pm^{0.140}_{0.044}$	983	26	2.659±0.146
0.00085	25	$1.154\pm0.058\pm^{0.044}_{0.195}$	1244	13	2.519±0.126
0.00155	25	$0.862\pm0.052\pm^{0.102}_{0.051}$	920	30	1.501±0.090
0.00268	25	$0.730\pm0.044\pm^{0.088}_{0.057}$	844	5	1.624±0.099
0.00465	25	$0.626\pm0.051\pm^{0.179}_{0.037}$	411	6	1.702±0.138
0.00085	35	$1.474\pm0.084\pm^{0.182}_{0.270}$	971	24	2.198±0.125
0.00155	35	$1.117\pm0.074\pm^{0.084}_{0.068}$	763	8	1.308±0.086
0.00268	35	$0.837\pm0.055\pm^{0.065}_{0.040}$	765	15	1.294±0.085
0.00465	35	$0.726\pm0.056\pm^{0.128}_{0.019}$	493	0	1.128±0.088
0.00085	50	$1.797\pm0.126\pm^{0.230}_{0.391}$	649	33	1.895±0.133
0.00155	50	$1.376\pm0.105\pm^{0.075}_{0.156}$	539	10	1.088±0.083
0.00268	50	$1.028\pm0.079\pm^{0.062}_{0.061}$	544	2	0.958±0.073
0.00465	50	$0.892\pm0.077\pm^{0.070}_{0.025}$	414	0	0.840±0.073
0.00775	50	$0.664\pm0.069\pm^{0.169}_{0.017}$	262	0	0.687±0.072
0.00155	65	$1.508\pm0.131\pm^{0.264}_{0.333}$	462	14	0.769±0.067
0.00268	65	$1.060\pm0.096\pm^{0.038}_{0.094}$	386	3	0.652±0.059
0.00465	65	$0.939\pm0.093\pm^{0.029}_{0.069}$	318	0	0.606±0.060
0.00775	65	$0.711\pm0.076\pm^{0.059}_{0.079}$	272	0	0.489±0.053
0.01414	65	$0.627\pm0.079\pm^{0.274}_{0.013}$	167	0	0.741±0.093
0.00155	125	$2.036\pm0.202\pm^{0.639}_{0.337}$	360	14	1.091±0.108
0.00268	125	$1.352\pm0.110\pm^{0.272}_{0.146}$	521	8	0.924±0.075
0.00465	125	$0.946\pm0.087\pm^{0.011}_{0.084}$	372	1	0.654±0.060
0.00775	125	$0.965\pm0.090\pm^{0.012}_{0.030}$	375	0	0.688±0.064
0.01414	125	$0.618\pm0.055\pm^{0.096}_{0.031}$	368	0	0.787±0.070
0.02828	125	$0.593\pm0.079\pm^{0.339}_{0.018}$	144	0	0.985±0.131
0.00465	250	$1.430\pm0.187\pm^{0.264}_{0.270}$	221	7	0.323±0.042
0.00775	250	$0.848\pm0.120\pm^{0.024}_{0.100}$	159	2	0.275±0.039
0.01414	250	$0.674\pm0.084\pm^{0.054}_{0.043}$	202	0	0.373±0.046
0.02828	250	$0.602\pm0.079\pm^{0.078}_{0.021}$	201	6	0.311±0.041
0.05657	250	$0.399\pm0.077\pm^{0.197}_{0.020}$	68	0	0.335±0.064

Table A.14: $F_2(x,Q^2)$ as obtained from an analysis where the data was binned in x and Q^2, reconstructed using the double angle method, and unfolded via an iterative method.

x	Q^2	$F2$ ±stat ±syst	$N_{\rm obs}$	$N_{\rm php}$	σ ±stat
0.00775	500	$1.015\pm0.195\pm^{0.269}_{0.207}$	93	1	0.186±0.036
0.01414	500	$0.726\pm0.134\pm^{0.048}_{0.110}$	89	1	0.179±0.033
0.02828	500	$0.736\pm0.137\pm^{0.017}_{0.113}$	87	0	0.196±0.036
0.05657	500	$0.615\pm0.123\pm^{0.048}_{0.149}$	79	0	0.173±0.034
0.11310	500	$0.333\pm0.106\pm^{0.146}_{0.003}$	27	0	0.095±0.030
0.00775	1000	$1.358\pm0.717\pm^{0.594}_{0.115}$	15	0	0.027±0.014
0.01414	1000	$0.969\pm0.246\pm^{0.002}_{0.367}$	45	2	0.127±0.032
0.02828	1000	$0.646\pm0.215\pm^{0.180}_{0.009}$	35	5	0.048±0.016
0.05657	1000	$0.438\pm0.155\pm^{0.098}_{0.011}$	25	0	0.046±0.016
0.02828	2000	$0.623\pm0.333\pm^{0.206}_{0.070}$	11	0	0.036±0.019
0.05657	2000	$0.359\pm0.169\pm^{0.016}_{0.101}$	13	2	0.030±0.014
0.11310	2000	$0.948\pm0.445\pm^{0.053}_{0.166}$	18	0	0.035±0.016
0.11310	5000	$0.539\pm0.354\pm^{0.000}_{0.049}$	11	0	0.009±0.006

Table A.15: $F_2(x,Q^2)$ as obtained from an analysis where the data was binned in x and Q^2, reconstructed using the double angle method, and unfolded via an iterative method (cont'd).

x	Q^2	A	c	s	p	$\delta_{\rm RC}$	$\delta^{\rm acc}_{\rm RC}$	δ_{F_L}	$\delta_{\rm ctr}$	δ_{F_3}	$\delta_{\rm weak}$
0.00015 0.00030	7 10	0.46	1.16	0.21	0.25	0.457	0.805	0.068	0.051	0.000	1.000
0.00030 0.00060	7 10	0.54	0.92	0.21	0.19	1.490	1.041	0.013	0.001	0.000	1.000
0.00030 0.00060	10 14	0.69	0.84	0.26	0.22	0.764	0.685	0.026	0.041	0.000	1.000
0.00030 0.00060	14 20	0.60	1.17	0.27	0.32	0.015	0.088	0.041	0.039	0.000	1.000
0.00060 0.00120	14 20	0.78	0.78	0.21	0.17	0.679	0.320	0.008	-0.016	0.000	1.000
0.00030 0.00060	20 28	0.40	2.07	0.22	0.46	0.249	0.202	0.127	0.067	0.000	1.000
0.00060 0.00120	20 28	0.76	0.95	0.33	0.32	0.718	0.578	0.022	0.036	0.000	1.000
0.00060 0.00120	28 40	0.69	1.12	0.42	0.47	0.531	0.419	0.046	0.034	0.000	1.000
0.00120 0.00200	28 40	0.82	0.88	0.33	0.29	0.733	0.525	0.011	0.020	0.000	1.000
0.00200 0.00360	28 40	0.81	0.88	0.24	0.21	1.085	0.585	0.003	0.004	0.000	1.000
0.00060 0.00120	40 56	0.51	1.51	0.34	0.51	0.838	0.458	0.101	0.038	0.000	1.000
0.00120 0.00200	40 56	0.81	1.09	0.41	0.44	0.609	0.386	0.024	0.028	0.000	1.000
0.00200 0.00360	40 56	0.80	1.03	0.30	0.30	0.657	0.364	0.007	0.014	0.000	1.000
0.00360 0.00600	40 56	0.83	0.98	0.20	0.20	1.036	0.482	0.002	0.006	0.000	1.000
0.00120 0.00200	56 80	0.78	1.09	0.40	0.44	0.445	0.132	0.042	-0.003	0.000	1.000
0.00200 0.00360	56 80	0.84	0.90	0.40	0.36	0.452	0.193	0.011	0.011	0.000	1.000
0.00360 0.00600	56 80	0.80	0.91	0.25	0.23	0.710	0.313	0.003	-0.000	0.000	1.000
0.00120 0.00200	80 160	0.35	1.91	0.23	0.44	1.550	0.446	0.178	0.025	0.000	1.000
0.00200 0.00360	80 160	0.72	1.18	0.42	0.49	0.991	0.539	0.047	0.052	0.000	1.000
0.00360 0.00600	80 160	0.83	0.92	0.37	0.34	1.052	0.738	0.013	0.028	0.000	1.000
0.00600 0.01000	80 160	0.84	0.85	0.25	0.21	1.424	0.686	0.004	0.012	0.000	1.000
0.00600 0.01000	160 320	0.56	1.20	0.31	0.38	1.387	0.944	0.016	0.045	0.000	1.000
0.01000 0.02000	160 320	0.67	1.16	0.28	0.32	1.175	0.796	0.004	0.012	0.000	1.000
0.02000 0.04000	160 320	0.74	1.19	0.21	0.25	1.069	0.338	0.001	-0.014	0.000	1.000

Table A.16: Bin properties for analyses in (x,Q^2) bins, using the electron only reconstruction method.

x	Q^2	A	c	s	p	$\delta_{\rm RC}$	$\delta_{\rm RC}^{\rm acc}$	$\delta_{\rm F_L}$	$\delta_{\rm ctr}$	$\delta_{\rm F_3}$	$\delta_{\rm weak}$
0.00030 0.00060	10 14	0.78	1.06	0.24	0.25	0.258	0.175	0.026	0.045	0.000	1.000
0.00060 0.00120	10 14	0.83	0.77	0.33	0.25	1.299	0.645	0.005	0.012	0.000	1.000
0.00120 0.00200	10 14	0.76	0.88	0.26	0.23	1.836	0.544	0.001	-0.003	0.000	1.000
0.00060 0.00120	14 20	0.91	0.89	0.32	0.28	0.288	0.004	0.008	-0.014	0.000	1.000
0.00120 0.00200	14 20	0.94	0.85	0.35	0.30	0.705	0.083	0.002	-0.018	0.000	1.000
0.00200 0.00360	14 20	0.83	1.19	0.32	0.39	0.776	-0.118	0.001	-0.024	0.000	1.000
0.00060 0.00120	20 28	0.89	0.94	0.32	0.30	0.735	0.371	0.022	0.031	0.000	1.000
0.00120 0.00200	20 28	0.95	0.83	0.33	0.28	1.166	0.488	0.006	0.028	0.000	1.000
0.00200 0.00360	20 28	0.94	0.94	0.38	0.35	1.378	0.326	0.002	0.011	0.000	1.000
0.00360 0.00600	20 28	0.74	1.61	0.26	0.41	1.675	0.039	0.001	-0.006	0.000	1.000
0.00060 0.00120	28 40	0.86	1.03	0.31	0.31	0.553	0.236	0.046	0.007	0.000	1.000
0.00120 0.00200	28 40	0.95	0.86	0.34	0.30	0.837	0.339	0.011	0.019	0.000	1.000
0.00200 0.00360	28 40	0.96	0.85	0.46	0.39	1.103	0.394	0.003	0.017	0.000	1.000
0.00360 0.00600	28 40	0.94	1.11	0.41	0.45	1.264	0.158	0.001	0.004	0.000	1.000
0.00060 0.00120	40 56	0.75	1.20	0.23	0.28	0.799	0.260	0.101	-0.012	0.000	1.000
0.00120 0.00200	40 56	0.93	0.99	0.33	0.32	0.866	0.337	0.024	0.019	0.000	1.000
0.00200 0.00360	40 56	0.96	0.88	0.44	0.39	1.053	0.321	0.007	0.014	0.000	1.000
0.00360 0.00600	40 56	0.97	1.01	0.40	0.40	1.279	0.231	0.002	0.012	0.000	1.000
0.00600 0.01000	40 56	0.93	1.25	0.42	0.52	1.335	0.030	0.001	-0.003	0.000	1.000
0.00120 0.00200	56 80	0.94	0.86	0.38	0.33	0.718	0.200	0.042	-0.024	0.000	1.000
0.00200 0.00360	56 80	0.97	0.85	0.44	0.37	0.641	0.086	0.011	0.011	0.000	1.000
0.00360 0.00600	56 80	0.96	0.94	0.39	0.37	0.883	0.055	0.003	0.005	0.000	1.000
0.00600 0.01000	56 80	0.96	0.89	0.43	0.38	1.342	0.116	0.001	-0.004	0.000	1.000
0.01000 0.02000	56 80	0.79	1.80	0.31	0.57	1.212	-0.342	0.000	-0.037	0.000	1.000
0.00120 0.00200	80 160	0.67	1.18	0.28	0.34	1.613	0.208	0.178	-0.012	0.000	1.000
0.00200 0.00360	80 160	0.95	0.96	0.42	0.40	1.317	0.435	0.047	-0.006	0.000	1.000
0.00360 0.00600	80 160	0.96	0.87	0.51	0.44	1.474	0.566	0.013	0.026	0.000	1.000
0.00600 0.01000	80 160	0.97	0.92	0.48	0.44	1.406	0.355	0.004	0.015	0.000	1.000
0.01000 0.02000	80 160	0.96	1.05	0.53	0.56	1.887	0.417	0.001	0.008	0.000	1.000
0.02000 0.04000	80 160	0.72	2.54	0.22	0.57	1.976	-0.271	0.000	-0.032	0.000	1.000
0.00360 0.00600	160 320	1.00	0.82	0.53	0.43	1.492	0.341	0.058	-0.015	0.000	1.000
0.00600 0.01000	160 320	0.98	0.89	0.56	0.49	1.418	0.514	0.016	0.011	0.000	1.000
0.01000 0.02000	160 320	0.97	0.92	0.62	0.57	1.526	0.557	0.004	0.012	0.000	1.000
0.02000 0.04000	160 320	0.98	0.80	0.56	0.45	1.788	0.507	0.001	0.016	0.000	1.000
0.04000 0.08000	160 320	0.81	2.04	0.27	0.55	1.515	-0.092	0.000	-0.036	0.000	1.000

Table A.17: Bin properties for analyses in $(x.Q^2)$ bins. using the double angle reconstruction method.

x	Q^2	A	c	s	p	$\delta_{\rm RC}$	$\delta_{\rm RC}^{\rm acc}$	$\delta_{\rm F_L}$	$\delta_{\rm ctr}$	$\delta_{\rm F_3}$	$\delta_{\rm w}$
0.00600 0.01000	320 640	0.86	0.97	0.41	0.39	3.695	0.898	0.078	-0.043	0.000	0.9
0.01000 0.02000	320 640	0.94	0.99	0.58	0.57	1.773	0.563	0.016	0.015	0.000	0.9
0.02000 0.04000	320 640	0.96	1.11	0.50	0.56	1.320	0.231	0.003	0.005	0.000	0.9
0.04000 0.08000	320 640	0.95	1.07	0.51	0.54	1.381	0.241	0.000	0.010	0.000	0.9
0.08000 0.16000	320 640	0.84	1.52	0.32	0.48	0.829	-0.170	0.000	-0.043	0.000	0.9
0.00600 0.01000	640 1280	0.60	0.56	0.20	0.11	1.879	-0.392	0.245	-0.001	0.000	0.9
0.01000 0.02000	640 1280	0.87	1.30	0.62	0.80	4.797	0.534	0.075	-0.029	0.001	0.9
0.02000 0.04000	640 1280	0.95	0.78	0.67	0.52	1.757	0.241	0.012	0.047	0.001	0.9
0.04000 0.08000	640 1280	0.96	0.92	0.65	0.60	1.386	0.176	0.002	0.010	0.001	0.9
0.02000 0.04000	1280 2560	0.60	1.00	0.40	0.40	5.301	0.842	0.056	0.035	0.005	0.9
0.04000 0.08000	1280 2560	0.94	1.38	0.50	0.69	1.774	0.468	0.008	-0.005	0.005	0.9
0.08000 0.16000	1280 2560	1.00	1.00	0.29	0.29	1.345	-0.218	0.001	0.028	0.004	0.9
0.08000 0.16000	2560 10000	1.00	0.43	1.00	0.43	2.557	0.083	0.009	0.007	0.022	0.9

Table A.18: Bin properties for analyses in $(x.Q^2)$ bins. using the double angle reconstruction method (cont'd).

x	Q^2	F_2	$y_{\rm el}\downarrow$	$\delta_{\rm lo}$	$\delta^{\rm lin}$	$E_e\uparrow$	$E_e\Uparrow$	Box$\downarrow$	Box$\uparrow$	Vtx	$y_{\rm JB}\downarrow$	$y_{\rm JB}\uparrow$
0.00021	8	1.43	-0.06	0.07	0.11	0.00	0.01	-0.07	0.11	0.00	0.00	0.00
0.00042	8	1.06	0.09	0.08	0.07	0.00	0.09	0.15	0.10	0.00	0.00	0.00
0.00042	12	1.55	-0.08	-0.05	-0.29	0.00	-0.07	-0.08	-0.06	0.00	0.00	0.00
0.00042	15	1.32	0.14	0.23	-0.18	0.00	0.19	0.14	0.15	0.00	0.00	0.00
0.00085	15	1.08	0.02	0.01	0.01	0.00	0.02	0.02	0.01	0.00	0.00	0.00
0.00042	25	1.89	-0.08	0.09	-0.34	0.00	-0.20	-0.08	-0.08	0.00	0.00	0.00
0.00085	25	1.34	-0.02	-0.01	-0.09	0.00	-0.01	-0.02	-0.02	0.00	0.00	0.00
0.00085	35	1.46	0.03	0.09	-0.13	0.00	0.05	0.03	0.0	0.00	0.00	0.00
0.00155	35	1.22	-0.02	-0.02	-0.02	0.00	-0.02	-0.02	-0.02	0.00	0.00	0.00
0.00268	35	1.04	-0.08	-0.08	-0.08	0.00	-0.08	-0.08	-0.08	0.00	0.00	0.00
0.00085	50	1.62	-0.01	0.11	-0.24	0.00	-0.04	-0.01	-0.01	0.00	0.00	0.00
0.00155	50	1.31	0.03	0.04	-0.02	0.00	0.04	0.03	0.03	0.00	0.00	0.00
0.00268	50	1.52	-0.24	-0.24	-0.22	0.00	-0.24	0.24	-0.24	0.00	0.00	0.00
0.00465	50	1.02	-0.13	-0.13	-0.11	0.00	-0.13	-0.13	-0.13	0.00	0.00	0.00
0.00155	65	1.48	-0.05	-0.02	-0.20	0.00	-0.06	-0.05	-0.05	0.00	0.00	0.00
0.00268	65	1.13	-0.03	-0.04	-0.02	0.00	-0.03	-0.03	-0.03	0.00	0.00	0.00
0.00465	65	1.06	-0.14	-0.14	-0.12	0.00	-0.13	-0.14	-0.14	0.00	0.00	0.00
0.00155	125	1.04	0.12	0.22	0.00	0.00	0.16	0.12	0.12	0.00	0.00	0.00
0.00268	125	1.44	-0.08	-0.05	-0.21	0.00	-0.03	-0.08	-0.08	0.00	0.00	0.00
0.00465	125	1.05	-0.04	-0.04	-0.03	0.00	-0.04	-0.04	-0.04	0.00	0.00	0.00
0.00775	125	1.17	-0.24	-0.25	-0.23	0.00	-0.24	-0.24	-0.24	0.00	0.00	0.00
0.00775	250	0.45	0.21	0.21	0.15	0.00	0.21	0.21	0.21	0.00	0.00	0.00
0.01414	250	1.22	-0.30	-0.30	-0.29	0.00	-0.30	-0.30	-0.30	0.00	0.00	0.00
0.02828	250	0.53	-0.02	-0.02	-0.02	0.00	-0.02	-0.02	-0.02	0.00	0.00	0.00

Table A.19: Systematic checks for the analysis in $(x.Q^2)$ bins. using the electron only reconstruction method.

x	Q^2	F_2	$y_{el}\downarrow$	δ_{lo}	δ^{hi}	$E_e\uparrow$	$E_e\Uparrow$	Box$\downarrow$	Box$\uparrow$	Vtx	$y_{JB}\downarrow$	$y_{JB}\uparrow$
0.00042	12	1.11	-0.03	0.07	-0.24	-0.04	-0.08	-0.03	-0.03	-0.03	-0.01	-0.03
0.00085	12	0.81	-0.02	0.03	-0.14	-0.02	-0.03	-0.01	-0.04	-0.00	0.02	-0.04
0.00155	12	0.70	-0.02	0.00	-0.08	-0.02	-0.02	-0.01	-0.07	-0.01	0.06	0.08
0.00085	15	0.97	-0.01	0.04	-0.17	-0.02	-0.04	-0.01	-0.02	-0.02	0.01	-0.04
0.00155	15	0.76	-0.01	0.01	-0.10	-0.01	-0.01	-0.00	-0.03	-0.04	0.04	-0.02
0.00268	15	0.66	0.01	0.02	-0.04	0.01	0.01	0.01	0.01	0.02	0.14	0.00
0.00085	25	1.15	-0.02	0.04	-0.18	-0.04	-0.07	-0.01	-0.02	-0.00	-0.01	-0.02
0.00155	25	0.86	0.03	0.07	-0.05	0.02	0.02	0.03	0.03	0.03	0.05	-0.01
0.00268	25	0.73	-0.00	0.01	-0.06	-0.00	-0.01	-0.01	-0.00	0.02	0.09	-0.01
0.00465	25	0.63	0.00	0.01	-0.03	0.01	0.01	0.00	0.00	-0.01	0.18	0.00
0.00085	35	1.47	0.01	0.17	-0.21	-0.09	-0.17	0.02	0.00	0.07	0.02	0.01
0.00155	35	1.12	0.02	0.06	-0.07	0.01	-0.01	0.02	0.02	0.04	0.03	0.01
0.00268	35	0.84	0.01	0.03	-0.03	0.01	0.01	0.01	0.01	0.03	0.05	-0.03
0.00465	35	0.73	-0.01	0.00	-0.02	-0.01	-0.01	-0.01	-0.01	-0.01	0.13	0.00
0.00085	50	1.80	-0.00	0.24	-0.37	0.00	0.00	0.01	-0.03	-0.10	0.00	-0.00
0.00155	50	1.38	0.01	0.07	-0.12	-0.04	-0.10	0.01	0.00	0.02	0.02	-0.01
0.00268	50	1.03	-0.00	0.01	-0.04	-0.01	-0.01	-0.00	-0.01	0.06	0.00	-0.04
0.00465	50	0.89	-0.01	0.00	-0.01	-0.01	-0.01	-0.01	-0.00	0.02	0.07	-0.02
0.00775	50	0.66	-0.00	-0.00	-0.02	-0.00	-0.00	-0.00	-0.00	0.01	0.17	0.00
0.00155	65	1.51	0.05	0.25	-0.19	-0.15	-0.27	0.05	0.04	0.05	0.05	0.05
0.00268	65	1.06	0.00	0.03	-0.09	-0.01	-0.02	0.00	-0.01	0.01	0.01	-0.03
0.00465	65	0.94	-0.01	0.00	-0.03	-0.01	-0.01	-0.01	-0.01	-0.01	0.03	-0.06
0.00775	65	0.71	-0.01	-0.00	-0.01	-0.01	-0.01	-0.01	-0.01	-0.03	0.06	-0.07
0.01414	65	0.63	-0.01	-0.00	0.00	-0.01	-0.00	-0.01	-0.00	0.03	0.27	0.00
0.00155	125	2.04	0.11	0.60	-0.27	0.00	0.00	0.16	0.04	-0.19	0.12	0.13
0.00268	125	1.35	0.11	0.21	-0.03	-0.10	-0.14	0.11	0.11	0.05	0.12	0.11
0.00465	125	0.95	-0.01	0.01	-0.07	-0.02	-0.03	-0.01	-0.01	-0.02	0.01	-0.02
0.00775	125	0.97	-0.01	-0.01	-0.01	-0.01	-0.01	-0.01	-0.01	-0.02	0.01	-0.02
0.01414	125	0.62	-0.00	-0.00	-0.01	-0.00	-0.00	-0.00	-0.00	0.04	0.09	-0.03
0.02828	125	0.59	-0.01	-0.01	-0.00	-0.01	-0.01	-0.01	-0.01	-0.01	0.34	0.00
0.00465	250	1.43	0.06	0.24	-0.15	-0.06	-0.22	0.07	0.05	-0.00	0.07	0.06
0.00775	250	0.85	-0.01	0.02	-0.08	-0.03	-0.05	-0.01	-0.01	0.01	-0.01	-0.01
0.01414	250	0.67	-0.01	-0.01	-0.03	-0.01	-0.01	-0.01	-0.01	0.05	-0.00	-0.02
0.02828	250	0.60	0.01	0.02	0.00	0.01	0.01	0.01	0.01	0.03	0.07	-0.02
0.05657	250	0.40	-0.01	-0.01	-0.00	-0.01	-0.01	-0.01	-0.01	0.00	0.20	0.00

Table A.20: Systematic checks for the analysis in $(x.Q^2)$ bins, using the double angle reconstruction method.

x	Q^2	F_2	$y_{el}\downarrow$	δ_{lo}	δ^{hi}	$E_e\uparrow$	$E_e\Uparrow$	Box$\downarrow$	Box$\uparrow$	Vtx	$y_{JB}\downarrow$	$y_{JB}\uparrow$
0.00775	500	1.02	-0.03	0.22	-0.08	-0.19	0.00	0.11	0.08	0.04	0.09	0.08
0.01414	500	0.73	-0.02	-0.00	-0.10	-0.01	-0.02	-0.02	-0.02	0.05	-0.02	-0.02
0.02828	500	0.74	-0.03	-0.02	-0.10	-0.03	-0.03	-0.03	-0.03	0.02	-0.01	-0.04
0.05657	500	0.61	-0.02	-0.01	-0.04	-0.02	-0.02	-0.02	-0.02	0.05	-0.01	-0.14
0.11310	500	0.33	0.00	0.00	-0.00	0.00	0.00	0.00	0.00	0.02	0.14	0.00
0.00775	1000	1.36	-0.01	0.27	0.17	0.00	0.00	0.53	-0.12	0.00	0.00	0.00
0.01414	1000	0.97	-0.14	1.06	-0.23	-0.27	0.00	-0.03	-0.08	0.00	-0.06	-0.06
0.02828	1000	0.65	0.07	0.10	-0.01	0.07	0.07	0.07	0.07	0.08	0.07	0.03
0.05657	1000	0.44	0.01	0.06	-0.01	0.01	0.01	0.01	0.01	0.08	0.01	0.01
0.02828	2000	0.62	0.00	0.17	-0.07	0.00	0.00	0.00	0.00	0.12	0.00	0.00
0.05657	2000	0.36	-0.02	0.01	-0.02	-0.02	-0.02	-0.02	-0.02	-0.09	0.01	-0.02
0.11310	2000	0.95	0.00	0.05	-0.05	0.00	0.00	0.00	0.00	-0.16	0.00	0.00
0.11310	5000	0.54	0.00	0.00	-0.05	0.00	0.00	0.00	0.00	0.00	0.00	0.00

Table A.21: Systematic checks for the analysis in $(x.Q^2)$ bins, using the double angle reconstruction method (cont'd).

x	Q^2	$F2$ ±stat ±syst	$N_{\rm obs}$	$N_{\rm php}$	σ ±stat
0.00049	8	$0.974\pm0.029\pm^{0.156}_{0.082}$	3720	0	10.710±0.315
0.00024	8	$1.378\pm0.044\pm^{0.109}_{0.228}$	3178	0	9.738 ±0.308
0.00069	12	$1.274\pm0.041\pm^{0.034}_{0.277}$	3311	0	6.698 ±0.214
0.00034	12	$1.578\pm0.060\pm^{0.026}_{0.286}$	2072	0	6.386 ±0.244
0.00086	15	$1.050\pm0.041\pm^{0.077}_{0.144}$	2157	27	4.014 ±0.159
0.00043	15	$1.456\pm0.066\pm^{0.127}_{0.392}$	1490	0	4.070 ±0.185
0.00029	15	$1.864\pm0.134\pm^{0.096}_{0.244}$	503	14	4.756 ±0.342
0.00143	25	$0.957\pm0.047\pm^{0.051}_{0.220}$	1344	0	2.500 ±0.124
0.00072	25	$1.489\pm0.085\pm^{0.009}_{0.222}$	916	0	2.757 ±0.157
0.00048	25	$1.991\pm0.153\pm^{0.106}_{0.490}$	455	14	2.980 ±0.230
0.00334	35	$1.006\pm0.061\pm^{0.087}_{0.325}$	807	0	2.240 ±0.136
0.00200	35	$1.114\pm0.062\pm^{0.015}_{0.171}$	1000	0	2.200 ±0.122
0.00100	35	$1.283\pm0.087\pm^{0.103}_{0.073}$	645	0	1.670 ±0.114
0.00067	35	$1.834\pm0.151\pm^{0.044}_{0.416}$	439	11	1.712 ±0.141
0.00477	50	$1.015\pm0.074\pm^{0.120}_{0.271}$	557	0	1.501 ±0.110
0.00286	50	$1.347\pm0.092\pm^{0.130}_{0.250}$	620	0	1.787 ±0.122
0.00143	50	$1.282\pm0.104\pm^{0.085}_{0.021}$	451	6	1.120 ±0.091
0.00095	50	$1.758\pm0.169\pm^{0.009}_{0.383}$	325	6	1.029 ±0.099
0.00620	65	$0.956\pm0.084\pm^{0.105}_{0.208}$	390	0	1.073 ±0.094
0.00372	65	$0.995\pm0.087\pm^{0.005}_{0.125}$	412	0	0.848 ±0.074
0.00186	65	$1.182\pm0.117\pm^{0.114}_{0.014}$	311	7	0.735 ±0.073
0.00124	65	$2.119\pm0.238\pm^{0.228}_{0.672}$	238	2	0.785 ±0.088
0.01192	125	$0.902\pm0.075\pm^{0.125}_{0.210}$	424	0	1.249 ±0.104
0.00715	125	$1.075\pm0.084\pm^{0.092}_{0.185}$	501	0	1.117 ±0.087
0.00358	125	$1.092\pm0.099\pm^{0.026}_{0.067}$	364	0	0.833 ±0.076
0.00238	125	$1.192\pm0.144\pm^{0.185}_{0.177}$	198	2	0.655 ±0.079
0.02384	250	$0.651\pm0.091\pm^{0.019}_{0.243}$	156	0	0.436 ±0.061
0.01431	250	$0.794\pm0.100\pm^{0.108}_{0.050}$	204	22	0.565 ±0.071
0.00715	250	$0.887\pm0.152\pm^{0.005}_{0.189}$	92	0	0.546 ±0.094

Table A.22: $F_2(x, Q^2)$ as obtained from an analysis where the data was binned in y and Q^2, reconstructed using the electron only method, and unfolded via an iterative method.

A.2.2 Analysis in bins of (y, Q^2)

x	Q^2	$F2$ ±stat ±syst	$N_{\rm obs}$	$N_{\rm php}$	σ ±stat
0.00114	12	$0.703\pm0.027\pm^{0.106}_{0.062}$	2326	10	4.086±0.156
0.00069	12	$0.786\pm0.030\pm^{0.167}_{0.084}$	2362	49	3.631±0.139
0.00143	15	$0.748\pm0.033\pm^{0.105}_{0.080}$	1641	11	2.831±0.126
0.00086	15	$0.936\pm0.041\pm^{0.084}_{0.145}$	1699	32	3.056±0.134
0.00043	15	$1.081\pm0.058\pm^{0.299}_{0.090}$	1071	51	2.614±0.141
0.00238	25	$0.772\pm0.042\pm^{0.095}_{0.053}$	1085	32	1.993±0.109
0.00143	25	$0.836\pm0.045\pm^{0.152}_{0.038}$	1187	49	1.844±0.100
0.00072	25	$1.304\pm0.078\pm^{0.066}_{0.230}$	860	11	2.097±0.125
0.00572	35	$0.623\pm0.071\pm^{0.171}_{0.019}$	229	1	0.523±0.059
0.00334	35	$0.819\pm0.051\pm^{0.072}_{0.058}$	820	15	1.534±0.095
0.00200	35	$1.027\pm0.060\pm^{0.025}_{0.097}$	928	8	1.724±0.101
0.00100	35	$1.172\pm0.081\pm^{0.312}_{0.046}$	678	44	1.266±0.088
0.00067	35	$2.571\pm0.195\pm^{0.229}_{0.903}$	520	22	1.819±0.138
0.00817	50	$0.545\pm0.077\pm^{0.179}_{0.002}$	145	0	0.323±0.046
0.00477	50	$0.973\pm0.072\pm^{0.017}_{0.111}$	550	2	1.217±0.090
0.00286	50	$1.048\pm0.075\pm^{0.032}_{0.106}$	605	5	1.149±0.083
0.00143	50	$1.271\pm0.099\pm^{0.087}_{0.143}$	515	6	0.973±0.076
0.00095	50	$2.100\pm0.190\pm^{0.085}_{0.768}$	391	27	0.997±0.090
0.01063	65	$0.600\pm0.096\pm^{0.206}_{0.018}$	115	0	0.264±0.042
0.00620	65	$0.893\pm0.077\pm^{0.014}_{0.140}$	404	0	0.832±0.072
0.00372	65	$1.004\pm0.090\pm^{0.075}_{0.031}$	404	16	0.722±0.065
0.00186	65	$1.100\pm0.103\pm^{0.192}_{0.116}$	372	6	0.600±0.056
0.00124	65	$2.686\pm0.260\pm^{0.369}_{1.299}$	353	7	0.758±0.073
0.02861	125	$0.672\pm0.109\pm^{0.092}_{0.164}$	94	0	0.569±0.092
0.02044	125	$0.083\pm0.025\pm^{0.145}_{0.143}$	64	17	0.035±0.010
0.01192	125	$0.807\pm0.067\pm^{0.066}_{0.144}$	433	0	0.948±0.079
0.00715	125	$1.001\pm0.081\pm^{0.048}_{0.102}$	476	4	0.888±0.072
0.00358	125	$0.985\pm0.092\pm^{0.138}_{0.043}$	371	3	0.657±0.061
0.00238	125	$1.567\pm0.152\pm^{0.450}_{0.206}$	369	29	0.638±0.062
0.00179	125	$3.042\pm0.344\pm^{0.078}_{1.382}$	247	2	1.220±0.138
0.04087	250	$0.524\pm0.111\pm^{0.023}_{0.086}$	79	1	0.118±0.025
0.02384	250	$0.794\pm0.095\pm^{0.064}_{0.176}$	213	0	0.431±0.052
0.01431	250	$0.595\pm0.078\pm^{0.107}_{0.015}$	183	0	0.319±0.042
0.00715	250	$0.932\pm0.132\pm^{0.060}_{0.166}$	164	1	0.259±0.037
0.00477	250	$1.498\pm0.236\pm^{0.890}_{0.432}$	175	19	0.224±0.035
0.00358	250	$2.719\pm0.395\pm^{0.624}_{1.500}$	139	1	0.395±0.057

Table A.23: $F_2(x, Q^2)$ as obtained from an analysis where the data was binned in y and Q^2, reconstructed using the double angle method, and unfolded via an iterative method.

x	Q^2	$F2$ ±stat ±syst	$N_{\rm obs}$	$N_{\rm php}$	σ ±stat
0.04768	500	$0.833\pm0.154\pm^{0.133}_{0.235}$	82	0	0.236±0.044
0.02861	500	$0.396\pm0.089\pm^{0.409}_{0.076}$	58	0	0.114±0.026
0.01431	500	$0.625\pm0.142\pm^{0.143}_{0.099}$	64	1	0.111±0.025
0.00954	500	$0.787\pm0.197\pm^{0.284}_{0.016}$	55	0	0.100±0.025
0.00715	500	$1.905\pm0.461\pm^{0.051}_{0.685}$	61	0	0.089±0.022
0.09537	1000	$0.474\pm0.176\pm^{0.043}_{0.070}$	22	0	0.045±0.017
0.05722	1000	$0.606\pm0.193\pm^{0.027}_{0.252}$	33	0	0.051±0.016
0.02861	1000	$0.571\pm0.224\pm^{0.017}_{0.105}$	20	0	0.043±0.017
0.01907	1000	$0.767\pm0.272\pm^{0.180}_{0.128}$	23	0	0.056±0.020
0.01431	1000	$1.711\pm0.475\pm^{0.255}_{0.717}$	38	0	0.091±0.025
0.19074	2000	$0.741\pm0.314\pm^{0.103}_{0.121}$	14	0	0.055±0.023
0.11444	2000	$0.362\pm0.165\pm^{0.074}_{0.004}$	17	2	0.026±0.012
0.03815	2000	$1.418\pm0.712\pm^{0.121}_{0.242}$	11	0	0.027±0.014

Table A.24: $F_2(x,Q^2)$ as obtained from an analysis where the data was binned in y and Q^2, reconstructed using the double angle method, and unfolded via an iterative method (cont'd).

y	Q^2	A	c	s	p	$\delta_{\rm RC}$	$\delta^{\rm acc}_{\rm RC}$	$\delta_{\rm F_L}$	$\delta_{\rm ctr}$	$\delta_{\rm F_3}$	$\delta_{\rm weak}$
0.16000 0.30000	7 10	0.54	0.89	0.22	0.20	1.588	1.137	0.009	-0.040	0.000	1.000
0.30000 0.50000	7 10	0.54	0.91	0.28	0.25	0.442	0.604	0.048	0.029	0.000	1.000
0.16000 0.30000	10 14	0.75	0.75	0.24	0.18	0.832	0.482	0.008	-0.038	0.000	1.000
0.30000 0.50000	10 14	0.63	1.00	0.25	0.25	-0.013	0.033	0.041	0.033	0.000	1.000
0.16000 0.30000	14 20	0.78	0.79	0.23	0.18	0.565	0.214	0.008	-0.009	0.000	1.000
0.30000 0.50000	14 20	0.67	0.96	0.30	0.29	-0.130	-0.117	0.039	0.061	0.000	1.000
0.50000 0.70000	14 20	0.39	1.95	0.20	0.40	-0.619	-0.483	0.109	0.001	0.000	1.000
0.16000 0.30000	20 28	0.80	0.80	0.31	0.25	1.704	1.203	0.007	-0.039	0.000	1.000
0.30000 0.50000	20 28	0.71	1.08	0.36	0.39	0.008	-0.012	0.033	0.024	0.000	1.000
0.50000 0.70000	20 28	0.50	1.64	0.29	0.48	-0.376	-0.314	0.094	-0.030	0.000	1.000
0.08000 0.16000	28 40	0.81	1.05	0.24	0.25	1.598	0.800	0.002	0.002	0.000	1.000
0.16000 0.30000	28 40	0.81	0.90	0.39	0.36	0.656	0.465	0.006	-0.036	0.000	1.000
0.30000 0.50000	28 40	0.75	1.04	0.44	0.46	0.275	0.136	0.031	0.029	0.000	1.000
0.50000 0.70000	28 40	0.58	1.15	0.41	0.47	-0.391	-0.346	0.082	-0.041	0.000	1.000
0.08000 0.16000	40 56	0.83	1.01	0.28	0.28	1.764	0.938	0.002	0.000	0.000	1.000
0.16000 0.30000	40 56	0.79	1.05	0.38	0.40	0.875	0.611	0.006	-0.039	0.000	1.000
0.30000 0.50000	40 56	0.81	1.10	0.46	0.50	0.557	0.325	0.029	0.025	0.000	1.000
0.50000 0.70000	40 56	0.68	1.08	0.42	0.45	-0.081	-0.185	0.077	-0.047	0.000	1.000
0.08000 0.16000	56 80	0.80	1.00	0.27	0.27	1.439	0.432	0.002	0.022	0.000	1.000
0.16000 0.30000	56 80	0.83	0.87	0.41	0.36	0.677	0.361	0.005	-0.025	0.000	1.000
0.30000 0.50000	56 80	0.82	1.07	0.42	0.45	0.522	0.264	0.028	0.046	0.000	1.000
0.50000 0.70000	56 80	0.68	1.01	0.42	0.42	-0.170	-0.301	0.073	-0.032	0.000	1.000
0.08000 0.16000	80 160	0.81	1.05	0.29	0.31	1.249	0.413	0.001	-0.018	0.000	1.000
0.16000 0.30000	80 160	0.84	0.88	0.44	0.38	1.485	0.994	0.005	-0.057	0.000	1.000
0.30000 0.50000	80 160	0.82	0.98	0.53	0.52	0.984	0.702	0.023	0.006	0.000	1.000
0.50000 0.70000	80 160	0.69	1.20	0.53	0.63	0.164	-0.086	0.062	-0.047	0.000	1.000
0.08000 0.16000	160 320	0.77	1.01	0.27	0.27	1.139	0.411	0.001	-0.018	0.000	1.000
0.16000 0.30000	160 320	0.71	1.06	0.41	0.43	1.149	0.791	0.004	-0.036	0.000	1.000
0.30000 0.50000	160 320	0.46	1.40	0.31	0.43	0.825	0.754	0.020	-0.052	0.000	1.000

Table A.25: Bin properties for analyses in (y,Q^2) bins, using the electron only reconstruction method.

y	Q^2	A	c	s	p	δ_{RC}	$\delta_{\mathrm{RC}}^{\mathrm{acc}}$	$\delta_{\mathrm{F_L}}$	δ_{ctr}	$\delta_{\mathrm{F_3}}$	δ_{weak}
0.08000 0.16000	10 14	0.81	0.80	0.36	0.29	2.085	0.928	0.003	0.026	0.000	1.000
0.16000 0.30000	10 14	0.85	0.79	0.32	0.25	0.538	0.240	0.008	-0.031	0.000	1.000
0.08000 0.16000	14 20	0.93	0.87	0.45	0.39	1.100	0.316	0.002	0.048	0.000	1.000
0.16000 0.30000	14 20	0.92	0.90	0.34	0.31	0.191	-0.082	0.008	-0.006	0.000	1.000
0.30000 0.50000	14 20	0.78	1.16	0.23	0.27	-0.329	-0.372	0.039	0.058	0.000	1.000
0.08000 0.16000	20 28	0.95	0.92	0.45	0.41	1.497	0.494	0.002	0.020	0.000	1.000
0.16000 0.30000	20 28	0.94	0.83	0.42	0.35	1.549	0.829	0.007	-0.031	0.000	1.000
0.30000 0.50000	20 28	0.83	1.06	0.28	0.30	-0.011	-0.142	0.033	0.010	0.000	1.000
0.06000 0.08000	28 40	0.93	1.10	0.24	0.26	0.485	-0.282	0.001	-0.005	0.000	1.000
0.08000 0.16000	28 40	0.96	0.91	0.49	0.45	1.879	0.760	0.002	0.019	0.000	1.000
0.16000 0.30000	28 40	0.95	0.89	0.45	0.40	0.724	0.269	0.006	-0.037	0.000	1.000
0.30000 0.50000	28 40	0.90	0.97	0.37	0.36	0.335	0.019	0.031	0.026	0.000	1.000
0.50000 0.70000	28 40	0.77	1.16	0.23	0.26	-0.414	-0.513	0.082	-0.042	0.000	1.000
0.06000 0.08000	40 56	0.95	1.13	0.27	0.30	0.469	-0.327	0.001	-0.013	0.000	1.000
0.08000 0.16000	40 56	0.97	1.00	0.48	0.48	2.104	0.671	0.002	0.014	0.000	1.000
0.16000 0.30000	40 56	0.95	0.91	0.47	0.43	1.316	0.544	0.006	-0.043	0.000	1.000
0.30000 0.50000	40 56	0.94	0.94	0.41	0.39	0.865	0.335	0.029	0.007	0.000	1.000
0.50000 0.70000	40 56	0.83	1.05	0.25	0.27	-0.105	-0.326	0.077	-0.047	0.000	1.000
0.06000 0.08000	56 80	0.96	1.11	0.32	0.36	-0.212	-0.664	0.000	0.011	0.000	1.000
0.08000 0.16000	56 80	0.97	0.95	0.51	0.49	1.532	0.262	0.002	0.031	0.000	1.000
0.16000 0.30000	56 80	0.97	0.91	0.48	0.44	0.806	0.115	0.005	-0.009	0.000	1.000
0.30000 0.50000	56 80	0.96	0.86	0.47	0.41	0.860	0.351	0.028	0.017	0.000	1.000
0.50000 0.70000	56 80	0.90	0.82	0.35	0.29	-0.004	-0.352	0.073	-0.042	0.000	1.000
0.04000 0.06000	80 160	0.87	2.35	0.21	0.49	0.891	-0.598	0.000	-0.035	0.000	1.000
0.06000 0.08000	80 160	0.97	1.00	0.23	0.23	0.055	-0.520	0.000	0.262	0.000	1.000
0.08000 0.16000	80 160	0.97	0.93	0.57	0.53	1.387	0.328	0.001	-0.007	0.000	1.000
0.16000 0.30000	80 160	0.98	0.89	0.65	0.58	1.915	0.710	0.005	-0.050	0.000	1.000
0.30000 0.50000	80 160	0.94	0.94	0.58	0.54	1.357	0.550	0.023	-0.020	0.000	1.000
0.50000 0.70000	80 160	0.96	0.94	0.53	0.50	0.336	-0.160	0.062	-0.065	0.000	1.000
0.70000 0.90000	80 160	0.57	1.28	0.28	0.36	1.042	-0.146	0.129	-0.117	0.000	1.000
0.06000 0.08000	160 320	0.96	0.67	0.25	0.17	0.041	-0.401	0.000	-0.027	0.000	1.000
0.08000 0.16000	160 320	0.97	0.88	0.56	0.49	1.312	0.295	0.001	-0.012	0.000	1.000
0.16000 0.30000	160 320	0.98	0.93	0.62	0.58	1.314	0.483	0.004	-0.068	0.000	1.000
0.30000 0.50000	160 320	1.00	0.81	0.66	0.53	1.217	0.395	0.020	-0.023	0.000	1.000
0.50000 0.70000	160 320	1.00	0.84	0.51	0.43	0.646	-0.116	0.055	-0.052	0.000	1.000
0.70000 0.90000	160 320	0.82	0.93	0.51	0.48	0.532	-0.254	0.110	-0.176	0.000	1.000

Table A.26: Bin properties for analyses in $(y.Q^2)$ bins, using the double angle reconstruction method.

y	Q^2	A	c	s	p	δ_{RC}	$\delta_{\mathrm{RC}}^{\mathrm{acc}}$	$\delta_{\mathrm{F_L}}$	δ_{ctr}	$\delta_{\mathrm{F_3}}$	δ_{we}
0.08000 0.16000	320 640	0.94	1.13	0.48	0.55	1.152	0.046	0.001	-0.024	0.000	0.99
0.16000 0.30000	320 640	0.96	1.16	0.54	0.62	1.417	0.354	0.003	0.005	0.000	0.99
0.30000 0.50000	320 640	0.89	0.85	0.55	0.46	1.199	0.315	0.015	-0.026	0.000	0.99
0.50000 0.70000	320 640	0.93	1.05	0.54	0.57	0.932	0.318	0.047	-0.067	0.000	0.99
0.70000 0.90000	320 640	0.94	0.55	0.44	0.24	0.921	-0.181	0.094	-0.135	0.000	0.99
0.08000 0.16000	640 1280	1.00	0.95	0.53	0.50	0.785	-0.129	0.000	-0.010	0.001	0.99
0.16000 0.30000	640 1280	0.94	0.71	0.71	0.50	1.362	0.158	0.002	-0.118	0.001	0.99
0.30000 0.50000	640 1280	0.89	1.00	0.63	0.63	0.940	-0.064	0.011	-0.039	0.001	0.99
0.50000 0.70000	640 1280	0.91	1.16	0.68	0.79	0.612	0.123	0.037	-0.012	0.001	0.99
0.70000 0.90000	640 1280	0.93	1.00	0.60	0.60	0.663	-0.278	0.073	-0.201	0.001	0.99
0.08000 0.16000	1280 2560	1.00	2.00	0.50	1.00	1.394	-0.370	0.000	-0.110	0.004	0.98
0.16000 0.30000	1280 2560	1.00	1.08	0.71	0.77	1.480	0.466	0.001	-0.068	0.004	0.98
0.50000 0.70000	1280 2560	1.00	1.25	0.80	1.00	1.265	-0.467	0.027	-0.039	0.005	0.98

Table A.27: Bin properties for analyses in $(y.Q^2)$ bins, using the double angle reconstruction method (cont'd).

y	Q^2	F_2	$y_{\rm el}\downarrow$	$\delta_{\rm lo}$	$\delta^{\rm hi}$	$E_e\uparrow$	$E_e\Uparrow$	Box$\downarrow$	Box$\uparrow$	Vtx	$y_{\rm JB}\downarrow$	$y_{\rm JB}\uparrow$
0.00049	8	0.97	0.11	0.10	0.12	0.00	0.11	0.15	0.11	0.00	0.00	0.00
0.00024	8	1.38	-0.02	0.05	0.10	0.00	-0.01	-0.05	0.10	0.00	0.00	0.00
0.000 9	12	1.27	-0.04	-0.05	-0.04	0.00	-0.04	-0.04	-0.06	0.00	0.00	0.00
0.000 4	12	1.58	-0.10	-0.03	0.00	0.00	-0.08	-0.12	-0.06	0.00	0.00	0.00
0.00086	15	1.05	0.05	0.04	0.06	0.00	0.05	0.05	0.05	0.00	0.00	0.00
0.00043	15	1.46	-0.05	0.01	-0.34	0.00	-0.04	-0.05	-0.04	0.00	0.00	0.00
0.00029	15	1.86	-0.12	0.10	-0.02	0.00	-0.05	-0.12	-0.11	0.00	0.00	0.00
0.00143	25	0.96	0.04	0.04	0.05	0.00	0.04	0.04	0.04	0.00	0.00	0.00
0.00072	25	1.49	-0.06	-0.03	-0.20	0.00	-0.04	-0.06	-0.06	0.00	0.00	0.00
0.00048	25	1.99	-0.11	0.11	-0.41	0.00	-0.30	-0.11	-0.11	0.00	0.00	0.00
0.00334	35	1.01	-0.10	-0.10	-0.09	0.00	-0.10	-0.10	-0.10	0.00	0.00	0.00
0.00200	35	1.11	-0.02	-0.03	-0.02	0.00	-0.02	-0.02	-0.03	0.00	0.00	0.00
0.00100	35	1.28	0.05	0.09	-0.06	0.00	0.06	0.05	0.05	0.00	0.00	0.00
0.00067	35	1.83	-0.10	0.04	-0.40	0.00	-0.08	-0.10	-0.10	0.00	0.00	0.00
0.00477	50	1.02	-0.13	-0.13	-0.12	0.00	-0.13	-0.13	-0.13	0.00	0.00	0.00
0.00286	50	1.35	-0.14	-0.14	-0.13	0.00	-0.14	-0.14	-0.14	0.00	0.00	0.00
0.00143	50	1.28	0.06	0.07	-0.02	0.00	0.07	0.06	0.06	0.00	0.00	0.00
0.00095	50	1.76	-0.10	-0.00	-0.36	0.00	-0.03	-0.10	-0.10	0.00	0.00	0.00
0.00620	65	0.96	-0.12	-0.12	-0.11	0.00	-0.12	-0.12	-0.12	0.00	0.00	0.00
0.00372	65	1.00	-0.02	-0.02	0.01	0.00	-0.01	-0.02	-0.02	0.00	0.00	0.00
0.00186	65	1.18	0.06	0.09	0.02	0.00	0.07	0.06	0.06	0.00	0.00	0.00
0.00124	65	2.12	-0.34	-0.30	-0.66	0.00	-0.23	-0.34	-0.34	0.00	0.00	0.00
0.01192	125	0.90	-0.13	-0.14	-0.12	0.00	-0.13	-0.13	-0.13	0.00	0.00	0.00
0.00715	125	1.07	-0.11	-0.11	-0.09	0.00	-0.11	-0.11	-0.11	0.00	0.00	0.00
0.00358	125	1.09	0.01	0.01	-0.05	0.00	0.01	0.01	0.01	0.00	0.00	0.00
0.00238	125	1.19	-0.00	0.08	-0.17	0.00	0.17	-0.00	-0.00	0.00	0.00	0.00
0.02384	250	0.65	-0.02	-0.02	-0.02	0.00	-0.02	-0.02	-0.02	0.00	0.00	0.00
0.01431	250	0.79	0.02	0.02	0.03	0.00	0.02	0.02	0.02	0.00	0.00	0.00
0.00715	250	0.89	-0.04	-0.02	-0.17	0.00	-0.04	-0.04	-0.04	0.00	0.00	0.00

Table A.28: Systematic checks for the analysis in $(y.Q^2)$ bins. using the electron only reconstruction method.

y	Q^2	F_2	$y_{\rm el}\downarrow$	$\delta_{\rm lo}$	$\delta^{\rm hi}$	$E_e\uparrow$	$E_e\Uparrow$	Box$\downarrow$	Box$\uparrow$	Vtx	$y_{\rm JB}\downarrow$	$y_{\rm JB}\uparrow$
0.00114	12	0.70	0.05	0.07	-0.04	0.04	0.04	0.06	0.01	0.06	0.10	0.05
0.00069	12	0.79	0.09	0.17	-0.07	0.08	0.06	0.09	0.09	0.11	0.11	0.08
0.00143	15	0.75	0.02	0.04	-0.07	0.02	0.02	0.02	-0.00	-0.00	0.09	0.02
0.00086	15	0.94	0.02	0.08	-0.14	0.01	-0.00	0.02	0.02	0.01	0.04	-0.01
0.00043	15	1.08	0.15	0.26	-0.08	0.12	0.05	0.16	0.14	0.15	0.18	0.15
0.00238	25	0.77	0.01	0.03	-0.05	0.01	0.01	0.01	0.01	0.02	0.08	-0.01
0.00143	25	0.84	0.07	0.12	-0.04	0.07	0.05	0.07	0.07	0.07	0.09	0.05
0.00072	25	1.30	-0.02	0.07	-0.19	-0.08	-0.14	-0.01	-0.02	-0.01	-0.01	-0.02
0.00572	35	0.62	-0.00	-0.00	-0.01	-0.00	-0.00	0.00	0.00	-0.02	0.17	0 00
0.00334	35	0.82	-0.01	0.01	-0.04	-0.01	-0.01	-0.01	-0.01	0.00	0.06	-0.05
0.00200	35	1.03	-0.03	0.01	-0.09	-0.03	-0.04	-0.03	-0.03	0.00	-0.02	-0.04
0.00100	35	1.17	0.14	0.24	-0.04	0.09	0.04	0.14	0.13	0.17	0.15	0.13
0.00067	35	2.57	-0.48	-0.25	-0.78	-0.77	-0.52	-0.47	-0.49	-0.41	-0.48	-0.48
0.00817	50	0.54	0.02	0.02	0.00	0.02	0.02	0.02	0.02	0.04	-0.18	0.02
0.00477	50	0.97	-0.09	-0.08	-0.10	-0.09	-0.10	-0.09	-0.09	-0.07	-0.02	-0 11
0.00286	50	1.05	-0.03	-0.01	-0.09	-0.04	-0.06	-0 03	-0.04	0.03	-0.03	-0.06
0.00143	50	1.27	0.02	0.09	-0.10	-0.02	-0.09	0.02	0.02	0.03	0.03	0.01
0.00095	50	2.10	-0.18	0.06	-0.57	-0.65	-0.27	0.16	-0.19	-0.29	-0.18	-0.18
0.01063	65	0.60	-0.01	-0.01	-0.02	-0.01	-0.01	-0.01	-0.01	0.04	0.20	-0.01
0.00620	65	0.89	-0.07	-0.07	-0.07	-0.07	-0.07	-0.07	-0.07	-0.08	-0.01	-0.14
0.00372	65	1.00	0.01	0.03	-0.03	0.01	0.01	0.01	0.01	0 02	0.03	-0.03
0.00186	65	1.10	0.07	0.19	-0.07	0.03	-0.04	0.08	0.06	0.05	0.07	0.06
0.00124	65	2.69	-0.63	-0.37	-1.07	-1.11	-0.61	-0.62	-0.64	-0.57	-0.63	-0.63
0.02861	125	0.67	-0.10	-0.10	-0.10	-0.10	-0.10	-0.10	-0.10	-0.16	0.58	-0.09
0.02044	125	0.08	0.64	0.64	0.65	0.64	0.64	0.64	0.64	0.70	0.77	0.14
0.01192	125	0.81	-0.12	-0.12	-0.12	-0.12	-0.12	-0.12	-0.12	-0.08	-0.08	-0.14
0.00715	125	1.00	-0.06	-0.06	-0.10	-0.06	-0.06	-0.06	-0.07	-0.06	-0.05	-0.07
0.00358	125	0.98	0.07	0.12	-0.03	0.02	-0.01	0.07	0.07	0.07	0.08	0.06
0.00238	125	1.57	0.11	0.36	-0.11	-0.18	-0.07	0.13	0.11	0.03	0.12	0.11
0.00179	125	3.04	-0.63	-0.10	-1.03	-0.73	-0.73	-0.59	-0.74	-1.27	-0.63	-0.63
0.04087	250	0.52	-0.06	-0.05	-0.04	-0.06	-0.06	-0.06	-0.06	-0.08	-0.03	-0 03
0.02384	250	0.79	-0.12	-0.12	-0.13	-0.12	-0.12	-0.12	-0.12	-0.08	-0.07	-0.16
0.01431	250	0.60	0.03	0.03	-0.01	0.03	0.03	0.03	0.03	0.11	0.03	0.03
0.00715	250	0.93	-0.03	0.06	-0.15	-0.05	-0.06	0.03	-0.03	-0.04	-0 03	-0.03
0.00477	250	1.50	0.32	0.56	-0.14	0.12	-0.43	0.32	0.32	0.23	0.32	0.31
0.00358	250	2.72	-1.08	-0.79	-0.62	-0.62	-0.62	-0.95	-1.17	-0.62	-1.08	-1.08

Table A.29: Systematic checks for the analysis in $(y.Q^2)$ bins. using the double angle reconstruction method.

y	Q^2	F_2	$y_{el}\downarrow$	δ_{lo}	δ^{hi}	$E_e\uparrow$	$E_e\Uparrow$	Box$\downarrow$	Box$\uparrow$	Vtx	$y_{JB}\downarrow$	$y_{JB}\uparrow$
0.04768	500	0.83	-0.18	-0.17	-0.21	-0.18	-0.18	-0.18	-0.18	-0.13	-0.17	-0.19
0.02861	500	0.40	0.22	0.22	0.18	0.22	0.21	0.22	0.22	0.23	0.23	0.22
0.01431	500	0.63	0.01	0.03	-0.09	0.01	0.01	0.01	0.01	0.14	0.01	0.01
0.00954	500	0.79	0.11	0.17	-0.01	0.03	0.03	0.11	0.11	0.21	0.11	0.09
0.00715	500	1.90	-0.35	-0.05	-0.56	-0.44	-0.44	-0.40	-0.43	-0.64	-0.43	-0.43
0.09537	1000	0.47	-0.05	0.02	-0.07	-0.05	-0.05	-0.05	-0.05	0.01	-0.05	-0.05
0.05722	1000	0.61	-0.12	-0.12	-0.16	-0.12	-0.12	-0.12	-0.12	-0.09	-0.12	-0.14
0.02861	1000	0.57	-0.01	0.02	-0.07	-0.06	-0.06	-0.01	-0.01	-0.03	-0.01	-0.04
0.01907	1000	0.77	0.02	1.54	-0.09	-0.03	-0.08	0.02	0.02	0.18	0.02	0.02
0.01431	1000	1.71	-0.26	-0.33	-0.26	-0.26	-0.26	-0.40	-0.57	-0.26	-0.57	-0.57
0.19074	2000	0.74	-0.00	0.10	-0.06	-0.00	-0.00	-0.00	-0.00	-0.11	-0.00	-0.00
0.11444	2000	0.36	0.05	0.05	0.05	0.05	0.05	0.05	0.05	0.02	0.05	0.05
0.03815	2000	1.42	-0.01	0.12	-0.17	-0.01	-0.01	-0.01	-0.01	-0.17	-0.01	-0.01

Table A.30: Systematic checks for the analysis in $(y.Q^2)$ bins, using the double angle reconstruction method (cont'd).

Bibliography

[A+69] V. Albrecht et al. Separation of σ_t and σ_l in the Region of Deep Inelastic Electron-Proton Scattering. *DESY*. 46. 1969.

[A+76] H. L. Anderson et al. Measurement of Nucleon Structure Functions in Muon Scattering at 147 GeV/c. *Phys. Rev. Lett.*. 37:4 7. 1976.

[A+91] C. Alvisi et al. The ZEUS Vertex Detector: Design and Prototype. *Nucl. Instrum. Meth. A*. 305:30 38. 1991.

[Abr92] H. Abramowicz. Isitamu. 1992. algorithm to flag possible muons. ZEUS PHANTOM program library.

[ACS95] H. Abramowicz. A. Caldwell. and R. Sinkus. Neural Network Based Electron Identification in the ZEUS Calorimeter. *DESY*. 54. 1995.

[AEM78] G. Altarelli. R. K. Ellis. and G. Martinelli. Leptoproduction and Drell-Yan Processes Beyond the Leading Approximation in Chromodynamics. *Nucl. Phys. B*. 143:521 545. 1978.

[AGLP89] B. Andersson. G.Gustafson. L. Lönnblad. and U. Petterson. Coherence Effects in Deep Inelastic Scattering. *Z. Phys. C*. 43:625 632. 1989.

[Alt92] G. Altarelli. QCD and Experiment: Status of α_s. In P. M. Zerwas and H. A. Kastrup. editors. *QCD 20 Years Later*. pages 172 202. World Scientific. Singapore. 1992.

[AP77] G. Altarelli and G. Parisi. Asymptotic Freedom in Parton Language. *Nucl. Phys B*. 126:298 318. 1977.

[App92] Application Software Group. *HBOOK Reference Manual*. Computing and Networks Division. CERN. 1992. Version 4.15.

[App93] Application Software Group. *PAW Physics Analysis Workstation*. Computing and Networks Division. CERN. 1993. Version 2.03.

[B+67] W. Bartel et al. A Magnetic Spectrometer for High Energy Electron Scattering Experiments. *Nucl. Instr. Meth.*. 53:293 198. 1967.

[B+70] W. Bartel et al. Electromagnetic Proton Form Factors at Squarted Four-Momentum between 1 and 3 GeV/c^2. *Phys. Lett. B*. 33(3):245 248. 1970.

[B+79] A. Bodek et al. Experimental Studies on the Neutron and Proton Electromagnetic Structure Functions. *Phys. Rev.*. D20(7):1471 1552. 1979.

[B+87] R. Brun et al. Technical report. 1987.

[BAB88] H. Brückmann. B. Anders. and U. Behrens. Hadron Sampling Calorimetry. A Puzzle of Physics. *Nucl. Instrum. Meth. A*. 263:136 149. 1988.

[Ban93] D. Bandyopadhyay. Mutrig. 1993. algorithm to find the muon background events in the TLT. ZEUS PHANTOM program library.

[BB94] U. Bassler and G. Bernardi. On the Kinematic Reconstruction of Deep Inelastic Scattering at HERA: the Σ Method. *DESY*. 231. 1994. HEP-EX-9412994.

[BBDM78] W. A. Bardeen. A. J. Buras. D. W. Duke. and T. Muta. Deep Inelasitc Scattering Beyond the Leading Order in Asymptotically Free Gauge Theories. *Phys. Rev. D*. 18(11):3998 4017. 1978.

[BBRK91] J. Bartels. M. Besancon. A. De Roeck. and J. Kurzhoefer. Measurements of Hot Spots at HERA. In W. Buchmuller and G. Ingelmann. editors. *Physics at HERA*. pages 203 213. DESY. Hamburg. Germany. 1991.

[BCD87a] BCDMS Collaboration. A. C. Benvenuti et al. A High Statistics Measurement of the Nucleon Structure Function $F_2(x, Q^2)$ from Inelastic Muon Carbon Scattering at High q^2. 1987.

[BCD87b] BCDMS Collaboration. R. Voss. Charged Lepton Interactions. In W. Bartel and R. Rückl. editors. *Int. Symposium on Lepton and Photon Interactions*. page 581. North-Holland. Amsterdam. 1987.

[BCD90] BCDMS Collaboration. A. C. Benvenuti et al. A High Statistics Measurement of the Deuteron Structure Functions $F_2(x, Q^2)$ and r from Inelastic Muon Scattering at High q^2. 1990.

[BCF91] J. Bartels. K. Charchule. and J. Feltesse. $F_2(x, Q^2)$ Scaling Violations at Very Small x. In W. Buchmuller and G. Ingelmann. editors. *Physics at HERA*. pages 193 201. DESY. Hamburg. Germany. 1991.

[BCKK91] B. Badelek. K. Charchula. M Krawczyk. and J. Kwieciński. Small x Physics. *DESY*. 124. 1991.

[BDK93] F. Boodjema. A. Djouadi. and J. L. Kneus. Excited Fermions at e^+e^- and ep Colliders. *Z. Phys. C*. 57:425 449. 1993.

[BEB85] BEBC. P. Allasin et al. q^2 Dependence of the Proton and Neutron Structure Functions from Neutrino and Antineutrino Scattering in Deuterium. 1985.

[BEB90] BEBC. G. T. Jones et al. A Measurement of the Proton Structure Functions from Neutrino-Hydrogen and Antineutrino-Hydrogen Charged-Current Interactions. 1990.

[Ben91] S. Bentvelsen. Optimal Use of Kinematical Variables for $x - q^2$ Reconstruction in Hard NC Events. Technical Report 14. ZEUS-Note. 1991.

[Ben94] S. Bentvelsen. *Measurement of the Proton Structure Function at HERA Using the ZEUS Detector*. PhD thesis. University of Amsterdam. 1994.

[BFH92] Ulf Behrens. Mariusz Flasinski. and Lars Hagge. ZEXP - The ZEUS Expert System. *DESY*. 141. 1992.

[BFHO94] Ulf Behrens. Mariusz Flasiński. Lars Hagge. and Kars Ohrenberg. ZEX An Expert System for ZEUS. *IEEE Trans. Nucl. Sci.*. 41(1):152 156. 1994.

[BFHV92] Ulf Behrens. Mariusz Flasinski. Lars Hagge. and Wolfgang O. Vogel. The Eventbuilder of the ZEUS Experiment. In *Proc. Computing in High Energy Physics*. 1992.

[BFP86] BFP. P. D. Meyers et al. Measurement of the Nucleon Structure Function in Iron Using 215- and 93-gev Muons. 1986.

[BHV93] Ulf Behrens. Lars Hagge. and Wolfgang O. Vogel. The Eventbuilder of the ZEUS Experiment. *Nucl. Instr. & Meth. A*. 332:346 353. 1993.

[BHV94] Ulf Behrens. Lars Hagge. and Wolfgang O. Vogel. The ZEUS Eventbuilder: Experience with a Distributed Real-Time Parallel Transputer System. *IEEE Trans. Nucl. Sci.*. 41(1):239 245. 1994.

[BI93] P. Bruni and G. Ingelmann. In *Europhysics Conference on HEP*. 1993.

[Bjo69] J. D. Bjorken. Asymptotic Sum Rules at Infinite Momentum. *Phys. Rev.* 179(5):1547 1553. 1969.

[BL78] Y. Y. Balitskij and L. N. Lipatov. The Pomeranchuk Singularity in Quantum Chromodynamics. *Sov. J. Nucl. Phys.*. 28(6):822 829. 1978.

[Blo84] V. Blobel. Unfolding Methods in High Energy Physics Experiments. *DESY*. 118. 1984.

[Blü90] J. Blümlein. Leading Log Radiative Corrections to Deep Inelastic Neutral and Charged Current Scattering at HERA. *Z. Phys. C*. 47:89 93. 1990.

[BR91] J. Bartels and M. G. Ryskin. Absorptive Corrections to Structure Functions at Small-x. *Z. Phys. C*. 60:751 756. 1991.

[BRW87] W. Buchmüller. R. Rückl. and D. Wyler. Leptoquarks in Lepton-Quark Collisions. *Phys. Lett. B*. 191(4):442 448. 1987.

[Cal70] C. G. Callan. Broken Scale Invariance in Scalar Field Theory. *Phys. Rev. D*. 2(8):1541 1547. 1970.

[Cas74] W. Caswell. Asymptotic Behaviour of Non-Abelian Gauge Theories to Two-Loop Order. *Phys. Rev. Lett.*. 33(4):244 246. 1974.

[CCF92] CCFR. E. Oltman et al. Nucleon Structure Functions from High Energy Neutrino Interactions. 1992.

[CCG+94] A. Caldwell. F. Chlebana. I. Gialas. A Goussiou. D. Krakauer. M. Lancaster. and R. Yoshida. An Electron Energy Correction Method: A Preliminary Implementation and its Effect on the F_2 Measurement. Technical Report 51. ZEUS-Note. 1994.

[CDH83] CDHS. H. Abramowicz et al. Neutrino and Antineutrino Charged-Current Inclusive Scattering in Iron in the Energy Range $20 < e_\nu < 300$ gev. 1983.

[CDH91] CDHSW. P. Berge et al. A Measurement of Differential Cross-Sections and Nucleon Structure Functions in Charged-Current Neutrino Interactions on Iron. 1991.

[CG69] C. G. Callan and D. J. Gross. High-Energy Electroproduction and the Constitution of the Electric Current. *Phys. Rev. Lett.*. 22(4):156 158. 1969.

[CH56] E. E. Chambers and R. Hofstadter. Structure of the Proton. *Phys. Rev.*. 103(5):1454 1463. 1956.

[CHA84] CHARM. F. Bergsma et al. Experimental Study of the Nucleon Longitudinal Structure Function in Charged-Current Neutrino and Anti-Neutrino Interactions. 1984.

[CHI79] CHIO. B. A. Gordon et al. Measurement of the Nucleon Structure Function. 1979.

[CR92] A. Caldwell and J. Repond. Eexotic. 1992. algorithm to find the most likely scattered electron. ZEUS PHANTOM program library.

[CSDL91] A. M. Cooper-Sarkar, R. C. E. Devenish. and M. Lancaster. Measurements of $F_L(x, Q^2)$ at Low-x and Extraction of the Gluon Distribution. In W. Buchmuller and G. Ingelmann. editors. *Physics at HERA*. pages 155–170. DESY. Hamburg. Germany. 1991.

[CTE93] CTEQ Collaboration. J. Botts et al. CTEQ Parton Distributions and Flavor Dependence of Sea Quarks. 1993.

[CTE94] CTEQ Collaboration. H. L. Lai et al. Global QCD Analysis and CTEQ Parton Distributions. 1994. HEP-PH-9410404.

[D+91] M. Derrick et al. Design and Construction of the ZEUS Barrel Calorimeter. *Nucl. Instrum. Meth. A*. 309:77–100. 1991.

[d'A94a] G. d'Agostini. A Multidimensional Unfolding Method Based on Bayes' Theorem. *DESY*. 099. 1994.

[d'A94b] G. d'Agostini. A Multidimensional Unfolding Method Based on Bayes' Theorem. talk given at DESY. May 4^{th}. 1994.

[DDR83] A. Devoto. D. Duke. and J. Owens R. G. Roberts. Direct Analysis of Scaling Violations in Large-Q^2 Deep-Inelastic Neutrino and Muon Scattering. *Phys. Rev. D*. 27(3):508 522. 1983.

[dJ92] P. de Jong. Hebbes. 1992. algorithm to identify the most likely scattered electron.

[DKMT91] Y. L. Dokshitzer. V. A. Khoze. A. H. Mueller. and S. I. Troyan. *Basics of Perturbative QCD*. Editions Frontiéres. Gif-sur-Yvette Cedex. France. 1991.

[DO84] D. Duke and J. Owens. q^2-Dependent Parametrizations of Parton Distribution Functions. *Phys. Rev. D*. 30(1):49 54. 1984.

[Doc92] T. Docker. Beamelec. 1992. algorithm to identify the most likely scattered electron.

[Dok77] Y. L. Dokshitzer. Calculation of Structure Functions of Deep-Inelastic Scattering and e^+e^- Annihilation by Perturbation Theory in Quantum Chromodynamics. *Sov. Phys. JETP*. 46(4):641 653. 1977.

[DW64] S. D. Drell and J. D. Walecka. Electrodynamic Processes with Nuclear Targets. *Ann. Phys.*. 28:18 33. 1964.

[DY70] S. D. Drell and T. M. Yan. Connection of Elastic Electromagnetic Nucleon Form Factors at Large q^2 and Deep Inelastic Structure Functions Near Threshold. *Phys. Rev. Lett.*. 24(4):181 186. 1970.

[DY71] S. D. Drell and T. M. Yan. Partons and Their Applications at High Energies. *Ann. Phys.*. 66:578 623. 1971.

[E6694] E665 Collaboration. New Experimental Results on F_2 from E665. talk given by H. Schellman at the Workshop on Deep Inelastic Scattering and QCD. Paris. France. April 24-28. 1994.

[EKL94] R. K. Ellis. Z. Kunszt. and E. M. Levin. The Evolution of Parton Distributions at Small-x. *Nucl. Phys. B*. 420:517 549. 1994.

[EMC81] EMC Collaboration. J. J. Aubert et al. Measurement of the Nucleon Structure Function F_2 in Muon-Iron Interactions at 120. 250 and 280 gev. 1981.

[EMC86] EMC Collaboration. J. J. Aubert et al. A Detailed Study of the Nucleon Structure Functions in Deep-Inelastic Muon Scattering in Iron. 1986.

[EMC87] EMC Collaboration. J. J. Aubert et al. Measurement of the Nucleon Structure Functions F_2^N in Deep Inelastic Muon Scattering from Deuterium and Comparison with Those from Hydrogen and Iron. 1987.

[EMC88a] EMC Collaboration. J. Ashman et al. Measurement of the Ratios of Deep Inelastic Muon-Nucleus Cross Sections on Various Nuclei Compared to Deuterium. *Phys. Lett. B*. 202(4):603 610. 1988.

[EMC88b] EMC Collaboration. M. Arneodo et al. Shadowing in Deep Inelastic Muon Scattering from Nuclear Targets. *Phys. Lett. B*. 211(4):493 499. 1988.

[EMC90] EMC Collaboration. M. Arneodo et al. Measurement of the Nucleon Structure Function in the Range $0.002 < x < 0.17$ and $0.2 < Q^2 < 8$ GeV^2 in Deuterium. Carbon and Calcium. 1990.

[F+93] B. Foster et al. The Performance of the ZEUS Central Tracking Detector z-by-Timing Electronics in a Transputer Based Data Acquisition System. *Nucl. Phys. B*. 32:181 188. 1993.

[Fey72] R. P. Feynman. *Photon-Hadron Interactions*. W A. Benjamin. New York. 1972.

[FHM53] H. R. Fechter. R. Hofstadter. and J. A. McIntyre. Scattering of High Energy Electrons and the Method of Nuclear Recoil. *Phys. Rev.*. 91:422 423. 1953.

[Fla81] Matt Flavin. *Fundamental Concepts of Information Modeling*. Yourdon Press. Englewood Cliffs. N.J.. 1981.

[Fle94] I. Fleck. *Nachweis von Elektronen aus der e-p Streuung mit dem Hadron-Elektron-Separator im ZEUS-Experiment.* PhD thesis. University of Hamburg. 1994. (in German).

[Fro61] M. Froissart. Asymptotic Behaviour and Subtractions in the Mandelstam Representation. *Phys. Rev.*. 123(3):1053–1057. 1961.

[Gin93] Douglas M. Gingrich. The Application of Transputers in the ZEUS Experiment. In *Proc. 8th Conference on Real-Time Computer Applications in Nuclear, Particle and Plasma Physics.* 1993. (TRIUMF-93-1).

[GKR94] K. Golec-Biernat, M. W. Krasny, and S. Riess. Recombination Effects in the Structure Function Evolution at Low x. Can They Be Observed at HERA? *DESY.* 131. 1994.

[GL72] V. N. Gribov and L. N. Lipatov. *Sov. J. Nucl. Phys.*. 15:438 and 675. 1972.

[GLR83] V. N. Gribov, E. M. Levin, and M. G. Ryskin. Semihard Processes in QCD. *Phys. Rep.*. 100:1–150. 1983.

[GM13] H. Geiger and E. Marsden. *Phil. Mag.*. 25:604. 1913.

[GM64] M. Gell-Mann. A Schematic Model of Baryons and Mesons. *Phys. Lett.*. 8:214f. 1964.

[GML54] M. Gell-Mann and F. E. Low. Quantum Electrodynamics at Small Distances. *Phys. Rev.*. 95(2):1300–1312. 1954.

[GNS94] E. Gallo, S. Nickel, and J. K. Sedgbeer. The 1993 TLT and DST Selection of the Structure Function Group. Technical Report 26. ZEUS-Note. 1994.

[GRV90] Glück, Reya, and Vogt. Radiatively Generated Parton Distributions for High Energy Collisions. *Z. Phys. C.* 48:471–482. 1990.

[GRV92] Glück, Reya, and Vogt. Parton Distributions for High Energy Collisions. *Z. Phys. C.* 53:127–134. 1992.

[H1 93a] H1 collaboration. I. Abt et al. Measurement of the Proton Structure Function $F_2(x, Q^2)$ in the low-x region at HERA. *Nucl. Phys. B.* 407:515–538. 1993.

[H1 93b] H1 Collaboration. I. Abt et al. The H1 Detector at HERA. *DESY.* 103. 1993.

[H1 93c] H1 collaboration. T. Ahmed et al. Total Photoproduction Cross-Section Measurement at HERA Energies. *Phys. Lett. B.* 299:374–384. 1993.

[H1 94] H1 collaboration. T. Ahmed et al. First Measurement of the Charged Current Cross-Section at HERA. *Phys. Lett. B.* 324:241–248. 1994.

[H1 95] H1 collaboration. T. Ahmed et al. A Measurement of the Proton Structure Function $F_2(x, Q^2)$. *DESY.* 6. 1995.

[Hab89] C. Habfast. *Großforschung mit kleinen Teilchen - DESY 1956-1970.* Springer-Verlag. Berlin. Germany. 1989. (in German).

[Han63] L. Hand. Experimental Investigation of Pion Electroproduction. *Phys. Rev.* 129(4):1834–1846. 1963.

[HER87] HERA workshop. R. D. Peccei (ed.). *Physics at HERA.* DESY. Hamburg. Germany. 1987.

[HER90] HERMES Collaboration. A Proposal to Measure the Spin-Dependent Structure Functions of the Neutron and the Proton at HERA. 1990.

[HER91] HERA workshop. W. Buchmüller, G. Ingelmann (eds.). *Physics at HERA.* DESY. Hamburg, Germany. 1991. Workshop held October 29-30. 1991. at DESY.

[HER94] HERA-*B* Collaboration. T. Lohse et al. HERA-*b*: An Experiment to Study CP Violation in the B System Using an Internal Target at the HERA Proton Ring. Technical report. DESY-PRC. 1994.

[HKZ85] K. Hagiwara, S. Komaniya, and D. Zeppenfeld. Excited Lepton Production at LEP and HERA. *Z. Phys. C.* 29:115–122. 1985.

[HM55] R. Hofstadter and R. W. McAllister. Electron Scattering from the Proton. *Phys. Rev.*. 98:217f. 1955.

[HM84] F. Halzen and A. D. Martin. *Quarks & Leptons.* John Wiley & Sons, Inc., Singapore. 1984.

[Hol87] W. Hollik. Radiative Corrections in Deep Inelastic Scattering – Essentials for HERA Processes. In R. D. Peccei, editor. *Physics at HERA.* pages 579–604. DESY. Hamburg, Germany. 1987.

[HP87] Derek J. Hatley and Imtiaz A. Pirbhai. *Strategies for Real-Time System Specification.* Dorset House Publishing Co., Inc., 353 West 12th Street, NewYork, NY 10014. 1987.

[IR89] G. Ingelmann and R. Ruckl. Quark Momentum Distributions from ep Collisions: Strategies and Prospects. *DESY.* 25. 1989.

[Jaf85] R. L. Jaffe. Deep Inelastic Scattering with Application to Nuclear Targets. In A. Picklesimer M. B. Johnson, editor. *Relativistic Dynamics and Quark-Nuclear Physics.* pages 537–618. Los Alamos National Laboratory. John Wiley & Sons. 1985.

[JB79] F. Jacquet and A. Blondel. In U. Amaldi, editor. *Proc. of the study of an ep facility for Europe.* page 391. DESY. Hamburg. Germany. 1979. (report 79/48).

[Jon74] D. R. T. Jones. Two-Loop Diagrams in Yang-Mills Theory. *Nucl. Phys. B.* 75:531–538. 1974.

[Kla88] R. Klanner. Test Program for the ZEUS Calorimeter. *Nucl. Instrum. Meth. A.* 265:200–209. 1988.

[KLF77] E. A. Kuraev, L. N. Lipatov, and V. S. Fadin. The Pomeranchuk Singularity in Nonabelian Gauge Theories. *Sov. Phys. JETP.* 45(2):199–204. 1977.

[KMRS90] J. Kwiecinski, A. D. Martin, R. G. Roberts, and W. J. Stirling. Parton Distributions at Small-x. *Phys. Rev. D*, 42(11):3645–3659, 1990.

[Krü92] J. Krüger. The Uranium Scintillator Calorimeter for the ZEUS Detector at the Electron-Proton Collider HERA — The Heart of ZEUS —. Internal Report F35-92-02, DESY, 1992.

[KS74] J. Kogut and L. Susskind. Parton Models and Asymptotic Freedom. *Phys. Rev. D*, 9(12):3391–3399, 1974.

[KSM91a] A. Kwiatkowski, H. Spiesberger, and H.-J. Möhring. Characteristics of Radiative Events in Deep Inelastic ep Scattering at HERA. *Z. Phys. C*, 50:165–178, 1991.

[KSM91b] A. Kwiatkowski, H. Spiesberger, and H.-J. Möhring. HERACLES. An Event Generator for ep Interactions at HERA Including Radiative Processes. In W. Buchmüller and G. Ingelmann, editors, *Physics at HERA*, pages 1294–1310. DESY, Hamburg, Germany, 1991. (Version 4.1).

[Lev92] E. M. Levin. Parton Density at Small x. In P. M. Zerwas and H. A. Kastrup, editors, *QCD — 20 Years Later*, pages 310–334. World Scientific, Singapore, 1992.

[Lev95] A. Levy. The Energy Behaviour of Real and Virtual Photon-Proton Cross Sections. *DESY*, 22, 1995.

[Loh92] E. Lohrmann. *Hochenergiephysik*. Teubner Studienbücher, Stuttgart, Germany, 1992. (4th revised edition, in German).

[Lön92] L. Lönnblad. Ariadne Version 4 - A Program for Simulation of QCD Cascades Implementing the Colour Dipole Model. *Comp. Phys. Comm.*, 71:15–31, 1992.

[LP72] P. V. Landshoff and J. C. Polkinghorne. Models for Hadronic and Leptonic Processes at High Energy. *Phys. Rep. C*, 5(1):1–55, 1972.

[M+93] J. Mitchell et al. The Pulsed Light Calibration System of the ZEUS Calorimeter. *Nucl. Phys. B*, 32:106–114, 1993.

[Man94] O. Manczak. The Computing Environment for Physics Analysis for ZEUS Experiment at HERA. In S. C. Loken, editor, *Computing in High Energy Physics*, pages 351–353. Lawrence Berkeley Laboratory, Berkeley, California 94720, 1994.

[Mar92] G. Marchesini. Structure Function for Large and Small x. In L. Cifarelli and Y. Dokshitzer, editors, *QCD at 200 TeV*, pages 183–193. Plenum Press, New York, 1992. and references therein.

[Mar93] A. D. Martin. Structure Functions and Small x Physics. In F. Barreiro, L. Hervas, and L. Labarga, editors, *Physics at HERA*, pages 250–292. Universidad Autonoma de Madrid, Spain, World Scientific, Singapore, 1993.

[Mot29] N. F. Mott. The Scattering of Fast Electrons by Atomic Nuclei. *Proc. Roy. Soc.*, 124:425–442, 1929.

[MQ86] A. H. Mueller and J. Qiu. Gluon Recombinations and Scattering at Small Values of x. *Nucl. Phys. B*, 268:427–452, 1986.

[MRS93a] A. D. Martin, Roberts, and Stirling. Parton Distributions Updated. *Phys. Lett. B*, 306(1.2):145–150, 1993.

[MRS93b] A. D. Martin, R. G. Roberts, and W. J. Stirling. New Information on Parton Distributions. *Phys. Rev. D*, 47(3):867–882, 1993.

[MS94] A. D. Martin and W. J. Stirling. Parton Distributions of the Proton. *RAL (Preprint)*, 94-055, 1994. HEP-PH-9406314.

[MT69] L. W. Mo and Y. S. Tsai. Radiative Corrections to Elastic and Inelastic ep and μp Scattering. *Rev. Mod. Phys.*, 41(1):205–295, 1969.

[MT91] J. G. Morfin and W. K. Tung. Parton Distributions from a Global QCD Analysis of Deep Inelastic Scattering and Lepton Pair Production. *Z. Phys. C*, 52:13–29, 1991.

[Mue90] A. H. Mueller. Small-x Behavior and Parton Saturation: A QCD Model. *Nucl. Phys. B*, 335:115–137, 1990.

[Mue91] A. H. Mueller. Jets at LEP and HERA. *J. Phys. G*, 17:1443–1454, 1991.

[Nac91] O. Nachtmann. *Elementarteilchenphysik: Phänomene und Konzepte*. Friedr. Vieweg & Sohn, Braunschweig, Germany, 1991. (revised reprint, in German).

[NIK90] NIKHEF, Electronic Department, Amsterdam, The Netherlands. *Short Hardware Description of the 2TP_VME Module*, September 1990.

[NMC91] NMC Collaboration, P. Amaudruz et al. Gottfried Sum from the Ratio F_2^n/F_2^p, 1991.

[NZ92] N. N. Nikolaev and B. G. Zakharov. Pomeron Structure Function and Diffraction Dissociation fo Virtual Photons in Perturbative QCD. *Z. Phys. C*, 53:331–345, 1992.

[Ohr96] K. Ohrenberg. PhD Thesis, University of Hamburg, 1996. (in preparation).

[OT92] J. F. Owens and W. K. Tung. Parton Distribution Functions of Hadrons. *Ann. Rev. Nucl. Part. Sci.*, 42:291–332, 1992.

[Par94] Particle Data Group, L. Montanet et al. Standard Model of Electroweak Interactions. *Phys. Rev. D*, 50(3):1304–1311, 1994.

[PB93] H. Plothow-Besch. PDFlib: A Library of all Available Parton Density Functions of the Nucleon, the Pion and the Photon and the Corresponding α_s Calculations. *Comp. Phys. Comm.*, 75:396–416, 1993.

[Pen83] M. R. Pennington. Cornerstones of QCD. *Rep. Prog. Phys.*, 46:393–513, 1983.

[Pri93] A. Prinias, Alhalo, 1993. algorithm to find beam halo muon candidates in BCAL. ZEUS PHANTOM program library.

[Pry93] K. Prytz. Probing the Gluon Density at HERA. *J. Phys. G*, 19:1628–1630, 1993.

[Pry94] K. Prytz. An Approximate Next-to-Leading Order Relation Between the Low-x F_2 Scaling Violations and the Gluon Density. *Phys. Lett. B*, 332:393–397, 1994.

[PZ94] K. Piotrzkowski and M. Zachara. Determination of the ZEUS Luminosity in '93. Technical Report 167. ZEUS-Note. 1994.

[Rep92] J. Repond. Elec5. 1992. algorithm to find the most likely scattered electron. ZEUS PHANTOM program library.

[Rob90] R. G. Roberts. *The Structure of the Proton: Deep Inelastic Scattering*. Cambridge University Press. Cambridge. England. 1990.

[Ros50] M. N. Rosenbluth. High Energy Elastic Scattering of Electrons on Protons. *Phys. Rev.*. 79(4):615–618. 1950.

[Ros94] J. L. Rosner. Overview of the Standard Model. In *Physics from Planck Scale to Electroweak Scale*. World Scientific. Singapore. 1994. EFI 94-59 and HEP-PH-9411396.

[Rut11] E. Rutherford. *Phil. Mag.*. 21:669. 1911.

[S+91] H. Spiesberger et al. Radiative Corrections at HERA. In W. Buchmuller and G. Ingelmann. editors. *Physics at HERA*. pages 798–839. DESY. Hamburg. Germany. 1991.

[Sax88] D. H. Saxon. Multicell Drift Chambers. *Nucl. Instrum. Meth. A*. 265:20–32. 1988.

[SB87] T. Sjöstrand and M. Bengtsson. The Lund Monte Carlo for Jet Fragmentation and e^+e^- Physics - JETSET Version 6.3 - An Udate. *Comp. Phys. Comm.*. 43:367–379. 1987.

[Sch92a] S. Schlenstedt. Evtake. 1992. algorithm to reject events which were taken when the experiment was not fully operational. ZEUS PHANTOM program library.

[Sch92b] S. Schlenstedt. Rmspark. 1992. algorithm to find isolated bad cells in the calorimeter. ZEUS PHANTOM program library.

[Sch92c] Thorsten Schlichting. Überwachung und Auswertung des Datenflusses am ZEUS Eventbuilder. Diplomarbeit. University of Hamburg. April 1992.

[Sjö86] T. Sjöstrand. The Lund Monte Carlo for Jet Fragmentation and e^+e^- Physics - JETSET. *Comp. Phys. Comm.*. 39:347–407. 1986.

[SP53] E. C. G. Stückelberg and A. Petermann. *Helv. Phys. Acta*. 26:499. 1953.

[ST64] A. A. Sokolov and M. Ternov. *Sov. Phys. Doklady*. 8:1203. 1964.

[Sym70] K. Symanzik. Small Distance Behaviour in Field Theory and Power Counting. *Comm. Math. Phys.*. 18:227–246. 1970.

[Tay75] R. Taylor. In W. T. Kirk. editor. *Proc. International Symposium on Lepton and Photon Interactions at High Energies*. page 679. 1975.

[Tay91] R. Taylor. An Historical Review of Lepton Proton Scattering. In J. Hawthorne. editor. *Lepton-Hadron Scattering*. pages 1–19. 19th SLAC Summer Institute on Particle Physics. 1991. SLAC-report-398.

[Tok93] K. Tokoshuku. electronic news #365. folder ZEUS.GENERAL. on node VXDESY.DESY.DE. 1993.

[Tsu92] T. Tsurugai. Comcos. 1992. algorithm to flag QED Compton / cosmic muon events. ZEUS PHANTOM program library.

[Uij92] H. Uijterwaal. *The Global Second Level Trigger for ZEUS*. PhD thesis. University of Amsterdam. 1992.

[Vir92] Virchaux. Nucleon Structure Functions. In P. M. Zerwas and H. A. Kastrup. editors. *QCD - 20 Years Later*. pages 205–271. World Scientific. Singapore. 1992.

[Wai93] L. Wai. Islands. 1993. algorithm to assign calorimeter cell to islands. ZEUS PHANTOM program library.

[Whi92] J. Whitmore. Lxelid. 1992. algorithm to identify the most likely scattered electron. ZEUS PHANTOM program library.

[Wig88] R. Wigmans. High Resolution Hadron Calorimetry. *Nucl. Instrum. Meth. A*. 265:273–290. 1988.

[Wol94] G. Wolf. HERA Physics. *DESY*. 22. 1994. Lectures given at 42^{nd} Scottish Universities Summer School in Physics. 1993.

[WRD+92] L. W. Whitlow. E. M. Riordon. S. Dasu. S. Rock. and A. Bodek. Precise Measurements of the Proton and Deuteron Structure Function from a Global Analysis of the SLAC Deep Inelastic Electron Scattering Cross Sections. *Phys. Lett. B*. 282(3.4):475–482. 1992.

[WW79] B. H. Wiik and G. Wolf. *Electron-Positron Interactions*. volume 86 of *Springer Tracts in Modern Physics*. Springer-Verlag. Berlin. 1979.

[You89] Edward Yourdon. *Modern Structured Analysis*. Yourdon Press Computing Series. Prentice-Hall. Inc.. Englewood Cliffs. New Jersey 07632. 1989.

[ZEU89] ZEUS UK Collaboration. C. B. Brooks et al. Development of the ZEUS Central Tracking Detector. *Nucl. Instrum. Meth. A*. 283:477–483. 1989.

[ZEU91a] ZEUS Calorimeter Group. A. Andresen et al. Construction and Beam Test of the ZEUS Forward and Rear Calorimeter. *Nucl. Instrum. Meth. A*. 309:101–142. 1991.

[ZEU91b] ZEUS Calorimeter Group. A. Andresen et al. Construction and Beam Test of the ZEUS Forward and Rear Calorimeter. *Nucl. Instrum. Meth. A*. 309:101–142. 1991.

[ZEU92a] ZEUS Collaboration. M. Derrick et al. A Measurement of $\sigma_t(\gamma p)$ at $\sqrt{s} = 210$ gev. *Phys. Lett. B*. 293:465–477. 1992.

[ZEU92b] ZEUS Luminosity Monitor Group. J. Andruszków et al. First Measurement of HERA Luminosity by ZEUS Lumi Monitor. *DESY*. 66. 1992

[ZEU93a] ZEUS Collaboration. The ZEUS Detector. Status Report. DESY. 1993.

[ZEU93b] ZEUS Collaboration. ZEUS ADAMO DDL Listing. 1993. ZEUS online and offline data format definitions.

[ZEU93c] ZEUS Collaboration. M. Derrick et al. Hadronic Energy Distributions in Deep Inelastic Electron-Proton Scattering. *Z. Phys. C.* 59:231 242. 1993.

[ZEU93d] ZEUS Collaboration. M. Derrick et al. Measurement of the Proton Structure Function F_2 in ep Scattering at HERA. *Phys. Lett. B.* 316:412 426. 1993.

[ZEU93e] ZEUS Collaboration. M. Derrick et al. Observation of Events with a Large Rapidity Gap in Deep Inelastic Scattering at HERA. *Phys. Lett. B.* 315. 1993.

[ZEU93f] ZEUS Structure Function Group. H. Abramowicz et al. A Determination of F_2 with the 1992 Data. Technical Report 78. ZEUS-Note. 1993.

[ZEU94a] ZEUS Collaboration. M. Derrick et al. Comparison of Energy Flows in Deep Inelastic Scattering With and Without a Large Rapidity Gap. *Phys. Lett. B.* 338:483 496. 1994.

[ZEU94b] ZEUS Collaboration. M. Derrick et al. Comparison of Energy Flows in Deep Inelastic Scattering Events With and Without a Large Rapidity Gap. *Phys. Lett. B.* 338. 1994.

[ZEU94c] ZEUS Collaboration. M. Derrick et al. Observation of Jet Production in Deep Inelastic Scattering With a Large Rapidity Gap at HERA. *Phys. Lett. B.* 332:228 243. 1994.

[ZEU95a] ZEUS Collaboration. M. Derrick et al. Extraction of the Gluon Density of the Proton at Small x. *Phys. Lett. B.* 345:576 588. 1995.

[ZEU95b] ZEUS Collaboration. M. Derrick et al. Measurement of Charged and Neutral Current e^-p Deep Inelastic Scattering Cross Sections at High Q^2. *DESY.* 053. 1995.

[ZEU95c] ZEUS Collaboration. M. Derrick et al. Measurement of the Proton Structure Function F_2 from the 1993 HERA Data. *Z. Phys. C.* 65:379 398. 1995.